

**9<sup>th</sup> International Workshop on  
Chemical Exchange Saturation  
Transfer Imaging**

**CEST 2022**

**Emory University  
Atlanta, GA**

# CEST 2022

## Emory Atlanta

Day 0, August 7 <sup>th</sup> , 2022 (Sunday)		
2:00 – 5:00	Registration	@ Emory Amphitheater
4:00 – 6:00 Education Session	Peter van Zijl: Basics of the Z-spectrum, CEST, NOE and MTC Dean Sherry: paraCEST agents: opportunities & limitations Ravinder Reddy: Basics of T1p and Chemical Exchange Under Spin-Locking	@ Emory Amphitheater (40 min/ talk)
6:00 – 8:00	Opening Reception	@ Silverbell Pavilion
Scientific Sessions (45 min/session): One invited talk (15 min) + Four selected talks (7-8 min/each)		
Day 1, August 8 <sup>th</sup> , 2022 (Monday) – Emory Amphitheater		
7:00 – 9:00	Expanded Continental Breakfast	@ Emory Break Room
8:00 – 8:10	Welcome/Introduction: Elizabeth Krupinski, Phillip Sun	
8:15 – 8:45	Keynote Lecture - Imaging of sugar-based contrast agents: challenges and opportunities (Linda Knutsson)	Peter van Zijl
8:45 – 9:15	Keynote Lecture - Imaging Exchange with T1rho (John Gore)	
15 min break		
9:30 – 10:20  (5 min Q&A)	SESSION 1. CEST Methods and Rigor	Tao Jin, Ravi Reddy
	Invited: QUASS CEST analysis	Phillip Sun
	Quantification of Electrostatic Molecular Binding Model Using the Water Proton Signal	Peter van Zijl
	Optimization of Saturation Power for pH-weighted MRI in Stroke Rodents	Julius Chung
	Guanidinium and amide CEST mapping of the human brain by high spectral resolution CEST at 3T	Kexin Wang
	Phosphate Form Spectroscopically Dark State Assembly Formation in Common Aqueous Solutions	Jiaqi Lu
10 min break		
10:30 – 11:20  (5 min Q&A)	SESSION 2. CEST MRI in Oncology I	Xiang Xu Daniel Gochberg
	Invited: Sugar CEST	Gil Navon
	A pH-sensitizer can improve cancer immunotherapy treatment as monitored with acidoCEST MRI	Renee L. Chin
	ALAw-CEST MRI of the ASCT2 transporter in a mouse model of prostate cancer	Behnaz Ghaemi
	Implementing a new spatial filter for improving clinical brain tumor APTw contrast at 3T	Feriel Romdhane
	Evaluation of contributors to APT-weighted imaging and NOE-weighted imaging in tumors at high fields	Zhongliang Zu
10 min break		
11:30 – 12:30	Discussion I: Rigor in CEST measurement (Quantification, Specificity and Standardization)	Greg Stanisz
Lunch		@ Dining Room
2:00 – 3:00  (15 min Q&A)	SESSION 3. Novel CEST Methods/Processing/Applications	Zhongliang Zu Mike McMahon
	Invited: Adventures in Machine learning for CEST fingerprinting	Chris Farrar
	A Generative Adversarial Network for Accelerated and Quantitative 3D Semisolid MT/CEST MRI: a Multi-Center Brain and Leg Human Study	Jonah P. W. Weigand
	Which method provides most insight into tumors – 3T (fluid suppr.) APTw, 3T CEST-MRF or 7T multi-pool CEST?	Maria Sedykh Chris Farrar
	Improved Bloch fitting and machine learning methods that analyze acidoCEST MRI	Marty Pagel
	DeepCEST: Fast mapping of 7T CEST MRI parameters with uncertainty quantification (virtual)	Leonie Hunger Moritz Zaiss
15 min break		

# CEST 2022

## Emory Atlanta

3:15	<b>SESSION 4. CEST MRI in Neurology</b>	<b>Kejia Cai, Seth Smith</b>
–	<b>Invited:</b> <i>Clinical CEST imaging of Alzheimer's disease and Parkinson's disease</i>	Jinyuan Zhou
4:15	<i>A comparison of APT analyses in acute stroke – Demonstration of highly sensitive and specific pH-weighted MRI</i>	Phillip Sun
(15 min Q&A)	<i>Early-Stage Cerebral Glutamate Mapping in APPNL-F/NL-F Mouse Model of Alzheimer's Disease Using GluCEST MRI</i>	Narayan Datt Soni
	<i>Omega plot-based quantitative in vivo CEST MRI</i>	Iris Yuwen Zhou
	<i>The application of the proton exchange rate (kex) of CEST MRI constructed from direct-saturation-removed Omega plots in ischemic stroke</i>	Keijia Cai
15 min break		
4:30 – 5:30	<b>Discussion II: How to measure exchange rate/concentration (Accuracy/limitation of reported exchange rates &amp; how to improve)</b>	<b>Tao Jin</b>
3 hours break		
8:30 – 9:30	Poster Session I	@ Hickory Room

Day 2 - August 9 <sup>th</sup> , 2022 (Tuesday) – Emory Amphitheater		
7:00 – 9:00	Expanded Continental Breakfast	@ Emory Break Room
8:15 – 8:45	Keynote Lecture – Transmembrane ion gradients using exchangeable and non-exchangeable properties of magnetic resonance (Fahmeed Hyder)	Jeff Bulte
8:45 – 9:15	Keynote Lecture – Mixed signals – past and future challenges for the understanding of in vivo CEST MRI (Moritz Zaiss)	
15 min break		
9:30 – 10:20  (5 min Q&A)	SESSION 5. CEST MRI in Oncology II	Iris Zhou Jinyuan Zhou
	Invited: Using CEST MRI to determine genetic markers in human gliomas	Shanshan Jiang
	ssMT and APT-weighted CEST imaging predict clinical outcome in the first follow up after completion of radiotherapy in glioma patients at 3T	Florian Kroh
	Enhanced diagnostic performance of APT-weighted MRI to advanced non-contrast MRI techniques in patients with post-treatment high-grade gliomas	Qianqi Huang
	Improved diagnostic accuracy of Amide Proton Transfer weighted imaging versus Dynamic Susceptibility Contrast Perfusion for the discrimination of radiation necrosis from tumor progression in brain metastases	Lucia Nichelli Stefano Casagrande
	Glioma response assessment by asymmetry-based, Lorentzian-fit-based and relaxation-compensated CEST MRI of the APT and ssMT is influenced by glioma location at 3T	Nikolaus von Knebel Doeberitz
10 min break		
10:30 – 11:20  (5 min Q&A)	SESSION 6. Emerging CEST Thoughts and Development	Guanshu Liu Daniel Paech
	Invited: Towards specific amine CEST imaging and its interpretation	Zhongliang Zu
	Fast Multi-slice Quasi-steady-state (QUASS) APT MRI – Application to Brain Tumor Patients at 3 Tesla	Hahnsung Kim
	Development of a standard phantom for CEST MRI	Marty Pagel
	Fast WASAB1 post-processing: access to rapid B0 and B1 correction in clinical routine for CEST MRI	Christos Papageorgakis
	Enhanced multipool fitting with quasi-steady-state (QUASS) CEST MRI	Phillip Sun
10 min break		
11:30 – 12:30	Discussion III: NOE/rNOE Their relative contributions to in vivo CEST and interpretation	Peter van Zijl
Lunch		@ Dining Room

# CEST 2022

## Emory Atlanta

2:00 – 3:00 (15 min Q&A)	<b>SESSION 7. CEST MRI in Body</b>	<b>Moriel Vandsburger Rachelle Crescenzi</b>
	<b>Invited:</b> Advances in cardiac CEST	Moriel Vandsburger
	<i>Spatial-Spectral Selective Pulses for B1 Compensation and Improved Saturation Homogeneity in Cardiac CEST</i>	Cindy Ayala
	<i>In vivo CEST-Dixon in axillary lymph nodes with and without biopsy-confirmed malignancy: potential for non-invasive determination of lymph node metastasis</i>	Rachelle Crescenzi
	<i>Optimization of pH-Weighted CEST Contrast in the Spinal Cord</i>	Alicia Cronin
	<i>The z-spectrum as a way to monitor fibrosis</i>	Nabeelah Jinnah
15 min break		
3:15 – 4:15 (15 min Q&A)	<b>SESSION 8. Responsive CEST contrast agents and delivery</b>	<b>Alicia Cronin Marty Pagel</b>
	<b>Invited:</b> Functional imaging of the kidneys using CEST MRI	Mike McMahon
	<i>Quantitative imaging of gene therapy delivery vehicles using CEST-NMR/MRI</i>	Bonnie Lam
	<i>Simultaneous evaluations of pH and enzyme activity with a CEST MRI contrast agent</i>	Marty Pagel
	<i>Bioconjugation of Lactate CEST-Sensors to Virus Like Particles</i>	Laurel M. Hagge
	<i>Determining the optimal saturation time for a CEST experiment</i>	Julius Chung
15 min break		
4:30 – 5:30	<b>Discussion IV: pH imaging (Exogenous vs. endogenous pH, limitations, and future developments)</b>	<b>Dean Sherry</b>
30 min break		
6:00 – 8:00	Closing Reception	@ Salon IV and Salon V
8:30 – 9:30	Poster Session II	@ Hickory Room

Day 3 - August 10 <sup>th</sup> , 2022 (Wednesday) – Emory Amphitheater		
7:00 - 9:00	Expanded Continental Breakfast	@ Emory Break Room
8:15 – 9:15 (15 min Q&A)	<b>SESSION 9. Breakthrough Applications/Analysis/Sequences</b>	<b>Jiadi Xu, Chris Farrar</b>
	<b>Invited:</b> Theranostic CEST MRI: from small molecular drugs to nanomedicine	Guanshu Liu
	<i>Mapping pH using chemical exchange mediated stimulated echoes</i>	Daniel Gochberg
	<i>GraspCEST: 3D Steady-State CEST MRI Using Golden-Angle Radial Sparse MRI</i>	Rodolphe Leforestier Xiang Xu
	<i>SNR Optimized 3D EPI CEST Imaging Using Unevenly Segmented RF Irradiation</i>	Hahnsung Kim
	<i>New Advanced Principal Component Analysis method for an improved and safe clinical 3T CEST MRI denoising</i>	Stefano Casagrande
15 min break		
9:45 – 11:00 (15 min Discussion)	<b>SESSION 10. CEST Preclinical/Clinical Translation/Partnership</b> Olea Medical, Philips, Bruker, Siemens (virtual), and GE (virtual)	Hui Mao, Marty Pagel
15 min break		
11:15 – 11:45	<b>Panel Discussion - Academic/Industry Coordination</b>	Linda Knutsson Daniel Paech
11:45 – 12:00	<b>CEST ISMRM Study Group, Farewell, and CEST2024</b>	Jiadi Xu, Phillip Sun Daniel Paech, Moritz Zaiss



## Poster program

### Session 1 (August 8<sup>th</sup>, 2022)

Presenter	Title
Zilin Chen	Relayed nuclear Overhauser effect (rNOE) and amide CEST detects myelin changes in cuprizone mouse model at 3T
Eleni Demetriou	The use of frequency selective pulses with filtered frequencies for eliminating magnetization transfer contrast in CEST.
Joseph H. C. Lai	Relayed nuclear Overhauser effect (rNOE) imaging for deferoxamine (DFX) treatment effect in intracerebral hemorrhage (ICH) at 3T
Anna M. Li	Age dependent cerebrospinal fluid-tissue water exchange detected by non-invasive magnetization transfer indirect spin labeling MRI
Fang Frank Yu	Healthy vs pathological tau can be differentiated by CEST NMR
Haochuan Gan	Brain glioma PH imaging using chemical exchange saturation transfer (CEST) MRI
Lihua Lai	Amide proton transfer imaging allows early detection of a therapeutic response with temozolomide in glioma
Se Weon Park	Multiparametric monitoring local brain tumor treatment using CEST-detectable liposomal hydrogel at 3T
Michal Rivlin	Glucosamine Chemical Exchange Saturation Transfer (GlcN-CEST) MRI in breast cancer: from mice to humans
Moritz Zaiss	Removing fluid artifacts in APTw: why spillover correction and fluid suppression are two sides of the same coin
Joshua Brown	Chemical Exchange Saturation Transfer MRI in Non-Lesional Temporal Lobe Epilepsy Imaging
Ibrahim Khormi	Utility of Amide Proton Transfer Weighted Imaging in Multiple Sclerosis
Ravi Prakash Reddy Nanga	CEST imaging of Glutamate and myo-Inositol <i>in vivo</i> for early-stage changes in 5xFAD Alzheimer's mouse model
Jianzhong Yin	Distinguish the progressive penumbra of the diffusion-perfusion mismatch region by amide proton transfer MRI
Moritz Simon Fabian	7T multi-pool CEST MRI in multiple sclerosis patients

### Session 2 (August 9<sup>th</sup>, 2022)

Eleni Demetriou	High rotating frame relaxation MRI mapping for detecting ischemia in rats
Giulia Vassallo	31ParaCEST: 31P MR-CEST Imaging based on the formation of ternary adduct between HPO <sub>4</sub> <sup>2-</sup> and Eu(III)DO <sub>3</sub> A
Jianpan Huang	Effect of hyperoxia on dynamic glucose enhanced MRI in mouse brain at 3T
Kasturee Chakraborty	Creatine Chemical Exchange Saturation Transfer (CrCEST) MRI Reproducibility in healthy adults at 3T
Peihong Zhang	Quantitative Study on Monitoring Cartilage Degeneration of Porcine Knee Based on 7.0T Multimodal MRI
Blake Benyard	Reproducibility of 3D NOE-MTR in healthy human volunteers at 7T
David R. Roalf	An automated and robust analysis pipeline for 7T GluCEST data
Moritz Simon Fabian	7T comprehensive CEST – a clinically feasible multi-exchange-regime CEST protocol

Lukas Kamm	comprehenCEST: a clinically feasible CEST protocol to cover all existing CEST preparation schemes by snapshot readout and reduction of overhangs
Rhith Saai Pemmasani Prabakaran	Multi-offset super-resolution for accelerating CEST MRI acquisition using deep-transfer learning
Patrick Schunke	Simultaneous Mapping of B0, B1 and T1 With Aleatory and Epistemic Uncertainty Estimations
Jianping Xu	Accelerating chemical exchange saturation transfer imaging using a model-based deep neural network
Fabian T. Gutjahr	Saturation and Phase Sensitive Water Exchange Spectroscopy
Mehran Shaghghi	Toward in vivo MRI of tissue proton exchange rate
Ding Xia	CEST MRI Using Golden-Angle Cartesian Acquisition at 7T
Yaotian Tian	Three-Dimensional Amide Proton Transfer (APT) Imaging Can Identify the Changes of Cerebral Cortex in Parkinson's Disease

Day 1 (Monday, 8<sup>th</sup> August 2022)

# Quantification of Electrostatic Molecular Binding Model Using the WaterProton Signal

Peter C. M. van Zijl<sup>1,2</sup>, Chongxue Bie<sup>1,2,3</sup>, Yang Zhou<sup>1,2,4</sup>, Jiadi Xu<sup>1,2</sup>, Chao Zou<sup>4</sup>, and Nirbhay N. Yadav<sup>1,2</sup>

<sup>1</sup> F.M. Kirby Research Center for Functional Brain Imaging, Kennedy Krieger Institute, 707 N. Broadway, Baltimore MD 21205 (USA); <sup>2</sup> The Russell H. Morgan Department of Radiology, The Johns Hopkins University School of Medicine, 720 Rutland Ave, Baltimore, MD 21205 (USA); <sup>3</sup> Department of Information Science and Technology, Northwest University, No.1 Xuefu Avenue, Xi'an, Shaanxi 710127 (China); <sup>4</sup> Key Laboratory for Magnetic Resonance and Multimodality Imaging of Guangdong Province, Shenzhen Institute of Advanced Technology, Chinese Academy of Sciences, 1068 Xueyuan Avenue, Shenzhen University Town, Shenzhen, Guangdong 518055 (China)

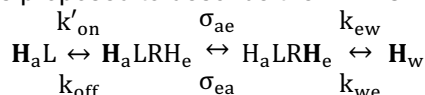
□ Apply Student/Postdoc Travel Fund; ☒ Either Oral or Poster Presentation | Contact Email: pvanzijl@jhu.edu

KEYWORD: ☒ Contrast Mechanism ☒ Novel Acquisition

## INTRODUCTION:

Electrostatic interactions play a fundamental role in mediating molecular interactions in many biochemical processes. It was previously shown that transient molecular binding can be imaged using a saturation transfer (ST) approach for enhancing sensitivity,<sup>1</sup> the so-called IMMOBILISE (for “IMaging of MOlecular BLinding using Ligand Immobilization and Saturation Exchange”) method. We show that this approach can be used to image the binding of small charged molecules (arginine, Arg, choline, Cho, and acetylcholine, ACh) via electrostatic interactions to immobile ionic receptors. We describe the mechanism of signal enhancement through molecular binding and relayed NOEs, and quantify binding affinities.

**METHODS:** The aliphatic protons of free ligands were selectively labelled using RF, and the labelling transferred to water via several possible binding-mediated pathways (**Figure 1**). The following four-pool model was proposed to describe the “IMMOBILISE” process,



$k_{on}$  and  $k_{off}$  are ligand binding on/off rates. At equilibrium,  $k_{on}[R][L] = k_{off}[LR]$ ;  $[L]$ ,  $[R]$  and  $[LR]$  are concentrations of free ligand, free receptor, and bound receptor, resp. Total receptor concentration  $[R_T] = [LR] + [R]$ .

$k'_{on} = k_{on}[R]$ .  $\sigma_{ae}$  and  $\sigma_{ea}$  are the effective cross relaxation rates from receptor-bound-ligand aliphatic protons ( $H_aLR$ ) to either exchangeable protons ( $LRH_e$ ) or bound water in the macromolecule and back.  $k_{ew}$  and  $k_{we}$  are effective saturation transfer rates from  $LRH_e$  to free water ( $H_w$ ) and back, corresponding to either the proton or water molecular exchange rates. The analytical solution of the rNOE signal was obtained:  $rNOE = rNOE_{max} \cdot ([L]/([L] + K_D))$ , in which  $rNOE_{max}$  is a constant that determines the maximum detected signal,  $K_D$  ( $K_D = k_{off}/k_{on}$ ), the dissociation constant. Various concentrations (10-200 mM) of Arg, Cho, and ACh were dissolved in PBS and mixed with ion-exchange media (Macro-Prep CM Support, with functional groups -COO-). The mixture was pH-adjusted (7.2) and transferred to the imaging tube.

**RESULTS:** The Z-spectra of IMMOBILISE experiments for Arg, Cho, and ACh are in **Figure 2**, showing aliphatic rNOE signals for Arg at -0.9, -1.6, and -2.0 ppm, for Cho at -1.6 ppm, and for ACh at -1.6 and -2.6 ppm. ACh has no exchangeable protons, proving one pathway to be intermolecular rNOEs. The results (**Table 1**) show that  $K_D$  values fitted from three individual peaks of Arg were ~130 mM. ACh has a higher binding affinity (smaller  $K_D$ ) compared to Cho.

**DISCUSSION AND CONCLUSION:** The quantification of electrostatic molecular binding using IMMOBILISE MRI was demonstrated for several small charged molecules. Experimentally, we showed that the molecular binding of mM level concentration of ligands can be detected by the signal enhancement mechanism, showing potential for the possibility of in vivo studies of molecular binding using IMMOBILISE MRI.

**REFERENCES:** 1) Yadav NN et al. Sci Rep. 2017;7:10138.

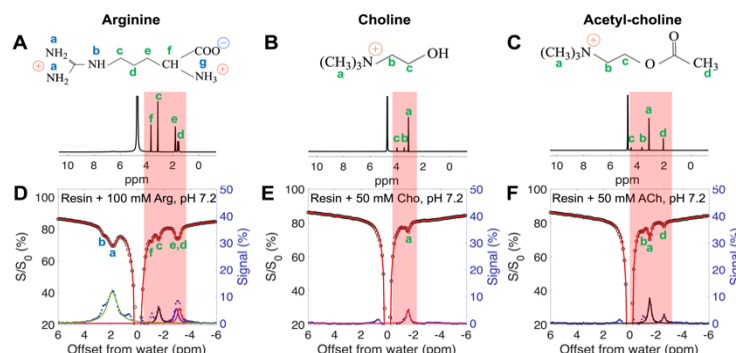
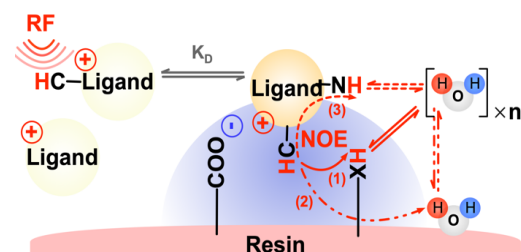


**Figure 2.** Z-spectra of small charged molecules mixed with ionic resin.

**Table 1.** Estimated  $K_D$  (mM) for L-arginine, Choline, and Acetylcholine binding with ionic resin (-COO-).

	Arg			Cho	ACh	
$\Omega_a^L$ (ppm)	-1.6	-2.9	-3.1	-1.6	-1.6	-2.6
0.3 $\mu$ T	101 $\pm$ 47	150 $\pm$ 51	122 $\pm$ 55	145 $\pm$ 56	91 $\pm$ 18	105 $\pm$ 62
0.5 $\mu$ T	147 $\pm$ 37	147 $\pm$ 40	139 $\pm$ 40	194 $\pm$ 73	61 $\pm$ 10	109 $\pm$ 58
0.7 $\mu$ T	117 $\pm$ 32	113 $\pm$ 32	126 $\pm$ 35	174 $\pm$ 76	68 $\pm$ 12	99 $\pm$ 45
multi-B <sub>1</sub>	128 $\pm$ 34	132 $\pm$ 34	133 $\pm$ 33	160 $\pm$ 22	70 $\pm$ 8	103 $\pm$ 30

# Optimization of Saturation Power for pH-weighted MRI in Stroke Rodents

Julius Chung and Tao Jin

Department of Radiology, University of Pittsburgh, Pittsburgh, PA 15203

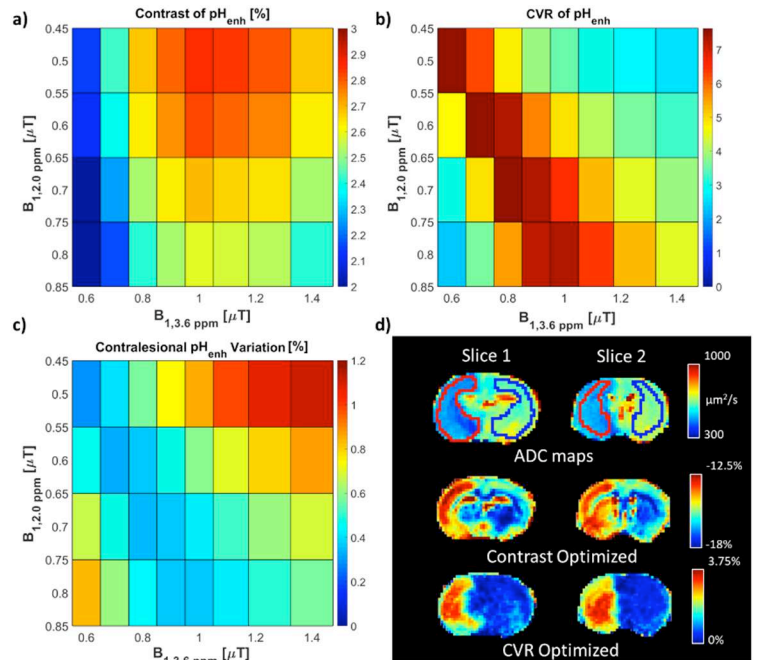
✉ Apply Student/Postdoc Travel Fund ✉ Either Oral or Poster Presentation | Contact Email: juc98@pitt.edu

KEYWORD: ✉ CEST agents ✉ Contrast Mechanism

**INTRODUCTION:** The sensitivity of CEST to pH makes it a potential modality for the assessment of intracellular pH alterations under pathologic conditions. Our group has previously introduced a method for pH-weighted MRI<sup>1</sup> (pH<sub>enh</sub> MRI) which capitalizes off of the ubiquity of peptide bonds bearing amide protons and amino acid side chains containing guanidyl protons in the brain to enhance the pH sensitivity of CEST imaging. However, since amide protons and guanidyl protons bear disparate exchange rates, optimal saturation power for these two labile proton species is also different. In this study, we seek to determine saturation powers for imaging both of these exchangeable protons to optimize either the contrast or contrast-to-variation ratio (CVR) between healthy and ischemic tissue in stroke rats in order to optimize pH-weighted MRI.

**METHODS:** Imaging of MCAO rats (n=5) was performed 3-4 hours post-operation using 4-s continuous wave saturation preparation with B<sub>1</sub>=0.50, 0.60, 0.70, and 0.80  $\mu$ T at 2.0 ppm, B<sub>1</sub>=0.60, 0.70, 0.80, 0.90, 1.00, 1.10, 1.25, and 1.40  $\mu$ T at 3.6 ppm, and a 300 ppm image at B<sub>1</sub>=1.00  $\mu$ T. Two slice spin-echo EPI was read-out: matrix size= 80×80, field of view= 32×32 mm, slice thickness= 2 mm, TR= 8 s and TE= 20 ms. ADC maps were acquired and ROIs were drawn in the lesion and then reflected over the center of the brain to obtain an ROI over which the contralesional signal would be averaged over. CEST signals for pH weighting were calculated as follows: pH<sub>enh</sub>= (S<sub>3.6ppm</sub>[B<sub>1,3.6ppm</sub>]-S<sub>2.0ppm</sub>[B<sub>1,2.0ppm</sub>])/S<sub>0</sub><sup>1</sup>. Contrast was calculated by subtracting the pH<sub>enh</sub> averaged over the contralesional ROI from the average over the lesion while the spatial variation was calculated by the standard deviation of pH<sub>enh</sub> over the whole contralesional hemisphere with CVR being the ratio between this contrast and variation value.

**RESULTS:** The contrast between the lesion and contralesional tissue for pH<sub>enh</sub> is greatest using a B<sub>1,2.0ppm</sub> of 0.5  $\mu$ T and a B<sub>1,3.6ppm</sub> of 1.0  $\mu$ T with a mean contrast of 2.86% (Fig. 1a). However, the CVR for this pairing was only 3.47 (Fig. 1b) due to the high variation in the tissue which resulted in a relatively large standard deviation in the contralesional tissue of 0.86% (Fig. 1c). Conversely, the largest CVR between the lesion and contralesional tissue for pH<sub>enh</sub>, 7.62, was obtained using a B<sub>1,2.0ppm</sub> of 0.6  $\mu$ T and a B<sub>1,3.6ppm</sub> of 0.7  $\mu$ T. This was a result of the contrast between the tissues being 2.38% while the variation was a standard deviation of 0.32%. Maps of pH<sub>enh</sub> in an exemplary rodent demonstrate the differences in optimal parameters for contrast and CVR (Fig. 1d). Optimizing purely for contrast result in pH<sub>enh</sub> signals that are inherently negative. Scaling the maps around the contrast between the lesion and contralesional results in a relatively broad scale (~5.5%) from -18% to -12.5% while it is clear that there is a significant amount of contrast between grey and white matter that is not specific to pH change. On the other hand, optimizing around CVR results in scaling that while being narrower (~3.75%) remains purely positive (0 to 3.75%). Optimizing around CVR minimizes contrast within the contralesional tissue while preserving the contrast between the two tissues.



**DISCUSSION:** There were two major targets for optimization of pH-weighted MRI, contrast and CVR. CVR was strongly affected by the spatial heterogeneity in the pH<sub>enh</sub> map which can have significant contributions that are non-specific to CEST and, hence, pH (e.g. MT and NOE). Optimizing CVR would be favorable for applications where the differentiation of spatial regions with a small pH change is important. In contrast, optimizing contrast may play a role when the detection of a temporal change of pH is desired so that the spatial heterogeneity is less important since it is unlikely to change over time and will ultimately be subtracted out.

**CONCLUSION:** pH<sub>enh</sub> MRI is a useful method for the detection of pH alterations which can be tuned by optimization of either contrast or CVR to maximize sensitivity to pH changes or minimize background spatial contrasts.

## REFERENCES:

1. Jin T, *et al.* Neuroimage 2017;157:341-350.



# Guanidinium and amide CEST mapping of human brain by high spectral resolution CEST at 3T

Kexin Wang<sup>1,2\*</sup>, Sooyeon Park<sup>1,2\*</sup>, David Olayinka Kamson<sup>2</sup>, Yuguo Li<sup>1,2</sup>, Guanshu Liu<sup>1,2</sup>, Jiadi Xu<sup>1,2</sup>

<sup>1</sup> Kennedy Krieger Research Institute <sup>2</sup> Johns Hopkins University School of Medicine, Baltimore, MD, USA

☑ Oral Presentation ☐ Poster ☐ Either Oral or Poster Presentation | Contact Email: xuj@kennedykrieger.org

**KEYWORD:** You are encouraged to choose one or two keywords. ☐ CEST agents ☑ Contrast Mechanism

☐ Tumor ☐ Stroke ☑ Neurology ☐ Body & MSK ☐ Standardization ☐ Novel Acquisition ☐ Machine Learning

**INTRODUCTION:** Guanidinium CEST (GuanCEST) denotes the peak at 2 ppm, including mixed signal of ArgCEST with creatine and phosphocreatine CEST (CrCEST/PCrCEST), which has been observed at the high field but never on 3T MRI. Recently, a study on rat brain at 4.7T clearly showed the feasibility of ArgCEST mapping at lower fields with high spectral resolution (HSR) CEST (1), which is further supported by our latest measurement of *in vivo* ArgCEST exchange rate at around 70 s<sup>-1</sup> (2). Here HSR-CEST was applied to extract both Guan and amide CEST using polynomial Lorentzian line-shape fitting (PLOF) at 3T. Two rapid CEST acquisition schemes, i.e. continuous wave gradient- and spin-echo (cwGRASE) and steady-state EPI (ssEPI), were applied and compared to achieve multi-slice in clinically feasible time.

**METHODS:** 12 healthy subjects (22-62 years old) went through scans on a Philips MR Ingenia Elition 3.0T. A single slice cw Turbo Spin-Echo (cwTSE) sequence was used to optimize the B<sub>1</sub> value (found to be 0.8 μT and fixed for all the three methods) and serve as a reference for determining the labeling efficiency. The cw saturation = 1 s, TR/TE = 3500/5.6 ms, refocusing angle = 120°, TSE factor = 37. The total 69 saturation offsets were swept from 8.0 to -2.2 ppm with a step of 0.2 ppm with denser sampling in the range of 1.1 to 4.0 ppm (a step of 0.1 ppm). Two fast acquisition methods: cwGRASE and ssEPI, use the same geometry but 13 slices. For 3D readout cwGRASE, saturation = 0.95 s, TR/TE = 3000/13 ms, EPI factor = 13, TSE factor = 13, and scan time = 7 min. For the multi-slice ssEPI: EPI factor = 17, TR/TE = 1326/6.9 ms, flip angle = 10°, and total scan time = 6 min.

**RESULTS:** The PLOF fitting method was demonstrated for the background fitting (Fig. 1a) and the Guan/amide peaks (Fig. 1b-c yellow/green). Center offsets of (2.28 ± 0.04) and (3.50 ± 0.03) ppm for Guan and amideCEST were extracted. Both Guan and amideCEST maps are homogenous across the whole brain acquired with cwGRASE (Fig. 2a), while strong WM/GM contrasts were observed for both Guan and amideCEST maps collected with ssEPI (Fig. 2b). The averaged Guan and amideCEST values in GM (Fig. 2c) and WM (Fig. 2d) recorded with cwTSE (n=6), cwGRASE (n=3), and ssEPI (n=3) are shown in Figs. 2c&d.

**DISCUSSION AND CONCLUSION:** The strong GuanCEST signal can be clearly visible at 3T with HSR-CEST and B<sub>1</sub>=0.8 μT. The extracted HSR-CEST spectrum with the PLOF approach is closely resemble to the downfield MRS from exchangeable protons recorded on the human brain (3), which further validates the fitting method. The GuanCEST has not been well studied on 3T MRI mainly due to (i) too few offsets to separate the overlapped Guan and amideCEST peaks, (ii) too high saturation power (around 2 μT) which dramatically decreases the Guan signal. The cw scheme provides the highest signal as measured by both cwTSE and cwGRASE methods. Therefore, the cwGRASE method is suggested for Guan and amideCEST studies. In the steady-state CEST method, i.e. ssEPI, the contrast is completely different from that of cw labeling, which leads to great difficulty in modeling it. This study paves the way for simultaneously Guan and amide CEST mapping within a clinically feasible scan time.

**REFERENCES:** 1. Zhou M, *et al.* Magn Reson Med 2019;81:645-652; 2. Wang K, *et al.* bioRxiv 2022; DOI: 10.1101/2022.02.14.480399; 3. Považan M, *et al.* Magn Reson Med 2021; 87: 1661-1672

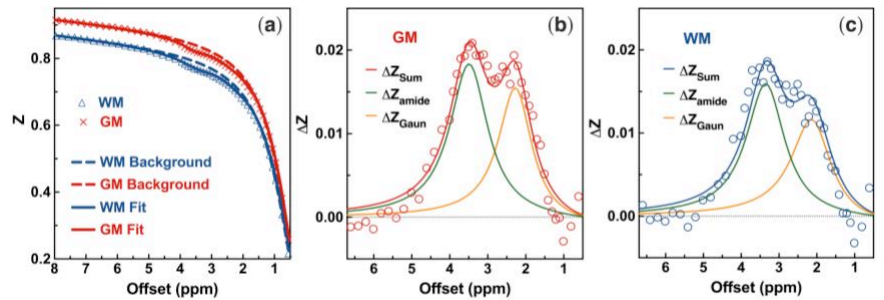


**Figure 1.** Extraction and quantification of Guan and amide CEST with the PLOF method for the TSE method. (a) PLOF fitting of both background and Z-spectra. Guan (yellow line) and amide (green line) CEST peaks and the sum of them are presented for (b) GM and (c) WM.

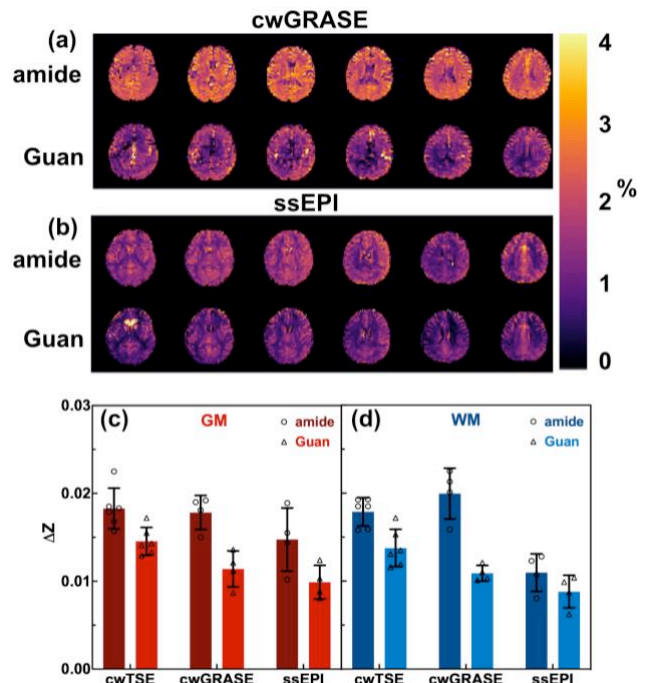


**Figure 2.** Typical amide and Guan CEST maps of (a) cwGRASE and (b) ssEPI on the same subject. Averaged amide and Guan CEST signal extracted from the Z-spectra recorded with three methods in (c) GM and (d) WM.



# Phosphate Form Spectroscopically Dark State Assembly Formation in Common Aqueous Solutions

Jiaqi Lu<sup>1</sup>, Joshua Straub<sup>2</sup>, Mesopotamia Nowotarski<sup>2</sup>, Tanvi Sheth<sup>2</sup>, Sally Jiao<sup>2</sup>, Matthew P.A. Fisher<sup>2</sup>, M. Scott Shell<sup>2</sup>, Matthew E. Helgeson<sup>2</sup>, Song-I Han<sup>2</sup>, Alexej Jerschow<sup>1</sup>

New York University, NY, US<sup>1</sup>, University of California - Santa Barbara, CA, US<sup>2</sup>

☒ Apply Student/Postdoc Travel Fund

☐ Oral Presentation ☐ Poster ☒ Either Oral or Poster Presentation | Contact Email: j110440@nyu.edu

KEYWORD: You are encouraged to choose one or two keywords. ☒ CEST agents ☒ Contrast Mechanism

Phosphates and polyphosphates play ubiquitous roles in biology as integral structural components of cell membranes and bone, or as vehicles of energy storage via adenosine triphosphate and phosphocreatine. The solution phase space of phosphate species appears more complex than previously known. We present NMR based experiments that suggest phosphate species including orthophosphates, pyrophosphates and adenosine phosphates associate into dynamic assemblies in dilute solutions that are spectroscopically 'dark'.

<sup>31</sup>P NMR is commonly used to characterize the composition, dynamics and structural properties of biomolecules and lipid interfaces. While performing <sup>31</sup>P NMR to investigate the native state of phosphate species as a function of temperature, we encountered peculiar line broadening and relaxation effects that cannot be explained by typical dynamical processes of small molecules (Fig. 1). We will present results showing that phosphate containing species reversibly assemble into unreported spectroscopically "dark" species that have much higher R<sub>1</sub> and R<sub>2</sub> rates and whose population is in exchange with the NMR-detectable phosphate species.

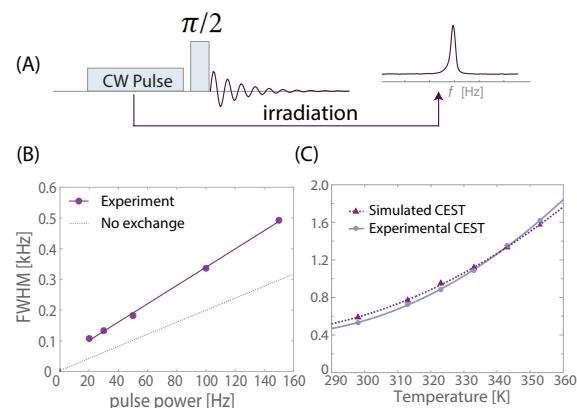


**Figure 2.** <sup>31</sup>P CEST results for 100mM orthophosphate (pH=4.5). (A) CEST pulse sequence (B) CEST z-spectra linewidth as a function of irradiation power at room temperature. (C) Experimental and Simulated CEST z-spectra linewidth as a function of temperature with 150Hz of irradiation power.

supporting our hypothesis that orthophosphates assemble into assemblies, some of which are spectroscopically invisible but are in exchange with the detectable phosphate species.

The NMR-based observation is shown to be consistent with the formation of soft phosphate assemblies. The formation of spectroscopically dark states appears largely reversible (by cooling to room temperature) with a minor irreversible component. These findings suggest an entropically driven association mechanism, with enhanced populations and/or exchange rates at elevated temperatures. We show that assembly can be facilitated by the addition of depletants and modulated by changing counterion salt type, with trends found in line with the Hofmeister series. <sup>31</sup>P NMR Diffusion Oriented Spectroscopy (DOSY) revealed an increase in diffusion coefficients at elevated temperatures of 70 °C, indicative of dehydration.

This study presents the surprising discovery that phosphate-containing molecules ubiquitously present in the biological milieu can readily form dynamic assemblies largely invisible to NMR spectroscopy under a wide range of commonly used solution conditions, highlighting a hitherto unreported property of phosphate's native state in biological solutions.

## References:

[1] Vallurupalli, Bouvignies, and Kay, *Journal of the American Chemical Society* 134, 8148-8161 (2012).

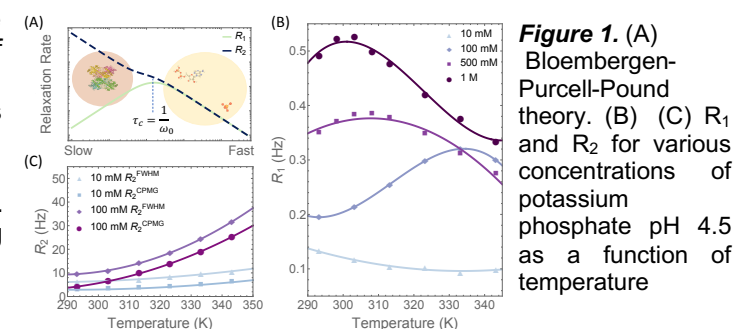


**Figure 1.** (A) Bloembergen-Purcell-Pound theory. (B) (C) R<sub>1</sub> and R<sub>2</sub> for various concentrations of potassium phosphate pH 4.5 as a function of temperature

To further explore whether the phosphate species are in exchange with a spectroscopically dark population, we performed chemical exchange saturation transfer (CEST) experiments. CEST provides a means of identifying signatures of exchangeable species with distinct chemical shifts from the visible species, but far below NMR spectroscopic detection limits. This effect is achieved by saturating a selected region in the (spectroscopically invisible) spectrum, followed by the detection of the signal of a major species that is in exchange with the species below the NMR detection limit. Repeating these experiments with different saturation regions allows scanning a whole spectrum for potentially exchanging species. This procedure can also be used to prove the existence of macromolecular pools with broad spectroscopic features, and has been employed, for example, to identify "dark" and weakly populated states in peptides and proteins.[1] Our CEST dip widths were found to be much wider than what one would expect from the spectral linewidth (by approximately a factor 2-3 larger than the rf saturation bandwidth) in the absence of exchange (Fig. 2B). The results indicate that exchange occurs with a population with a broad spectroscopic signature, invisible in direct spectroscopic measurements. This population appears to increase with temperature as shown by an increase in dip width (Fig. 2C), thereby

## A pH-sensitizer can improve cancer immunotherapy treatment as monitored with acidoCEST MRI

Renee L. Chin,<sup>1,2</sup> Jorge de la Cerda,<sup>1</sup> F. William Schuler,<sup>1</sup> Mark D. Pagel<sup>1</sup>

<sup>1</sup> Department of Immunology, University of Texas MD Anderson Cancer Center, Houston, TX, USA

<sup>2</sup> Department of Cancer Systems Imaging, University of Texas MD Anderson Cancer Center, Houston TX, USA

✉ Either Oral or Poster Presentation | Contact Email: [mdpagel@mdanderson.org](mailto:mdpagel@mdanderson.org)

KEYWORD: ☑ Tumor

**INTRODUCTION:** Tumor acidosis causes resistance to immune checkpoint blockade (ICB), primarily by inhibiting T cell activation in the tumor microenvironment.<sup>1</sup> Reducing tumor acidosis by inhibiting mechanisms of extracellular acidification may improve the effect of immunotherapy.<sup>2</sup> We refer to these inhibitors as “pH-sensitizers”. AcidoCEST MRI can longitudinally measure extracellular pH (pHe) in the tumor microenvironment.<sup>3</sup> Therefore, acidoCEST MRI may be able to evaluate the early response to pH-sensitizers to ensure that the tumor has been sufficiently sensitized before starting ICB treatment.

**METHODS:** To perform *in vitro* studies, we screened a panel of small molecule inhibitors that target 4T1 and tumor cell mechanisms that acidify the tumor microenvironment. We used a Seahorse instrument to measure the proton efflux rate and extracellular acidification rate. We also tested the toxicity of each inhibitor against 4T1 tumor cells and T cells, and we evaluated T cell inactivation after treatment with each inhibitor.

To perform *in vivo* studies, we treated a 4T1 orthotopic tumor model with esomeprazole (a VATPase inhibitor) and immune checkpoint blockade (anti-CTLA-4 and anti-PD-1), with 0, 1, and 3 days between treatment with the inhibitor vs. ICB. We also tested esomeprazole, ICB, and no treatment as controls. We monitored tumor volume and survival following treatment. We also performed flow cytometry to characterize the T cell infiltration and activation in tumors. In a separate *in vivo* study, we used acidoCEST MRI to measure tumor pHe 1 day after administering esomeprazole to the 4T1 model.

**RESULTS:** The *in vitro* studies identified esomeprazole as the best inhibitor for raising tumor pHe, while causing no significant toxicity to tumor cells or T cells, and without inhibition of T cell activation. The *in vivo* studies showed that esomeprazole followed one day later with ICB significantly delayed tumor growth and increased survival, while combinations with different timings did not significantly improve treatment effect, and treatments with only esomeprazole or ICB also showed no significant effect (Figure 1). The effective combination of esomeprazole followed 1 day by ICB increased the intratumoral ratio of CD8<sup>+</sup> T cell to Ly6C<sup>+</sup> myeloid cells, showing that esomeprazole enhanced T cell activity.

AcidoCEST MRI measurements of tumor pHe 1 day after administering esomeprazole revealed a range of increases in pHe among the tested tumors, indicating variability in response to esomeprazole. This variability in pHe response was an advantage in our study, because the mass of 4T1 tumors treated with esomeprazole and ICB negatively correlated with tumor pHe measured 1 day of esomeprazole treatment (Figure 2).

**DISCUSSION:** Our results demonstrate that a single dose of esomeprazole can improve tumor control with ICB. However, testing multiple doses of esomeprazole is warranted, and other pH-sensitizers should also be tested, to optimize the pH-sensitization prior to starting ICB treatment. Testing other tumor cell types is especially warranted to investigate the robustness of this approach for improving immunotherapy against many cancer types. Furthermore, the effect of esomeprazole on tumor

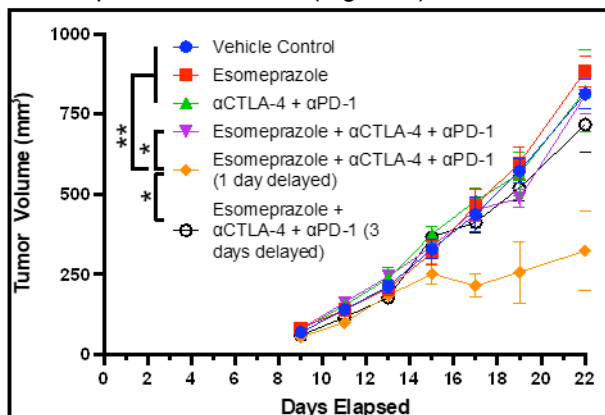


**Figure 1: Combination of ICB and esomeprazole delivered one day prior delays tumor growth by increasing tumor immunogenicity.** Mice orthotopically implanted with or 4T1 cells were treated with the respective treatments, and the resulting tumor growth kinetics are shown.  $n = 4 - 5$ .

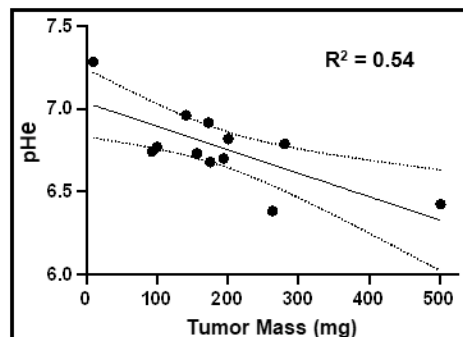


**Figure 2: Esomeprazole and 1-day delayed ICB promotes tumor response in a pHe-specific manner.** 4T1 tumor weights 22 days after esomeprazole and ICB treatment significantly correlated with pHe as measured with acidoCEST MRI. The 95% confidence interval is shown as dotted lines, and the  $R^2$  correlation coefficient is also listed.

pHe measured 1 day after treatment was variable, suggesting that acidoCEST MRI measurements of tumor pHe at earlier or later time points may be needed to monitor the longitudinal effect of a pH-sensitizer.

**CONCLUSIONS:** A pH-sensitizer can improve cancer immunotherapy treatment as monitored with acidoCEST MRI.

**ACKNOWLEDGMENTS:** Our research is supported by the NIH/NCI through grants R01 CA231513 and P30 CA016672.

**REFERENCES:** 1. Gerweck LE, Seetharaman K. Cellular pH gradient in tumor versus normal tissue: potential exploitation for the treatment of cancer. *Cancer Res* 1996;56:1194-1198. 2. Pilon-Thomas S, *et al.* Neutralization of Tumor Acidity Improves Antitumor Responses to Immunotherapy. *Cancer Res*, 2016;76:1381-1390. 3. Chen LQ, *et al.* Evaluations of extracellular pH within in vivo tumors using acidoCEST MRI. *Magn Reson Med*, 2014;72:1408-1417.

# ALAw-CEST MRI of the ASCT2 transporter in a mouse model of prostate cancer

Behnaz Ghaemi<sup>1,2</sup>, Yuguo Li<sup>3</sup>, Martin G. Pomper<sup>1</sup>, Jeff W.M. Bulte<sup>1,2</sup>, Peter C.M. van Zijl<sup>1,3</sup>, Aline M. Thomas<sup>1,2</sup>

<sup>1</sup>The Russell H. Morgan Department of Radiology and Radiological Science, School of Medicine, Johns Hopkins University, Baltimore, MD; <sup>2</sup>Cellular Imaging Section and Vascular Program, Institute for Cellular Engineering, Johns Hopkins School of Medicine, Baltimore, MD; <sup>3</sup>F.M. Kirby Center for Functional Brain Imaging, Kennedy Krieger Institute, Baltimore, MD.

☑ Apply Student/Postdoc Travel Fund

☐ Oral Presentation ☐ Poster ☑ Either Oral or Poster Presentation | Contact Email: [bghaemi1@jhu.edu](mailto:bghaemi1@jhu.edu)

**KEYWORD:** You are encouraged to choose one or two keywords. ☑ CEST agents ☐ Contrast Mechanism

☑ Tumor ☐ Stroke ☐ Neurology ☐ Body & MSK ☐ Standardization ☐ Novel Acquisition ☐ Machine Learning

## INTRODUCTION:

Alanine serine cysteine transporter 2 (ASCT2), a neutral amino acid transporter, is a prognostic marker for several types of cancer<sup>1-3</sup>. CEST MRI can detect alanine, a well-recognized substrate for ASCT2<sup>4</sup>, through the water-exchanging protons in its amine group<sup>5-7</sup>. We investigated the utility of alanine-weighted (ALAw)-CEST MRI to evaluate ASCT2 by comparing LNCaP and DU-145 prostate cancer cells, which have higher and lower ASCT2 expression, respectively<sup>8,9</sup>.

## METHODS:

**Prostate cancer model:** DU-145 (2-3x10<sup>6</sup>; n=9) or LNCaP (3-5x10<sup>6</sup>; n=8) cells were subcutaneously injected into 6-10 week old Rag2<sup>-/-</sup> mice. **Immunostaining:** Cells were stained with rabbit anti-ASCT2 (Cell Signaling Technology, clone v501). **CEST MRI:** Mice were imaged using a Bruker 11.7T horizontal bore spectrometer and an 8-channel TR coil. Dynamic CEST images were collected at the +3.1 ppm amine proton frequency (B<sub>1</sub> = 3.6  $\mu$ T, t<sub>sat</sub> = 3 s) prior to alanine (6 mmole/kg IV) injection to establish a baseline and over a period of 60 minutes after injection. Dynamic CEST enhancement ( $\Delta S(t)/S_0$ ) was quantified by subtracting the signal (S/S<sub>0</sub>) at time t from the average signal obtained prior to injection. **Statistics:** A two-way ANOVA was performed with p<0.05 considered significant.

## RESULTS:

ASCT2 expression was higher in the LNCaP prostatic cell line (**Figure 1**). CEST enhancement trends were significantly higher in LNCaP tumors than DU-145 tumors (**Figure 2**).

## DISCUSSION:

CEST MRI detected the higher uptake of alanine, a natural ASCT2 substrate, in LNCaP versus DU-145 tumors, as expected based on the uptake of [14C]-labeled glutamine and other ASCT2 substrates *in vitro*<sup>10,11</sup>.

## CONCLUSION:

This work preliminarily demonstrates the potential of CEST MRI to monitor ASCT2, a prognostic marker of many cancers and an active target for cancer therapy.

## REFERENCES:

- (1) Sun, H.-W., et al., PLOS ONE, 2016. 11(12): p. e0168907. (2) Shimizu, K., et al., British Journal of Cancer, 2014. 110(8): p. 2030-2039. (3) Bernhardt, S., et al., Breast Cancer Research, 2017. 19(1): p. 112. (4) Foster, A.C., et al., PLOS ONE, 2016. 11(6): p. e0156551. (5) Chen, J., et al., NMR in Biomedicine, 2020. 33(1): p. e4188. (6) Cai, K., et al., Molecular Imaging and Biology. 2014. 16(5):670-9. (7) Walker-Samuel, S., et al., Nature Medicine. 2013. 19(8):1067-72. (8) Wang, Q., et al., The Journal of Pathology, 2015. 236(3): p. 278-289. (9) Cardoso, H.J., et al., Cellular Oncology, 2021. 44(2): p. 385-403. (10) Okudaira, H., et al., Molecular Imaging and Biology, 2014. 16 (6), p. 756-764. (11) Oka, S., et al., Nuclear Medicine and Biology, 2012. 39 (1), p. 109-119.

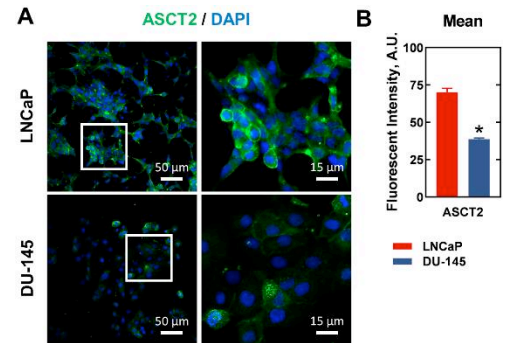


**Figure 1. ASCT2 expression in prostate cancer cell lines.**

(A) Visualization and (B) quantification of the ASCT2 transporter in LNCaP and DU-145 cell lines.

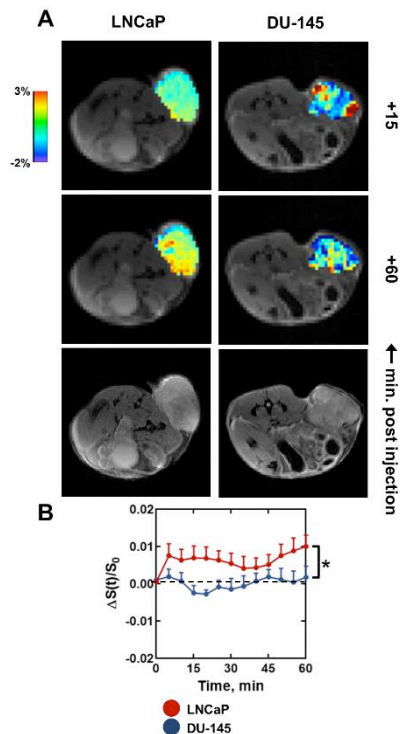


**Figure 2. CEST MRI in prostate tumors.** (A) Visualization of CEST signal enhancement at the +3.1 ppm frequency upon alanine injection in LNCaP tumors (Left; n=8) and DU-145 tumors (Right; n=9). T2-weighted images are shown for reference. (B) Quantification in tumors over the course of the scan. \* indicate significant differences (p<0.05).



# Implementing a new spatial filter for improving clinical brain tumor APTw contrast at 3T

Feriel Romdhane<sup>1,2</sup>, Dario Livio Longo<sup>1</sup>, Christos Papageorgakis<sup>2</sup>, Eleni Firippi<sup>2</sup>, Laura Mancini<sup>3,4</sup>, Sotirios Bisdas<sup>3,4</sup>, Moritz Zaiss<sup>5</sup> and Stefano Casagrande<sup>2</sup>

<sup>1</sup>*Institute of Biostructures and Bioimaging (IBB), National Research Council of Italy (CNR), Torino, Italy*

<sup>2</sup>*Department of Research & Innovation, Olea Medical, La Ciotat, France*

<sup>3</sup>*Lysholm Department of Neuroradiology, University College of London Hospitals NHS Foundation Trust, London, United Kingdom*

<sup>4</sup>*Institute of Neurology UCL, London, United Kingdom*

<sup>5</sup>*Department of Neuroradiology, University Clinic Erlangen, Friedrich-Alexander Universität Erlangen-Nürnberg (FAU), Erlangen, Germany*

☑ Apply Student/Postdoc Travel Fund

☐ Oral Presentation ☐ Poster ☑ Either Oral or Poster Presentation | Contact Email: feriel.ramdhane@olea-medical.com

**KEYWORD:** You are encouraged to choose one or two keywords. ☐ CEST agents ☑ Contrast Mechanism

☑ Tumor ☐ Stroke ☐ Neurology ☐ Body & MSK ☐ Standardization ☐ Novel Acquisition ☐ Machine Learning

**INTRODUCTION:** APT-weighted CEST MR imaging in clinical therapy has attracted a considerable interest for its diagnostic potential in the characterization of brain tumors at 3T. However, a proper tumor delineation and quantification of APTw images remain challenging due to their low signal-to-noise ratio (SNR).

**METHODS:** This study aims to improve the 3T APTw contrast and to reduce noise in brain images by using a new spatial filter dubbed “NLmCED” which is a combination between a Non-Local Mean filter and an Anisotropic Diffusion Tensor that was successfully applied in preclinical CEST studies [1]. This new filter was tested in two different datasets: a simulated brain tumor phantom and in real clinical data. Simulated Z-Spectra were obtained by fitting raw Z-Spectra from clinical APTw data acquired on a 3T MRI scanner (Prisma, Siemens Healthineers, Germany), using Bloch-McConnell equations modified to include 5 pools model, to generate a full brain dataset as ground-truth. The simulated brain phantom was corrupted by two percentage levels of Rician noise (0.5%, 1%) in the spatial domain and then denoised by NLmCED and compared to Cubic Smoothing Splines [2]. For real clinical data, two datasets acquired with different duty cycle have been denoised by both by NLmCED and Cubic Smoothing Splines with smoothing factor 0.99. Quantitative indexes such as PSNR and SSIM were calculated on the APTw contrast map (computed using MTR-asym metric [3] at the relative amide frequency offset of 3.5 ppm from the water one).

**RESULTS:** Visually, for the simulated datasets (Figure 1), NLmCED filter succeeded to remove noise and outperformed the Cubic Smoothing Spline method for both additive Rician noise levels in the APTw maps. Quantitatively, both PSNR and SSIM indexes provided the highest values to the denoised APTw maps by the NLmCED filter (Figure 2) especially at high level 1%. Similar performance in the real clinical brain data were obtained (Figure 3). NLmCED filter reduced noise and preserved contours and accurate homogeneous area inside the tumor regions.

**DISCUSSION and CONCLUSION:** This work showed that the NLmCED filter can improve the APTw contrast in clinical brain tumor images while reducing noise and maintaining all the significant information in the tumor region. Further validation will be performed by comparing it with other denoising methods usually applied to CEST MRI images at 3T.

**ACKNOWLEDGMENTS:** The research leading to these results has received funding from AIRC MFAG 2017 - ID. 20153 project – P.I. Longo Dario Livio. This project has received funding from the European Union’s Horizon 2020 research and innovation program under grant agreement No 667510 and the Department of Health’s NHR-funded Biomedical Research Centre at University College London. SB and LM are supported by the National Institute of Health Research Biomedical Research Council, UCL Hospitals NHS Trust.

**REFERENCES:** 1- Romdhane F, *et al.* Magn Reson Med 2021;00:1–18. 2-Stancanella J, *et al.* Contrast Media Mol Imaging 2008; 3(4):136-49. 3- Zhou J, *et al.* 2003;9(8):1085-90.

**FIGURES:** **Figure 1:** APTw maps for synthetic APTw brain: upper row for results at 0.5% noise level, bottom row results for 1% noise level. **Figure 2:** Quantitative metrics for synthetic data: A) PSNR metric, B) SSIM metric. **Figure 3:** APTw maps for clinical datasets: upper row with Duty Cycle 50 %, bottom row with Duty Cycle 90 %.

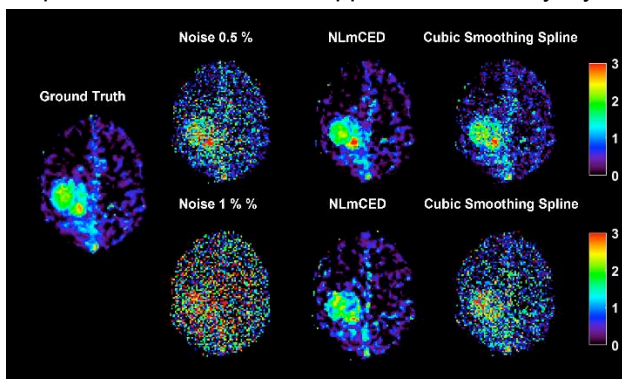


Figure 1

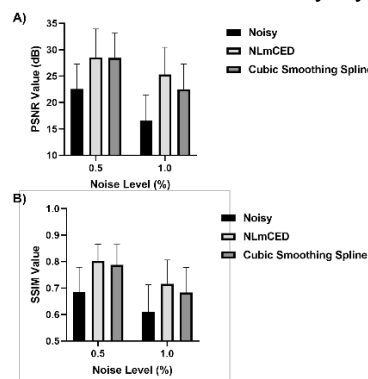


Figure 2

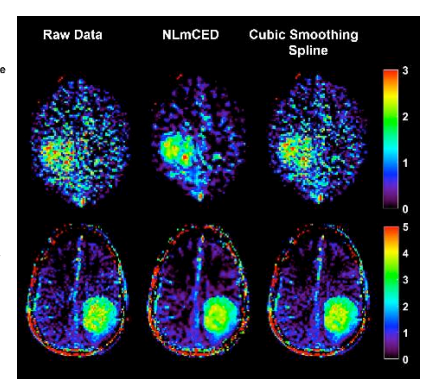


Figure 3

□ Apply Travel Fund

□ Oral Presentation □ Poster ☒ Either Oral or Poster Presentation | Contact Email: Zhongliang.zu@vumc.org

KEYWORD: You are encouraged to choose one or two keywords. □ CEST agents ☒ Contrast Mechanism

□ Tumor □ Stroke □ Neurology □ Body & MSK ☒ Standardization □ Novel Acquisition □ Machine Learning

## INTRODUCTION:

As an indirect method for molecular imaging, CEST signals depend not only on the solute molecular concentration ( $f_s$ ), but solute-water exchange rate ( $k_{sw}$ ) and solute  $T_2$  ( $T_{2s}$ ), as well as non-exchange specific factors including  $T_{1w}$  and background signal including contributions from the direct water saturation (DS) and magnetization transfer (MT) effects. In tumors, changes in both  $T_{1w}$  and MT effects have been observed. Although the magnetization transfer ratio (MTR) determined APT-weighted signal at 3.5 ppm and NOE-weighted signal at -3.5ppm have been widely applied in tumors previously, the contributions from these non-specific factors to the MTR contrast have not been evaluated. Previously, we have shown that there are two types of  $T_{1w}$  effects which have inverse influences on the MTR at low fields where there are usually significant DS effects, and so the MTR may be insensitive to  $T_{1w}$  by using appropriate saturation powers. In this work, we evaluate the dependence of MTR on these sample parameters at high fields where DS are usually weak. We first provide a signal model in which the contributors to MTR and the dependence of MTR on these contributors can be intuitively observed. We then measured the change of sample parameters in animal tumor models through which we calculate the relative contributions from each of these contributors to the MTR contrast in tumors.

**METHODS:** MTR can be described by (1)

$$MTR \approx \frac{1}{R_{1w}} \left( \frac{S_{ref}}{S_0} \right)^2 R_{ex}^{CEST} \quad (1)$$

In which,  $R_{ex}^{CEST} = \frac{f_s k_{sw} \omega_1^2}{\omega_1^2 + (R_{2s} + k_{sw}) k_{sw}}$  and  $S_{ref} \approx \frac{S_0 R_{1w}}{R_{1w} + R_{ex}^{MT}}$  (DS effect is ignored);  $R_{ex}^{CEST}$  represents the clean CEST effect which only depends on parameters from the solute of interest. The term ' $1/R_{1w}$ ' shows the  $T_{1w}$  recovery effect which has no relationship with DS, MT, and CEST effects, but scales MTR (1). The term ' $(S_{ref}/S_0)^2$ ' represents the background signals which should mostly arise from MT effect at high fields. It does not depend on CEST effect, but also scale MTR. Since MT effect also depends on  $R_{1w}$ ,  $R_{1w}$  in  $S_{ref}$  is termed the  $T_{1w}$ -related MT effect. In tumors, all these sample parameters may vary and contribute to the MTR contrast ( $C_{MTR} = MTR_t / MTR_n$ ) between tumor (t) and normal tissue (n),

$$C_{MTR} \approx C_{R_{1w}} C_{ref} C_{f_s} C_{k_{sw} R_{2s}} \quad (2)$$

In which  $C_{R_{1w}} = R_{1w,n} / R_{1w,t}$ , which represents the contribution from the variation of the  $T_{1w}$  recovery effect to  $C_{MTR}$ ;  $C_{ref} = (S_{ref,t} / S_{0,n})^2 / (S_{ref,n} / S_{0,t})^2$ , which represents the contribution from the variation of the reference signal.  $C_{f_s} = f_{s,t} / f_{s,n}$ , which represents the contribution from the variation of  $f_s$  to  $C_{MTR}$ .  $C_{k_{sw} R_{2s}} = k_{sw,t} / k_{sw,n} \cdot (\omega_1^2 + (R_{2s,n} + k_{sw,n}) k_{sw,n}) / (\omega_1^2 + (R_{2s,t} + k_{sw,t}) k_{sw,t})$ , which represents the contribution from the variation of  $k_{sw}$  and  $R_{2s}$  to  $C_{MTR}$ .

Eight rats bearing 9L tumors were included in this study. CEST measurements were performed by applying a CW-CEST sequence with a 5-s CW irradiation pulse with  $\omega_1$  of 0.25  $\mu T$ , 0.5  $\mu T$ , and 1  $\mu T$  followed by single-shot SE-EPI acquisition at 9.4T. Z-spectra were acquired with RF offsets at  $\pm 4000$ ,  $\pm 3500$ ,  $\pm 3000$ , and from -2000 to 2000 Hz with a step of 50 Hz. A six-pool model Lorentzian fit were used to process the CEST Z-spectrum.  $S_{ref}$  for APT and NOE was obtained by the sum of all Lorentzians except the corresponding pool. MTR for APT and NOE were obtained by subtracting CEST signals from  $S_{ref}$ .  $R_{ex}^{CEST}$  for APT and NOE were obtained by inversely subtracting CEST signals from  $S_{ref}$  and with  $T_{1w}$  normalization (2). MTR,  $R_{ex}^{CEST}$ , and  $S_{ref}$  were obtained from CEST signals with  $\omega_1$  of 1  $\mu T$  which is a widely used saturation power for measuring APT and NOE at high fields.  $R_{1w}$  was measured by an inversion recovery sequence. To further study the contributions from  $f_s$ ,  $k_{sw}$ , and  $R_{2s}$ , these parameters were also obtained by fitting  $R_{ex}^{CEST}$  acquired with the three  $\omega_1$  values.

**RESULTS:** Table 1 lists the measured sample parameters from tumors (T) and contralateral normal tissue (N). \*  $P < 0.05$

		MTR (%)	$R_{1w}$ (s <sup>-1</sup> )	$S_{ref}/S_0$	$R_{ex}^{CEST}$ (%s <sup>-1</sup> )	$f_s$ (%)	$k_{sw}$ (s <sup>-1</sup> )	$T_{2s}$ (ms)
APT	T	6.27 $\pm$ 1.10*	0.42 $\pm$ 0.03*	0.80 $\pm$ 0.02*	4.62 $\pm$ 0.78	0.12 $\pm$ 0.03*	81.53 $\pm$ 50.13	1.20 $\pm$ 0.34
	N	4.16 $\pm$ 0.49	0.50 $\pm$ 0.02	0.72 $\pm$ 0.02	4.70 $\pm$ 0.59	0.10 $\pm$ 0.01	109.63 $\pm$ 80.03	1.70 $\pm$ 0.54
NOE	T	11.66 $\pm$ 0.72	0.42 $\pm$ 0.03	0.80 $\pm$ 0.02*	9.54 $\pm$ 0.73	0.89 $\pm$ 0.10*	14.30 $\pm$ 2.55*	0.52 $\pm$ 0.09
	N	12.36 $\pm$ 0.81	0.50 $\pm$ 0.02	0.70 $\pm$ 0.03	16.96 $\pm$ 1.38*	1.40 $\pm$ 0.24	19.94 $\pm$ 4.26	0.45 $\pm$ 0.06

Table 2 lists each contributor in Eq. (2).

	$C_{MTR}$	$C_{R_{1w}}$	$C_{ref}$	$C_{R_{ex}}$	$C_{f_s}$	$C_{k_{sw} R_{2s}}$
APT	1.51 $\pm$ 0.19	1.21 $\pm$ 0.05	1.24 $\pm$ 0.05	0.99 $\pm$ 0.13	1.33 $\pm$ 0.30	0.78 $\pm$ 0.16
NOE	0.95 $\pm$ 0.11	1.21 $\pm$ 0.05	1.39 $\pm$ 0.04	0.57 $\pm$ 0.06	0.65 $\pm$ 0.10	0.86 $\pm$ 0.17

**DISCUSSION:** Although APT effect has no significant change, MTR determined APT has significant change in tumors. Although NOE effect has significant change, MTR determined NOE has no significant change in tumors.

**CONCLUSION:** APT-weighted imaging at high fields shows 'positive' contrast in tumors which mainly arises from the decreased  $R_{1w}$  and MT effects in tumors. NOE-weighted imaging at high fields shows nearly no contrast in tumors which is due to the cancellation of the decreased  $R_{1w}$  and MT effects and the decreased NOE effect.

**REFERENCES:** 1. Zu Z. NMR in Biomedicine 2018;31(7):e3934; 2 Zhang XY, *et al.* NMR in Biomedicine 2017;30(7):e3716

# A Generative Adversarial Network for Accelerated and Quantitative 3D Semisolid MT/CEST MRI: a Multi-Center Brain and Leg Human Study

Jonah P. W. Weigand<sup>1</sup>, Maria Sedykh<sup>2</sup>, Kai Herz<sup>3,4</sup>, Jaime Coll-Font<sup>1,5</sup>, Elizabeth Gerstner<sup>1</sup>, Christopher Nguyen<sup>1,5,6</sup>, Moritz Zaiss<sup>2,3</sup>, Christian T. Farrar<sup>1</sup>, Or Perlman<sup>1</sup>

<sup>1</sup>A. A. Martinos Center for Biomedical Imaging, Massachusetts General Hospital and Harvard Medical School, Charlestown, MA, USA; <sup>2</sup>Friedrich-Alexander Universität Erlangen-Nürnberg (FAU), Erlangen, Germany; <sup>3</sup>Max Planck Institute for Biological Cybernetics, Tübingen, Germany; <sup>4</sup>University of Tübingen, Tübingen, Germany; <sup>5</sup>Cardiovascular Research Center, Massachusetts General Hospital, Charlestown, MA, United States; <sup>6</sup>Health Science Technology, Harvard-MIT, Cambridge, MA, United States | [operlman@mgh.harvard.edu](mailto:operlman@mgh.harvard.edu) | **Keywords:** Machine Learning, Tumor

**INTRODUCTION:** Although CEST-weighted protocols are being increasingly investigated in clinical studies and were recently FDA approved for some vendors, the semi-quantitative nature of the typical CEST analysis metric may bias the interpretation of the observed effects. Recently, semisolid MT and CEST MR-Fingerprinting (MRF) were developed, allowing a quantitative reconstruction of the proton exchange parameters<sup>1-3</sup>. Nevertheless, the prolonged acquisition time required for applying this approach for 3D imaging is still a limiting factor for adoption into clinical routine. The goal of this work was to considerably shorten the acquisition time required for quantitative 3D CEST and semisolid MT imaging and validate the robustness of the developed method under multiple imaging scenarios, scanner hardware, and imaging sites.

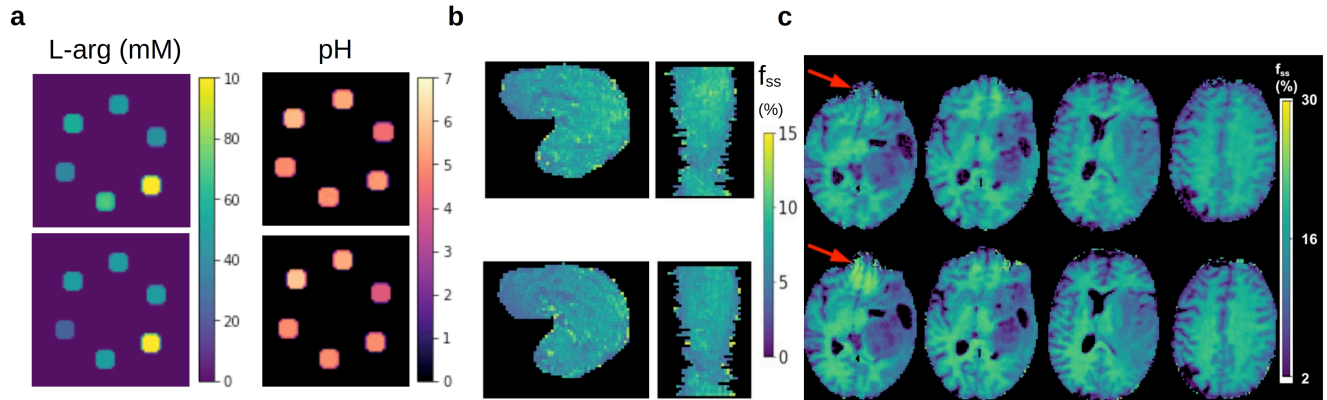


**Fig. 1.** Comparing GAN-CEST (top) with ground-truth or CEST-MRF (bottom). **a.** Ground truth L-arginine concentration and pH maps are in excellent agreement with the GAN-CEST based corresponding maps. The normalized root mean squared error is less than 1.5% for both L-arg concentration and pH mapping. **b.** Quantitative in vivo calf imaging in a cardiac rehabilitation patient. Note the good agreement between the semisolid MT volume fraction ( $f_{ss}$ ) maps obtained using GAN-CEST (top) and CEST-MRF (bottom). **c.** In vivo whole-brain imaging of a GBM tumor patient. Note the improved performance of GAN-CEST (top) for regions with large susceptibility artifacts (red arrows).

**METHODS:** 3D CEST and semisolid MT MRF datasets of L-arginine phantoms, in-vivo human whole-brains, and in-vivo human leg calf-muscles were acquired using the open-source pulseseq-CEST framework<sup>4</sup>, implemented in 3T clinical scanners at 3 different sites, using 3 different scanner models. A generative adversarial network supervised framework (GAN-CEST) was then designed and trained to learn the mapping from a reduced input data space to the quantitative exchange parameter space while preserving perceptual and quantitative content.

**RESULTS AND DISCUSSION:** The total acquisition time for GAN-CEST was 33%-80% shorter than CEST-MRF (e.g, 1:38 instead of 8:30 [min:sec]). The whole-brain quantitative reconstruction took less than 4 sec. Excellent agreement was observed between the GAN-CEST estimated L-arginine concentrations and the known concentrations (Pearson's  $r = 0.967$ ), and between the estimated proton exchange rates and the reference QUESP calculated values (Pearson's  $r = 0.967$ ). GAN-CEST images from a brain tumor subject scanned in a site and a scanner model that were not seen by the GAN-CEST network during training yielded a semi-solid volume fraction and exchange rate NRMSE of  $0.036 \pm 0.010$  and  $0.065 \pm 0.021$ , respectively, and structural similarity index (SSIM) of  $0.966 \pm 0.014$  and  $0.950 \pm 0.021$ , respectively. The mapping of the calf-muscle exchange parameters from an unseen cardiac rehabilitation patient, yielded NRMSE of  $0.036 \pm 0.0102$  and  $0.046 \pm 0.014$  for the semi-solid volume fraction and exchange rates, respectively, and SSIM of  $0.966 \pm 0.015$  and  $0.947 \pm 0.024$ , respectively. At regions with large susceptibility artifacts, GAN-CEST has demonstrated improved performance and reduced noise compared to MRF.

**CONCLUSION:** GAN-CEST has demonstrated the ability to substantially reduce the acquisition time for quantitative semisolid MT/CEST mapping while reducing artifacts and retaining performance across imaging sites, scanner models, and pathology.

## REFERENCES

1. Cohen O, *et al.* Magn Reson Med 2018;80:2449-2463.
2. Heo HY, *et al.* Neuroimage 2019;189:202-213.
3. Perlman O, *et al.* Nature Biomedical Engineering 2022;6:648-657.
4. Herz K, *et al.* Magn Reson Med 2021;86:1845-1858.



# Which method provides most insight into tumors – 3T (fluid suppress.) APTw, 3T CEST-MRF or 7T multi-pool CEST?

Maria Sedykh<sup>1</sup>, Moritz Fabian<sup>1</sup>, Kai Herz<sup>2,3</sup>, Or Perlman<sup>4</sup>, Chris Farrar<sup>4</sup>, Angelika Mennecke<sup>1</sup>, Manuel Schmidt<sup>1</sup>, Arnd Dörfler<sup>1</sup>, and Moritz Zaiss<sup>1,2</sup>

<sup>1</sup>Institute of Neuroradiology, Universitätsklinikum Erlangen, Friedrich-Alexander Universität Erlangen Nürnberg, Germany,

<sup>2</sup>Magnetic Resonance Center, Max-Planck-Institute for Biological Cybernetics, Tübingen, Germany,

<sup>3</sup>Department of Biomedical Magnetic Resonance, University of Tübingen, Tübingen, Germany, <sup>4</sup>Athinoula A. Martinos Center for Biomedical Imaging, Department of Radiology, Massachusetts General Hospital and Harvard Medical School, Charlestown, MA, USA

☑ Oral or Poster | Contact Email: [moritz.zaiss@fau.de](mailto:moritz.zaiss@fau.de) KEYWORD: ☑ Tumor ☑ Novel Acquisition

**INTRODUCTION:** Many CEST techniques were shown to provide insight into tumors, e.g. 3T APTw imaging, 3T CEST fingerprinting, and 7T multi-pool CEST. Herein we report one case of a patient diagnosed with glioblastoma, WHO grade IV, who could be measured with all above mentioned techniques to reveal their relative performance and correlations.

**METHODS:** The patient was measured at a Siemens PRISMA scanner (3T, 64-Rx, 1Tx) and Siemens TERRA scanner (7T, 32-Rx, 8 pTx coil) after written informed consent. The **3T APTw** following the standard APTw\_001<sup>(3)</sup> (pulsed rf irradiation of 2 s duration at DC = 90% and a 2  $\mu$ T B1 level) was applied followed by a 3D snapshot GRE readout. The **3T CEST MRF** pulseseq-files<sup>(1,2)</sup> were played out followed by a 3D-EPI readout. The post-processing of the data included the usage of neural networks and was performed according to <sup>(2)</sup>, generating maps for MT pool fraction  $f_{mt}$  and exchange rate  $k_{mt}$ , and solute amide fraction  $f_s$  and exchange rate  $k_s$ . The **7T multi-pool CEST** protocol was measured with the MIMOSA approach <sup>(4)</sup> at 0.72  $\mu$ T and 1.00  $\mu$ T followed by a 3D snapshot GRE. Figure 1 shows data of the techniques in tumor and WM ROIs.

**RESULTS:** The tumor area can be outlined in all presented maps Figure 2, but with different apparent features. The 3T-APT<sub>w</sub> highlights the overall tumor area, including necrotic and the liquefied tissue in the cyst, identified on the MPRAGE in Figure 2a. The fluid suppressed APT<sub>w</sub> FS-APT<sub>w</sub> (see separate abstract) the liquid areas are suppressed. In most 3T MRF and all 7T multi-pool contrasts, the cyst and the necrotic area are hypo-intense, in 3T MRF  $k_{mt}$  necrosis is hyper-intense. While the selective 7T-amide-CEST shows similar areas highlighted as 3T-APT<sub>w</sub> (except for cyst and necrosis) and as 3T FS-APT<sub>w</sub>, the quantitative MRF amide exchange rate  $k_s$  and concentration  $f_s$  do not show elevated signals. Most contrast in 3T MRF is seen in the MT pool fraction  $f_{mt}$  and exchange rate  $k_{mt}$ , the latter correlated to the MT line-width. The most plausible correlation is observed between  $f_{mt}$ , 7T MT and 7T NOE and T1 and T2, as lowered MT pool size  $f_{mt}$  is (anti-)correlated with all values:  $f_{mt}$ , 7T MT and 7T NOE all are hypo-intense in the tumor region, and WM brighter than GM, T1 and T2 the other way around. The 3T MRF MT exchange rate map shows increased values in the tumor area, but  $k_{mt}$  was found to be decreased in animal tumors<sup>(2)</sup>.

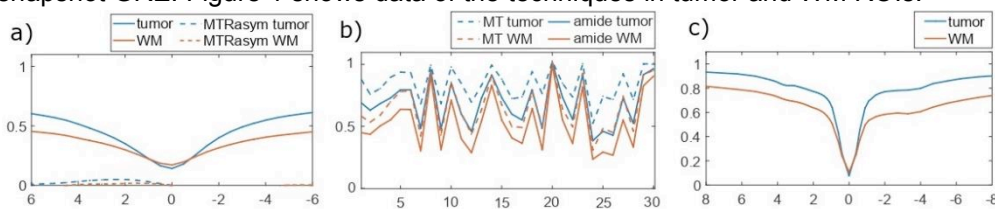


**Figure 1:** a) 3T APT<sub>w</sub> Z-spectrum b) 3T CEST MRF fingerprint and c) 7T multi-pool Z-spectrum in tumor and WM ROI of the same patient.

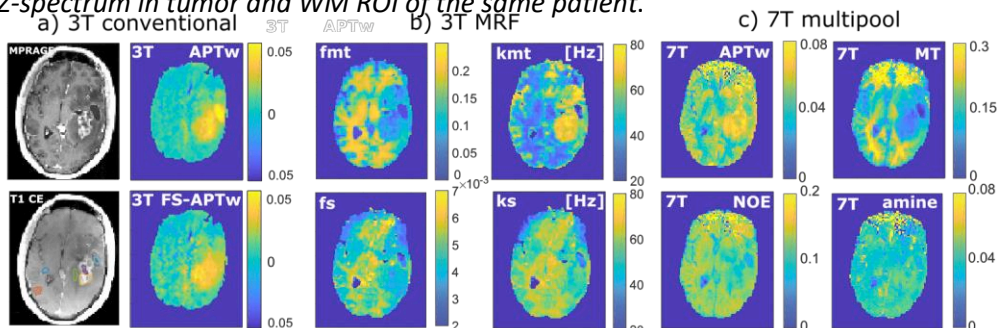


**Figure 2:** a) 3T clinical imaging post-CA and conventional APT<sub>w</sub> imaging. b) 3T CEST MRF fingerprinting concentration and exchange rate maps given in unit fraction and Hz and T1/T2 maps. c) 7T multi-pool CEST Lorentzian amplitude maps.

The most plausible correlation is observed between  $f_{mt}$ , 7T MT and 7T NOE and T1 and T2, as lowered MT pool size  $f_{mt}$  is (anti-)correlated with all values:  $f_{mt}$ , 7T MT and 7T NOE all are hypo-intense in the tumor region, and WM brighter than GM, T1 and T2 the other way around. The 3T MRF MT exchange rate map shows increased values in the tumor area, but  $k_{mt}$  was found to be decreased in animal tumors<sup>(2)</sup>.

**DISCUSSION:** Most prominent findings are (i) that 3T APT<sub>w</sub> has a strong relaxation and MT contribution and shows a liquid artifact. Interestingly, 3T FS-APT<sub>w</sub> and isolated Lorentzian 7T amide CEST partly correlate in the tumor area, but 7T shows finer structures. (ii) 7T and most MRF maps identify the necrosis and the cyst properly hypointense, while APT<sub>w</sub> shows the cyst even brighter than the contrast enhancing tumor area. (iii) The MRF  $f_{mt}$  contrast is in line with MT and relaxation findings, however, the outcome of MRF  $k_{mt}$ ,  $f_s$  and  $k_s$  is unexpected compared to previous animal data, as well as compared to the 7T insights. As MRF has the most complicated pipeline, further investigations are needed for a better interpretation of the method. **CONCLUSION:** We showed an unseen variety of CEST imaging methods applied in the same brain tumor patient. Coarse features can be observed in all methods, with MRF and 7T CEST being more versatile in some tumor parts. Isolation, separation and smarter combination of different contrast is still needed to improve the diagnostic performance of CEST.

**REFERENCES:** 1. Herz K, et al. *MRM* 2021 Oct;86(4):1845-1858. 2. Perlman O, et al. <https://doi.org/10.1101/2020.03.05.977793>. 3. [https://github.com/kherz/pulseseq-cest-library/tree/master/seq-library/APTw\\_3T\\_001\\_2uT\\_36SincGauss\\_DC90\\_2s\\_brainumor](https://github.com/kherz/pulseseq-cest-library/tree/master/seq-library/APTw_3T_001_2uT_36SincGauss_DC90_2s_brainumor). 4. Liebert A, et al. *Magnetic resonance in medicine* 2019 82:2. 5. Khakzar K, 7 tricks for 7T CEST, CEST Workshop 2020.

# Improved Bloch fitting and machine learning methods that analyze acidoCEST MRI

Tianzhe Li,<sup>1,2</sup> Julio Cárdenas-Rodríguez,<sup>3</sup> Kyle M. Jones,<sup>1</sup> and Mark D. Pagel<sup>1</sup>

<sup>1</sup> Department of Cancer Systems Imaging, University of Texas MD Anderson Cancer Center, Houston, TX, USA

<sup>2</sup> University of Texas Health Science Center, Houston, TX, USA

<sup>3</sup> Data Translators LLC, Oro Valley, AZ, USA

✉ Either Oral or Poster Presentation | Contact Email: [mdpagel@mdanderson.org](mailto:mdpagel@mdanderson.org)

KEYWORDS: ✉ Tumor ✉ Machine Learning

**INTRODUCTION:** AcidoCEST MRI is used to measure extracellular pH in the tumor microenvironment by evaluating CEST spectra of an exogenous agent that produces two CEST signals, with at least one pH dependent signal.<sup>1</sup> The Bloch-McConnell equations modified to include pH as a fitting parameter can be used to analyze CEST MRI, known as “Bloch fitting”.<sup>2</sup> However, these equations also fit for T1, T2, B1, and B0, raising questions about whether this multiparametric fitting is the best approach. These equations also fit for concentration, and temperature can also affect chemical exchange rates, raising concerns that concentration and temperature can affect the pH measurement.

More recently, machine learning methods have been used to evaluate CEST MRI.<sup>3</sup> AcidoCEST MRI provides an intriguing opportunity for machine learning methods, because CEST spectra of an exogenous agent can be difficult to visualize by humans (so that human learning is often reduced to focusing on one saturation frequency) and yet the spectra are rich in information for machine learning. Both classification methods and regression methods can be employed to evaluate acidoCEST spectra.

**METHODS:** To refine the analysis of acidoCEST MRI, we acquired 20,000 CEST spectra of iopamidol (Isovue™, Bracco Diagnostics) at 4 concentrations, 5 T1 relaxation times, 5 temperatures, 5 saturation powers, 5 saturation times, and 8 pH values. We also measured T1, T2, B1 and B0 of each sample, and carefully controlled and validated the sample temperature. We used an advanced QUESP method to measure chemical exchange rates of iopamidol over a range of pH, and the Bloch fitting method was recalibrated with these results. Bloch fitting was used to estimate pH using only CEST spectra or by including T1, T2, B1, and/or B0 measurements (16 combinations). We analyzed how the pH estimates from Bloch fitting were potentially dependent on concentration and temperature. Computation time was measured for the analyses with the 16 combinations.

The same experimental dataset was split into sets of training data (70%) and testing data (30%) to assess machine learning methods. We trained and validated the Linear Regression Classification (LFC) model and the Random Forest Classification (RFC) model to classify pH as  $> 7.0$  or  $pH < 6.5$ . We evaluated the sensitivity, specificity, PPV and NPV for each classification. We also trained and validated a regression approach using a Random Forest Regression (RFR) model and a LASSO model to estimate pH between 6.2 – 7.4. We evaluated the mean absolute error of the pH measurements.

**RESULTS:** Our Bloch fitting method could accurately and precisely measure pH throughout the range of pH 6.2-7.3, using CEST results without the need for experimental T1, T2, B1, or B0 measurements. As expected, computation time was longest for analyses that only included CEST results. The most accurate and precise pH estimates were obtained with saturation power of 3  $\mu T$  and saturation time of 3 sec. The pH estimates were dependent on temperature, and independent of concentration and T1 time.

For the evaluation of machine learning methods, the RFC produced the best classifications at both pH thresholds of  $> 7.0$  and  $< 6.5$  pH units, with a positive predictive value of 0.96 and negative predictive value of 0.94 for both thresholds. The RFR measured pH with a mean absolute error of 0.031 pH units that was consistent throughout the pH range, which performed better than LASSO that showed a mean absolute error of 0.24 pH units that was biased against low and high pH. The most accurate and precise pH estimates were obtained with saturation power of 3  $\mu T$  and saturation time of 3 sec.

**DISCUSSION:** We have shown that the Bloch fitting method is robust for estimating pH with acidoCEST MRI. Obviating the need for experimental T1, T2, B1, or B0 measurements reduces total acquisition time, although lengthy analysis time is then required for the multiparametric Bloch fitting process. A concern remains that a biological milieu may interact with iopamidol, altering the pH measurement. However, the independence of the pH estimate from the Bloch fitting method on concentration and T1 mitigates this concern.

The outstanding pH classifications with RFC machine learning can be used for clinical diagnoses. A pH  $> 7.0$  is an outstanding threshold for differentiating cancer vs. non-cancer lesions. A pH  $< 6.5$  is an excellent threshold for differentiating highly aggressive and metastatic tumors from more benign tumors. The outstanding accuracy and precision of pH estimates from RFR can be used to provide a more quantitative diagnosis of tumor status and treatment effect. Importantly, these machine learning methods are very fast, which addresses a pitfall of the Bloch fitting method.

**CONCLUSIONS:** This study concludes our development of the Bloch fitting method for acidoCEST MRI. This study demonstrates opportunities to apply machine learning to the clinical translation of acidoCEST MRI.

**ACKNOWLEDGMENTS:** Our research is supported by the NIH/NCI through grants R01 CA231513 and P30 CA016672.

**REFERENCES:** 1. Chen LQ, *et al.* Evaluations of extracellular pH within in vivo tumors using acidoCEST MRI. *Magn Reson Med*, 2014;72:1408-1417. 2. Jones KM, *et al.* Respiration gating and Bloch fitting improve pH measurements with acidoCEST MRI in an ovarian orthotopic tumor model. *Proc SPIE* 2016;9788:978815. 3. Goldenberg JM, *et al.* Machine learning improves classification of preclinical models of pancreatic cancer with chemical exchange saturation transfer MRI. *Magn Reson Med* 2019;81:594-601.

# DeepCEST: Fast mapping of 7T CEST MRI parameters with uncertainty quantification

Leonie Hunger<sup>1</sup>, Junaid Rajput<sup>1,2</sup>, Kiril Klein<sup>1</sup>, Angelika Mennecke<sup>1</sup>, Moritz Fabian<sup>1</sup>, Manuel Schmidt<sup>1</sup>, Felix Glang<sup>3</sup>, Kai Herz<sup>4</sup>, Patrick Liebig<sup>5</sup>, Armin Nagel<sup>6</sup>, Klaus Scheffler<sup>3,4</sup>, Arnd Dörfler<sup>1</sup>, Andreas Maier<sup>2</sup>, Moritz Zaiss<sup>1,3\*</sup>

<sup>1</sup>Institute of Neuroradiology, University Hospital Erlangen, Erlangen, Germany

<sup>2</sup>Pattern Recognition Lab Friedrich-Alexander-University Erlangen-Nürnberg

<sup>3</sup>Magnetic Resonance Center, Max Planck Institute for Biological Cybernetics, Tübingen, Germany

<sup>4</sup>Department of Biomedical Magnetic Resonance, Eberhard Karls University Tübingen, Tübingen, Germany

<sup>5</sup>Siemens Healthineers, Erlangen Germany

<sup>6</sup>Institute of Radiology, University Hospital Erlangen, Erlangen, Germany

✉ Either Oral or Poster | Contact: moritz.zaiss@fau.de KEYWORD: ☒ Tumor ☒ Machine Learning

## INTRODUCTION:

To make 7T CEST MRI more available for radiologists, we developed a deepCEST pipeline for 7T MRI that predicts CEST contrasts from just one scan with robustness against B1 inhomogeneities. The pipeline includes an uncertainty quantification and a confidence map to directly evaluate the quality of the predictions. The proposed approach results in a reduction of 50% of the measurement time and delivers the predicted CEST contrast with in 1 sec.

**METHODS:** The input data for a neural network (NN) consisted of 7T in vivo raw Z-spectra of a single B1 level (1  $\mu$ T), and B1 and B1-CP maps. The 7T raw data was acquired using the 3D snapshot GRE MIMOSA CEST<sup>3</sup> at a Siemens MAGNETOM 7T scanner. These inputs were mapped voxel-wise on target data consisting of Lorentzian amplitudes conventionally generated by 5-pool-Lorentzian fitting performed on normalized, denoised, B0- and B1-corrected Z-spectra<sup>1</sup>. The network consisted of two fully connected hidden layers with RELU activation and was trained with Gaussian negative log likelihood loss. The output layer consisted of 10 nodes with linear activation to obtain amplitudes and log variance of the 5-pool Lorentzian fit. Exponential activation was applied to the log variance during inference to obtain the uncertainties.

**RESULTS:** Figure 1 shows the Lorentzian fit and the prediction of the amide and rNOE contrast in a tumor patient with a B0 shift, as well as the segmented uncertainty map over all contrasts with a threshold of 5%. The first row (Fig. 1a) shows the predictions and uncertainty for the measurement made with a bad shim. Such a strong B0 shift was not part of the training distribution. Therefore, the predictions and fits do not match. Consequently, the NN outputs a high uncertainty for these voxels. In the second row (Fig. 1b), the Z-spectra of the patient were centered, resulting in NN predictions that agree well with the fit, show the tumor highlighted, and only a low uncertainty is yielded. In figure 1c the histogram of the B0 map from case a and b is shown, in which the strong B0 shift is shown. The B1 homogeneity of the deepCEST prediction, inferred from only one B1 level (1  $\mu$ T) is as good as the fit, generated by B1-interpolation of 0.72  $\mu$ T and 1  $\mu$ T CEST data<sup>4</sup>. Predicted maps were also observed to be more homogeneous and smoother owed to the denoising ability of the deepCEST networks.

**DISCUSSION and CONCLUSION:** The deepCEST approach has already shown very promising results for 3T, the clear advantage of 7T data is the better SNR and higher spectral resolution. The 7T deepCEST approach uses only one B1 level, this saves about 50% of scan time (now 6:22 min), but still predicts accurately with low uncertainty and provides both B0- and B1-corrected homogeneous CEST contrast together with an uncertainty map, increasing the diagnostic confidence.

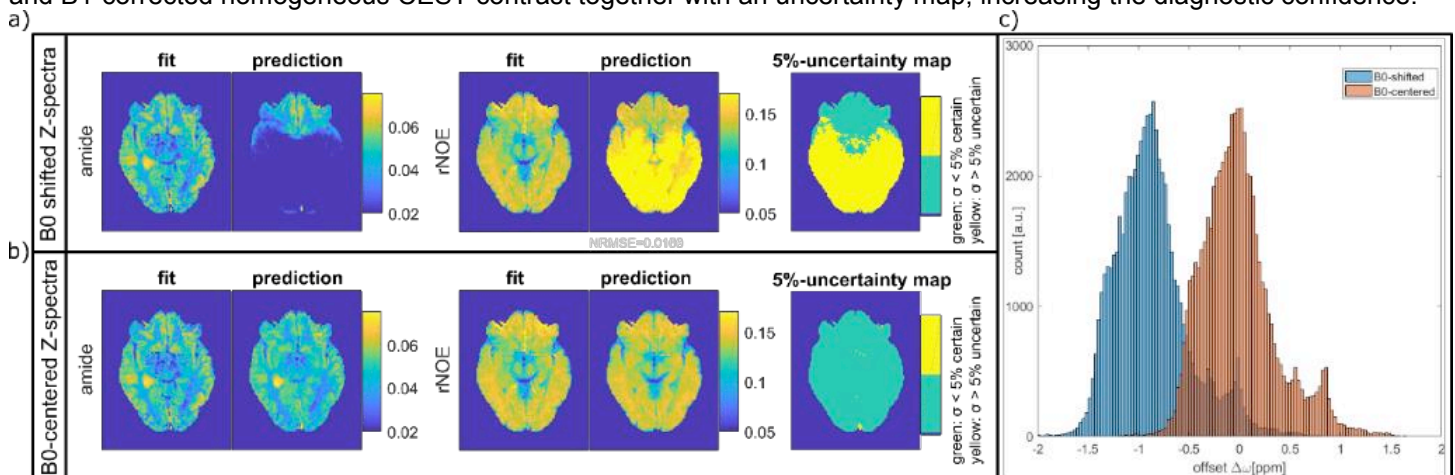


Figure 1: Importance and practicability of uncertainty quantification: (a) wrong predictions due to bad shim are detected. (b) With centered Z-spectra the NN prediction is close to the ground truth and only low uncertainty indicated. All predicted contrasts in (b) show similar or better B1 homogeneity as the two-B1-level fit, despite using only a single B1 CEST scan.

**REFERENCES:** 1. Mennecke et al NMR Biomed 2022 55.1:e4717  
2. Glang et al MRM. 2020; 84: 450-466

3. Zaiss et al NRM Biomed 2018 31.4:e3879.  
4. Windschuh et al. 2015;28(5):529-37.



# A comparison of APT analyses in acute stroke – Demonstration of highly sensitive and specific pH-weighted MRI

Dongshuang Lu<sup>1</sup>, Phillip Zhe Sun<sup>1-3</sup> \*

<sup>1</sup> Martinos Center for Biomedical Imaging, MGH, Harvard Medical School. <sup>2</sup> Emory Primate Research Center, Emory University. <sup>3</sup> Department of Radiology and Imaging Sciences, Emory University School of Medicine.

☐ Oral Presentation ☐ Poster ☒ Either Oral or Poster Presentation | Contact Email: [PZHESUN@EMORY.EDU](mailto:PZHESUN@EMORY.EDU)

**KEYWORD:** You are encouraged to choose one or two keywords. ☒ Standardization ☒ Neurological Disorders

**INTRODUCTION:** APT MRI has been increasingly used to image pH following acute stroke (1,2). Whereas MT asymmetry has been widely used in CEST MRI, it has limitations due to contributions such as tissue relaxation, RF saturation amplitude, and duration. In addition, in vivo CEST quantification is confounded by the concomitant saturation effects, most notably, semisolid MT, amine, and guanidyl CEST effects (3,4). Recently, a quasi-steady-state (QUASS) algorithm was proposed to account for not sufficiently long TR and saturation time (TS), which provides a practical strategy to expedite the CEST scans without a loss in the magnitude of CEST measurement (5-7). Our study evaluated common quantification approaches following QUASS reconstruction, from  $MTR_{asym}$  to multi-pool Lorentzian fitting in an animal stroke model, and compared their CNR and effect size using Cohen's d.

**METHODS:** We performed MRI scans on 7 adult male Wistar rats following a standard middle cerebral artery occlusion (MCAO) surgery. One rat had a small lesion in the hypothalamus and was excluded from the analysis. Multiparametric MRI scans were performed at a 4.7 Tesla small-bore Bruker MRI system. We used spin-echo EPI with a FOV of 25 x 25 mm<sup>2</sup> (matrix = 64 x 64, slice thickness/slice gap = 1.8/0.2 mm, 5 slices). We acquired diffusion-weighted, T<sub>1</sub>-weighted, T<sub>2</sub>-weighted, and CEST Z-spectral imaging. We calculated  $MTR_{asym}^{app,QUASS}$ ,  $AREX^{app,QUASS}$ ,  $LDA^{app,QUASS}$ ,  $MRAPTR^{app,QUASS}$ , and  $Z\ fitting^{app,QUASS}$ , as described previously (8). We used a two-tailed paired t-test, and the results were regarded as statistically significant for P values less than 0.05.

**RESULTS:** All pH-weighted indices showed significant signal drops following ischemia. The QUASS analysis enhanced pH-weighted contrast over the apparent CEST measurements, indicating the advantage of reconstructing the equilibrium CEST states. For the normal and ischemic areas, we have QUASS  $MTR_{asym}$  (-3.9±0.6% vs. -5.5±0.7%), T<sub>1</sub>-normalized  $MTR_{asym}$  (-2.6±0.5% vs. -3.3±0.7%), AREX (-5.6±1.0 vs. -7.4±1.1%), LDA (0.7±0.1% vs. 0.5±0.1%), multi-pool Lorentzian fitting (3.5±0.2 vs. 2.7±0.3%), and MRAPTR (-0.0±0.0% vs. -1.3±0.4%).

Fig. 1 shows multiparametric MRI and common analyses of QUASS pH-weighted MRI. There was a slight but significant T<sub>1</sub> increase in the ischemic lesion. In addition, the ischemic lesion had a substantial decrease in ASL and ADC from the normal area (the lesion was automatically segmented and mirrored to the intact tissue). Whereas  $MTR_{asym}$ ,  $MTR_{asym}/T_1$ , and AREX depicted ischemic lesion, there was notable heterogeneity in the intact normal area. In comparison, MRAPTR showed enhanced contrast between the ischemic and normal regions. Although the LDA decrease in the ischemic tissue is not well demarcated from the surrounding tissue, the multi-pool Lorentzian fitting showed a clear ischemic tissue signal drop. Both MRAPT and Lorentzian fitting maps depicted a mild signal drop in the cortex (pink arrows). Most notably, the Cohen's d was 4.8 for MRAPTR, substantially higher than other indices (ranging from 1.6 to 2.9).

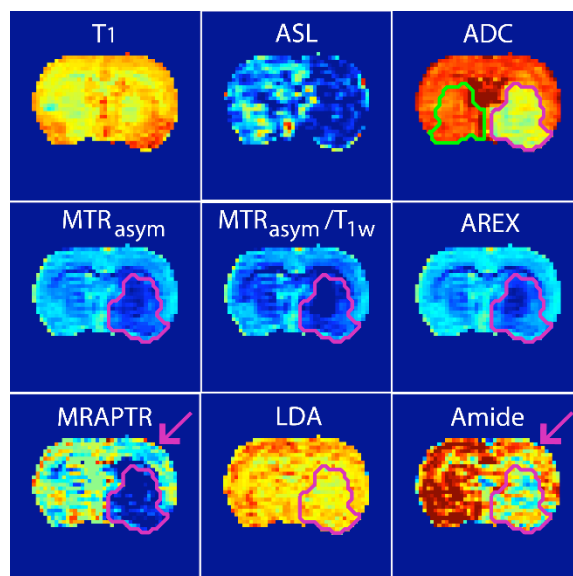


Fig. 1, Comparison of QUASS pH-weighted MRI analyses of an acute stroke rat model, including  $MTR_{asym}$ , T<sub>1</sub>-normalized  $MTR_{asym}$ , AREX, MRAPTR, LDA and amide peak from Lorentzian fitting. Also, T<sub>1</sub>, ASL and ADC images were provided.

**CONCLUSION:** Our study compared commonly used pH-weighted MRI indices following the QUASS analysis and demonstrated a high sensitivity of pH-specific MRAPTR analysis to acute ischemia, warranting further evaluation in the stroke clinic.

**References:** 1) Zhou et al. Nat Med 2003;9(8):1085-90. 2) Wang et al. Neuroimage 2019;191:610-7. 3) Zaiss M et al. NMR Biomed 2014;27(3):240-252. 4) NeuroImage 2012;59(2):1218-27. 5) Sun. Magn Reson Med 2021;85:3281-9. 6) Wu et al. Neuroimage: Clinical 2022;33:102890. 7) Kim et al. Magn Reson Med 2022;87:810-9. 8) Foo et al. Magn Reson Med 2021;85:2188-200

# Early-Stage Cerebral Glutamate Mapping in APP<sup>NL-F/NL-F</sup> Mouse Model of Alzheimer's Disease Using GluCEST MRI

Narayan Datt Soni<sup>1</sup>, Anshuman Swain<sup>1</sup>, Ravi Prakash Reddy Nanga<sup>1</sup>, Halvor Juul<sup>1</sup> and Ravinder Reddy<sup>1</sup>

<sup>1</sup>Department of Radiology, Center for Advance Metabolic Imaging in Precision Medicine, Perelman School of Medicine at The University of Pennsylvania, Philadelphia, PA, USA

✉ Apply Travel Fund

☑ Oral Presentation ☐ Poster ☐ Either Oral or Poster Presentation

Contact Email: [Narayan.soni@penndmedicine.upenn.edu](mailto:Narayan.soni@penndmedicine.upenn.edu)

KEYWORD: ☑ Contrast Mechanism ☑ Neurology

**INTRODUCTION:** Alzheimer's disease (AD) is the most common neurodegenerative disorder characterized by progressive loss of cognitive and intellectual abilities including memory<sup>1</sup>. Glutamate being the major excitatory neurotransmitter in the mammalian central nervous system<sup>2</sup>, regulates various cognitive functions including learning and memory<sup>3</sup>. <sup>1</sup>H NMR spectroscopic studies conducted with AD animal models<sup>4,5</sup> and human subjects<sup>6</sup> have revealed a consistent reduction in the levels of cortical glutamate. These reports points to the importance of cerebral glutamate mapping in early diagnosis of AD onset. In the current study our objective was to perform GluCEST imaging-based, region wise *in vivo* mapping of cerebral glutamate in 6-month-old APP<sup>NL-F/NL-F</sup> mouse model of AD. These mice harbor Swedish (APP<sup>KM670/671NL</sup>) and the Iberian (APP<sup>I716F</sup>) mutations in APP gene<sup>7</sup>, and recapitulate typical AD-associated pathologies, including amyloid- $\beta$ 1-42 plaques, synaptic loss and microgliosis. Further we compared the results obtained from GluCEST maps with regional levels of glutamate measured using localized *in vivo* <sup>1</sup>H-MRS.

**METHODS:** The protocol used for animal experiments was approved by the IACUC committee of University of Pennsylvania. The study was performed using 6-month-old C57BL6/J (control, n=7; 6 male and 1 female) and APP<sup>NL-F/NL-F</sup> (AD, n=6; 5 male and 1 female) mice. For *in vivo* MRS/I, a 20mm diameter volume <sup>1</sup>H transceiver coil (RAPID Biomedical GmbH, Germany) and a 30cm horizontal bore 9.4T magnet interfaced with Avance III HD console (Bruker Biospin, Germany) were used. The entire imaging protocol consisted of a localizer followed by T1-FLASH (acquisition time = ~4 min), T2-MSME (acquisition time = ~9 min) (Fig. 1), GluCEST ( $B_{1rms}$ =5.87 $\mu$ T; pulse-duration=1000ms (series of 200ms pulses); offsets=  $\pm$ 2.4 to  $\pm$ 3.6ppm; step-size=0.2ppm; averages=4; acquisition time = ~15 min) and WASSR<sup>8</sup>. These data were acquired from 1mm thick axial slice (-2.8mm from lambda covering hippocampal regions, surrounding cortex and thalamus) and 0.146mm x 0.146mm in-plane resolution. At last, single-voxel <sup>1</sup>H MRS localized in the hippocampus (Voxel size: 6x1x2mm<sup>3</sup> (Fig. 1), TE=16ms; TR=3000ms; dummy-scans=4; acquisition duration = ~13 min). Spectra acquired were analyzed using the LCModel for the quantification of different metabolites. Region of interest covering hippocampus was drawn in post-processed B<sub>0</sub>-corrected GluCEST map (Fig. 1). The obtained mean value reflected the glutamate levels in the hippocampus and was compared across the two groups. To find the statistical significance of differences between these values, two-tailed t-test assuming unequal variance was performed. At last, a correlation curve was plotted between hippocampal glutamate levels obtained from <sup>1</sup>H-MRS (Y axis) and GluCEST maps (X axis) of both the control and AD mice.

**RESULTS:** Mean GluCEST values in hippocampus of AD mice (23.87 $\pm$ 1.82) was significantly lower (-10.3%; p=0.02) compared to that of controls (26.61 $\pm$ 1.64). This was further supported by spectroscopic results, which revealed a significantly reduced (-14.1%; p=0.01) level of glutamate in the hippocampus of AD mice (14.56 $\pm$ 1.47 mM) compared to controls (16.95 $\pm$ 0.61). Additionally, the levels of NAA, taurine and creatine were also found to be reduced in the hippocampus of AD mice (p $\leq$ 0.02) (Fig 2A). Our correlation analysis suggested a very strong association ( $R^2$ =0.998) between hippocampal gluCEST contrast and glutamate levels (Fig. 2B).

**DISCUSSION:** The results obtained from this investigation clearly suggest a significant loss glutamate in the hippocampus of the AD mice at early stage in this model which is in accordance with the previous reports<sup>4,5,6</sup>. Further studies will be performed at later time points to clearly understand the pattern of perturbations in the glutamate homeostasis with

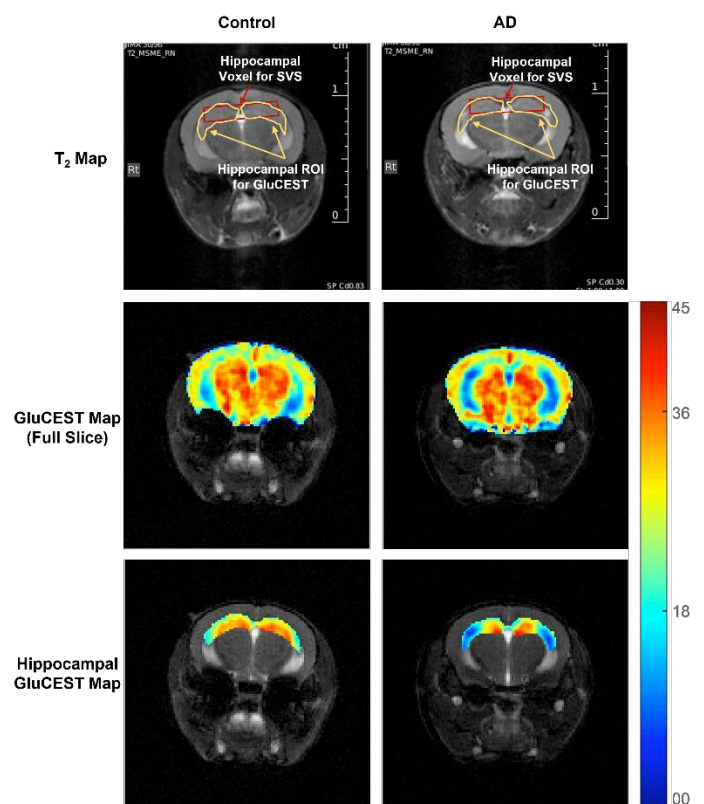


**Figure 1:** Top panel shows representative anatomical (T<sub>2</sub> weighted) images showing SVS voxel position and hippocampal ROI for GluCEST mapping, middle and bottom panels show GluCEST images of entire brain slice and hippocampal ROI resp., from control (left) and AD (right) mice.

## Omega plot-based quantitative in vivo CEST MRI

Yang Ji<sup>1</sup>, Dongshuang Lu<sup>1</sup>, Phillip Zhe Sun<sup>1,2,3</sup>, Iris Y. Zhou<sup>1\*</sup>,

<sup>1</sup> Athinoula A. Martinos Center for Biomedical Imaging, Department of Radiology, Massachusetts General Hospital and Harvard Medical School, Charlestown, MA, USA

<sup>2</sup> Yerkes Imaging Center, Yerkes National Primate Research Center, Emory University, Atlanta, GA, USA

<sup>3</sup> Department of Radiology and Imaging Sciences, Emory University School of Medicine, Atlanta, GA, USA

☒ Apply Travel Fund

☒ Oral Presentation ☐ Poster ☐ Either Oral or Poster Presentation | Contact Email: iris.zhou@mgh.harvard.edu

KEYWORD: You are encouraged to choose one or two keywords. ☐ CEST agents ☒ Contrast Mechanism

☐ Tumor ☒ Stroke ☐ Neurology ☐ Body & MSK ☐ Standardization ☐ Novel Acquisition ☐ Machine Learning

**INTRODUCTION:** In vivo CEST MRI quantification remains challenging because routine asymmetry analysis (MTR<sub>asym</sub>) or Lorentzian decoupling measures a combined effect from changes in the labile proton concentration and its exchange rate.<sup>1,2</sup> It is interesting to transition from CEST-weighted MRI toward quantitative CEST (qCEST) MRI that simultaneously determine exchange rate and CEST agent content. Our study aimed to quantify changes in amide proton exchange rate independently from the amide proton concentration using omega plot analysis in a cardiac arrest-induced global ischemia rat model.

**METHODS:** Global ischemia was induced in adult male Wistar rats by a lethal dose of potassium chloride injection. MRI scans were performed on six animals (N = 6) before and after global cerebral ischemia using a 4.7T Bruker scanner. Z-spectra were acquired from -6 to 6 ppm with intervals of 0.05 ppm and B<sub>1</sub>=0.25, 0.35, 0.5, and 1 μT. The amide proton CEST (APT) effect was decoupled from tissue water, macromolecular magnetization transfer, nuclear overhauser enhancement, guanidinium, and amine protons using the Image Downsampling Expedited Adaptive Least-squares (IDEAL) fitting algorithm<sup>3</sup> on Z-spectra obtained under multiple RF power levels, before and immediately after global ischemia. Omega plot analysis was applied by linear regression of the inverse of decoupled APT effect (1/APT<sub>ind</sub>) over the inverse of RF powers (1/ω<sub>1</sub><sup>2</sup>),<sup>1,2</sup> for the simultaneous determination of labile amide proton concentration and exchange rate. The determined labile proton exchange rate was then used to estimate pH map.<sup>1</sup>

**RESULTS:** Figure 1 shows the Z-spectra averaged across all brain voxels of 6 rats before and after global ischemia at B<sub>1</sub> levels of 0.25, 0.35, 0.5, and 1 μT. Global ischemia induces a significant APT signal drop from that of the intact tissue. A relatively moderate B<sub>1</sub> level (i.e., ≤ 1 μT) can maximize the APT signal contrast to noise ratio (CNR) between the ipsilateral ischemic and contralateral normal tissue. Using the omega plot analysis, we found that the amide proton exchange rate decreased from 29.6 ± 5.6 to 12.1 ± 1.3 s<sup>-1</sup> (P < 0.001), while the labile amide proton concentration showed a non-significant change (0.241 ± 0.035 % vs. 0.202 ± 0.034 %, P = 0.074) following global ischemia in Figure 2. Figure 3 shows parametric maps of the exchange rate and relative labile proton ratio of amide protons a) before and b) after global ischemia obtained by two-parameter fitting of the iteratively less downsampled spillover-corrected APT images and corresponding pH maps estimated from exchange rate maps.

**CONCLUSION:** Our study implemented the omega plot analysis with multi-pool Lorentzian decoupling and IDEAL fitting algorithms, which enables in vivo quantification of the labile proton concentration and exchange rate underlying the APT contrast. The significant change in exchange rate but not amide proton concentration demonstrated that the APT effect is specific to pH change during tissue ischemia.

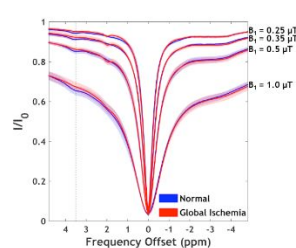


**Figure 1** CEST Z-spectra averaged across all brain voxels before and after global ischemia.

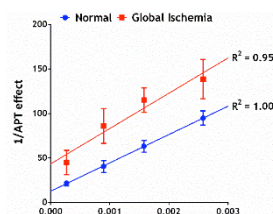


**Figure 2** Omega plot analysis of decoupled APT effect before and after global ischemia.

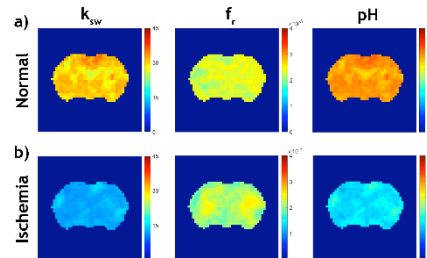


**Figure 3** Omega-plot based quantification of Exchange rate, relative labile proton ratio of amide protons, and pH maps a) before and b) after global ischemia.

## REFERENCES:

- [1] Sun PZ, et al. Phys Med Biol. 2013;58:N229-N40.
- [2] Zaiss M, et al. NMR in biomedicine 2013;26:507-18.
- [3] Zhou IY, et al. Sci Rep 2017;7:84.



# The application of the proton exchange rate ( $k_{ex}$ ) of CEST MRI constructed from direct-saturation-removed Omega plots in ischemic stroke

Yiran Zhou<sup>1</sup>, Mehran Shaghghi<sup>2</sup>, Kejia Cai<sup>2</sup>, Wenzhen Zhu<sup>1</sup>

<sup>1</sup> Department of Radiology, Tongji Hospital, Tongji Medical College, Huazhong University of Science and Technology, Wuhan, Hubei province, China

<sup>2</sup> Departments of Radiology, University of Illinois Hospital & Health Sciences System, Chicago, USA

☐ Apply Student/Postdoc Travel Fund

☐ Oral Presentation ☒ Poster ☐ Either Oral or Poster Presentation | Contact Email: zhou\_yiran@126.com

**KEYWORD:** You are encouraged to choose one or two keywords. ☐ CEST agents ☐ Contrast Mechanism

☐ Tumor ☒ Stroke ☐ Neurology ☐ Body & MSK ☐ Standardization ☐ Novel Acquisition ☐ Machine Learning

## INTRODUCTION:

Proton exchange rate ( $k_{ex}$ ) MRI has recently been developed and preliminarily shown its potential value for evaluating reactive oxygen species (ROS) in vivo (1,2). As the elevated ROS was demonstrated to play a crucial role in the pathogenesis of ischemic brain injury (3), the dynamic change of  $k_{ex}$  in ischemic tissue deserves further investigation to elucidate the detailed environmental evolutions of the infarcted area and improve our understanding of the pathophysiology of stroke. In addition, this study aims to explore the correlation of  $k_{ex}$  between stroke severity and prognosis.

**METHODS:** 96 ischemic stroke patients were included in this study and divided into 3 groups based on stroke phases (acute, subacute and chronic). A spin echo planar imaging sequence with pre-saturation chemical exchange saturation power of 1.5, 2.5, and 3.5  $\mu T$  was implemented to obtain Z-spectra which were fitted to remove the water direct saturation (DS) effect.  $k_{ex}$  maps were constructed from DS-removed omega plots. Relative  $k_{ex}$  ( $rk_{ex}$ ) and relative apparent diffusion coefficient (rADC) were calculated by taking the ratio of  $k_{ex}$  or ADC in the infarcts over that of the mirrored contralateral tissue, respectively. Pearson's correlation analysis was implemented to evaluate the correlations between  $k_{ex}$  &  $rk_{ex}$  and the National Institute of Health Stroke Scale (NIHSS).  $k_{ex}$ ,  $rk_{ex}$ , rADC, and lesion volume were evaluated for predictive performance of acute stroke outcome using receiver operating characteristic curve.

**RESULTS:** The  $k_{ex}$  of ischemic lesions was significantly higher compared to the mirrored contralateral tissue at all stages (acute phase: ischemic lesion  $935.1 \pm 81.5 s^{-1}$  vs contralateral tissue  $777.3 \pm 45.1 s^{-1}$ ,  $P < 0.001$ ; subacute phase:  $881.4 \pm 55.7 s^{-1}$  vs  $762.2 \pm 36.6 s^{-1}$ ,  $P < 0.001$ ; chronic phase:  $866.9 \pm 76.7 s^{-1}$  vs  $756.3 \pm 36.7 s^{-1}$ ,  $P < 0.001$ ). Besides, the  $k_{ex}$  of acute lesions was higher than subacute and chronic lesions ( $P < 0.05$ ,  $P < 0.01$ ). However, the difference between subacute and chronic lesions was not significant. Lesion's  $k_{ex}$  &  $rk_{ex}$  showed moderate correlation with the NIHSS score only for acute cases ( $r = 0.406$ ,  $P = 0.016$ ;  $r = 0.531$ ,  $P = 0.001$ ). Acute patients with poor prognosis had significantly higher  $k_{ex}$  &  $rk_{ex}$  of lesion compared to patients with good prognosis ( $991.1 \pm 78.2$  vs.  $893.1 \pm 55.1 s^{-1}$ ,  $P < 0.001$ ;  $1.28$  vs.  $1.15$ ,  $P < 0.001$ ). These measures showed favorable predictive performance for acute stroke outcome with area under the curve (AUC) of 0.837 and 0.880, slightly while not significantly higher than lesion volume (AUC: 0.730) and rADC (AUC: 0.673).

**DISCUSSION:** The previous study (2) drew a hypothesis that the increased  $k_{ex}$  in ischemic lesions may be due to the excessive ROS production as  $k_{ex}$  has been demonstrated its sensitivity and specificity for ROS (1). Besides, the three distinct phases of ROS generation after cellular ischemia and hypoxia all occurred in the acute period based on the previous study (4). Our study was consistent with it as the  $k_{ex}$  was significantly higher in the acute than in the subacute and chronic infarct lesions. Reduced inflammation over time may be another reason, as inflammation was the main cause of extracellular ROS production (5). A positive correlation between  $k_{ex}$  &  $rk_{ex}$  and the NIHSS score and the potential predictive value for stroke outcome in acute patients was found in our study. ROS have significant cellular effects including lipid peroxidation, protein denaturation, enzyme inactivation, nucleic acid, and DNA damage, ultimately leading to tissue destruction and cell death (6). Neuronal cells are very sensitive and vulnerable to oxidative stress (5). ROS has been demonstrated to be a pivotal damaging event leading to neuronal death and an indicator of stroke prognosis (7,8). The invasive measurement of tissue ROS to precisely elucidate the correlation between  $k_{ex}$  and ROS is necessary in future studies on animal models.

**CONCLUSION:**  $k_{ex}$ -MRI is promising for ischemic stroke diagnosis and management as it may reflect oxidative stress of stroke lesions at different stages and predict the prognosis.

## REFERENCES:

1. Tain RW, *et al.* J Magn Reson Imaging 2019;50:583-91.
2. Wang Z, *et al.* J Neurosci Methods 2020;346:108926.
3. Nanetti L, *et al.* Mol Cell Biochem 2007;303:19-25.
4. Abramov AY, *et al.* J Neurosci 2007;27:1129-38.
5. Jelinek M, *et al.* Antioxidants (Basel) 2021;10.
6. Allen C, *et al.* Int J Stroke. 2009;4:461-70.
7. Sanderson TH, *et al.* Mol Neurobiol 2013;47:9-23.
8. Alexandrova M, *et al.* J Clin Neurosci 2004;11:501-6.

# Relayed nuclear Overhauser effect (rNOE) and amide CEST detects myelin changes in cuprizone mouse model at 3T

Zilin Chen<sup>1#</sup>, Jianpan Huang, PhD<sup>1#</sup>, Joseph H. C. Lai<sup>1</sup>, Kai-Hei Tse, PhD<sup>2</sup>, Jiadi Xu, PhD<sup>3</sup>, Kannie W.Y. Chan, PhD<sup>1,3,4,5,6,\*</sup>

<sup>1</sup> Department of Biomedical Engineering, City University of Hong Kong, Hong Kong, China

<sup>2</sup> Department of Health Technology and Informatics, The Hong Kong Polytechnic University, Hong Kong, China

<sup>3</sup> Russell H. Morgan Department of Radiology and Radiological Science, The Johns Hopkins University School of Medicine, Baltimore, MD 21205, USA

<sup>4</sup> Hong Kong Centre for Cerebro-Cardiovascular Health Engineering (COCHE), Hong Kong, China

<sup>5</sup> City University of Hong Kong Shenzhen Research Institute, Shenzhen, 518057, China

<sup>6</sup> Tung Biomedical Science Centre, City University of Hong Kong, Hong Kong, China

\* Corresponding author

# These authors contributed equally to this work.

✉ Apply Student/Postdoc Travel Fund

□ Oral Presentation □ Poster ✉ Either Oral or Poster Presentation | Contact Email: zilinch9-c@my.cityu.edu.hk

KEYWORD: You are encouraged to choose one or two keywords. □ CEST agents □ Contrast Mechanism

□ Tumor □ Stroke ✉ Neurology □ Body & MSK □ Standardization □ Novel Acquisition □ Machine Learning

**INTRODUCTION:** Chemical exchange saturation transfer (CEST) sensitively detects molecular alterations in the brain, such as relayed nuclear Overhauser effect (rNOE) CEST contrast at -3.5 ppm representing aliphatic protons in both lipids and proteins (1), and CEST contrast at 3.5 ppm correlates with protein amide protons (2,3). Myelin is rich in lipids (4), thus CEST could be explored as biomarkers for myelin pathology, which could contribute to multiple sclerosis (MS) diagnosis and prognostic.

**METHODS:** In this study, preclinical 3T MRI was performed in male C57BL/6 mice at 8-week-old. Cuprizone (CPZ) was employed for demyelination and remyelination, recapitulating myelinated pathology in MS(5). Mice in normal control group (NC, n=9) were fed with normal diet for the whole course, while mice in CPZ group (n=10) were fed with CPZ for 10 weeks followed by 4 weeks with normal diet. Relaxation-compensated CEST contrasts (AREX) of rNOE (-3.5 ppm) and amide (3.5 ppm) in brain regions of corpus callosum (CC) were extracted for comparison.

**RESULTS:** We observed significantly decreased rNOE ( $4.85 \pm 0.09$  %/s vs  $3.88 \pm 0.18$  %/s,  $P = 0.007$ ) and amide contrasts ( $3.20 \pm 0.10$  %/s vs  $2.46 \pm 0.16$  %/s,  $P = 0.02$ ) in CC after 8 weeks on CPZ diet. During the remyelination phase at week 14, rNOE contrast in CPZ group recovered to a comparable level as NC at week 14 ( $P = 0.39$ ), while amide contrast remained at a relatively low level as NC ( $P = 0.051$ ).

**DISCUSSION:** Both rNOE and amide CEST could detect myelin changes in demyelination phase of CPZ model. The distinctive observations at week 14, i.e. the recovery in rNOE and unchanged in amide CEST contrast, indicated rNOE is relatively higher sensitivity than amide CEST in detecting remyelination.

**CONCLUSION:** Significant rNOE and amide changes validated with immunohistochemistry results of the demyelination and remyelination demonstrated great potential of CEST in revealing myelin pathology, which has implications in MS identification at the clinical-field strength 3T.

**ACKNOWLEDGMENTS:** RGC: 11102218, PDFS2122-1S01, C1134-20G; CityU: 7005433, 7005626, 9667198, 9609307 and 9610560; NSFC: 81871409-H1808; Tung Biomedical Sciences Centre; Hong Kong Centre for Cerebro-cardiovascular Health Engineering.

## REFERENCES:

1. Zhou J, *et al.* Nat Med 2003;9(8):1085-1090. 2. Zu Z, *et al.* Magn Reson Med 2020;84(4):1961-1976. 3. Han X, *et al.* Theranostics 2020;10(5):2215-2228. 4. Morell P, *et al.* Basic Neurochemistry: Molecular, Cellular and Medical Aspects. 6th ed 1999. 5. Kipp M, *et al.* Acta Neuropathol 2009;118(6):723-736.

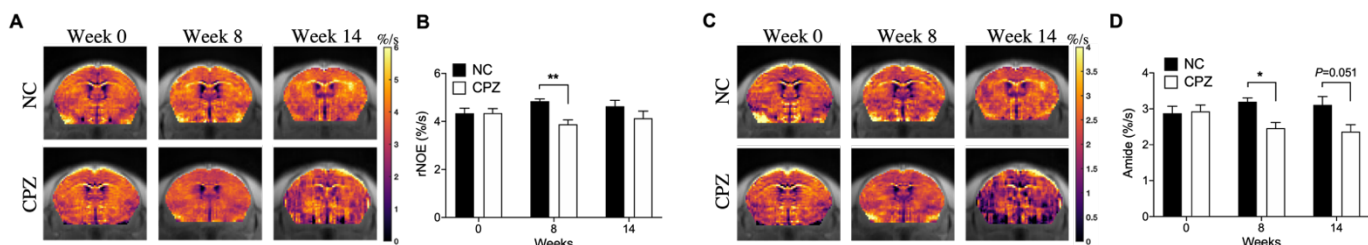


**Figure 1.** (A) Representative AREX maps of rNOE at -3.5 ppm and (C) amide at 3.5 ppm. (B) Comparison of rNOE and (D) amide contrast between normal control (NC) and cuprizone (CPZ) group on corpus callosum. Data was presented as mean±SEM and analyzed via two-way ANOVA.

## The use of frequency selective pulses with filtered frequencies for eliminating magnetization transfer contrast in CEST.

Eleni Demetriou<sup>1,2</sup>, Sarina Khamoshi<sup>2</sup>, Jack Wells<sup>3</sup>, Anke Henning<sup>2</sup>, Xavier Golay<sup>1</sup>

<sup>1</sup>Brain repair and Rehabilitation, Institute of Neurology, University College London, UK

<sup>2</sup>Advanced imaging research center, UTSouthwestern, Dallas, USA

<sup>3</sup>Centre for Advanced Biomedical Imaging, University College London, UK

**Introduction:** In this work, we extend the previously published PRO-QUEST technique (1), (2) with the incorporation of frequency selective pulses with filtered frequencies for eliminating magnetization transfer (MT) contrast and for measuring MT free amide proton relaxation rate. We hypothesised that relaxation in the presence of RF irradiation is governed by  $R_{\text{RHO}}(3.5 \text{ ppm}) = R_{\text{eff}}(3.5 \text{ ppm}) + R_{\text{ex}}(3.5 \text{ ppm}) + R_{\text{MT}}(3.5 \text{ ppm})$  (3) while this is modified to  $R'_{\text{RHO}}(3.5 \text{ ppm}) = R_{\text{eff}}(3.5 \text{ ppm}) + R_{\text{MT}}(3.5 \text{ ppm})$  when the resonance frequencies at 3.5 ppm are removed from the off-resonance pulse we used to induced CEST contrast for APT. In other words, by using a two-step acquisition (i.e. acquiring PRO-QUEST data with and without filtering frequencies) we can correct for the MT effects which co-exist with CEST by subtracting  $R_{\text{RHO}}(3.5 \text{ ppm}) - R'_{\text{RHO}}(3.5 \text{ ppm}) = R_{\text{ex/MTcorrected}}(3.5 \text{ ppm})$ .

**Methods: Filter:** A series of sinc-gauss pulses ( $N=200$ ,  $\text{tsat}=16.3\text{msec/BW}=1\text{ppm}$  or  $\text{tsat}=6.77\text{msec/BW}=2.5\text{ppm}$ ) were used to generate a periodic signal. Then, a low band filter was applied to remove low frequency components of the signal which was subsequently Fourier transformed. Next the signal was multiplied by the carrier frequency which was set at 3.5 ppm and a bandstop filter was applied to cut a range of frequencies around the central frequency i.e. 3.5 ppm. **Samples:** 10 mM of glutamine in 30g/l agar at various pH values were used to validate the method. **In vivo:** 3 rats were scanned with the standard pulse and the filtered pulse using PRO-QUEST MRI at 3 irradiation amplitudes: 0.78 uT, 1.53 uT, and 2.56 uT. The flip angle for the filter/non-filter RF pulse was calculated to produce the same B1 level for both acquisitions (tsat was kept the same for filter/non-filter pulse). The filter size of the pulse was 200 Hz and applied at 3.5 ppm. Another 2 rats were scanned with pulses generated with different filter sizes e.g. 200 Hz or 100Hz. We also tested the effect of  $B_0$  on the generated pulses by acquiring data at 3.0ppm and 3.7 ppm. **Simulations:** Bloch simulations were applied to assess whether we detect any sidebands because of the removal of frequencies from the pulse.

**Results:** Figure 1 shows the Fourier transform of the sinc-gauss pulse we used to generate CEST contrast (a) and the Fourier transform of the filtered pulse (b) we used for inducing MT and direct water saturation (DWS) at 3.5ppm. The pulses we used are also shown in figure 1c. Figure 1d shows simulated  $M_z$  for 2 filter sizes. When the filter size is above 200 Hz sidebands are generated which induce extra MT effects. Therefore, the filter size should be chosen to avoid such sidebands. Figure 1e shows PRO-QUEST curves from glutamine agar sample with/without filtered pulses. Figure 2 displays the Rex maps calculated in a single representative rat and the Rex/MT corrected maps for all the B1 levels used. The size of the filter doesn't show a measurable effect on the Rex/MT corrected maps (see Figure 3). Finally, the effect of  $B_0$  is negligible for the high bandwidth pulses we used in our study.

**Discussion:** We could show Rex/MT corrected maps in vivo when a filtered pulse is applied by acquiring an additional PRO-QUEST scan using similar B1 settings as the ones we used without the application of the filter. The MT contrast at 3.5 ppm is substantial and induces a flat baseline which adds to the calculated Rex of amide protons. The effect of the filter size and  $B_0$  is negligible for the high bandwidth pulses we used and should not affect the design of the pulses, however, when the filter is too large this induces sidebands which should be avoided. Finally, this 2-step method does not require any prior knowledge of the MT or DWS since they are measured experimentally and accounted when we calculate the correct estimates of Rex for APT. This is done in a clinically feasible scan time (10 mins) and by avoiding long post-processing steps for individually fitting and correcting for MT and DWS.

# Relayed nuclear Overhauser effect (rNOE) imaging for deferoxamine (DFX) treatment effect in intracerebral hemorrhage (ICH) at 3T

Joseph H.C. Lai<sup>1</sup>, Jiaxin Liu<sup>2</sup>, Tian Yang<sup>3</sup>, Jianpan Huang<sup>1</sup>, Yang Liu<sup>1,2</sup>, Zilin Chen<sup>1</sup>, Youngjin Lee<sup>3</sup>, Gilberto K. K. Leung<sup>2</sup>, and Kannie W.Y. Chan<sup>1,4,5,6,7\*</sup>

<sup>1</sup>Department of Biomedical Engineering, City University of Hong Kong, Hong Kong; <sup>2</sup>Department of Surgery, School of Clinical Medicine, Li Ka Shing Faculty of Medicine, The University of Hong Kong, Hong Kong; <sup>3</sup>Department of Neuroscience, City University of Hong Kong, Hong Kong; <sup>4</sup>Russell H. Morgan Department of Radiology and Radiological Science, The Johns Hopkins University School of Medicine, Baltimore, MD, USA; <sup>5</sup>City University of Hong Kong Shenzhen Research Institute, Shenzhen, China; <sup>6</sup>Hong Kong Centre for Cerebro-Cardiovascular Health Engineering (COCHE), Hong Kong; <sup>7</sup>Tung Biomedical Science Centre, City University of Hong Kong, Hong Kong, China;

\*Corresponding author

☑ Apply Student/Postdoc Travel Fund

☐ Oral Presentation ☐ Poster ☑ Either Oral or Poster Presentation | Contact Email: josephlai5-c@my.cityu.edu.hk

**KEYWORD:** You are encouraged to choose one or two keywords. ☐ CEST agents ☐ Contrast Mechanism

☐ Tumor ☑ Stroke ☐ Neurology ☐ Body & MSK ☐ Standardization ☐ Novel Acquisition ☐ Machine Learning

**INTRODUCTION:** Lipid plays a vital role during the evolution of ICH, especially lipid peroxidation (1), which can cause white matter injury in the brain (2). Since we have demonstrated that rNOE could detect myelin-related neuropathology (3), we hypothesized that rNOE could detect the myelin changes at the hematoma of an ICH brain and identify the treatment outcome under DFX treatment, which is a clinical-available drug for iron chelation treatment (4,5).

**METHODS:** We imaged an ICH mouse model (6) with and without DFX treatment (n=5), in which the treatment was given by the intraperitoneal injection of saline or DFX (200mg/kg per dose) twice a day for 7 consecutive days, using rNOE (-3.5ppm) and APT (3.5ppm) contrast over two weeks at 3T. After that, representative mice (n=3) from each time point were sacrificed for immunohistochemical studies by co-staining with Myelin Basic Protein (MBP) and FluoroMyelin™ (FM, ThermoFisher) to study the protein and myelin pathology, respectively.

**RESULTS:** We observed temporal signal changes at hematoma for rNOE and APT (Fig. 1). The rNOE signal on day 3 dropped after DFX treatment (Fig. 1B,  $P < 0.05$ ), while the change in APT was not significant (Fig. 1C). The treatment effect at other time points was not pronounced. We further compared the fluorescence intensities of FM and MBP with the corresponding CEST signals (Fig.2), and we found that only FM gave a significant correlation with rNOE (Fig. 2A & C,  $P < 0.05$ ).

**DISCUSSION:** rNOE is sensitive to lipid pathologies (7). The observed rNOE decrease on day 3 could be due to the change in myelin-related lipids or protein during regeneration. As to our histological results, rNOE was significantly correlated with FM but not with MBP, indicating that the rNOE signal change came from the myelin lipid.

**CONCLUSION:** rNOE could identify the DFX treatment effect, and the significant rNOE changes correlated well with the histologic findings, especially with myelin lipids. Our result has indicated the uniqueness of rNOE at 3T in monitoring molecular changes during ICH and treatment, which has the potential to be translated to the clinical level.

**REFERENCES:** 1. Duan X, et al. Intracerebral Hemorrhage, Oxidative Stress, and Antioxidant Therapy. 2016;2016. 2. Fu X, et al. White Matter Injury After Intracerebral Hemorrhage. Front. Neurol. 2021;12 doi: 10.3389/fneur.2021.562090. 3. Huang J, et al. NeuroImage : Clinical Relayed nuclear Overhauser effect weighted ( rNOEw ) imaging identifies multiple sclerosis. NeuroImage Clin. 2021;32:102867 doi: 10.1016/j.nicl.2021.102867. 4. Selim M, et al. Safety and tolerability of deferoxamine mesylate in patients with acute intracerebral hemorrhage. Stroke 2011;42:3067–3074 doi: 10.1161/STROKEAHA.111.617589. 5. Selim M, et al. Deferoxamine mesylate in patients with intracerebral haemorrhage (i-DEF): a multicentre, randomised, placebo-controlled, double-blind phase 2 trial. Lancet Neurol. 2019;18:428–438 doi: 10.1016/S1474-4422(19)30069-9. 6. Li M, et al. Colony stimulating factor 1 receptor inhibition eliminates microglia and attenuates brain injury after intracerebral hemorrhage. J. Cereb. Blood Flow Metab. 2017;37:2383–2395 doi: 10.1177/0271678X16666551. 7. Jones CK, et al. Nuclear Overhauser enhancement (NOE) imaging in the human brain at 7T. Neuroimage 2013;77:114–124 doi: 10.1016/j.neuroimage.2013.03.047.

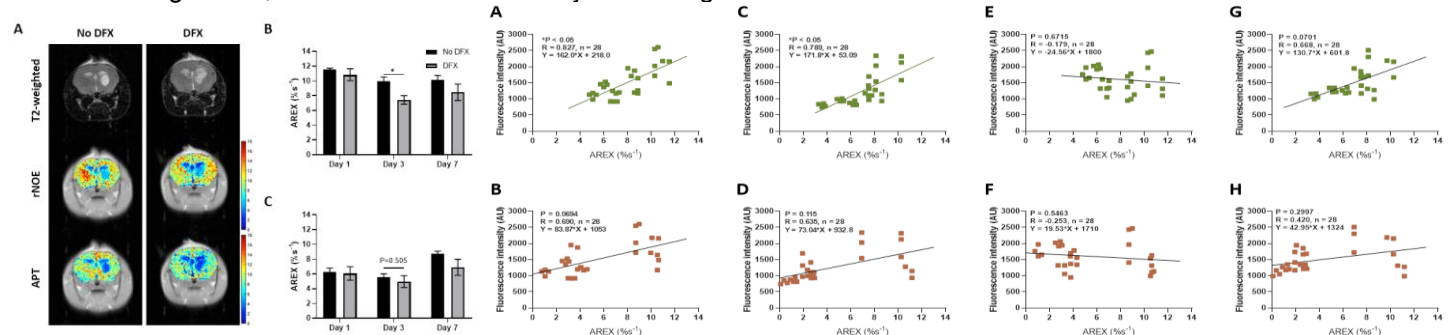


**Fig. 1.** The representative ICH brains on day 3 are showed in (A). (B) and (C) show the rNOE and APT changes, respectively, after DFX treatment up to day 7.

**Fig. 2.** The correlation of no DFX group for (A) FM vs rNOE; (B) FM vs APT; (E) MBP vs rNOE; and, (F) MBP vs APT. The correlation of DFX group for (C) FM vs rNOE; (D) FM vs APT; (G) MBP vs rNOE; and, (H) MBP vs APT.



# Age dependent cerebrospinal fluid-tissue water exchange detected by non-invasive magnetization transfer indirect spin labeling MRI

Anna M. Li<sup>1</sup>, Lin Chen<sup>1,2,3</sup>, Hongshuai Liu<sup>2</sup>, Yuguo Li<sup>1,2</sup>, Wenzhen Duan<sup>2</sup>, Jiadi Xu<sup>1,2\*</sup>

<sup>1</sup>Kennedy Krieger Research Institute <sup>2</sup>The Johns Hopkins University School of Medicine, <sup>3</sup>Xiamen University

**INTRODUCTION:** The CSF exchange with other tissues, e.g., the parenchyma and ependymal layers, and the correlation with brain function were not well documented. The CSF water exchange may also impact the recently discovered glymphatic system. We developed one non-invasive and translational MRI technique, Magnetization transfer indirect spin labeling (MISL), to assess the CSF water exchanging process with surrounding tissues by selectively labeling water molecules in the other tissues, e.g., ependyma, parenchyma, and blood. (Fig. 1a)

**METHODS:** MISL sequence labels the macromolecules in the brain tissues using an train of saturation pulses (Fig. 1c). The labeled magnetization will be transferred to water from the abundant macromolecules in those tissues (Fig. 1b). CSF signal was not attenuated by the pulses due to the trace protein concentration (200 times lower than blood plasma). (1) The signal reduction of CSF is due to water exchange between tissues and CSF. Therefore, the CSF water exchange can be monitored. (Fig. 1b) In the MISL, a train of Gaussian saturation pulses (30 ms pulse width, 4  $\mu$ T peak power, 100 pulse number) was applied. MISL signal ( $\Delta Z$ ) was obtained by the subtraction of the label MRI at -3.5 ppm from the control MRI at 200 ppm (Fig. 1c). Cerebrospinal fluid (CSF) was extracted from the mouse ventricles for the MISL optimization and validation. The sequence is identical to the conventional pulsed and continuous wave CEST sequence, except one PLD can be added before the MRI readout.

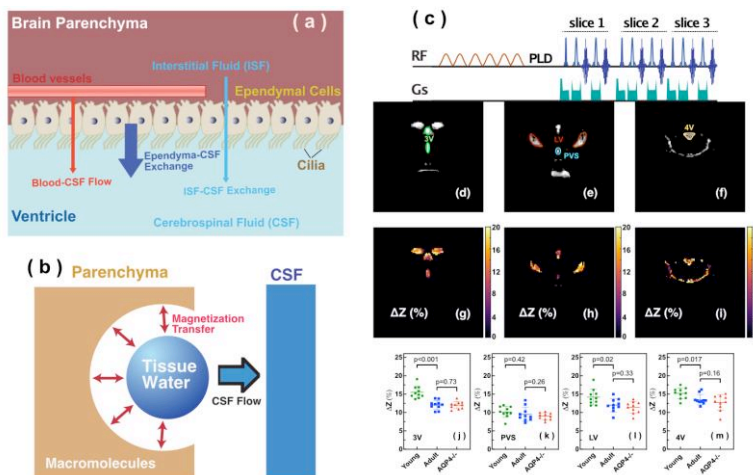


Fig. 1 (a) Illustration of the possible water flow and exchange processes that contribute to the observed MISL signal, i.e., CSF water exchange. (b) Illustration of the principal of the MISL method. (c) Timing diagram of the MISL sequence. (d-i) Representative multi-slice images acquired with LongTE-TSE and the corresponding  $\Delta Z$  maps of a WT mouse brain acquired using the MISL scheme. (j) The regional MISL  $\Delta Z$  signal for the third ventricle, (k) the paravascular space, (l) the lateral ventricle, and (m) the fourth ventricles in young WT (green circle), adult WT (blue square), and AQP4<sup>-/-</sup> (red triangle) mice. The MISL  $\Delta Z$  of adult WT and AQP4<sup>-/-</sup> mice shows an apparent reduction compared to young WT mice in all ventricles.

**RESULTS & DISCUSSION:** The 4<sup>th</sup> ventricle (4V) showed the highest MISL  $\Delta Z$  signal ( $13.5 \pm 1.4$  %), and the 3<sup>rd</sup> ventricle (3V) ( $12.0 \pm 1.3$  %) had a similar MISL  $\Delta Z$  as lateral ventricles (LV) ( $12.0 \pm 1.8$  %). The paravascular space (PVS) MISL  $\Delta Z$  ( $9.5 \pm 1.9$  %) was significantly lower than the ventricles'  $\Delta Z$  ( $p < 0.028$ ). (Fig. 1m) The CSF water exchange value =  $1083 \pm 400$  ml/100ml/min for LV and  $R_{1a} = 1.25 \pm 0.34$  s<sup>-1</sup> were extracted from fitting curve. CSF water exchange value =  $1320 \pm 600$  ml/100ml/min and  $R_{1a} = 1.25 \pm 0.5$  s<sup>-1</sup> were determined for 3V. Significant differences were obtained between young wild type (WT) and adult WT for all the ventricles (LV: 13.7% reduction; 3V: 18.7% reduction; 4V: 9.3% reduction), while the PVS  $\Delta Z$  values of adult WT were not significantly lower than the young WT in trend. For the AQP4<sup>-/-</sup> mice, the LV and 4V  $\Delta Z$  and CSF water exchange values were smaller but not significant than those of the age-matched WT mice (LV: 8.3% reduction; 4V: 5.9% reduction; LV:  $p = 0.33$ ; 4V:  $p = 0.16$ ), while the 3V and PVS values were similar for the age-matched WT and AQP4<sup>-/-</sup> mice. (Fig. 1 j-m) The result highlights the sensitivity of the MISL approach in the non-invasive assessment of CSF water exchange in the brain. The results indicated that young mice (2-3 months) had significantly higher CSF water exchange than their adult counterparts (9-10 months). The AQP4<sup>-/-</sup> mice did not show significant CSF water exchange reduction compared to their age-matched wild-type counterparts. Differences between regional signal reduction show that water exchange is not uniform across ventricles. This non-invasive MRI method provided a technically achievable tool to examine the potential association between CSF water exchange and functional decline in many neurodegeneration diseases.

**CONCLUSION:** The results suggested that the novel MISL method has a far-reaching impact on studying, diagnosing, and treating a range of brain diseases, given their association with CSF water exchange. The current method only included the mouse brain, but it could be readily implemented on human scanners from low fields to high fields since the MT line shape covers an extensive range of frequencies.

**REFERENCES:** 1. Huhmer AF, et. al. Dis Markers 2006;22(1-2):3-26.

## Healthy vs pathological tau can be differentiated by CEST NMR

Fang Frank Yu<sup>1</sup>, James Ratnakar<sup>2</sup>, Bryan Ryder<sup>3</sup>, Brian Hitt<sup>4</sup>, A Dean Sherry<sup>1,2</sup>, and Elena Vinogradov<sup>1,2</sup>

<sup>1</sup>Radiology, University of Texas Southwestern Medical Center, Dallas, TX, US, <sup>2</sup>Advanced Imaging Research Center, University of Texas Southwestern Medical Center, Dallas, TX, US, <sup>3</sup>Center for Alzheimer's and Neurodegenerative Diseases, University of Texas Southwestern Medical Center, Dallas, TX, US, <sup>4</sup>Neurology, University of California, Irvine Medical Center, Irvine, CA, US

☐ Apply Student/Postdoc Travel Fund

☐ Oral Presentation ☐ Poster ☒ Either Oral or Poster Presentation |

Contact Email: Elena.Vinogradov@UTSouthwestern.edu

KEYWORD: You are encouraged to choose one or two keywords. ☒ CEST agents ☐ Contrast Mechanism

☐ Tumor ☐ Stroke ☒ Neurology ☐ Body & MSK ☐ Standardization ☐ Novel Acquisition ☐ Machine Learning

**INTRODUCTION:** Alzheimer's Disease (AD) is the leading cause of dementia, afflicting 45 million worldwide, and is defined biologically by the presence of neuritic plaques composed of amyloid- $\beta$  (A $\beta$ ) peptides and dystrophic neurites, neurofibrillary tangles (NFTs) of hyperphosphorylated tau protein, and neuronal loss as formalized under the AT(N) research framework. In particular, NFTs have drawn considerable interest as potential therapeutic targets due to their strong association with neurodegeneration. Chemical Exchange Saturation Transfer (CEST) has emerged as a promising MRI technique that can detect low concentration chemical species with exchangeable protons, which are non-visible by standard MRI methods. Studies have demonstrated the sensitivity of CEST to protein state, including conformation and folding structure, in vitro as well as in vivo. In this study, CEST experiments were performed on purified full-length tau monomer and aggregated tau fibrils to examine whether each form of tau has a specific CEST signature. Differences in these signatures could potentially be used to inform future in vivo studies in animal models and ultimately in AD patients.

**METHODS:** Purified monomeric human full-length tau protein (2N4R) was created from cDNA coding for the protein that had been transformed into E. coli BL21. Tau fibrils (aggregated tau) phantoms were then generated from specimens of monomeric tau by incubating with heparin at 37°C for 3 days. Tau assembly was also induced using seed-competent tau and incubated at 37°C for 3 days. The CEST experiments were repeated multiple times and only last set is reported here.

All CEST experiments were performed using a 9.4 T vertical bore Varian NMR spectrometer. Four sets of RF pulse intensities (B<sub>1</sub>) were utilized: 10, 15, 24 and 36 Hz, and applied over a 2 second saturation pulse duration. These were performed at three temperatures: 25, 37, and 42 °C. Z-spectra were acquired in the +/-10ppm range, using 0.25 ppm steps (total of 82 points). The same set of acquisition parameters were utilized for the tau monomer and tau fibrils.

**RESULTS:** Figure 1 shows the Z-spectra of the tau monomer obtained at 37°C at different B<sub>1</sub>. A prominent peak is observed at 3.5 ppm. A smaller peak is observable at 1.75 ppm and a large asymmetry close to zero. With increasing RF saturation intensity, the signal intensity of the Z-spectrum peaks and MTR<sub>asym</sub> is increased. Figure 2 shows the Z-spectra of the tau fibrils obtained using seeding tau measured at 37°C. The tau fibrils demonstrated a pronounced peak at around 0.75 ppm. The intensity of this peak decreases with increasing temperature. A peak at 3.5 ppm is also present and increases with increasing temperature. Finally, a peak at 1.75 ppm is also observed, albeit with the lowest intensity, which increases with increasing temperature. Figure 3 shows the comparison of tau monomer to tau fibrils. The difference in peaks intensity and appearance is evident.

**DISCUSSION:** A possible explanation for our observations is that through forming structurally relevant hydrogen bonds in the fibrillated tau specimen, the effective exchange rate of internal amino acid residues sequestered from the water pool may become reduced and no longer detectable by CEST. Additionally, individual molecules of tau monomers have relatively rapid internal motions and molecular tumbling, potentially resulting in a sharper Z-spectrum. However, as proteins aggregate, the internal motions and tumbling tend to slow, resulting in broadening of the line-shape of the Z-spectrum and overall coalescence of the spectral features.

Currently, we are conducting a fitting of the experimental data using multi-pool Bloch-McConnell equations to provide exchange rates and could help elucidate the origins of the observed differences between monomeric and fibrillated tau.

**CONCLUSION:** We found differences in CEST z-spectra between purified full-length tau monomers and aggregated tau fibrils. While additional experiments are needed, including the influence of different tau preparation methods, this finding substantiates the potential use of CEST for ultimately monitoring disease progression in AD patients as reflected by increased NFT deposition.

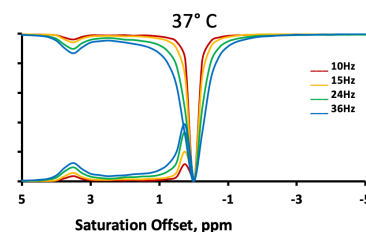


**Fig. 1.** Z-spectra and MTR<sub>asym</sub> of the tau monomer

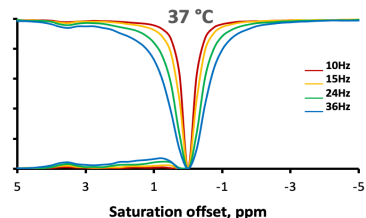


**Fig.2.** Z-spectra and MTR<sub>asym</sub> of the tau fibrils

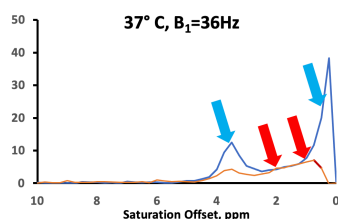


**Fig.3** MTR<sub>asym</sub> analysis of tau fibrils (red) and tau monomers (blue). Red arrows indicate peaks at 0.75 and 1.75 ppm. Blue arrows peaks at 3.5ppm and asymmetry close to zero.



# Brain glioma pH imaging using chemical exchange saturation transfer (CEST) MRI

Haochuan Gan, Renhua Wu

Department of Medical Imaging, the Second Affiliated Hospital, Medical College of Shantou University, Shantou 515041, China

✉ Either Oral or Poster Presentation | Contact Email: ganishen@163.com

KEYWORD: ☒ CEST agents ☒ Tumor

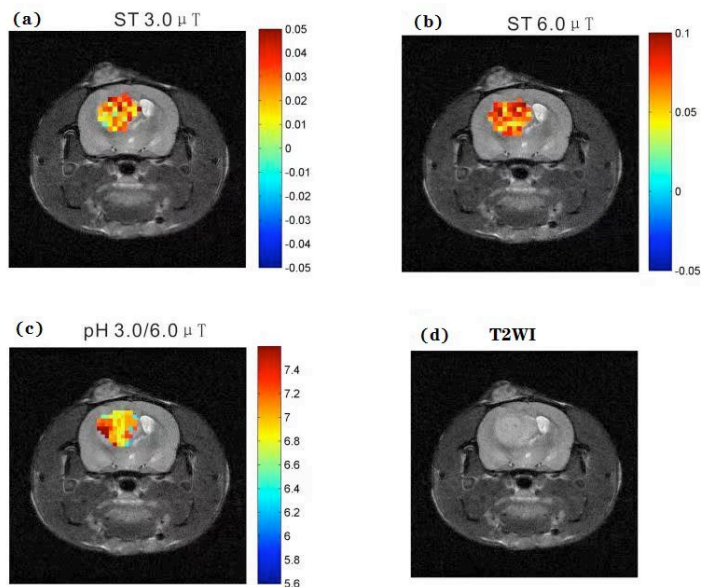
## INTRODUCTION:

To evaluate whether chemical exchange saturation transfer (CEST) techniques are able to detect extracellular pH (pHe) in rat with gliomas using nonionic x-ray iodinated contrast agents (Iobitridol)

**METHODS:** Chemical exchange saturation transfer pH imaging was performed on Iobitridol phantoms and rats with brain gliomas. All imaging was obtained on a 7.0 Tesla horizontal bore (bore size 160mm) small animal MRI scanner (Agilent Technologies, Santa Clara, CA, USA). Different RF powers (3.0 and 6.0  $\mu\text{T}$ ) were used based on ratio of RF power mismatch or RPM techniques.

**RESULTS:** Within a narrow pH range of 5.7-7.3, the logarithm of the CEST effect ratio of Iobitridol exhibited an excellent linear relationship with pH, which was not relative to the concentration of Iobitridol. The CEST pHe image was successfully depicted in vivo at the locality of gliomas tissue. The calculation of mean pHe by using pH<sub>3.0/6.0  $\mu\text{T}$</sub>  of gliomas was acidic (pH<sub>3.0/6.0  $\mu\text{T}$</sub>  = 6.92  $\pm$  0.13), which was consistent with previous studies.

**CONCLUSION:** For the first time, non-invasive CEST imaging was able to detect extracellular acidic microenvironment of brain gliomas. The results of our study indicated that it had potential clinical application



# Amide proton transfer imaging allows early detection of a therapeutic response with temozolomide in glioma

Lihua Lai

Department of Medical Imaging, second Affiliated Hospital, Shantou University Medical College, Shantou 515041, China

✓ Poster Contact Email: lailihua7@163.com

KEYWORD: CEST agents、Tumor

## INTRODUCTION:

Aim to offer a biomarker of early response in chemotherapy of TMZ, so as to improve the management of a patient suffering glioma.

## METHODS:

Constructed animal protocols with glioma on the Basal ganglia of the brain of SD rats. When the tumors reached a size of 3-5mm monitored under T2WI, the rats were randomly divided into 2 groups. T2WI and APT images were collected using a horizontal bore 7 T animal MRI before and in the 7th day of the treatment. In the treated group, the SD rats underwent a course of treatment with Temozolomide (TMZ, 80mg/Kg, for 4 days and rest for 3 days), while in the control group, 80mg/kg saline solution was injected into the control group. All the data were processed on matlab and image j.

## RESULTS:

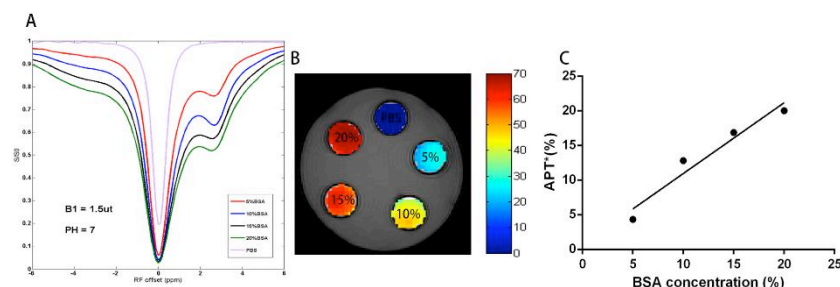


Figure 1. A. Z - spectra for different concentrations of BSA under pH=7 and B1=1.5ut. B. APT\* image for different concentrations of BSA under pH=7 and B1=1.5ut. C. The correlation analysis between APT\* signal and concentration:  $Y=1.022X+0.7154$ ,  $R^2=0.9441$ .

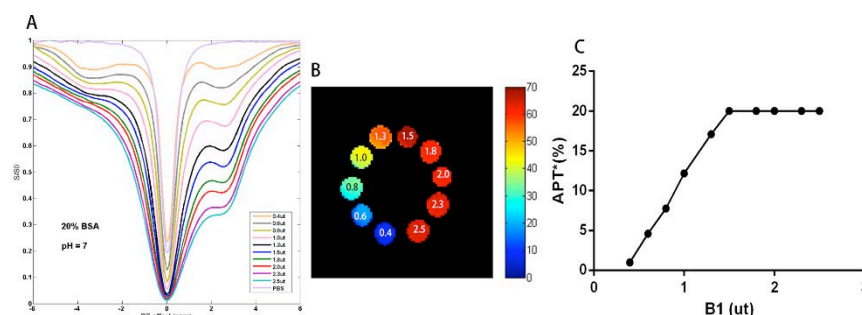


Figure 2. A. Z - spectra for different saturation pulse energy (B1) under 20%BSA and pH=7. B. APT\* image for different saturation pulse energy (B1) under 20%BSA and pH=7. C. The correlation analysis between APT\* signal and B1.

# Multiparametric monitoring local brain tumor treatment using CEST-detectable liposomal hydrogel at 3T

Se Weon Park<sup>1,2</sup>, Joseph H.C Lai<sup>1</sup>, Xiongqi Han<sup>3</sup>, Jianpan Huang<sup>1</sup>, Peng Xiao<sup>1</sup>, Kannie WY Chan<sup>1,2,4,5\*</sup>

<sup>1</sup>Department of Biomedical Engineering, City University of Hong Kong, Hong Kong, China; <sup>2</sup>Hong Kong Centre for Cerebro-Cardiovascular Health Engineering (COCHE), Hong Kong, China; <sup>3</sup>Sibionics, Shenzhen, China; <sup>4</sup>Russell H. Morgan Department of Radiology and Radiological Science, The Johns Hopkins University School of Medicine, Baltimore, MD, USA; <sup>5</sup>City University of Hong Kong Shenzhen Research Institute, Shenzhen, China.

✉ Apply Student/Postdoc Travel Fund

□ Oral Presentation □ Poster ✉ Either Oral or Poster Presentation | Contact Email: swpark3-c@my.cityu.edu.hk

**KEYWORD:** □ CEST agents □ Contrast Mechanism ✉ Tumor □ Stroke □ Neurology □ Body & MSK □ Standardization □ Novel Acquisition □ Machine Learning

**INTRODUCTION:** In order to treat brain tumor such as glioblastoma, several targeted drug delivery approaches, including Gliadel wafer(1) have shown promises, however the limited coverage and the resulted edema have limited the efficacy of this local treatment(1). Liposomal hydrogel loaded with CEST-detectable chemotherapeutics(2), such as Gemcitabine (Gem) and methotrexate (MTX), has been reported to demonstrate sustainable drug release and anti-U87 efficacy, in *in-vitro*(3). Moreover, signal at 3.5 ppm could indicate tumor recurrence(4) and liposome generated natural CEST contrasts at -3.5 ppm due to the presence of aliphatic protons(5). In this study, we injected the optimized liposomal hydrogel containing both Gem and MTX next to the mouse brain tumor and monitored the tumor size and CEST contrast longitudinally.

**METHODS:** Liposomes (DPPC: cholesterol: DSPE-PEG2000= 0.489:1.192:0.022) were prepared using thin-film hydration method. Gem solution was added to hydrate the lipid film, then sonicated. After filtration through polycarbonate filter and Sephadex column, MTX and alginate powder were mixed with liposome solution. The resulting mixture (MGLH) was mixed with calcium D-gluconate solution. The control hydrogel (LH) was fabricated in a similar manner without drugs. NOD-SCID mice (6-8 weeks, n=8) were injected with U-87 MG cell. After 2 weeks, hydrogel was injected right next to the tumor. Using 3T Bruker Biospec system (Bruker, Germany), T2-weighted images and CEST were acquired ( $B_1=0.8$  uT;  $T_{sat}=2$  secs) over 10 days. 3.5, 2.4 and -3.5 ppm were extracted for analysis using Lorentzian-fitted water signal.

**RESULTS & DISCUSSION:** We imaged two groups of mice, i.e, liposomal hydrogel with Gem and MTX (MGLH); and liposomal hydrogel without drugs (LH). Before hydrogel injection and on day 0, tumor sizes for two groups are comparable (Fig. 1C). Starting from day 3, we observed a decrease in tumor size in treatment MGLH and an increase in the tumor size in LH. MGLH showed a 43% reduction in tumor size on day 10, while LH showed over seven times increase in tumor size, when compared to that before hydrogel injection. A significant difference in the tumor size was observed from day 3 ( $P<0.0001$ ). This indicated the treatment effect of dual drug-loaded liposomal hydrogel. The persistent decrease in tumor size over 10 days supports our design that could facilitate a sustainable drug release locally. The MGLH showed significantly higher CEST signal of 3.7% compared to LH *in-vitro*, which was 0.6% at 2.4 ppm ( $P<0.0001$ ) (Fig. 1F), which is in line with our previous study that two drugs generate natural CEST contrast at 2.4 ppm. For CEST analysis *in-vivo*, two different ROIs, tumor and hydrogel region,

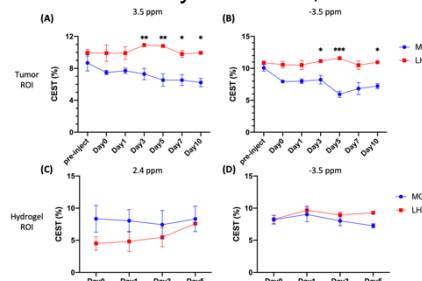


**Fig. 2.** CEST signals between MGLH and LH. 3.5 ppm (A) and -3.5 ppm (B) in tumor ROI. 2.4 ppm (C) and -3.5 ppm (D) in hydrogel ROI.

we analysed at the three corresponding offset frequencies. In tumor ROI (Fig. 2A,B), significant differences were observed at 3.5 ppm ( $P=0.007$ ) and -3.5 ppm ( $P=0.021$ ) from day 3. On day 10, tumor of MGLH showed a 28% decrease at both 3.5 ppm and -3.5 ppm, which corresponds to a significant decrease in tumor size in MGLH when compared to LH. Increase in tumor size might led to higher signal at 3.5 ppm, according to the previous study(4). The decrease in both CEST contrast at 3.5 ppm and -3.5 ppm in MGLH could be due to tumor necrosis or apoptosis(6), which indicated the treatment effect. In hydrogel ROI (Fig. 2C,D), CEST contrast at 2.4 ppm of MGLH was consistently higher than that of LH, which is in line with our *in-vitro* study. Moreover, trendline at -3.5 ppm for both MGLH and

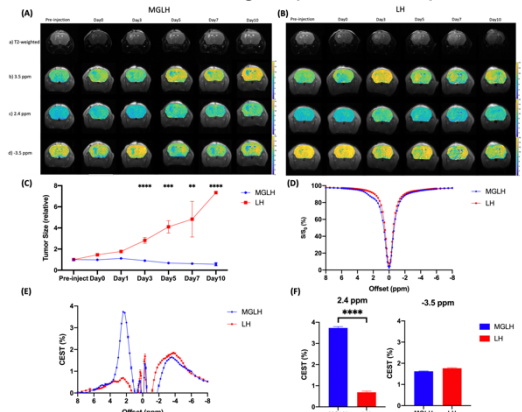


**Fig. 1.** T2-weighted and CEST map for MGLH (A) and LH (B). Tumor size change at different time points (C). Z-spectra (D) and corresponding CEST percentage (E). CEST contrast at 2.4 and -3.5 ppm *in-vitro* (F).

LH showed similar since both liposomes were released at the same time. Histology is underway for further validation.

**CONCLUSION:** In this study, we have shown therapeutic effect on tumor with the injection of dual drug-loaded liposomal hydrogel, as a result of decrease in tumor size and CEST contrast at 3.5 and -3.5 ppm. Moreover, CEST contrast at 2.4 ppm of MGLH was consistently higher than that of LH. This implies a promising approach to treat brain tumor locally and to monitor the treatment outcome longitudinally using multiple CEST contrast approach.

**ACKNOWLEDGMENTS:** RGC [11102218, PDFS2122-1S01, C1134-20G]; CityU [7005433, 7005626, 9667198, 9609307, 9610560]; NNSFC [81871409-H1808]; Tung Biomedical Sciences Centre; COCHE.

**REFERENCES:** 1. Bota DA, *et al.* Ther Clin Risk Manag. 2007;3(5):707-715. 2. Li Y, *et al.* Oncotarget. 2016;7(6):6369-6378. 3. Han X, *et al.* ISMRM & SMRT. 2021;#0077. 4. Zhou J, *et al.* Magn Reson Med. 2013;70(2):320-327. 5. Han X, *et al.* Theranostics. 2020; 10(5): 2215-2228. 6. Tan Z, *et al.* Sci Rep. 2020;10(1):21315

# Glucosamine Chemical Exchange Saturation Transfer (GlcN-CEST) MRI in breast cancer: from mice to humans

Michal Rivlin<sup>1</sup>, Gil Navon<sup>1</sup>

<sup>1</sup> School of Chemistry, Tel-Aviv University, Tel-Aviv, ISRAEL

☐ Apply Student/Postdoc Travel Fund

☒ Oral Presentation ☐ Poster ☐ Either Oral or Poster Presentation | Contact Email: [navon@tauex.tau.ac.il](mailto:navon@tauex.tau.ac.il)

**KEYWORD:** You are encouraged to choose one or two keywords. ☒ CEST agents ☐ Contrast Mechanism

☒ Tumor ☐ Stroke ☐ Neurology ☐ Body & MSK ☐ Standardization ☐ Novel Acquisition ☐ Machine Learning

**INTRODUCTION:** Chemical exchange saturation transfer (CEST) MRI of glucose and its analogues has been suggested for cancer diagnosis based on the known enhanced intake of these agents by cancerous tumors (1,2). While some of the glucose analogues are toxic at the high concentrations needed for clinical applications, others need to be tested for their safety. The feasibility of using glucosamine (2-amino-2-deoxy-D-glucose, GlcN) as an agent for CEST MR molecular imaging of tumors has recently been demonstrated in several animal breast tumor models (3,4). The lack of toxicity of GlcN strengthens its clinical promise, as evidenced by its widespread use as a food supplement. In this study, the translation of the GlcN CEST MRI method into the clinical MRI framework was demonstrated for the first time (5).

**METHODS:** CEST-MRI experiments were conducted in a 7 T MRI scanner (Bruker) on mice with implanted mammary tumors (4T1, MCF7) before and after different administration modes and doses of GlcN. Two CEST scan protocols were used: (I) Dynamic glucoCEST MRI experiment: CW pulse ( $t_{\text{sat}}=2$  s,  $B_1=2.5\mu\text{T}$ ) at a specific proton frequency offset of  $\pm 1.2$  ppm (relative to the water signal) over time. (II) Z spectra experiment: CW pulse ( $t_{\text{sat}}=2$  s,  $B_1=2.5\mu\text{T}$ ) at a series of frequency offsets in the range of  $\pm 6$  ppm (relative to the water signal). To decipher the specific contributions of metabolites to the CEST contrast, high resolution  $^{13}\text{C}$  NMR spectroscopy measurements were performed on extracts of the tumors after administration of  $[\text{UL-}^{13}\text{C}]\text{-GlcN}\cdot\text{HCl}$ . GlcN-CEST MRI scans were acquired in breast cancer patients (N=12, median age, 53 years) before and two hours after drinking a solution of 7.5 g of GlcN sulfate at a 3 T clinical scanner (Siemens, Prisma). Pre-saturation consisted of 5 Gaussian-shaped RF pulses (pulse length  $t_p=100$  ms, inter-pulse delay=61 ms, 2 s between measurements,  $B_1=2.5\mu\text{T}$ , recover time=5 s) at up to 24 frequency offsets sampled in the range of  $\pm 6$  ppm. CEST signal intensities were quantified in the tumor and in the surrounding tissue based on magnetization transfer ratio asymmetry (MTRasym) and a multi-Lorentzian/Gaussian fitting. Images were corrected for  $B_0$  field inhomogeneity, and fat suppression was employed.

**RESULTS:** In animals breast tumor models, there was a significant increase in the effect of CEST following the administration of GlcN, which was augmented with time. In the 4T<sub>1</sub> model, oral administration (PO) of 0.38–2.0 g/kg GlcN increased the CEST signals of the tumors by 4–12% relative to the baseline. 4T<sub>1</sub> is a more aggressive type of tumor than MCF7 and exhibited a larger CEST effect. Two modes of administration of the agents, IV and PO, gave similar results. GlcN CEST MRI observation of lung metastasis was confirmed by histology.  $^{13}\text{C}$  NMR spectroscopy of extracts of 4T<sub>1</sub> tumors treated with  $[\text{UL-}^{13}\text{C}]\text{-GlcN}\cdot\text{HCl}$  provided information regarding the transport of GlcN into tumors: along with the strong signal of GlcN, various metabolite products also contribute to the overall CEST effects, mainly phosphorylated products. A marked increase in lactic acid together with small but significant increase in other organic acids was observed. Patients with breast cancer had a detectable GlcN CEST effect within the tumor, with a mean average CEST signal increase of  $3.4\pm 0.8\%$  at 2 ppm from the water signal, which was in line with tumor location as demonstrated by T<sub>1</sub>W MRI (Fig.1). Significant GlcN CEST effects were observed for the hydroxyl, amine/amide exchangeable protons and for the NOE. All yielded larger CEST integrals in the tumor tissue after GlcN uptake by an averaged factor of  $2.2\pm 1.2$  ( $P<0.01$ ),  $1.4\pm 0.4$  ( $P=0.2$ ) and  $1.6\pm 0.6$  ( $P=0.05$ ), respectively.

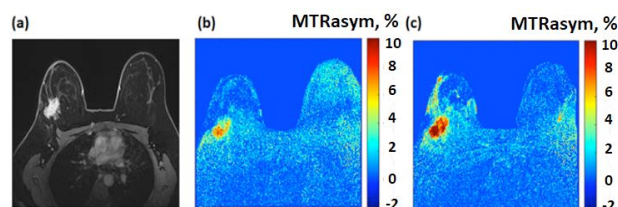


**Figure 1:** (a-c) A 34-year-old female patient with grade II-III invasive ductal carcinoma in the right breast  
(a) Gadolinium T<sub>1</sub> Weighted images,  
(b) and (c) are CEST MTRasym maps calculated at frequency offset of 2 ppm before and after oral administration of GlcN, respectively.

**DISCUSSION:** The strong GlcN CEST effect is a result of the improved uptake of GlcN by the tumors. Major CEST contribution can be attributed to several phosphorylated products of GlcN and the observation of a significant amount of lactate among the metabolic products points to acidification as one of the sources of the improved CEST effect of GlcN. The first human experience with GlcN CEST in breast cancer patients demonstrated the technique's ability to distinguish between breast tumor lesions and the surrounding tissue, based on the differential accumulation of GlcN in the tumors.

**CONCLUSION:** The findings of this preliminary study suggest that GlcN CEST MRI has the potential to identify breast cancer in a clinical setting.

**ACKNOWLEDGMENTS:** The study was supported by the Israel Science Foundation (ISF), the European Union Horizon 2020 research and innovation program, and the Earlier.org - Friends For an Earlier Breast Cancer Test foundation.

**REFERENCES:** 1. Chan K W Y, *et al.* Magn Reson Med 2012;68:1764–1773. 2. Rivlin M, Navon G, QIMS 2019; 9: 1731-1746. 3. Rivlin M, Navon G, Sci Rep 2016;6: 32648 4. Rivlin M, Navon G, NMR Biomed 2021; 34:e4431. 5. Rivlin, M. *et al.* Eur Radiol. 2022.



# Removing fluid artifacts in APTw: why spillover correction and fluid suppression are two sides of the same coin

Moritz Zaiss<sup>1</sup>, Stefano Casagrande<sup>2</sup>, Maria Sedykh<sup>1</sup>, Patrick Liebig<sup>3</sup>, Christos Papageorgakis<sup>2</sup>, Laura Mancini<sup>4,5</sup>, Sotirios Bisdas<sup>4,5</sup>, Manuel Schmidt<sup>1</sup>, Arnd Dörfler<sup>1</sup>

<sup>1</sup>Neuroradiology, University Clinic Erlangen, Friedrich-Alexander Universität Erlangen-Nürnberg (FAU), Germany, <sup>2</sup>Olea Medical, La Ciotat, France, <sup>3</sup>Siemens Healthcare GmbH, Erlangen, Germany, <sup>4</sup>Lysholm Department of Neuroradiology, University College of London Hospitals NHS Foundation Trust, London, UK, <sup>5</sup>Institute of Neurology UCL, London, UK

✉ Oral Presentation (in-person by: S. Casagrande) | Contact Email: moritz.zaiss@fau.de

**KEYWORD:** ☑ Contrast Mechanism ☑ Tumor

**INTRODUCTION:** Since more than 10 years there are disputes on the contamination from T1,T2 and MTC to APTw MRI. Early on, so-called spillover corrections<sup>1</sup> were suggested to improve APTw imaging, but never accepted for MTR<sub>asym</sub>-based APTw. The most likely reason for this was that the spillover correction changed the value scaling and thus the colormap limits of APTw imaging. Recently, so-called fluid suppression approaches for APTw imaging were suggested<sup>2,3</sup>, that also could suppress highlights in areas of long T1/T2 and low MTC (typical characteristics in fluid compartments), but had the benefit that the tissue APTw values (solid compartments) were almost unchanged and the same colorbar limits could be used. However the fluid-suppression formulas were heuristic and could never be properly derived from Bloch-McConnell (BMC) equations. Herein we show that fluid suppression can actually be understood as spillover correction, and we provide an adjusted version that can be properly derived, and used with the same colormap for APTw imaging.

**METHODS:** The fluid-suppression proposed in<sup>2</sup> introduced an additional weighting factor following the heuristic condition: (i) this factor must be 1 for tissue to keep the same colormap, (ii) and close to 0 for liquid tissue. Assuming the  $Z_{ref}$  and  $Z_{lab}$  values in tissue at  $\Delta\omega=3.5\text{ppm}$  are typically  $\approx 0.5$ , and in liquids  $\approx 1$ , the factor  $(2-Z_{ref}-Z_{lab})$  fulfils this condition.

$$\text{FS-MTR}_{\text{asym}} = \text{MTR}_{\text{asym}} \cdot (2 - Z_{ref} - Z_{lab}) \quad [1]$$

If we compare this to a spillover corrected metric, it does not fulfill conditions (i+ii), but regions with high  $Z$  will be upscaled using the formula from<sup>1</sup>

$$\text{MTR}_{\text{Rex}} = \text{MTR}_{\text{asym}} / (Z_{ref} \cdot Z_{lab}) \quad [2]$$

To achieve the same conditions (i+ii) we can transform this equation back to standard tissue with  $Z_{ref} = Z_{lab} = 0.5$  generating a spillover corrected fluid suppression

$$\text{SCFS-MTR}_{\text{asym}} = \text{MTR}_{\text{asym}} / (Z_{ref} \cdot Z_{lab}) \cdot (0.5 \cdot 0.5) \quad [3]$$

Now, condition (i) is directly fulfilled, and the factor of condition (ii) is not 0 but 0.25/1. Eq.[3] thus has similar features as Eq.[1], but is based on the BMC equations and thus theoretically justified.

**RESULTS:** Figure 1 shows that the heuristic fluid-suppression factor, and the spillover-correction-based fluid-suppression factor have similar course plotted over  $Z_{ref}$ , which explains their similar effect on the data and on (liquid) regions with high  $Z$ -values. The property of Eq. [1] to kill all effects at  $Z_{ref}=1$  is unrealistic, while the depletion to only 25% by Eq. [3] is both theoretical correct and plausible. Figure 2 shows differences of the original and newly proposed fluid-suppressed APTw method in tumor case at 3T: (first row) cyst and liquefied necrosis hotspots are suppressed by Eq. [1] and even more by Eq. [3]; (second row) both metrics suppress the signal from microfluid environment of an IDH mutant tumor; (third row) only the hotspot in the liquefied necrotic part is removed by fluid-suppression.

**DISCUSSION:** Spillover correction is asking 'how high would CEST effects in tissue be without spillover dilution'. On the other hand, fluid-suppression is asking 'how low would CEST effects in liquid areas be if we transform them to similar conditions as in tissue'. Thus, both make CEST effects of tissue and liquefied tissue comparable. The novelty here, to bring the spillover correction back to tissue values, allows to use the same colormap limits and makes MTR<sub>asym</sub> and spillover-corrected/fluid-suppressed metrics directly comparable on the same colormap. In tumor cases with clearly identified liquid regions, the new fluid-suppressed metric shows similar (and even improved) features as the previous heuristic one, and clearly removes hotspots of liquid areas, such as cysts, necrosis and microfluid environments. If this liquid-artifact or spillover-artifact is removed, the generated contrast might be better correlated to the actual exchange effects and has potentially higher diagnostic value, as first studies indicate<sup>4,5</sup>. **CONCLUSION:** Try fluid-suppression, it is great and removes liquid artifacts from APTw-CEST and can now be theoretically justified.

**ACKNOWLEDGMENTS:** Department of Health's NHR-funded Biomedical Research Centre at University College London.

**REFERENCES:** 1- Zaiss M *et al.* NMR in biomedicine. 2014;27(3):240-52.

2-Keupp J *et al.* ISMRM 2019; Abstract #3156. 3- Casagrande S *et al.* ISMRM 2021; Abstract #. 4- Nichelli L *et al.* ISMRM 2022; Abstract #0126. 5- Mancini L *et al.* Eur Jour of Nucl Med and Mol Imaging. 2022;pp.1-15.

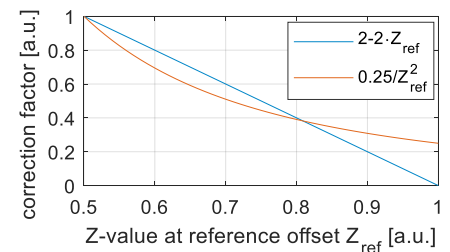


Figure 1: Heuristic (eq.[1]) and spillover-correction-based (eq.[3]) fluid suppression factors as a function of the  $Z$ -value.

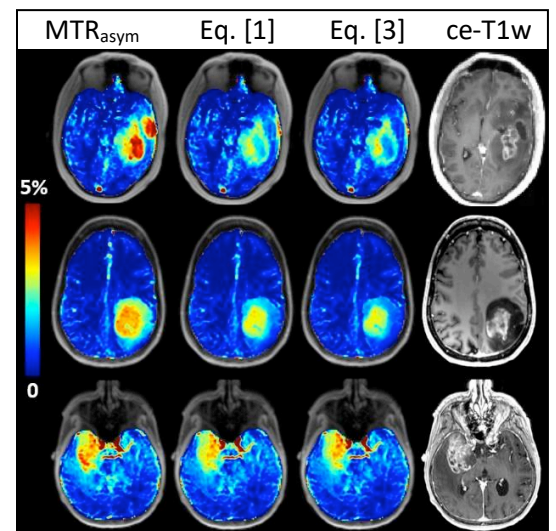


Figure 2: 3T snapshot-APT MRI of 3 patients with grade IV tumor. Furthermore, the one in the second row is a IDH mutant with T2 / FLAIR mismatch.

## Chemical Exchange Saturation Transfer MRI in Non-Lesional Temporal Lobe Epilepsy Imaging

Joshua Brown<sup>1</sup>, Hahnsung Kim<sup>2</sup>, Sagar Mandava<sup>1</sup>, Michael Essien<sup>1</sup>, Philip Sun<sup>1,2</sup>, Ranliang Hu<sup>1</sup>

<sup>1</sup> Department of Radiology and Imaging Sciences, Emory University, Atlanta, GA, USA

<sup>2</sup>Emory National Primate Research Center, Atlanta, GA, USA

☐ Apply Travel Fund

☐ Oral Presentation ☐ Poster ☒ Either Oral or Poster Presentation | Contact Email: jbro260@emory.edu

**KEYWORD:** *You are encouraged to choose one or two keywords.* ☐ CEST agents ☐ Contrast Mechanism

☐ Tumor ☐ Stroke ☒ Neurology ☐ Body & MSK ☐ Standardization ☐ Novel Acquisition ☐ Machine Learning

Chemical exchange saturation transfer (CEST) imaging is a promising tool to evaluate epilepsy patients for seizure focus lateralization. It has the potential to produce a major paradigm shift in epilepsy evaluation and improve the prognosis of a large medical-refractory epilepsy population. Routine epilepsy diagnosis includes multimodal imaging used to localize the source of seizures and is necessary for successful surgical intervention in drug-resistant cases. Unfortunately, up to one-third of epilepsy evaluations have no clear anatomical source of seizures and have non-lesional, normal brain MRIs. Glutamate levels in the brain are known to be increased in anatomical seizure foci. Conventional magnetic resonance spectroscopy (MRS) is limited in accurately detecting glutamate levels, but glutamate CEST (GluCEST) imaging has demonstrated higher sensitivity and spatial resolution. GluCEST has already demonstrated promising results in epilepsy evaluation on research 7T MRI scanners for patients<sup>(1,2)</sup>. It is feasible that GluCEST can accurately lateralize the epileptogenic hippocampal foci in patients with non-lesional imaging on 3T MRI scanners. GluCEST parameters and post-processing were optimized on the newly installed GE PET/MRI scanner. We plan to proceed with healthy controls (n = 5) then assess GluCEST in epilepsy patients (n = 10). Patients will be recruited from the Emory Epilepsy Center and GluCEST imaging will be analyzed using routine multimodal comprehensive epilepsy evaluation as the gold standard. This work has the potential to make a significant, positive impact on millions of patients in the epilepsy community. GluCEST would capture drug-resistant, non-lesional epilepsy patients, guide their surgical intervention, and thus greatly improve their prognosis. In addition, this work would facilitate transition of this advanced imaging technique to a clinical environment suitable for the standard hospital setting. This lays the foundation for future multi-center trials and will subsequently make a new profound diagnostic technique widely available to the benefit of epilepsy patients in need.

### REFERENCES:

1. K. A. Davis et al., Glutamate imaging (GluCEST) lateralizes epileptic foci in nonlesional temporal lobe epilepsy. *Sci Transl Med* 7, 309ra161 (2015).
2. P. N. Hadar et al., Volumetric glutamate imaging (GluCEST) using 7T MRI can lateralize nonlesional temporal lobe epilepsy: A preliminary study. *Brain Behav* 11, e02134 (2021).

## Utility of Amide Proton Transfer Weighted Imaging in Multiple Sclerosis

Ibrahim Khormi<sup>1,2,3</sup>, Oun Al-iedani<sup>1,2</sup>, Jeannette Lechner-Scott<sup>1,2,4</sup>, Abdulaziz Alshehri<sup>1,2,5</sup>, Stefano Casagrande<sup>6</sup>, Christos Papageorgakis<sup>6</sup>, Margarita Arango-Lievano<sup>6</sup>, Anne-Louise Ponsonby<sup>7,8</sup>, Patrick Liebig<sup>9</sup>, Saadallah Ramadan<sup>1,2</sup>

<sup>1</sup>University of Newcastle, Newcastle, NSW, Australia <sup>2</sup>Hunter Medical Research Institute, Newcastle, NSW, Australia

<sup>3</sup>University of Jeddah, Jeddah, Saudi Arabia <sup>4</sup>John Hunter Hospital, New Lambton Heights, NSW Australia <sup>5</sup>King Fahad University Hospital, Imam Abdulrahman Bin Faisal University, Dammam, Saudi Arabia <sup>6</sup>Olea Medical, La Ciotat, France

<sup>7</sup>The Florey Institute of Neuroscience and Mental Health, VIC, Australia <sup>8</sup>Murdoch Children's Research Institute, Melbourne, VIC, Australia <sup>9</sup>Siemens Healthcare GmbH, Erlangen, Germany

✉ Apply Student/Postdoc Travel Fund

□ Oral Presentation □ Poster ✉ Either Oral or Poster Presentation | Contact Email: Ibrahim.khormi@uon.edu.au

KEYWORD: Multiple Sclerosis, amide proton transfer. □ CEST agents □ Contrast Mechanism

□ Tumor □ Stroke ✉ Neurology □ Body & MSK □ Standardization □ Novel Acquisition □ Machine Learning

**INTRODUCTION:** Autoimmune attacks in Multiple Sclerosis (MS) disease cause inflammatory demyelination, leading to axonal loss and destruction of myelin that lead to the breakdown of myelin proteins<sup>1,2</sup>. Several advanced MRI techniques have validated their MRI findings with histological results of breakdown products of myelin proteins within macrophages/microglia in post-mortem MS brains<sup>3,4</sup>. Amide proton transfer weighted (APT<sub>w</sub>) imaging is a novel advanced MRI technique capable of indirectly measuring intra/extracellular proteins by detecting the chemical exchange between amide protons of mobile proteins and water protons. This study aimed to explore the role APT<sub>w</sub> might offer by studying the difference in APT<sub>w</sub> signal intensity between MS lesions and normal-appearing white matter (NAWM) to detect the breakdown products of myelin proteins that were previously described in histological studies.

**METHODS:** Nine people with relapsing-remitting multiple sclerosis (pw-RRMS, 6 women, 3 men) were recruited. MRI/APT<sub>w</sub> acquisitions were undertaken on a 3T scanner. For assessment of MS lesions, 3D T1-MPRAGE and T2-FLAIR were used. The APT<sub>w</sub> (DC=55%, B1=1.8μT+2.6μT) and WASAB1 sequences were performed using a 3D snapshot-GRE. The pre-/post-processing (including B0/B1 correction at B1=2.2 μT), co-registration of APT<sub>w</sub> map with structural MRI, and assigning regions of interest (ROIs) were performed with Olea Sphere 3.0 software (Olea Medical, La Ciotat, France). This pilot study computed the mean APT<sub>w</sub> signal intensity from 2 MS lesions and 2 NAWM ROIs per subject (Figure 1). The NAWM and lesion ROIs were of identical sizes. The statistical analysis of APT<sub>w</sub> signal intensity in ROIs was performed using the student's t-test, where p<0.05 was considered statistically significant.

**RESULTS:** A descriptive statistical boxplot for MS lesions in comparison to NAWM groups is shown in Figure 2. The independent t-test showed a statistically significant (p<0.001) increase of APT<sub>w</sub> mean signal intensity in MS lesions in comparison to NAWM ROIs (Table 1). The average APT<sub>w</sub> signal intensity in MS lesion ROIs were 0.44 ± 0.35 %, and NAWM ROIs were 0.05 ± 0.02 % (Table 1).

**DISCUSSION:** These preliminary results present a novel application for assessing APT<sub>w</sub> signal across different ROIs in pw-RRMS. We found significantly elevated APT<sub>w</sub> signal intensity in MS lesions compared to NAWM regions. These findings are consistent with few studies that confirmed higher APT<sub>w</sub> signal intensity among MS lesions<sup>5,6</sup>. These results could be explained by the increase of mobile myelin protein decomposition and accumulation from the demyelination process. Furthermore, the observed APT<sub>w</sub> signal intensity from the different MS lesions ROIs has a high variance between the various lesions of pw-RRMS, as shown in the boxplot of Figure 2. This result may suggest that the Gadolinium-free APT<sub>w</sub> maps could unravel different MS characteristics/stages based on demyelination status between the different lesions, which would show a potential advantage over the FLAIR hypersignal. This heterogeneity of APT<sub>w</sub> signal intensity of MS lesions will be investigated in future studies. While this is only a pilot study with a small number of lesions examined, it provides an enticement to investigate this method in large and diverse cohorts to understand these findings better.

**CONCLUSION:** The APT<sub>w</sub> technique is novel and has the potential to be a useful and sensitive tool for investigating the pathophysiology of MS. Increasing APT<sub>w</sub> signal intensity in MS lesions supports MS post-mortem histological results. Gadolinium-free APT<sub>w</sub> contrast mechanism provides promising insight into pathologies on a molecular level.

**ACKNOWLEDGMENTS:** This research was kindly supported by MS Research Australia. I. Khormi was supported by a PhD scholarship with annual grant support from the University of Jeddah, Saudi Arabia.

**REFERENCES:** 1. Weil M-T, *et al.* Cell reports 2016;16(2):314-322. 2. Lubetzki C, *et al.* Handbook of clinical neurology. Volume 122: Elsevier; 2014. p. 89-99. 3. De Groot CJ, *et al.* Brain 2001;124(Pt 8):1635-1645. 4. Kuhlmann T, *et al.* Acta Neuropathologica 2017;133(1):13-24. 5. Sartoretti E, *et al.* Frontiers in Neurology 2019;10:1307. 6. Dula AN, *et al.* Magn Reson Med 2011;66(3):831-838.

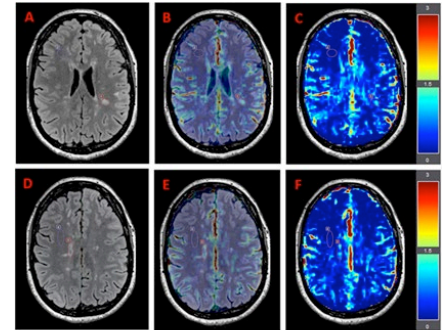


Figure 1. Two MS lesion ROIs (red) and two NAWM ROIs (violet) shown on FLAIR images (A&D) and on FLAIR with 50% APT<sub>w</sub> overlay (B&E) and corresponding APT<sub>w</sub> images (C&F) respectively of a 38 years-old female RRMS participant. Images (C&F) show higher APT<sub>w</sub> endogenous contrast in MS lesions ROIs comparing to NAWM.

Table 1. Independent t-test shows statistically APT<sub>w</sub> Signal Intensity (SI) mean differences between MS lesion and NAWM ROIs.

	t	df	p	Mean Difference	SE Difference	95% CI	
						Lower	Upper
APT <sub>w</sub> SI %	4.080	34	< 0.001	0.387	0.095	0.194	0.580

Note. Student's t-test.

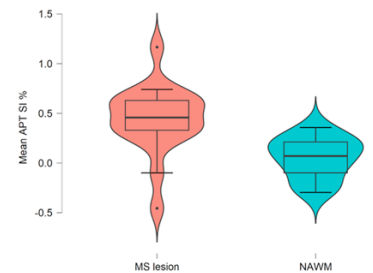


Figure 2. Boxplot of descriptive statistics for MS lesion and NAWM groups.



# CEST imaging of Glutamate and myo-Inositol *in vivo* for early-stage changes in 5xFAD Alzheimer's mouse model

Ravi Prakash Reddy Nanga<sup>1</sup>, Halvor Juul<sup>1</sup>, Narayan Datt Soni<sup>1</sup>, Blake Benyard<sup>1</sup>, Anshuman Swain<sup>1</sup>, Ryan Armbruster<sup>1</sup>, Paul Jacobs<sup>1</sup>, Ravinder Reddy<sup>1</sup>

<sup>1</sup>Department of Radiology, Center for Advance Metabolic Imaging in Precision Medicine, Perelman School of Medicine at The University of Pennsylvania, Philadelphia, PA, USA

☐ Apply Student/Postdoc Travel Fund

☒ Oral Presentation ☐ Poster ☐ Either Oral or Poster Presentation | Contact Email: [nravi@penmedicine.upenn.edu](mailto:nravi@penmedicine.upenn.edu)

**KEYWORD:** You are encouraged to choose one or two keywords. ☐ CEST agents ☒ Contrast Mechanism

☐ Tumor ☐ Stroke ☐ Neurology ☐ Body & MSK ☐ Standardization ☐ Novel Acquisition ☐ Machine Learning

## INTRODUCTION:

Glutamate is an important excitatory neurotransmitter and plays a major role in brain functions such as cognition and memory both of which are affected in Alzheimer's disease (AD)<sup>1-5</sup>. myo-Inositol on the other hand serves as brain osmolyte, and its levels are reported to be elevated in the AD mainly thought to be due to the result of functional reactive astrocytes<sup>6-8</sup>. In this study, our objective was to probe both the glutamate and myo-inositol metabolism in the aggressive transgenic 5xFAD mice<sup>9</sup> which represents five mutant human genes associated with AD using the chemical exchange saturation transfer of glutamate (GluCEST)<sup>10-15</sup> and myo-inositol (MICEST)<sup>16,17</sup>.

**METHODS:** A total of 10 mice (n=5/5, wild-type/5xFAD; all female) were scanned between 6-8months old using the 20mm diameter volume-coil (RAPID Biomedical GmbH, Germany) at 9.4T 30 cm horizontal bore magnet interfaced to Bruker console after obtaining the approval from University of Pennsylvania IACUC committee. Imaging protocol consisted of a localizer followed by T<sub>1</sub>-FLASH, T<sub>2</sub>-MSME, GluCEST (B<sub>1rms</sub>=5.87μT; pulse-duration=1000ms (series of 200ms pulses); offsets= ±2.4 to ±3.6ppm; step-size=0.2ppm; averages=4; acquisition time = ~15 min), MICEST (B<sub>1rms</sub>=1.8μT; pulse-duration=2000ms (series of 200ms pulses); offsets= ±0 to ±1.5ppm; step-size=0.1ppm; averages=2; acquisition time = ~15 min), WASSR<sup>18</sup> and single-voxel <sup>1</sup>H MRS covering the hippocampus 6x1x2mm<sup>3</sup> (TR=3000ms; TE=16ms; dummy-scans=4; acquisition time = ~13 min). Slice thickness was 1mm and in-plane resolution for all imaging and CEST protocols was 0.146mm x 0.146mm. Three regions of interest (ROI) consisting of cortex, hippocampus and thalamus were drawn on the post-processed B<sub>0</sub>-corrected GluCEST and MICEST maps and the values are reported here. Statistical analyses were performed using a two-sample t-test assuming unequal variances. <sup>1</sup>HMR spectra from hippocampus were analyzed with the LCModel<sup>19,20</sup>.

**RESULTS:** Representative GluCEST and MICEST maps for all the mice scanned are shown in Figure 1. Mean GluCEST values from cerebral cortex, hippocampus and thalamus of wild-type vs 5xFAD mice were 27.2±3.4 vs 24±2.5% (p=0.13), 27.8±2.8 vs 27.5±2.8% (p=0.86) and 33.1±2.5 vs 29.8±2.1% (p=0.06), respectively whereas for MICEST the values were 2.3±0.3 vs 2.8±0.6% (p=0.18), 2.1±1.3 vs 2.3±0.7% (p=0.7) and 4.7±1.1 vs 4.3±1.3%, respectively. Glutamate and myo-Inositol concentrations for wild-type vs 5xFAD mice calculated from LCModel of hippocampal spectroscopy were 14.97±1.66 vs 15.64±3.49 IU and 10.47±1.28 vs 12.13±1.84 IU, respectively.

**DISCUSSION & CONCLUSION:** Mean GluCEST values of hippocampus reported in this study differ from a previously reported study while that for thalamus the results are the same<sup>21</sup>. This difference could be due to the result of the segmentation approach employed in the prior study where CSF has been removed from the region of interest drawn on hippocampus. In our study, since some of the hippocampal regions has CSF components due to enlarged ventricles in this mouse model, performing the sub-regional analysis of hippocampus consisting of DA, CA1, CA2, CA3 and CSF would give much cleaner values along with important information indicating the metabolic changes. Towards this goal we are trying to explore the software such as ITK-SNAP and k-means cluster algorithm to perform sub-regional analysis of hippocampus and other cortical structures which are ongoing.

**ACKNOWLEDGMENTS:** Research reported in this publication was supported by the National Institute of Biomedical Imaging and Bioengineering of the National Institutes of Health under award Number P41EB029460 and by the National Institute of Aging of the National Institute of Health under award Number R01AG063869.

**REFERENCES:** References should use the suggested style below.

1. Fonnum F, et al. Neuroscience. 1981;6(5):863-873; 2. Fonnum F. J Neurochem. 1984;42(1):1-11; 3. Headley PM, et al. Trends Pharmacol Sci. 1990;11(5):205-211; 4. DeKosky ST, et al. Ann Neurol. 1990;27:457-464; 5. Terry RD, et al. Ann Neurol. 1991;30:572-580; 6. Carrillo-de Sauvage MA, et al. J Cereb Blood Flow Metab. 2015;35(6):917-921; 7. von Bartheld CS, et al. J Comp Neurol. 2016;524(18):3865-3895; 8. Sailasuta N, et al. Neuropsychiatr Dis Treat. 2011;7:495-499; 9. de Longprez H, et al. J Neurosci. 2006;26(40):10129-10140; 10. Cai K, et al. Nat Med. 2012;18(2):302-306; 11. Haris M, et al. NMR Biomed. 2013;26(4):386-391; 12. Crescenzi R, et al. Neuroimage. 2014;101:185-192; 13. Bagga P, et al. J



# Distinguish the progressive penumbra of the diffusion-perfusion mismatch region by amide proton transfer MRI

Jianzhong Yin<sup>1</sup>, Yalin Wu<sup>2</sup>, Han Li<sup>1</sup>, Chenyang Pei<sup>1</sup>, and Phillip Zhe Sun<sup>3</sup>

<sup>1</sup>Department of Radiology, Tianjin First Central Hospital, Tianjin, China; <sup>2</sup>Department of Radiology, Tianjin General Hospital of Tianjin Medical University, Tianjin, China; <sup>3</sup>Department of Radiology and Imaging Sciences, Emory University School of Medicine, Atlanta, GA, USA

□ Apply Student/Postdoc Travel Fund

□ Oral Presentation □ Poster □ Either Oral or Poster Presentation | Contact Email:

KEYWORD: You are encouraged to choose one or two keywords. □ CEST agents □ Contrast Mechanism

□ Tumor □ Stroke □ Neurology □ Body & MSK □ Standardization □ Novel Acquisition □ Machine Learning

**INTRODUCTION:** Amide proton transfer (APT) imaging was an effective tool to reflect tissue acidosis of acute ischemic stroke. This study was aimed to explore the ability of APT to distinguish progressive penumbra and benign oligemia in the diffusion-perfusion mismatch region.

**METHODS:** 38 acute cerebral infarction patients were recruited to receive a comprehensive MRI examination, including diffusion-weighted imaging (DWI), perfusion-weighted imaging (PWI), APT imaging, and a follow-up scan in one week. There were 12 DWI/PWI match cases. The mismatch patients were divided into 10 progressive cases and 16 stable cases according to the lesion size on the follow-up DWI image compared to the admission scan. Three ROIs in infarction lesion, peripheral, and contralateral normal regions were measured on each subject's MTRasym map. The Friedman test was used to compare the changes of MTRasym among three different regions within each group. The correlation between MTRasym of the peripheral region and the lesion enlargement was analyzed by the Spearman test.

**RESULTS:** The MTRasym at the infarction lesion of all three groups showed differences with the contralateral normal tissue. In the progressive mismatch group, both the MTRasym of the peripheral region within the DWI/PWI mismatch showed a difference with the contralateral normal region and no difference with the infarct core. Whereas the MTRasym at the peripheral region of the stable mismatch and match group had no significant difference with the contralateral side, the differences were significant from those of the central core. The MTRasym of the peripheral region showed a negative correlation with the lesion enlargement.

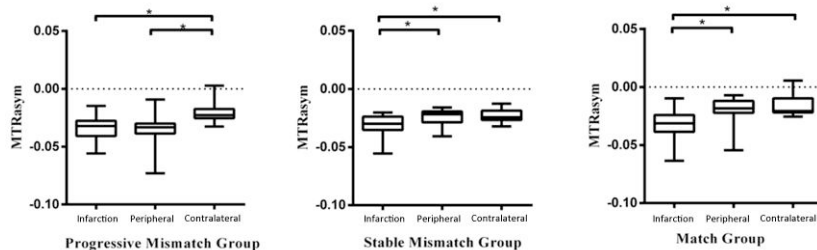


Figure1. The MTRasym differences among the infarction, peripheral, and contralateral regions in different groups. The MTRasym at the infarction lesion of all three groups showed a difference from the contralateral normal tissue. In the progressive mismatch group, the MTRasym at the peripheral region showed a difference with the contralateral normal cerebral region and no difference with the infarct lesion. Whereas in the mismatch stable and match groups, the MTRasym at the peripheral areas showed a statistical difference with the infarct lesion but no difference with the contralateral side.

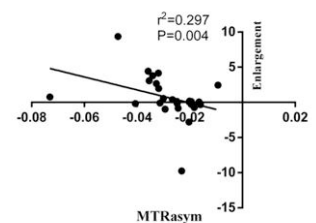


Figure2. Correlation between MTRasym of peripheral infarct region and lesion enlargement.

**DISCUSSION:** Our study has also proved that the progressive PWI/DWI mismatch with a pH reduction might be the penumbra, whereas the stable mismatch region kept the normal pH environment. The decrease of cerebral blood flow with a pH reduction suggests a likelihood of infarction[1,2]. The decreased MTRasym in the progressive PWI/DWI mismatch region implied the tissue experiences notable acidosis. In such an environment, transient depolarizations of the penumbra tissue are expected, and the repetition of such episodes finally produces an increasing metabolic injury and results in infarction enlargement[3]. Therefore, APT might be a sensitive marker for the progressive of the decreased cerebral blood flow region and penumbra, which should be different for benign oligemia. Our results also showed a negative correlation between the MTRasym of the peripheral region and lesion enlargement. Severe acidosis likely causes lesion progress more. Although it just a tendency, it can alert clinicians to correct acidosis in time to prevent the progression of infarction, thereby protecting cerebral tissue from damage.

**CONCLUSION:** APT could distinguish progressive penumbra with benign oligemia in the DWI-PWI mismatch region, implying the infarct prognosis and helping the clinical treatment.

## REFERENCES:

1. Paciaroni M, et al. European neurology 2009; 61: 321-30.
2. Sun PZ, et al. J Cereb Blood Flow Metab 2011; 31: 1743-50.
3. Harston GW, et al. Brain 2015; 138: 36-42.

## 7T multi-pool CEST MRI in multiple sclerosis patients

Moritz Simon Fabian<sup>1</sup>, Stefan Hock<sup>1</sup>, Angelika Barbara Mennecke<sup>1</sup>, Manuel Schmidt<sup>1</sup>, Arnd Dörfler<sup>1</sup>, and Moritz Zaiß<sup>1,2</sup>  
<sup>1</sup>Institute of Neuroradiology, University Hospital Erlangen, Erlangen, Germany, <sup>2</sup>High-field Magnetic Resonance Center, Max Planck Institute for Biological Cybernetics, Tübingen, Germany

✉ Either Oral or Poster Presentation | Contact Email: Moritz.fabian@uk-erlangen.de

**KEYWORD:** ☑ Neurology

**Introduction** For Multiple Sclerosis (MS), it is crucial to detect lesions and classify the MS-type as early as possible, in order to optimize treatment.[1,2] Interestingly, CEST MRI at 7T has shown to yield correlations with Gadolinium (Gd) contrast enhancement in tumours.[3] In this work, we are testing the same CEST approach in patients suffering from multiple sclerosis.

**Methods** Data were acquired from 3 patients (Relapsing Remitting MS RRMS: 2, Radiologic Isolated Syndrome RIS: 1), after written informed consent and under approval of the local ethics committee, at a MAGNETOM Terra 7 Tesla scanner (Siemens Healthcare GmbH, Erlangen, Germany) with an 32ch Rx and 8ch Tx head coil.

Homogeneous Gaussian pre-saturation was realized using the MIMOSA scheme (120 pulses,  $tp=15$  ms, duty cycle  $DC=60.56\%$ ) at two B1 levels of  $0.72\mu T$  and  $1.00\mu T$ . [4] Image readout was a centric 3D snapshot GRE [5]. GRAPPA 2 was applied in the first phase encoding direction [6]. 56 frequency offsets were distributed non-equidistantly between -100 and 100 ppm, finer between -5 and 5 ppm. The evaluation of CEST data was done according to [7,8].

**Results** CEST parameter amplitudes and clinical imaging of a RRMS patient are shown in Figure 1. Regions of interest (ROI's) were drawn by a trained neuroradiologist to capture a variety of inactive (old), active lesions and appropriate reference tissue. Our main hypothesis, that Gd enhancement of active MS lesions can also be seen with 7T amide CEST, could not be clearly verified. Examining the values of the lesion ROI's at Lorentzian fit parameters – amplitude, peak width and spectral position – did not yield additional insight. (data not shown).

**Discussion** With the CEST experiment employed here, MS-Lesions (>3mm diameter) were detectable in CEST parameter maps. The correlation of amide CEST and Gd enhancement (s.a. [3]) is only given in specific lesions. Direct correlations of CEST maps and clinical imaging are not confirmable. Together with high information content of CEST in general, a higher amide CEST value in active lesions – caused by a larger protein content – might originate from an acute immune reaction in that area. Likewise, a decreased amide/NOE/MT value in inactive regions – paired with a hypointensity in contrast enhanced T1 weighted imaging – refers to a direct damage of tissue, specifically depletion of myelin. This aligns well with the results of [9], where MS-Lesions were identified using NOE weighted imaging. In the findings of [10], separation of lesion type into active and non-active (old) was shown to be possible by applying a higher B1 level of approximately  $2.0\mu T$ . This B1 level is more sensitive to the exchange of Glutamate, which is said to be altered in Multiple Sclerosis lesions.

**Conclusion** We tested a 7T multi-pool CEST protocol in MS patients, which previously showed Gd-enhancement-like structures in brain tumors. While some active lesions showed hyperintensities, other active lesions in the three measured patients did not show a correlation with Gadolinium contrast enhancement.

## References

1. Min, Y., et al. Proceedings of the National Academy of Sciences, 106(9), 3154-3159.
2. Macrez, et al. The Lancet Neurology, 15(10), 1089-1102.
3. Goerke, S., et al. Magnetic resonance in medicine, 82(2), 622-632.
4. Liebert A, et al. Magnetic Resonance in Medicine 2019;82:693–705 doi: 10.1002/mrm.27762.
5. Zaiss M, et al. NMR in Biomedicine 2018;31:e3879 doi: 10.1002/nbm.3879
6. Griswold, Mark A., et al. Magnetic Resonance in Medicine 47.6 (2002): 1202-1210.
7. Johannes Windschuh et al. NMR in biomedicine 28.5 (2015), pp. 529–537.
8. Mennecke, A., et al. NMR in Biomedicine, e4717.
9. Huang, J., et al. NeuroImage: Clinical, 32, 1
10. Dula, A. N., et al. Magnetic Resonance in Medicine, 66(3), 831-838.

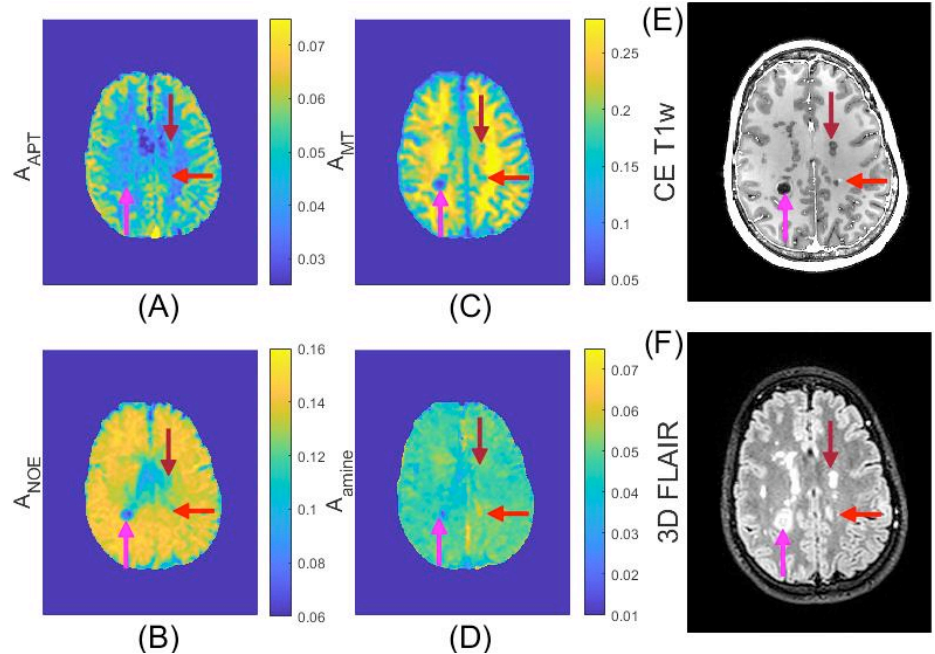


**Figure 1:** Patient suffering from RRMS. CEST amplitude maps for Amide (A), NOE (B), MT (C) Amine (D) as well as a contrast enhanced T1 weighted image (E) and a 3D FLAIR (F). Markings: active lesion (pink, red), inactive lesion (blue)

Day 2 (Tuesday, 9<sup>th</sup> August 2022)

## ssMT and APT-weighted CEST imaging predict clinical outcome in the first follow up after completion of radiotherapy in glioma patients at 3T

Florian Kroh<sup>1,6,‡</sup>, Nikolaus v. Knebel Doeberitz<sup>2,‡</sup>, Johannes Breitling<sup>1</sup>, Srdjan Maksimovic<sup>2</sup>, Laila König<sup>3</sup>, Jürgen Debus<sup>3,4,5</sup>, Peter Bachert<sup>1,6</sup>, Heinz-Peter Schlemmer<sup>2,5</sup>, Mark E. Ladd<sup>1,5,6</sup>, Andreas Korzowski<sup>2</sup>, Steffen Goerke<sup>1</sup>, Daniel Paech<sup>2,7</sup>

<sup>1</sup>Division of Medical Physics in Radiology, German Cancer Research Center (DKFZ), Heidelberg, Germany

<sup>2</sup>Division of Radiology, German Cancer Research Center (DKFZ), Heidelberg, Germany

<sup>3</sup>Department of Radiation Oncology, Heidelberg University Hospital, Heidelberg, Germany

<sup>4</sup>Clinical Cooperation Unit Radiation Oncology, German Cancer Research Center (DKFZ), Heidelberg, Germany

<sup>5</sup>Faculty of Medicine, University of Heidelberg, Heidelberg, Germany

<sup>6</sup>Department of Physics and Astronomy, University of Heidelberg, Heidelberg, Germany

<sup>7</sup>Department of Neuroradiology, University Hospital Bonn, Bonn, Germany

‡Authors contributed equally to the study

☒ **Apply Student/Postdoc Travel Fund**

☐ **Oral Presentation** ☐ **Poster** ☒ **Either Oral or Poster Presentation** | **Contact Email: [n.knebel@dkfz-heidelberg.de](mailto:n.knebel@dkfz-heidelberg.de)**

**KEYWORD:** ☐ **CEST agents** ☒ **Contrast Mechanism** ☒ **Tumor** ☐ **Stroke** ☐ **Neurology** ☐ **Body & MSK** ☐ **Standardization** ☐ **Novel Acquisition** ☐ **Machine Learning**

**INTRODUCTION:** Several groups have demonstrated the potential of CEST MRI to differentiate between radiation induced changes and glioma progression as early as 3 months following completion of radiotherapy<sup>1-6</sup>. However, CEST contrasts are heavily dependent on the metrics used for contrast extraction from the Z-spectra as well as applied magnetic field strengths<sup>5, 7-9</sup>. The purpose of this study was to compare the ability of asymmetry-based (APT<sub>w</sub>), Lorentzian-fit-based (PeakAreaAPT and MT<sub>Const</sub>) and relaxation-compensated (MTR<sub>Rex</sub>APT and MTR<sub>Rex</sub>MT) CEST contrasts of the APT and semi-solid magnetization transfer (ssMT) for early response assessment and prediction of progression free survival (PFS) in glioma patients in a prospective clinical trial.

**METHODS:** 61 patients underwent CEST MRI at 3T (Prisma®, Siemens) 4 to 6 weeks after completion of radiotherapy for diffuse glioma. Therapy response assessment and determination of progression free survival (PFS) were performed according to response assessment in neuro oncology (RANO) criteria with a median followup of 9.2 months (range 1.6–40.8)<sup>10</sup>. Contrast-enhancing glioma tissue (CE), whole tumor (WT) and normal appearing white matter (NAWM) were segmented on T1w-post-contrast and T2w images. Association of mean contrast values with RANO assessment and PFS were tested by receiver operator characteristic (ROC) analyses and Kaplan-Meier analyses with logrank-test, respectively.

**RESULTS:** Median age of the study cohort was 61 (Q1=50.5, Q3=71.0) years. Median PFS overall was 5.3 (Q1=2.1, Q3=9.7) months. MT<sub>Const</sub> (AUC=0.83, p<0.01) showed stronger association with RANO response assessment than PeakAreaAPT (AUC=0.74, p=0.01) and MTR<sub>Rex</sub>MT (AUC=0.71, p=0.02) and even enabled differentiation of patients with pseudoprogression (n=8) from those with true progression (AUC=0.82, p=0.02). Furthermore, MT<sub>Const</sub> (HR=3.04, p=0.01), PeakAreaAPT (HR=0.39, p=0.03) and APT<sub>w</sub> (HR=2.63, p=0.02) displayed significant association with PFS (**Figure**). MTR<sub>Rex</sub>APT was neither associated with RANO assessment nor with PFS.

**DISCUSSION:** In patients with glioma in the first followup after completion of radiotherapy, Lorentzian-fit-based MT<sub>Const</sub> and PeakAreaAPT showed stronger association with clinical outcome as assessed by RANO criteria than the asymmetry based APT<sub>w</sub> and the relaxation compensated MTR<sub>Rex</sub>MT.

**CONCLUSION:** CEST imaging of the APT and ssMT has great potential for supporting clinical therapy response assessment and outcome prediction in glioma patients early after completion of radiotherapy.

**ACKNOWLEDGMENTS:** This study was funded by the German Research Foundation (Grant No. 445704496)

### REFERENCES:

1. Zhou J, et al. *Nat Med* 2011;**17**: 130-4.
2. Park YW, et al. *Neuroradiology* 2021;**63**: 363-72.
3. Paech D, et al. *Eur Radiol* 2019;**29**: 4957-67.
4. Meissner JE, et al. *J Magn Reson Imaging* 2019;**50**: 1268-77.
5. Mehrabian H, et al. *Int J Radiat Oncol Biol Phys* 2018;**101**: 713-23.
6. Ma B, et al. *J Magn Reson Imaging* 2016;**44**: 456-62.
7. Goerke S, et al. *Magn Reson Med* 2019;**82**: 622-32.
8. Zaiss M, *Neuroimage* 2015;**112**: 180-8.
9. Zhou J, et al. *J Magn Reson Imaging* 2019;**50**: 347-64.



# Enhanced diagnostic performance of APT-weighted MRI to advanced non-contrast MRI techniques in patients with post-treatment high-grade gliomas

Qianqi Huang<sup>1,2</sup>, Nhat Le<sup>1,3</sup>, Hye Young Heo<sup>1</sup>, Peter van Zijl<sup>1,4</sup>, Jinyuan Zhou<sup>1</sup>, and Shanshan Jiang<sup>1</sup>

Departments of <sup>1</sup>Radiology, <sup>2</sup>Biomedical Engineering, and <sup>3</sup>Computer Science, Johns Hopkins University; <sup>4</sup>F.M. Kirby Research Center for Functional Brain Imaging, Kennedy Krieger Institute, Baltimore, Maryland, USA

☒ Apply Travel Fund ☒ Oral Presentation Contact Email: [sjiang21@jhmi.edu](mailto:sjiang21@jhmi.edu) KEYWORD: ☒ Tumor

**INTRODUCTION:** Newly developed or enlarged lesions in malignant gliomas after surgery and chemoradiation are associated with tumor recurrence or treatment effect. Due to similar image characteristics, conventional and most advanced MRI techniques are limited in distinguishing these two pathologies. Amide proton transfer-weighted (APTw) MRI has been applied to this field and shows great promising results. To explore a non-contrast MRI scan protocol for post-treatment glioma patients, we evaluated and compared the diagnostic performances of APTw MRI to diffusion-weighted imaging (DWI), susceptibility-weighted imaging (SWI), and pseudo-continuous arterial spin labeling (pCASL). We found that APTw images added value to pCASL and other advanced MR images for the differentiation of treatment effect and tumor recurrence

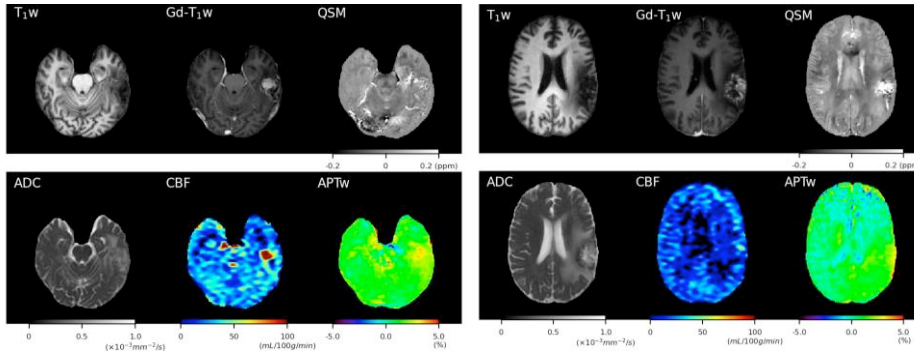
**METHODS:** 40 scans from 28 patients were collected (23 tumor recurrence vs. 17 treatment effect) (**A**). Apparent diffusion coefficient (ADC), quantitative susceptibility mapping (QSM), cerebral blood flow (CBF), and APTw images were respectively calculated from co-registered DWI, SWI, pCASL, and APTw images. Histogram analysis approach was employed to extract parameters from regions with gadolinium-enhancing boundary. Statistically significant parameters ( $P < 0.05$ ) were selected to train multivariable logistic regression models to evaluate the performances of MRI sequences.

**RESULTS:** Multiple histogram parameters, particularly those from APTw and pCASL images, demonstrated significant differences between treatment effect and recurrent tumor (**B**). The regression model trained on the combination of all significant histogram parameters achieved the best result with APTw + CBF + QSM (AUC = 0.90) (**C**).

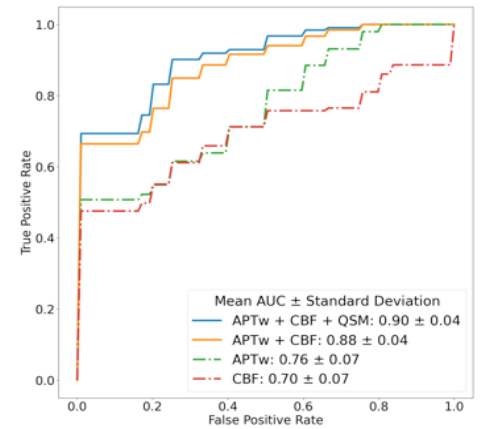
**DISCUSSION:** APTw hyperintensity typically exists in regions of tumor recurrence because of over-expressed proteins from higher cell proliferation and cellularity. Classification results indicate a stronger contribution from APTw and CBF to the classification model and the incremental value of APTw parameters.

**CONCLUSION:** APTw and pCASL MRI are two more useful techniques. APTw images added important clinical value to pCASL and other advanced MR images for the differentiation of treatment effect and tumor recurrence.

**ACKNOWLEDGMENTS:** We acknowledge our physician team for cooperation: Lindsay Blair, Karisa Schreck, David Kamson, Jaishri Blakeley, John Laterra, Matthias Holdhoff, Stuart Grossman, Debraj Mukherjee, Chetan Bettgowda



A: Comparison of MR images of a representative patient with tumor recurrence (left) and a representative patient with treatment effect (right).



C: Comparison of ROC curves in the test sets of multivariable logistic regression models trained with different parameters' combinations.

Histogram Parameter	QSM		ADC		CBF		APTw	
	p value	AUC (cutoff)	p value	AUC (cutoff)	p value	AUC (cutoff)	p value	AUC (cutoff)
Mean	0.244	0.43	0.144	0.40	** 0.001	0.79	* 0.023	0.69
Mode	* 0.023	<b>0.69 (-0.2)</b>	0.494	0.50	0.143	0.60	** 0.004	0.74
Skewness	0.194	0.58	0.080	<b>0.63 (0.18)</b>	0.085	0.37	0.069	0.36
Kurtosis	0.210	0.58	0.094	0.63	0.300	0.45	0.157	0.4
Peak	0.416	0.52	0.383	0.53	0.109	0.62	** 0.006	0.74
10th percentile	0.320	0.55	0.218	0.57	** 0.009	0.72	0.120	0.61
25th percentile	0.210	0.58	0.330	0.46	** 0.004	0.75	0.069	0.64
50th percentile	0.186	0.41	0.109	0.38	** 0.002	0.78	* 0.017	0.7
75th percentile	0.120	0.39	0.132	0.39	** 0.001	0.80	** 0.005	0.74
90th percentile	0.109	0.38	0.186	0.41	** 0.001	<b>0.81 (37.31)</b>	** 0.002	<b>0.77 (3.06)</b>

B: The Mann-Whitney test and ROC analysis results of histogram parameters from 4 different MRI sequences.

# Improved diagnostic accuracy of Amide Proton Transfer weighted imaging versus Dynamic Susceptibility Contrast Perfusion for the discrimination of radiation necrosis from tumor progression in brain metastases

Lucia Nichelli<sup>1,2</sup>, Mehdi Bensemain<sup>3</sup>, Christos Papageorgakis<sup>4</sup>, Daisy Villano<sup>4</sup>, Julian Jacob<sup>1</sup>, Charles Valery<sup>1</sup>, Patrick Liebig<sup>5</sup>, Moritz Zaiss<sup>6</sup>, Stéphane Lehericy<sup>1,2</sup> and Stefano Casagrande<sup>4</sup>

<sup>1</sup> Assistance Publique-Hôpitaux de Paris, Groupe Hospitalier Pitié-Salpêtrière-Charles-Foix, Sorbonne Université, Paris, France, <sup>2</sup> Paris Brain Institute – Institute du Cerveau (ICM), Centre de NeuroImagerie de Recherche (CENIR), Paris, France, <sup>3</sup> Nancy Regional University Hospital Centre, Nancy, France, <sup>4</sup> Olea Medical, La Ciotat, France, <sup>5</sup> Siemens Healthcare GmbH, Erlangen, Germany, <sup>6</sup> University Clinic Erlangen, Friedrich-Alexander Universität Erlangen-Nürnberg (FAU), Erlangen, Germany

☑ Oral Presentation ☐ Poster ☐ Either Oral or Poster Presentation | Contact Email: lucianichelli@gmail.com  
 ☑ Apply Student/Postdoc Travel Fund **KEYWORDS:** ☐ CEST agents ☐ Contrast Mechanism ☑ Tumor ☐ Stroke  
 ☑ Neurology ☐ Body & MSK ☐ Standardization ☐ Novel Acquisition ☐ Machine Learning

**INTRODUCTION:** Stereotactic radiosurgery (SRS) is an effective therapy for brain metastases<sup>1,2</sup>. After stereotactic body radiation-therapy (SBRT), radiation-induced enhancing lesions occur frequently, mimicking neoplastic recurrence. The distinction between tumor progression and radionecrosis currently relies on Dynamic Susceptibility Contrast (DSC) perfusion, despite its several limitations<sup>3</sup>. Amide Proton Transfer weighted (APT<sub>w</sub>) imaging enables to measure the Chemical Exchange Saturation Transfer (CEST) contrast between mobile protein/peptide amide protons and bulk water. This molecular technique promises to help in the assessment of treatment response, as tumor hypercellularity increases APT<sub>w</sub> signal intensity compared with lower cellular density of therapeutic remnants<sup>4</sup>. The aim of this study was to compare the diagnostic accuracy of APT<sub>w</sub> imaging and DSC perfusion in the distinction between metastasis recurrence and radionecrosis. In this study, two APT<sub>w</sub> maps are proposed, before and after fluid suppression<sup>5</sup>. The latter metric is applied to diminish hemosiderin signal, which is frequently encountered in previously irradiated tumor. **METHODS:** Twenty brain pre-irradiated enlarging lesions (22 ± 19 months from focal single dose of Gamma-Knife SRS) were prospectively examined with 3T MR scanner (MAGNETOM Skyra, Siemens, Erlangen, Germany) with a 64-channel head and neck coil. Diagnosis of tumor progression or radionecrosis was assessed by either (i) histological examination or (ii) at least 6 months imaging follow-up or (iii) CT-PET imaging. The APT<sub>w</sub> sequence (3:07 minutes) was acquired with a 3D snapshot-GRE (B1=2.22 μT, Duty Cycle=55%). The WASAB1 sequence (2:03 minutes) was performed for simultaneous B0 and B1 mapping. DSC perfusion was acquired after a single dose of gadolinium-chelated contrast agent (0.1 mmol/kg) and a low flip angle. Structural axial 3D FLAIR, axial diffusion, susceptibility imaging and axial 3D T1 spin echo sequences before and after contrast injection were also acquired. Olea Sphere 3.0 software (Olea Medical, La Ciotat, France) was used to: post-process APT<sub>w</sub>, WASAB1 and perfusion data; to calculate APT<sub>w</sub>, fluid-suppressed (F.S.) APT<sub>w</sub>, and relative Cerebral Brain Volume (rCBV) after leakage correction maps; to co-register APT<sub>w</sub> maps and rCBV maps with structural sequences; to delineate regions of interest (ROIs) in the lesion and in the contralateral normal appearing white matter (cNAWM). **RESULTS:** Among 22 cerebral lesions, 10 (45%) were evaluated as radionecrosis and 12 (55%) as tumoral progression. Area under the ROC Curve (AUC) were 0.641 for rCBV metrics (0.506-0.776) and 0.966 for APT<sub>w</sub> metrics (0.93-1) and 1 for F.S. APT<sub>w</sub> metrics (1-1), with a significative difference between the DSC and APT<sub>w</sub> metrics ( $p < 0.05$ ). The optimal cut-off point was 2.08 for rCBV, 0.637 for APT<sub>w</sub> and 0.505 for F.S. APT<sub>w</sub>. DSC perfusion discriminated cerebral lesions with a sensitivity of 66.7%, APT<sub>w</sub> and F.S. APT<sub>w</sub> with a sensitivity of 100%. DSC and APT<sub>w</sub> metrics had a specificity of 90%, while F.S. APT<sub>w</sub> metric of 100%. Figure1 shows the added value of APT<sub>w</sub> imaging compared to rCBV perfusion imaging, respectively in tumor progression and radionecrosis. Figure2 shows the boxplots of the different metrics extracted from the 22 patient maps with tumor progression and radionecrosis. The APT<sub>w</sub>/F.S. APT<sub>w</sub> metrics displayed are computed as the difference of the mean APT<sub>w</sub> signal between the lesion and the cNAWM ROIs, while the rCBV metrics as the ratio of the mean rCBV signal of the lesion ROI to the cNAWM ROI. **DISCUSSION:** APT<sub>w</sub> metrics are more accurate than rCBV values in the distinction between tumor recurrence and radio-induced tissue changes in brain metastasis. Fluid suppression enhances diagnostic accuracy of APT<sub>w</sub> imaging. **CONCLUSION:** This study supports the clinical importance of adding APT<sub>w</sub> imaging in post-therapeutic assessment of brain tumor. Despite the encouraging results of the F.S. APT<sub>w</sub> metric, these must be explored on a larger patient cohort (with a Duty Cycle > 90% for APT<sub>w</sub> MRI). **REFERENCES:** 1- Suh JH, *et al.* Nature reviews Clinical oncology 2020; 17(5):279-99. 2- Valiente M, *et al.* Trends in cancer 2018; 4(3):176-96. 3- Pope WB, *et al.* Handbook of clinical neurology 2018; 149:89-112. 4- Nichelli L, Casagrande S. Current Opinion in Oncology 2021; 33(6):597-607. 5- Casagrande S *et al.* ISMRM 29<sup>th</sup> An Meet 2020; Abstract #0500

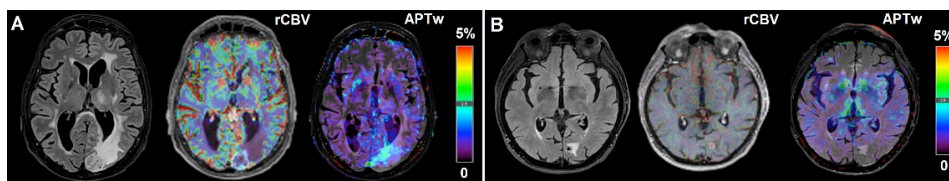


Figure1. Tumor progression (A) and radionecrosis (B) predicted by APT<sub>w</sub> maps.

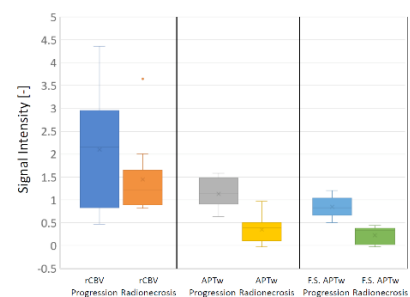


Figure2. Boxplots (rCBV, APT<sub>w</sub>, F.S.APT<sub>w</sub>)

## **Glioma response assessment by asymmetry-based, Lorentzian-fit-based and relaxation-compensated CEST MRI of the APT and ssMT is influenced by glioma location at 3T**

Nikolaus v. Knebel Doeberitz<sup>1,‡</sup>, Florian Kroh<sup>2,6,‡</sup>, Johannes Breitling<sup>2</sup>, Srdjan Maksimovic<sup>1</sup>, Laila König<sup>3</sup>, Jürgen Debus<sup>3,4,5</sup>, Peter Bachert<sup>2,6</sup>, Heinz-Peter Schlemmer<sup>1,5</sup>, Mark E. Ladd<sup>2,5,6</sup>, Andreas Korzowski<sup>2</sup>, Steffen Goerke<sup>2</sup>, Daniel Paech<sup>1,7</sup>

<sup>1</sup>Division of Radiology, German Cancer Research Center (DKFZ), Heidelberg, Germany

<sup>2</sup>Division of Medical Physics in Radiology, German Cancer Research Center (DKFZ), Heidelberg, Germany

<sup>3</sup>Department of Radiation Oncology, Heidelberg University Hospital, Heidelberg, Germany

<sup>4</sup>Clinical Cooperation Unit Radiation Oncology, German Cancer Research Center (DKFZ), Heidelberg, Germany

<sup>5</sup>Faculty of Medicine, University of Heidelberg, Heidelberg, Germany

<sup>6</sup>Department of Physics and Astronomy, University of Heidelberg, Heidelberg, Germany

<sup>7</sup>Department of Neuroradiology, University Hospital Bonn, Bonn, Germany

<sup>‡</sup>Authors contributed equally to the study

☒ **Apply Student/Postdoc Travel Fund**

☐ **Oral Presentation** ☐ **Poster** ☒ **Either Oral or Poster Presentation** | **Contact Email: [n.knebel@dkfz-heidelberg.de](mailto:n.knebel@dkfz-heidelberg.de)**

**KEYWORD:** ☐ **CEST agents** ☒ **Contrast Mechanism** ☒ **Tumor** ☐ **Stroke** ☐ **Neurology** ☐ **Body & MSK** ☐ **Standardization** ☐ **Novel Acquisition** ☐ **Machine Learning**

**INTRODUCTION:** Several groups have demonstrated the potential of CEST MRI for prognostication of clinical outcome and therapy response assessment in patients with diffuse glioma<sup>1-7</sup>. However, glioma is a heterogeneous disease entity which can affect various compartments of the central nervous system. In hemispherical brain locations, neuronal cell bodies and myelin-rich fibre tracts are restricted to gray and white matter structures, respectively, and thus can be nicely differentiated on MRI. However, in midline structures as the thalamus and brainstem, nerve nuclei are located in great proximity and are interspersed with projecting fibre tracts. This might influence CEST contrasts of gliomas with midline locations. Hence, in this study we evaluated the influence of glioma location on therapy response assessment by asymmetry-based (APTw), Lorentzian-fit-based (PeakAreaAPT and MT<sub>Const</sub>) and relaxation-compensated (MTR<sub>Rex</sub>APT and MTR<sub>Rex</sub>MT) CEST contrasts of the APT and semi-solid magnetization transfer (ssMT).

**METHODS:** 42 patients underwent CEST MRI at 3T (Prisma®, Siemens) 4 to 6 weeks after completion of radiotherapy in a cross-sectional clinical study. Therapy response assessment and determination of progression free survival (PFS) were performed according to response assessment in neuro oncology (RANO) criteria with a median followup of 7.9 months (range 1.6–34.1)<sup>10</sup>. Contrast-enhancing glioma tissue (CE), whole tumor (WT) and normal appearing white matter (NAWM) were segmented on T1w-post-contrast and T2w images. Associations of mean contrast values with tumor location, response assessment and PFS were tested by Mann-Whitney-U test, Receiver-Operator-Characteristic (ROC) analyses and Log-Rank test.

**RESULTS:** Median age of the study cohort was 60.5 (Q1=52.0, Q3=69.0) years. Median PFS overall was 2.6 (Q1=1.9, Q3=7.0) months. 37 patients had gliomas with hemispherical location and 5 with midline location. When comparing mean CEST contrast values overall, MTR<sub>Rex</sub>APT (p=0.01) and MT<sub>Const</sub> (p=0.03) showed significantly higher values for gliomas with midline locations compared to gliomas with hemispherical locations (**Figure**). Before stratification for tumor location MTR<sub>Rex</sub>MT (AUC=0.71, p=0.02), PeakAreaAPT (AUC=0.71, p=0.02) and MT<sub>Const</sub> (AUC=0.79, p<0.01) mean contrast values were significantly associated with response assessment in ROC analyses. However, none of the evaluated contrasts showed any association with PFS. After excluding gliomas with midline location from the analysis, association of MTR<sub>Rex</sub>MT with response assessment decreased below significance level (AUC=0.69, p=0.09), whilst the performances of PeakAreaAPT (AUC=0.74, p<0.01) and MT<sub>Const</sub> (AUC=0.83, p<0.01) increased slightly. After stratification for hemispherical tumor location, APTw (HR=2.63, p=0.02), PeakAreaAPT (HR=0.39, p=0.03) and MT<sub>Const</sub> (HR=3.04, p=0.01) mean contrast values showed an association with PFS.

**DISCUSSION:** Higher MTR<sub>Rex</sub>APT mean contrast values of gliomas with midline locations might indicate relevant APT signal contributions from adjacent nerve nuclei regardless of clinical outcome. The absence of an association of mean MTR<sub>Rex</sub>MT contrast values with tumor locations could be explained by signal contributions from T1 and/ or spill-over to the increased MT<sub>Const</sub> values of midline gliomas. The improving performance of the APTw, PeakAreaAPT and MT<sub>Const</sub> following stratification for hemispherical glioma may suggest that tumor location should be considered during response assessment and prognostication using asymmetry-based and Lorentzian-fit-based CEST contrasts.

**CONCLUSION:** Clinical studies evaluating the potential of CEST contrasts for response assessment in patients with glioma should consider tumor locations and possible contributions from surrounding brain structures.

**ACKNOWLEDGMENTS:** This study was funded by the German Research Foundation (Grant No. 445704496)



# Fast Multi-slice Quasi-steady-state (QUASS) APT MRI – Application to Brain Tumor Patients at 3 Tesla

Hahnsung Kim<sup>1,2</sup>, Lisa C Krishnamurthy<sup>3,4</sup>, Kimberly B Hoang<sup>5</sup>, Ranliang Hu<sup>2</sup>, Phillip Zhe Sun<sup>1,2</sup>

<sup>1</sup> Emory National Primate Research Center, <sup>2</sup> Department of Radiology & Imaging Sciences, Emory University, <sup>3</sup> Center for Visual and Neurocognitive Rehabilitation, <sup>4</sup> Department of Physics & Astronomy, Georgia State University, <sup>5</sup> Department of Neurosurgery, Emory University

✉ Apply Travel Fund ✉ Either Oral or Poster Presentation ✉ Standardization [hahnsung.kim@emory.edu](mailto:hahnsung.kim@emory.edu)

**INTRODUCTION:** CEST measurement depends not only on labile proton concentration and exchange rate but also on experimental parameters, such as the duration of RF saturation ( $T_s$ ) and the relaxation recovery delay ( $T_d$ ). Although the use of long RF irradiation enhances the CEST effect, it unavoidably prolongs the total scan time, making CEST MRI challenging for routine clinical use. For typical human CEST scans, the RF saturation time can range from 0.2 to 3.5 s at 3 T [1-3]. Therefore, CEST protocols vary substantially among centers, and it is urgent to unify results obtained under different  $T_s$  and  $T_d$ . A quasi-steady-state (QUASS) CEST algorithm has been recently proposed to reduce the impacts of experimental  $T_s$  and  $T_d$  parameters on the CEST measurement. We hypothesized that the QUASS algorithm can be generalized for multislice acquisition and evaluated it for fast multislice imaging in tumor patients.

**METHODS:** The apparent CEST Z-spectrum is calculated by normalizing the saturated scan signal ( $I'_{sat}$ ) with the unsaturated control scan signal ( $I'_0$ ):  $\frac{I'_{sat}(\Delta\omega)}{I'_0} = \frac{(1-e^{-R_{1w}T_d})e^{-R_{1p}T_s+\frac{R_{1w}}{R_{1p}}\cos^2\theta(1-e^{-R_{1p}T_s})}e^{-R_{1w}p_{ld}}}{1-e^{-R_{1w}(T_s+T_d+p_{ld})} + \frac{1-e^{-R_{1w}p_{ld}}}{1-e^{-R_{1w}(T_s+T_d+p_{ld})}}}$ , where  $R_{1w}$  is the bulk water longitudinal relaxation rate,  $I_0$  is the equilibrium magnetization,  $R_{1p}$  is the spin-lock relaxation rate and  $\theta = \text{atan}\left(\frac{\gamma B_1}{\Delta\omega}\right)$ , in which  $\gamma$  is the gyromagnetic ratio and  $B_1$  and  $\Delta\omega$  are the amplitude and offset frequency of the RF saturation, respectively. Under the assumption that  $T_s$  and  $T_d$  are much longer than the post-label delay (PLD) time, the PLD-corrected apparent CEST Z-spectrum can be derived as,  $\frac{I'_{sat}(\Delta\omega)}{I'_0} \cdot \left\{ \frac{1-e^{-R_{1w}(T_s+T_d)}}{1-e^{-R_{1w}T_d}} \right\} = e^{-R_{1p}T_s} + \frac{R_{1w}\cos^2\theta}{R_{1p}(1-e^{-R_{1w}T_d})} \cdot (1-e^{-R_{1p}T_s})$ , in which the superscript *pldcor* denotes the PLD-corrected apparent signals.  $R_{1p}$  can be numerically solved, and the QUASS-corrected CEST Z-spectrum can be

calculated as  $\left(\frac{I_{sat}(\Delta\omega)}{I_0}\right)^{QUASS} = \frac{R_{1w}}{R_{1p}}\cos^2\theta$ . Three healthy volunteers

and a brain tumor patient underwent CEST brain MRI using a 3T MR scanner (Magnetom Prisma, Siemens Medical Solutions, Erlangen, Germany) with a 64-channel head coil. Two sets of multislice brain images with different pairs of saturation duration and relaxation delays ( $T_s/T_d=1$  s/1 s and 2 s/2 s) were acquired in the axial orientation. The alternating offset frequencies of RF saturation ( $B_1 = 0.7$   $\mu$ T) were varied from -5 to 5 ppm, with increments of 0.125 ppm. The imaging parameters were: imaging readout time = 547 ms, TE = 33 ms, FOV = 220  $\times$  220 mm<sup>2</sup>, in-plane matrix = 110  $\times$  110, the number of slices = 8, interleaving slice ordering, slice thickness = 5 mm with 25% slice gap, with fat suppression, 1 average, and readout bandwidth = 1976 Hz/pix. Total imaging time was 3 min 31 s and 6 min 17 s for  $T_s/T_d$  of 1 s/1 s and  $T_s/T_d$  of 2 s/2 s.

**RESULTS:** Fig 1 shows CESTR', PLD-corrected CESTR', and CESTR<sup>QUASS</sup> of healthy human brain images at 3.5 ppm with  $T_s/T_d$  of 1/1 s and 2/2 s. The apparent CEST effects noticeably differed in the direction of the multislice acquisition and under different  $T_s$  and  $T_d$ . Although PLD-corrected apparent CEST effects showed little PLD dependency, there was a noticeable CEST contrast discrepancy between  $T_s/T_d$  of 1/1 s and 2/2 s. In contrast, the QUASS CEST effects were more consistent between  $T_s/T_d$  of 1/1 s and 2/2 s. Specifically, for WM, the PLD-corrected CESTR' was  $3.32\pm1.09\%$  and  $3.83\pm1.11\%$  for  $T_s/T_d$  of 1/1 s and 2/2 s, respectively, while CESTR<sup>QUASS</sup> being  $4.91\pm1.23\%$  and  $4.87\pm1.20\%$ . In GM, the PLD-corrected CESTR' was  $2.00\pm1.09\%$  and  $2.54\pm1.09\%$  for  $T_s/T_d$  of 1/1 s and 2/2 s, respectively, while their corresponding CESTR<sup>QUASS</sup> being  $3.36\pm1.56\%$  and  $3.28\pm1.34\%$ . Compared with the contralateral normal tissue, the tumor region shows greater CESTR in Fig 2. In particular, the apparent CEST effect increased with  $T_s$  and  $T_d$ , while the QUASS CEST effects showed little  $T_s$  and  $T_d$  dependency.

**CONCLUSION:** Our work demonstrated fast multislice CEST brain MRI with numerical simulation, healthy volunteer, and brain tumor patient scans. In addition, the QUASS algorithm minimizes the effect of the choice of saturation duration, relaxation delay, and post-label delay time on the CEST MRI quantification

**REFERENCE:** 1. Togao O, *et al.* NeuroOncol 2014; 16(3):441-448. 2. Harston GW *et al.*, Brain 2015;138(1):36-42 3. Goerke S *et al.*, Magn Reson Med 2021;86(1):393-404

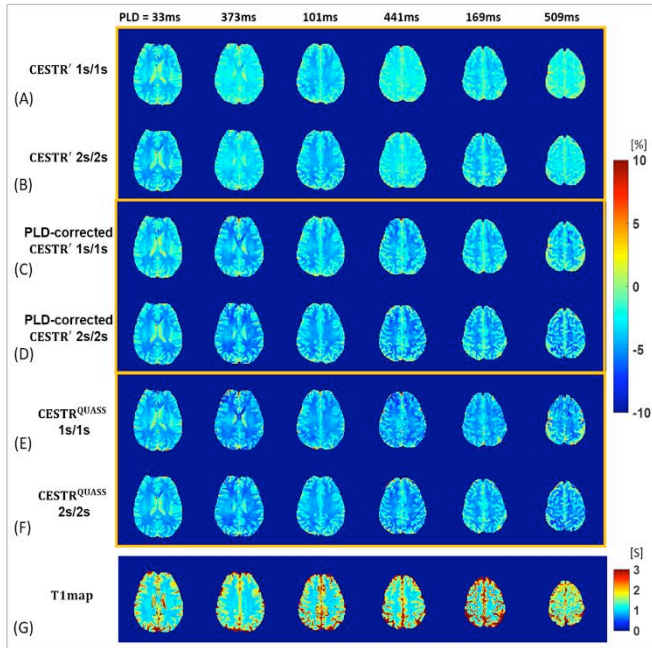


Fig 1. Comparison of multi-slice brain images obtained from apparent CESTR' (CESTR') images with  $T_s/T_d$  of 1/1 s (A), 2/2 s (B), PLD-corrected CESTR' images with  $T_s/T_d$  of 1/1 s (C), 2/2 s (D), QUASS-corrected CESTR images with  $T_s/T_d$  of 1/1 s (E), 2/2 s (F) and the corresponding T1 map images (G).

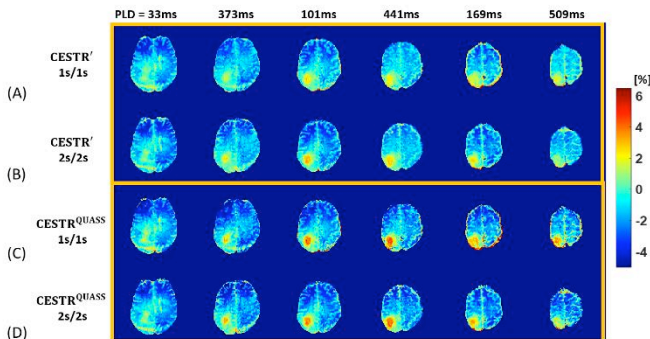


Fig 2. Comparison of multi-slice tumor patient images obtained from apparent CESTR (CESTR') images with  $T_s/T_d$  of 1/1s (A), 2/2 s (B), QUASS corrected CESTR images with  $T_s/T_d$  of 1/1 s (C), 2/2 s (D).



## Development of a standard phantom for CEST MRI

Tianzhe Li,<sup>1,2</sup> Alexander M. Quach,<sup>2</sup> Emily A. Thompson,<sup>2</sup> Erin P. Snoddy,<sup>2</sup> Jingfei Ma,<sup>3</sup> Mark D. Pagel<sup>1,3</sup>

<sup>1</sup> Department of Cancer Systems Imaging, University of Texas MD Anderson Cancer Center, Houston TX, USA

<sup>2</sup> University of Texas Health Science Center, Houston, TX, USA

<sup>3</sup> Department of Imaging Physics, University of Texas MD Anderson Cancer Center, Houston, TX, USA

✉ Either Oral or Poster Presentation | Contact Email: [mdpagel@mdanderson.org](mailto:mdpagel@mdanderson.org)

KEYWORD: ✉ Standardization ✉ CEST agents

**INTRODUCTION:** A standard phantom for clinical CEST MRI is needed to improve the comparisons and validations of different acquisition and analysis methods.<sup>1</sup> A standard is also needed for Quality Assurance / Quality Control (QA/QC) during clinical translation, clinical approval, and long-term clinical operation. The standard should accommodate a range of saturation frequencies, concentrations, T1 relaxation times, and pH values, while maintaining homogenous B1 and B0 field homogeneities at constant temperature.

**METHODS:** We have developed a “centisphere” phantom with 92 samples (Table 1) in a commercial phantom for a clinical 3T head coil (CaliberMRI, Inc.; Figure 1A). We have also developed an “alpha-cylinder” phantom with 24 samples (Table 1) in a commercial phantom for a clinical 7T head coil (Gold Standard Phantoms; Figure 1C). These phantoms have a range of materials with different CEST saturation frequencies, concentrations, T1 relaxation times (doped with Gadovist), and pH values. We have tested our phantoms with PureTemp37 (PureTemp LLC), a liquid crystal material that maintains the sample temperature at ~37.0 °C. We have also tested our phantoms with an ice/water slurry at 0 °C, and at room temperature. We have developed acquisition methods for measuring CEST, T1, T1, B1, and B0 with clinical 3T and 7T MRI scanners.

**RESULTS:** We have validated our recipes for each material at each concentration, T1 time and pH value. We have shown that PureTemp37 maintains the phantom at ~37.0 °C for > 4 hours (Figure 1B) and the ice/water slurry maintains temperature at 0 °C for ~1 hour, with outstanding temperature homogeneity throughout the phantom container. Studies of the repeatability and reproducibility of the phantoms at 3T and 7T magnetic field strength are ongoing. Initial studies demonstrate improved precision at 37 °C and 0 °C relative to room temperature that is not well-controlled.

**DISCUSSION:** A centisphere phantom (or a similar phantom) with a range of saturation frequencies, concentrations, T1 relaxation times, and pH values is designed to provide a universal phantom for CEST MRI research. A subset of these samples can be used in the alpha-cylinder phantom (or a similar phantom) for routine QA/QC during clinical CEST MRI.

**CONCLUSION:** Although our repeatability and reproducibility studies are a work in progress, our research community and radiology centers will soon have additional validated phantoms for CEST MRI.

**ACKNOWLEDGMENTS:** Our research is supported by the NIH/NCI through grants R01 CA231513 and P30 CA016672.

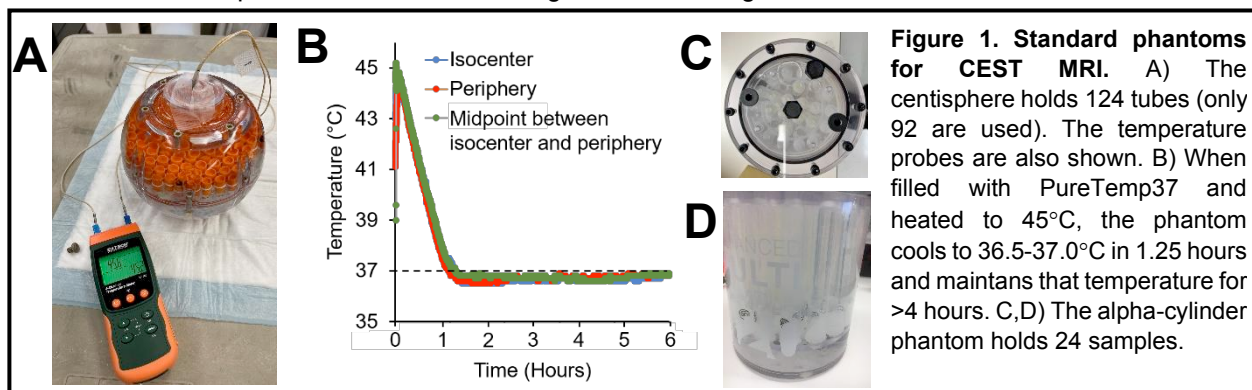
**REFERENCES:** 1. Yao, et al. A physical phantom for amine chemical exchange saturation transfer (cEST) MRI. *MAGNA* 2021;34:569-580.

Table 1. Composition of the CEST phantoms

Sample	Material	Source	Saturation Freq. (ppm)	Conc. (mM)	pH (number of values)	T1 time (sec)	Phantom <sup>2</sup>
paraCEST agent	Yb-HPDO3A <sup>1</sup>	Cage Chemicals	71, 99	10, 15, 20, 25, 50	6.0-7.5 (8)	0.2, 0.5, 1.0, 2.25	centisphere
diaCEST agent	Iopamidol (Isovue™)	Bracco Diagnostics	4.2, 5.6	10, 15, 20, 25, 50	6.0-7.5 (8)	0.2, 0.5, 1.0, 2.25	centisphere
gelatin	Verisol	Gelita	3.5	7.5% wt/vol	6.0-7.5 (5)	0.2, 0.5, 1.0, 2.25	centisphere, alpha-cylinder
peptide	poly-L-lysine	Sigma Aldrich	3.5	0.1% wt/vol	6.0-7.5 (5)	0.2, 0.5, 1.0, 2.25	centisphere
warm metabolite	creatine	Sigma Aldrich	1.8	10, 15, 20, 25, 50	6.0-7.5 (5)	0.2, 0.5, 1.0, 2.25	centisphere
glucose	glucose	Sigma Aldrich	0.8	10, 15, 20, 25, 50	6.0-7.5 (5)	0.2, 0.5, 1.0, 2.25	centisphere
cold metabolite	taurine	Sigma Aldrich	2.8	10, 15, 20, 25, 50	6.0-7.5 (5)	0.2, 0.5, 1.0, 2.25	alpha-cylinder

1. HPDO3A: 10-(2-hydroxypropyl)-1,4,7,10-tetraazacyclododecane-1,4,7-triacetic acid

2. The centisphere phantom is tested at 37 °C and room temperature, at 3T magnetic field strength. The alpha-cylinder is tested at 0°C and room temperature, at 3T and 7T magnetic field strengths.



# Fast WASAB1 post-processing: access to rapid B0 and B1 correction in clinical routine for CEST MRI

Christos Papageorgakis<sup>1</sup>, Eleni Firippi<sup>1</sup>, Benoit Gy<sup>1</sup>, Timothé Boutelier<sup>1</sup>, Ibrahim Khormi<sup>2,3,4</sup>, Oun Al-iedani<sup>2,3</sup>, Bryan Paton<sup>3,5</sup>, Jeannette Lechner-Scott<sup>3,6,7</sup>, Amir Fazlollahi<sup>8</sup>, Anne-Louise Ponsonby<sup>9,10</sup>, Patrick Liebig<sup>11</sup>, Saadallah Ramadan<sup>2,3</sup>, Moritz Zaiss<sup>12</sup>, and Stefano Casagrande<sup>1</sup>

<sup>1</sup> Department of Research & Innovation, Olea Medical, La Ciotat, France, <sup>2</sup> School of Health Sciences, College of Health, Medicine and Wellbeing, University of Newcastle, Newcastle, Australia, <sup>3</sup> Hunter Medical Research Institute, Newcastle, Australia, <sup>4</sup> College of Applied Medical Sciences, University of Jeddah, Jeddah, Saudi Arabia, <sup>5</sup> School of Psychology, College of Engineering, Science and Environment, University of Newcastle, Newcastle, Australia, <sup>6</sup> Department of Neurology, John Hunter Hospital, New Lambton Heights, Australia, <sup>7</sup> School of Medicine and Public Health, College of Health, Medicine and Wellbeing, University of Newcastle, Newcastle, Australia, <sup>8</sup> CSIRO Health and Biosecurity, Brisbane, Australia, <sup>9</sup> The Florey Institute of Neuroscience and Mental Health, Victoria, Australia, <sup>10</sup> Murdoch Children's Research Institute, Royal Children's Hospital, University of Melbourne, Victoria, Australia, <sup>11</sup> Siemens Healthcare GmbH, Erlangen, Germany, <sup>12</sup> Department of Neuroradiology, University Clinic Erlangen, Friedrich-Alexander Universität Erlangen-Nürnberg (FAU), Erlangen, Germany

☑ Oral Presentation ☐ Poster ☐ Either Oral or Poster Presentation | Contact Email: [christos.papageorgakis@olea-medical.com](mailto:christos.papageorgakis@olea-medical.com)

**KEYWORD:** ☐ CEST agents ☐ Contrast Mechanism ☐ Tumor ☐ Stroke ☑ Neurology ☐ Body & MSK ☑ Standardization ☐ Novel Acquisition ☐ Machine Learning

**INTRODUCTION:** CEST MRI is affected by inhomogeneities of the static magnetic (B0) and radiofrequency (RF) transmit (B1) fields. In<sup>1</sup> a single sequence is proposed for mapping both B0/B1 inhomogeneity maps, called "Simultaneous mapping of Water Shift And B1 (WASAB1)". Sampling of several frequency offsets around the water resonance frequency, a WASAB1-Spectrum is acquired and normalized using a M0 volume whose frequency is far from the water one.

The WASAB1 normalized intensities  $Z(\Delta\omega)$  of a single voxel can be modelled based on the Bloch equations as:  $Z(\Delta\omega) = |c - d f(B0, B1, \Delta\omega)|$  where parameters c and d describe WASAB1-Spectra amplitude, B1 its periodicity, and B0 its symmetry axis (Figure1A). However, the parameter estimation is difficult and unstable due to the presence of the absolute value in the above equation, that models the acquired MRI-magnitude and introduces discontinuity in the model (Figure1B). The original WASAB1 post-processing<sup>1</sup> searches exhaustively the parameter space than performs a nonlinear optimization step which significantly increases the computational time of the model fitting, making it prohibitive in clinical use. **METHODS:**

**Technical Solution:** Our proposed method is divided in two steps. For each voxel: i) retrieve the sign of some data points of the WASAB1-Spectra to generate a polarized dataset, ii) knowing the sign of the signal, the absolute value in the equation can be removed and the model becomes linear in parameters c and d. Hence, the variable projection method can be applied<sup>2</sup> to reduce the dimensionality of the nonlinear estimation problem. This makes the estimate of B0 and B1 faster by two orders of magnitude, more robust, and less sensitive to local minima. The polarized dataset is constructed by removing the data points that are unlikely to be positive (Figure1C). This yields a partial polarized WASAB1-Z-spectrum, from which first guess of B0 and B1 can be estimated. Those approximations are then used to refine the sign of the signal on the whole spectra, which is eventually used to derive the definitive estimate of B0 and B1 (Figure1D). **Patient Data Acquisition:** The WASAB1 data were acquired on a 3 Tesla MAGNETOM Prisma MRI scanner (Siemens, Erlangen, Germany) on 10 persons with relapsing-remitting multiple sclerosis (pw-RRMS), in the framework of a clinical CEST study, using 3D snapshot-GRE (WIP816B). **RESULTS:** The evaluation on the in vivo 3 Tesla data showed that our proposed method is in good agreement with the original WASAB1 method, showing differences between the estimated values of maps of each method below 0.02 for 99.2% of pairs in the Bland-Altman plots (Figure2). **DISCUSSION:** Our method led to an average computation time of 0.0007 seconds for a single WASAB1-Z-Spectrum compared to 18.3 seconds for the original method. Using parallel execution on the same 8-core processor an entire WASAB1 clinical multi-volume was processed in less than 5 seconds in Olea Sphere 3.0 (Olea Medical, La Ciotat; France). **CONCLUSION:** A new accelerated post-processing method has been proposed for simultaneous B0 and B1 mapping based on the WASAB1 sequence. Its outstanding acceleration permits its use in clinical routine for CEST inhomogeneity correction, without compromising the stability of the estimated B0 and B1 maps. **ACKNOWLEDGMENTS:** The clinical study was kindly supported by MS Research Australia. I.Khormi was supported by a PhD scholarship with annual grant support from the University of Jeddah, Saudi Arabia. **REFERENCES:** 1- Schuenke P. *et al.* Magn Reson Med 2017; 77(2), 571–580. 2- Golub G. *et al.* Inverse problems 2003; 19(2):R1.

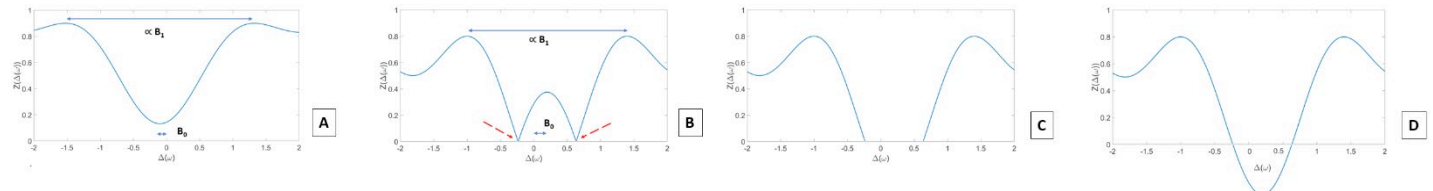


Figure1: WASAB1-Spectra (A), introduced cusp (B), data points that are likely to be positive (C) and the refined sign of the signal (D).

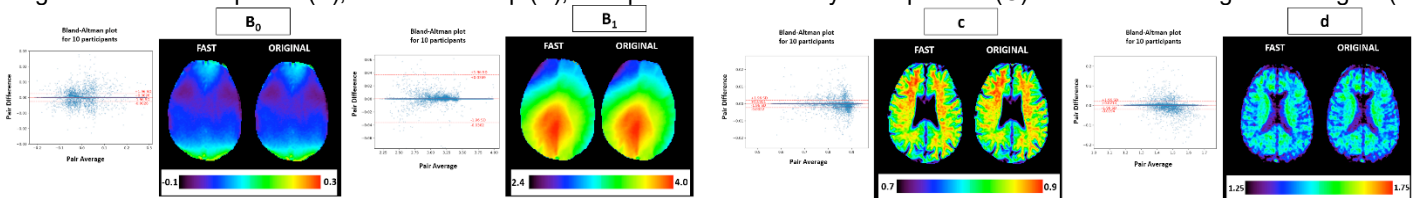


Figure2: Bland-Altman plots on the pair difference/average between the proposed and original method and the estimated maps.

# Enhanced multipool fitting with quasi-steady-state (QUASS) CEST MRI

Phillip Zhe Sun<sup>1,2 \*</sup>

<sup>1</sup> Imaging Center, Emory National Primate Research Center, Emory University, Atlanta, GA. <sup>2</sup> Department of Radiology and Imaging Sciences, Emory University School of Medicine, Atlanta, GA

☐ Oral Presentation ☐ Poster ☒ Either Oral or Poster Presentation | Contact Email: [pzhesun@emory.edu](mailto:pzhesun@emory.edu)

**KEYWORD:** You are encouraged to choose one or two keywords. ☒ Standardization ☐ Novel Applications

**INTRODUCTION:** CEST MRI is promising to characterize complex tissue changes in disorders such as acute stroke (1). However, quantitative CEST (qCEST) analysis has been challenging, particularly under non-steady-state acquisition and in the presence of relaxation time changes. Our study tested whether a spinlock model-based analysis of quasi-steady-state (QUASS) CEST reconstruction improves CEST quantification.

**METHODS:** We simulated the CEST effect using classical 3-pool Bloch McConnell (BM) equations in MATLAB (2). We varied the relaxation delay and saturation time from 2 to 5 s with intervals of 0.5 s, assuming a representative  $B_1$  amplitude of 0.75  $\mu$ T. In addition, the bulk water  $T_1$  was adjusted from 1 to 2 s, with intervals of 0.1 s. We assumed two labile proton groups at 3.5 ppm (amide) and 2 ppm (guanidine), with their labile proton concentration being 1:1500 and 1:2000 at exchange rates of 100 and 200  $s^{-1}$ , respectively. We compared two fitting approaches: 1) Routine Z-spectral fitting, being  $1 - Z^{app} \approx \sum_{i=1}^N \frac{A_i'}{(1 + 4 \left( \frac{\Delta\omega - \delta_i}{\sigma_i} \right)^2)}$  (3), and 2) The spinlock model-

based QUASS Z-spectral fitting, being  $Z^{QUASS} = \frac{R_1 \cos^2 \theta}{R_1 \cos^2 \theta + R_2 \sin^2 \theta + \sum_{i=1}^N \frac{A_i}{(1 + 4 \left( \frac{\Delta\omega - \delta_i}{\sigma_i} \right)^2)}} (4).$

**RESULTS:** Fig. 1 evaluates the fitting results of the apparent Z spectra as a function of  $T_s$  and  $T_1$ , using both the conventional Lorentzian fitting of  $1 - Z^{app}$  (Eq. 1) and the spinlock model-based fitting of  $Z^{app}$  (Eq. 2). The apparent Z-spectral fitting shows notable dependence on both  $T_1$  and  $T_s$ . This observation is because the saturation transfer effect accumulates over time, and as a result, the CEST effects increase with  $T_s$ . In addition, the amplitude from  $1 - Z^{app}$  fitting scales with  $T_1$ . Interestingly, the slope of the solved CEST peaks differed for amide and guanidine CEST effects. We had  $CESTR_{amide}^{app} = 1.9 * T_1 + 2.1$  ( $P < 0.01$ ) and  $CESTR_{guanidine}^{app} = 0.7 * T_1 + 2.5$  ( $P < 0.01$ ). We also tested the model-based  $Z^{app}$  fitting (Fig. 1c). As expected, the solution from  $Z^{app}$  fitting also shows dependence on  $T_s$  and, to a lesser degree,  $T_1$ . We found  $CESTR_{amide}^{app} = -0.9 * T_1 + 5.5$  ( $P < 0.01$ ) and  $CESTR_{guanidine}^{app} = -1.0 * T_1 + 5.2$  ( $P < 0.01$ ).

We further tested the fitting of the QUASS Z spectra. Fig. 2a shows the conventional 1-Z fitting of QUASS spectra (i.e.,  $1 - Z^{QUASS}$ ). Although QUASS reconstruction corrects  $T_s$  dependence, the fitting shows notable  $T_1$  dependence. We had  $CESTR_{amide}^{QUASS} = 3.2 * T_1 + 1.0$  ( $P < 0.01$ ) and  $CESTR_{guanidine}^{QUASS} = 1.9 * T_1 + 1.5$  ( $P < 0.01$ ). The spinlock model-based Z-spectral fitting ( $Z^{QUASS}$ , Fig. 2c) shows little dependence on  $T_s$  and  $T_1$ , with  $CESTR_{amide}^{QUASS} = -0.01 * T_1 + 4.90$  ( $P < 0.05$ ) and  $CESTR_{guanidine}^{QUASS} = 0.02 * T_1 + 4.55$  ( $P < 0.01$ ). Although the linear regression still shows a significant correlation with  $T_1$ , the slopes from the model-based fitting of  $Z^{QUASS}$  were much smaller than those from  $Z^{app}$  fittings (i.e.,  $Z^{app}$  and  $1 - Z^{app}$ ) and conventional fitting of  $1 - Z^{QUASS}$ . The simulation results suggest that model-based fitting of QUASS Z-spectrum provides quantification less dependent on  $T_1$  and experimental conditions of  $T_s$  and  $T_d$ .

**CONCLUSION:** The spinlock model-based QUASS Z-spectral fitting provides accurate quantification over the routine apparent Z-spectral fitting. The quantitative QUASS CEST MRI is promising for in vivo CEST imaging.

**References:** 1) Zhou et al. Nat Med 2003;9(8):1085-1090. 2) Woessner et al. MRM 2005;53:790-9. 3) Zaiss M et al. JMR 2011;211:149-55. 4) Sun MRM 2021;85:3281-9.

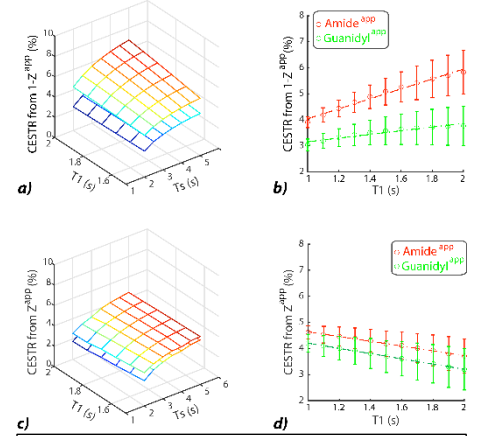


Fig. 1, Comparison of routine and spinlock model-based Lorentzian fitting of apparent Z-spectra. a) CEST amplitudes solved from fitting of  $1 - Z^{app}$ , as a function of  $T_s$  and  $T_1$ . b) Solved CEST signals as a function of  $T_1$ . c) CEST amplitudes solved from fitting of  $Z^{app}$ . d) Solved CEST signals as a function of  $T_1$ .

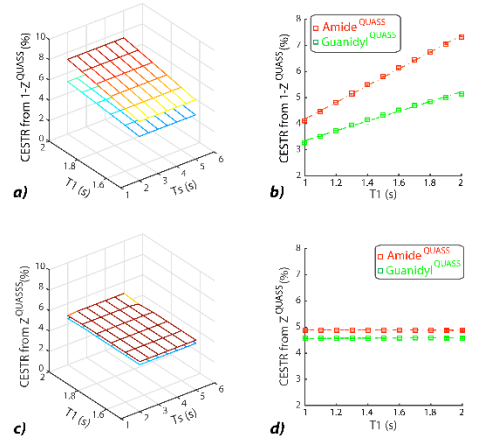


Fig. 2, Comparison of routine and spinlock model-based Lorentzian fitting of QUASS Z-spectra. a) CEST amplitudes solved from fitting of  $1 - Z^{QUASS}$ , as a function of  $T_s$  and  $T_1$ . b) Solved CEST signals as a function of  $T_1$ . c) CEST amplitudes solved from fitting of  $Z^{QUASS}$ . d) Solved CEST signals as a function of  $T_1$ .



# Spatial-Spectral Selective Pulses for B1 Compensation and Improved Saturation Homogeneity in Cardiac CEST

Cindy Ayala<sup>1</sup>, Huiwen Luo<sup>2</sup>, Kevin Godines<sup>1</sup>, William A. Grissom<sup>2</sup>, Moriel Vandsburger<sup>1</sup>

<sup>1</sup> University of California, Berkeley, Berkeley CA, USA <sup>2</sup> Vanderbilt University, Nashville, TN, USA

☒ Apply Student/Postdoc Travel Fund

☐ Oral Presentation ☐ Poster ☒ Either Oral or Poster Presentation | Contact Email: ciayala@berkeley.edu

KEYWORD: ☒ Novel Acquisition

**INTRODUCTION:** Chemical exchange saturation transfer (CEST) is highly sensitive to B1-field inhomogeneities. Current efforts to improve the accuracy of CEST include mitigating these B1 inhomogeneities<sup>1</sup>. However, these methods are often not applicable or translatable for cardiac imaging. Here, we evaluate the use of tailored spatial-spectral pulses for improved CEST contrast and B1 compensation across the myocardium.

**METHODS:** All in vivo studies were performed on a Siemens 3T Tim Trio scanner using a body matrix coil and a spine matrix coil. Five healthy volunteers have been recruited for this study to date. A B1 map was acquired in one midventricular short axis slice using a Turbo FLASH sequence with a prescribed saturation flip angle of 50°. Additional parameters included a slice thickness of 5mm, TE of 2.12ms, and TR of 2.73s. Using the measured B1 map for each subject, a tailored spatial-spectral pulse was designed and used to simulate a B1 map following previously described methods<sup>2</sup> via MATLAB version 2021b. The imaging sequence utilized 23 tailored saturation pulses, each with a duration of 36 ms, 1.2  $\mu$ T peak B1 power, saturation offsets ranging from -10ppm to +10ppm, and were followed by a 25° flip angle GRE readout. A reference scan was taken at 10000 Hz. Other scanning parameters included a FOV of 26 cm  $\times$  30 cm, TR of 1.45 s, and TE of 2.59 ms. ECG triggering was used to time readout during diastole. Every scanning subject required two sets of frequency offset acquisitions consisting of either a conventional Gaussian or tailored saturation. For each image, the myocardium was segmented into 6 regions consistent with current standards<sup>3</sup>. The mean signal intensity within each segment was normalized and the resulting z-spectrum was corrected for B0 shift using a WASSR correction<sup>4</sup>. CEST contrast was quantified by performing a 5-pool Lorentzian fitting of direct saturation, MT, creatine, amide, and NOE.

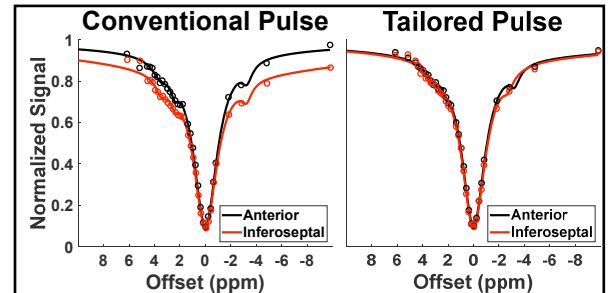


Figure 1: Z-spectra derived from the anterior and inferoseptal segments obtained with conventional Gaussian pulse or tailored spatial-spectral pulse. Conventional saturation leads to greater differences in derived z-spectra compared to tailored saturation.

**RESULTS:** Simulations showed the spatial-spectral pulses reduced flip angle variation across the myocardium from an average range of 24.1° with a Gaussian pulse to 15.6°. The subsequent impact upon Z-spectra derived from different myocardial regions is shown in Figure 1. Whereas the use of Gaussian pulses for CEST preparation resulted in significant regional variation in derived Z-spectra, spatial-spectral saturation pulse generated consistent Z-spectra across the heart. The subsequent impact on highly B1-sensitive parameters of direct saturation, MT, creatine, amide, and NOE is shown in Figure 2, which suggests a lower spatial variation of all parameters with spatial-spectral saturation.

**DISCUSSION:** The large average flip angle range of 24.1° in the experimental B1 maps demonstrate the effects of B1 inhomogeneity in cardiac scans. The B1 map illustrates the flip angle's spatial dependence which would result in inconsistent generation of CEST contrasts across the myocardium. The results of the simulated B1 map demonstrates an improved flip angle homogeneity of 15.6° with the tailored RF pulse. Importantly, the use of a tailored RF pulse for generation of CEST contrast results in improved spatial homogeneity of all targeted CEST contrasts. Figure 2 illustrates the span of each contrast by pulse shape, representing a more consistent impact upon direct saturation, MT, and creatine across the myocardium.

**CONCLUSION:** This work explored the use of tailored spatial-spectral pulses for in vivo application and showed that, when compared to conventional Gaussian saturation pulse, the tailored pulse reduced the flip angle variation by 8.5° on average. Preliminary results suggest that the tailored pulse reduced the variation of direct saturation, MT and creatine contrast across the myocardium. Future work includes increasing the sample size to fully explore the validity of the tailored spatial-spectral pulse.

**ACKNOWLEDGMENTS:** This study was supported by NIH 1R01HL28592-01, Silvian Foundation Award, AHA 19TPA34850040, NIH UH2EB028908-02, DGE 1752814

## REFERENCES:

1. Liu G, *et al.* NMR Biomed. 2013;26(7):810-828. doi:10.1002/nbm.2899
2. Luo H, *et al.* International Society for Magnetic Resonance in Medicine; 2020.
3. Cerqueira MD, *et al.* Circulation. 2002;105(4):539-542. doi:10.1161/hc0402.102975
4. Kim M, *et al.* Magn Reson Med. 2009;61:1441-1450. doi:10.1002/mrm.21873

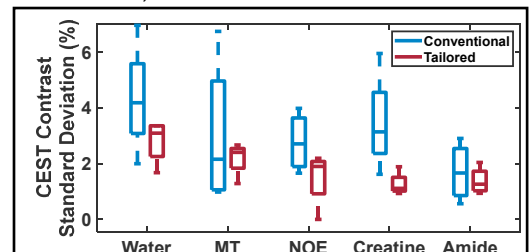


Figure 2: Comparison of CEST contrast variation across by pulse. The spatial variation in B1-sensitive contrast mechanisms suggests an increased spatial homogeneity using spatial-spectral tailored saturation pulses.



# ***In vivo* CEST-Dixon in axillary lymph nodes with and without biopsy-confirmed malignancy: potential for non-invasive determination of lymph node metastasis**

Rachelle Crescenzi<sup>1</sup>, Paula MC Donahue<sup>1</sup>, Randall S Jones<sup>1</sup>, Chelsea Lee<sup>1</sup>, Maria Garza<sup>1</sup>, Niraj J Patel<sup>1</sup>, Ingrid Meszoely<sup>1</sup>, Manus J Donahue<sup>1</sup>, <sup>1</sup>Vanderbilt University Medical Center, Nashville, TN, USA

□ Apply Student/Postdoc Travel Fund

☒ Oral Presentation □ Poster □ Either Oral or Poster Presentation | Contact Email: rachelle.crescenzi@vumc.org

KEYWORD: You are encouraged to choose one or two keywords. □ CEST agents □ Contrast Mechanism

☒ Tumor □ Stroke □ Neurology ☒ Body & MSK □ Standardization □ Novel Acquisition □ Machine Learning

**INTRODUCTION:** The overall goal of this work is to apply a novel CEST-Dixon MRI approach in the axillary lymph nodes (LNs) of women with breast cancer to test fundamental hypotheses about biochemical profiles in biopsy-confirmed benign versus malignant LNs. Axillary LNs are central to lymphatic immune function and represent the primary reservoir and route for metastatic breast cancer. LN malignancy cannot be discerned definitively from diagnostic imaging, and as such, LN removal during lumpectomy or mastectomy can be speculative, require added procedural time for accurate histological staging, and resections are often exaggerated thereby predisposing patients to immune complications and secondary lymphedema (1). CEST MRI methods have been sensitized to upper-extremities to provide imaging biomarkers of lymphedema, and distinct z-spectra in breast tumors versus healthy tissue; however, application of CEST to LN malignancy is largely unexplored (2-4). In this study, we evaluated whether *in vivo* 3T CEST profiles in axillary LNs are different among patients with benign versus malignant LNs.

**METHODS:** Female participants with breast cancer undergoing clinically-indicated axillary LN biopsy or dissection were

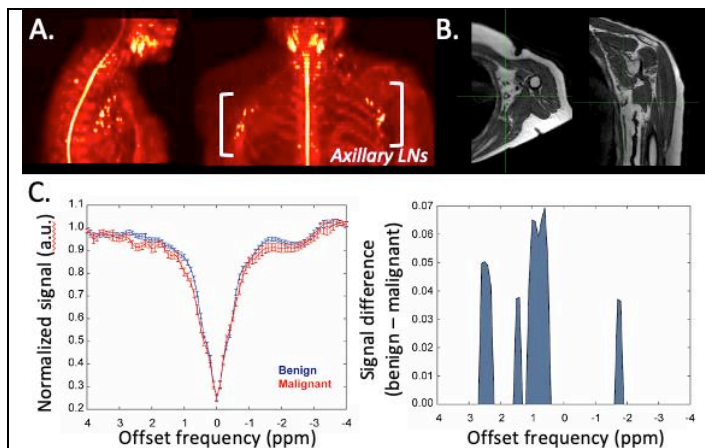


**Figure 1.** MRI acquisitions in the upper-extremity and torso were used to **A)** identify axillary lymph node (LN) regions on diffusion-weighted imaging with background suppression (DWIBS), and **B)** differentiate lymph nodes from surrounding axillary fat and muscle tissues on high-spatial resolution  $T_1$ -weighted MRI. **C)** Axillary LN z-spectra are displayed as the mean  $\pm$  standard deviation across subjects with benign ( $n=20$ ) versus malignant ( $n=20$ ) LNs, and signal differences in z-spectra are plotted for offset frequencies where the signal was significantly different.

prospectively enrolled from the surgical oncology services and provided written, informed consent. MRI at 3T was performed before LN removal, and the presence of LN malignancy was determined by the clinical pathology services. Axillary LNs were localized on diffusion-weighted-imaging-with-background-suppression (DWIBS) and 3D  $T_1$ -weighted MRI. CEST-Dixon MRI was performed using parameters optimized for body (4). A 3D turbo-gradient-echo readout (factor=25; TE1=1.32 ms;  $\Delta$ TE=1.1 ms; duration=6min30s) was performed using a train of sinc-gauss pulses (each pulse duration=100 ms; pulses/TR=4;  $B_1=1.5$  uT) at a spatial resolution of 2.5x2.5x6 mm (slices=10), with a saturation frequency offset range of -5.5 to +5.5 ppm (stepsize=0.2 ppm) with six equilibrium ( $S_0$ ) acquisitions. A  $B_1$  map was separately obtained to ensure >85% of the prescribed  $B_1$  over the axillary region (2). Voxel-wise CEST z-spectra were corrected for  $B_0$  inhomogeneity of the water resonance, normalized by  $S_0$ , and the z-spectra from the fat-suppressed Dixon reconstructions preserved. LNs were stratified from participants with or without biopsy-confirmed LN malignancy, and differences in axillary LN CEST proton transfer ratio (PTR) between groups were evaluated using a Student's t-test (significance criteria: two-sided  $p<0.05$ ).

**RESULTS:** A total of 40 axillary LNs were identified from 16 participants with benign and 7 participants with malignant LNs (20 LNs from each cohort were used for hypothesis testing to maintain identical comparator sample sizes). Participant groups were matched for age (malignant:  $54.0 \pm 11.6$  years; benign:  $53.5 \pm 11.3$  years), body-mass-index (malignant:  $28.3 \pm 7.0$ ; benign:  $26.6 \pm 5.2$  kg/m<sup>2</sup>), and race/ethnicity (white/non-Hispanic). More LNs were removed during surgery in the malignant ( $9.9 \pm 7.9$ ) vs. benign ( $3.4 \pm 1.7$ ) cohort. MRI of LNs identified by DWIBS and  $T_1$ -weighted images are shown in **Fig 1A,B**. Mean z-spectra and corresponding significant differences in cohorts with malignant vs. benign LNs were observed in regions of known chemical exchange for semi-solid magnetization transfer (-1.6 to -1.9 ppm PTR=0.087 vs. 0.051,  $p=0.04$ ), hydroxyl (+0.5 to +1.5 ppm PTR=0.272 vs. 0.212,  $p=0.003$ ), and amine (+2.3 to +2.6 ppm PTR=0.081 vs. 0.033,  $p=0.003$ ) protons (**Fig 1C**).

**DISCUSSION:** The quantified mean CEST z-spectra in axillary LNs of participants with biopsy-confirmed malignant LNs indicate a unique LN tissue microenvironment detectable by CEST-Dixon MRI, whereby enhanced hydroxyl exchange is consistent with tumor-associated acidification of interstitial fluid, especially for aggressive breast cancer tumors (4,5).

**CONCLUSION:** Malignant vs. benign LNs may exhibit unique CEST contrast relevant to multiple labile proton regimes; as such, LN CEST may have relevance for pre-surgical LN staging and for guiding resection decisions.

**REFERENCES:** [1] DiSipio T, *et al.* The Lancet Oncology 2013;14(6):500-515. [2] Crescenzi R, *et al.* Magn Reson Med 2020;83(5):1760-1773. [3] Donahue MJ, *et al.* Magn Reson Med 2016;75(1):345-355. [4] Zhang S, *et al.* Magn Reson Med 2018;80(3):895-903. [5] Anemone A, *et al.* British journal of cancer 2021;124(1):207-216.

# Optimization of pH-Weighted CEST Contrast in the Spinal Cord

Alicia Cronin<sup>\*,1,2</sup> Patrick Liebig,<sup>3</sup> Sarah Detombe,<sup>4</sup> Neil Duggal<sup>1,4</sup> and Robert Bartha<sup>1,2</sup>

<sup>1</sup>Department of Medical Biophysics; <sup>2</sup>Centre for Functional and Metabolic Mapping, Robarts Research Institute, The University of Western Ontario, London, ON, Canada; <sup>3</sup>Siemens Healthcare GmbH, Erlangen Germany; and <sup>4</sup>Department of Clinical Neurological Sciences, University Hospital, London Health Sciences Centre, London, ON, Canada

**KEYWORDS:** Neurology, Novel Acquisition

**INTRODUCTION:** Ischemia and hypoxia in the spinal cord can be caused by several factors, including compression, injury, muscular sclerosis, and vascular alterations. However, direct non-invasive evaluation of spinal cord ischemia and hypoxia using MRI methods is challenging in humans due to the inaccessibility, anatomy, and motion of the cord. Chemical Exchange Saturation Transfer (CEST) MRI can produce pH-weighted contrasts due to the pH-dependence of the amine and amide proton exchange rate.<sup>1</sup> Since hypoxia alters tissue pH, CEST measurement of tissue pH provides an indirect method to assess ischemia and hypoxia. Amine/amide concentration-independent detection (AACID) is a ratiometric pH measurement method that reduces sensitivity to tissue water and protein concentrations, which can impact amide proton transfer (APT) contrast.<sup>2</sup> Contrast based on nuclear Overhauser enhancement (NOE) originating from mobile macromolecules can also be generated by saturating protons upfield from water.<sup>3</sup> NOE contrast has also been shown to be pH-dependent and therefore could similarly provide a means to examine pH changes in the spinal cord due to hypoxia. The objective of this study was to optimize and compare the magnitude of amide proton and NOE contrast in the human spinal cord at 3.0 T to determine which would provide a more precise measure of tissue pH.

**METHODS:** On a 3.0 T Siemens MAGNETOM Prisma Fit MRI scanner, a Siemens prototype 3D CEST sequence was used consisting of a presaturation preparation period followed by a 3D gradient echo (GRE) readout. The optimal presaturation consisted of a train of 30 Gaussian-shaped RF pulses with pulse duration  $t_{\text{pulse}} = 100$  ms, interpulse delay  $t_{\text{delay}} = 1$  ms, resulting in a total saturation time of 3.03s. Presaturation was applied at 62 offsets ranging from -6.5 to 6.5 ppm. Other relevant imaging parameters included: TR/TE = 3.32/1.14 ms, voxel size = 2 mm x 2 mm, slice thickness = 5 mm, matrix 64x64x8, and 1 acquisition. To correct  $B_0$  inhomogeneities, a water saturation shift referencing (WASSR) spectrum was acquired using five Gaussian-shaped saturation pulses (same parameters as above, 25 offsets from -2.0 to 2.0 ppm) and used to correct the shifted CEST spectrum on a pixel-by-pixel basis. The linear dependence of the optimized AACID and NOE contrast on pH was assessed in egg white phantoms (pH range 5.2-9.0) using Pearson's correlation coefficient ( $r$ ). The contributions of bulk water, NOE, amide, and amine CEST effects were modelled and fitted in MATLAB to accurately estimate the AACID value and NOE effect. A respiratory correction method introduced by By *et al.*<sup>4</sup> was implemented, which interleaves non-saturated scans throughout the acquisition and uses the respiratory bellows to calculate respiration per unit time (RVT) to account for signal variation due to breathing. One healthy participant was recruited to evaluate the CEST effect and the respiratory correction in the cord.

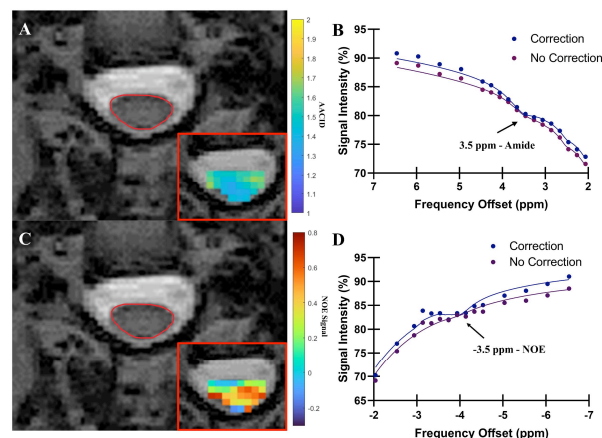


**Figure 1:** Axial T2-weighted anatomical of the healthy spinal cord with 5 mm thick AACID map (A) and 5 mm thick NOE map (C) displayed on inset. CEST spectra show the 3.5 ppm amide CEST effect (B) and the -3.5 ppm NOE CEST effect (D).

**RESULTS:** In egg white phantoms, both AACID value ( $p = 0.01$ ,  $r = -0.94$ ) and NOE effect ( $p = 0.04$ ,  $r = 0.90$ ) were found to be linearly dependent on pH. In the brain, the optimal amide CEST and NOE contrast were both achieved at a  $B_1$  value (continuous wave power equivalent) of 0.5  $\mu$ T (data not shown). Using this optimal pre-saturation  $B_1$  amplitude in the spinal cord (Figs. 1A, 1C), the average magnitude of the respiratory corrected measured amide CEST effect was 2.6%, compared to the non-corrected CEST effect of 1.7% (Fig. 1B). Similarly, the average magnitude of the respiratory corrected NOE effect was 1.2%, and the non-corrected effect was 0.3% (Fig. 1D).

**DISCUSSION:** Both the AACID value and the NOE effect demonstrated a linear pH dependence in the physiological range. The applied respiratory correction improved the quality of the CEST spectrum and increased the measured amide and NOE effects in the spinal cord. The detected amide CEST effect was more prominent than the NOE contrast suggesting the AACID measurement would be preferred for spine pH-weighted imaging.

**CONCLUSION:** Both amide proton and NOE contrast were successfully observed in the spinal cord using a prototype 3D CEST sequence at 3.0 T. Implementing a previously developed respiratory correction improved the measurement of both. Further refinement of the fitting will improve the fidelity of these measurements and increase the sensitivity to pH.

**REFERENCES:** 1. Dula A, *et al.* NMR Biomed 2016;29:1249-1257. 2. McVicar N, *et al.* J Cereb Blood Flow Metab 2014;34:690-698. 3. Jones CK, *et al.* NeuroImage 2013;77:114-124. 4. By S, *et al.* Magn Reson Med 2018;79:806-814.

## The z-spectrum as a way to monitor fibrosis

Nabeelah Jinnah<sup>1</sup>, Olivier Mougin<sup>1</sup>, Penny Gowland<sup>1</sup>

<sup>1</sup>Sir Peter Mansfield Imaging Centre, University of Nottingham, United Kingdom

☒ Apply Student/Postdoc Travel Fund

☐ Oral Presentation ☒ Poster ☐ Either Oral or Poster Presentation | Email: nabeelah.jinnah@nottingham.ac.uk

KEYWORD: You are encouraged to choose one or two keywords. ☐ CEST agents ☐ Contrast Mechanism

☐ Tumor ☐ Stroke ☐ Neurology ☒ Body & MSK ☐ Standardization ☐ Novel Acquisition ☐ Machine Learning

**INTRODUCTION:** Fibrosis is a common factor in many diseases and is implicated in a significant fraction of deaths in the developed world<sup>1</sup>, so it would be very valuable to be able to quantify it non-invasively. Fibrosis involves deposition of extracellular matrix components, particularly collagen. We aim to use the z-spectrum to characterize fibrosis, considering strictures of the bowel wall in Crohn's disease. We have studied the full z-spectrum of collagen at 7T and characterized MT at 3T of ex-vivo strictured bowel samples.

**METHODS:** To investigate changes in CEST pool sizes from bovine collagen solution, solutions of 5 %, 10 %, 20 % and 40 % collagen, and 40 % collagen at pH of 6.03, 6.99 and 7.26 were prepared. These were imaged at 37°C with a 3D-TFE readout on a 7T Achieva system using a NOVA 32ch receive, 8ch pTx head coil. 42 frequencies at four RF powers were sampled using semi-continuous wave saturation. Spectra were B1 corrected and fitted to a five-pool Bloch-McConnell model using a particle swarm optimization algorithm<sup>2</sup>.

Additionally, we acquired z-spectra from four fresh ex-vivo samples of bowel wall containing strictures, from patients with Crohn's disease who had just undergone bowel resection surgery. Histological analysis is ongoing and currently only macroscopic assessment of the position of strictures on the sample is available. Z-spectra were acquired using a 3T Ingenia system and a 3D-TFE readout, preceded by a train of 20 Gaussian-windowed sinc pulses. A three-pool Lorentzian model (water, fat and MT peaks) was fitted voxel-wise to the data from the segmented bowel wall. K-means clustering was used to cluster the maps of fitted MT peak amplitude.

### RESULTS:

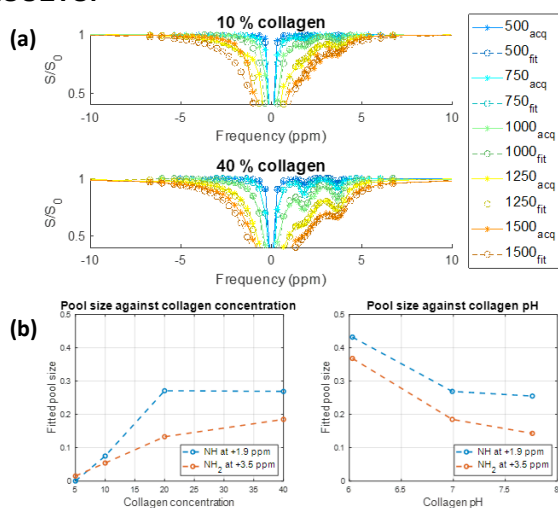


**Figure 1.** Z-spectra from (a) 10 % and 40 % collagen solutions acquired at multiple RF powers. (b) Results of fitted CEST pool sizes using a PSO algorithm based on the Bloch-McConnell model against concentration and pH of the collagen samples.

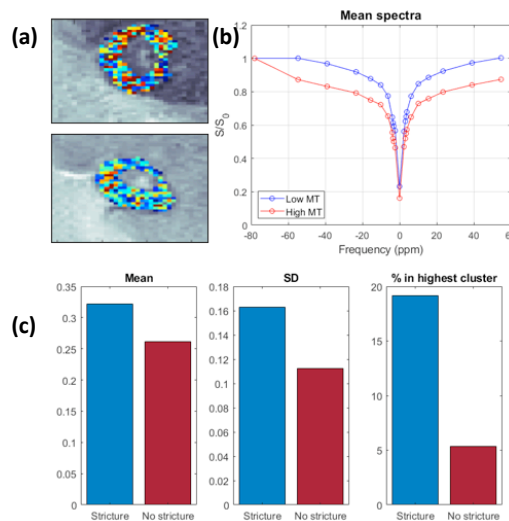


**Figure 2.** (a) Maps of fitted MT amplitude from ex-vivo sample for slice with stricture (above) and without (below). (b) Z-spectra from voxels with low and high MT. (c) Mean, SD of MT amplitude and percentage of voxels in the highest k-means cluster in the slice.

**DISCUSSION:** For the collagen samples, the amplitude of the CEST peaks at +1.9 ppm and +3.5 ppm increased with concentration and decreased with pH as expected (R-squared 0.71 and 0.86 for the NH pool, and 0.92 and 0.92 for the NH<sub>2</sub> pool for simple linear models). The pool amplitude of the +1.9 ppm did not increase at higher concentration, possibly due to saturation caused by overlap with the long T<sub>2</sub> water peak.

Initial analysis of two ex-vivo bowel wall samples suggest a relationship between areas of high fibrosis and clusters of high amplitude MT, and greater variation in MT amplitude (possibly indicating co-existing inflammation). Future work will investigate CEST signals in the samples at 7T. The ex-vivo protocol was also performed in-vivo prior to surgery, and analysis of these images is ongoing.

**CONCLUSION:** Z-spectrum imaging has promise as a method of characterizing fibrosis and differentiating between inflammation and fibrosis in the bowel wall, which could assist with guiding treatment decisions.

**REFERENCES:** 1. Wynn TA. Fibrotic disease and the T(H)1/T(H)2 paradigm. Nat Rev Immunol. 2004;4(8):583-594.  
2. Carradus A *et al.* ISMRM proceedings 2019, abstract 3999 (submitted NMR Biomedicine).



# Quantitative imaging of gene therapy delivery vehicles using CEST-NMR/MRI

Bonnie Lam<sup>1</sup>, Mark Velasquez<sup>1</sup>, Aaron J. Velasquez-Mao<sup>1</sup>, Kevin Godines<sup>1</sup>, Moriel H. Vandsburger<sup>1</sup>

<sup>1</sup> Department of Bioengineering, University of California, Berkeley, Berkeley, CA. USA.

☒ Apply Student/Postdoc Travel Fund

☒ Oral Presentation ☐ Poster ☐ Either Oral or Poster Presentation | Contact Email: [bonnie.lam@berkeley.edu](mailto:bonnie.lam@berkeley.edu)

**KEYWORD:** You are encouraged to choose one or two keywords. ☒ CEST agents ☐ Contrast Mechanism

☐ Tumor ☐ Stroke ☐ Neurology ☐ Body & MSK ☐ Standardization ☐ Novel Acquisition ☐ Machine Learning

**INTRODUCTION:** Over the last decade gene therapy has rapidly expanded to include in vivo somatic cell gene editing<sup>1</sup>, particularly the use of adeno-associated virus (AAV) vectors as delivery vehicles for gene editing machinery<sup>2</sup>. However, the reliance upon invasive biopsies to verify gene editing is a boundary to successful translation. CEST-MRI has been used to image the expression of genetically encoded reporter genes including the Lysine Rich Protein (LRP)<sup>3-5</sup>. In comparison to the 50-residue LRP, AAV2 capsids contain over 1,000 surface Lysine residues<sup>6</sup> that can potentially generate CEST contrast. We hypothesized that AAV2 capsids may generate endogenous CEST contrast similar to LRP. We tested this using NMR CEST under varying pH, density, biological transduction stage, across multiple serotypes, and in mixed biological media. Subsequent experiments determined the pH-dependent exchange rate and optimized CEST saturation schemes for AAV contrast detection at 7T.

**METHODS:** AAV Contrast at 800MHz: NMR-CEST experiments (Bruker 800MHz) were performed on AAV2 ( $5.23 \times 10^8$  viral genomes/ $\mu$ L) in solution at pH 7.0 and 37°C. Complete Z-spectra across a range of saturation powers (3-9 $\mu$ T) were serially acquired for all studies. MTR<sub>asym</sub> was assessed on AAV2 samples with varying capsid densities ( $5 \times 10^3$ - $5 \times 10^8$  vg/ $\mu$ L), pH values (4-7.5), and later multiple AAV serotypes (1, 5, 6, 7, 9). To test whether AAV2 generates CEST contrast during endosomal transport, HEK293T cells were transduced with AAV2 and then harvested at 0-, 30-, and 60-minutes following removal of viral media. Afterwards, endosomes were lysed, isolated, and buffered in solution for NMR-CEST experiments.

Exchange rate quantification: Four samples of AAV2 ( $5.26 \times 10^8$ vg/ $\mu$ L) were titrated to different pH values (5.8-6.9) prior imaging at 37° C. NMR-CEST Z-spectra were acquired at varying saturation powers (1-3  $\mu$ T) and subsequently fit with Bloch-McConnell equations for determining exchange rates of each sample.

Optimization at 7T: Phantoms containing AAV2 ( $5.26 \times 10^8$ vg/ $\mu$ L) were imaged at 7T with Z-spectra acquired following varying values for saturation B<sub>1</sub> (1-5  $\mu$ T), saturation pulse duration (11-54.8ms), and saturation duty cycle (0.6-0.85) across different combinations. CEST contrast was quantified by 2-pool Lorentzian fitting. To probe the impact of dilution in background tissue protein content, additional experiments were carried out on a phantom containing cell lysate (6.8mg protein) and AAV2 ( $5.26 \times 10^8$ vg/ $\mu$ L). Z-spectra were acquired following varying values for saturation B<sub>1</sub> (3-5  $\mu$ T), saturation pulse duration (27.4-54.8ms), and saturation duty cycle (0.7, 0.85) across all possible combinations. CEST contrast was quantified by 5-pool Lorentzian fitting (water, amine, amide, NOE, and AAV).

**RESULTS:** Water-suppressed NMR of AAV2 identified 3 potential groups of high-density protons at 0.6, 3.0, and 3.6ppm relative to water (Figure 1A) of which only the exchangeable protons at 0.6ppm generated significant CEST contrast (Figure 1B) across a range of saturation powers. CEST contrast of AAV2 at 0.6ppm correlated with capsid density and decreased with acidification. Similar CEST contrast was observed across other AAV serotypes. Quantification of viral titer and subsequent regression analysis revealed a positive linear correlation between CEST contrast and viral density. Fitting of Z-spectra at variable powers revealed an average exchange rate of approximately 1300Hz between pH 6-7. CEST contrast of AAV2 at 7T demonstrated a dependence upon saturation scheme parameters, but when optimized produced CEST contrast of 9-12% in phantoms (Figure 2). Dilution of AAV2 capsids in cell lysate altered the Z-spectral appearance and reduced CEST contrast of AAV2 to approximately 3.3%.

**DISCUSSION:** The results of this study reveal that AAV capsids generate endogenous CEST contrast around 0.6-0.8ppm. The most probable source of exchangeable protons is the conserved serine and threonine residues on the AAV capsid surface across serotypes. Based on the calculated exchange rates in the fast exchange regime, an optimized CEST saturation scheme generated robust CEST contrast in mixed biological media phantoms at 7T.

**CONCLUSION:** AAV2 viral capsids generates robust CEST contrast in vitro across a variety of chemical environments, concentrations, and saturation schemes. Additional experiments to explore the effectiveness of AAV2 viral capsids as an in vivo endogenous CEST contrast agent for gene therapy tracking is needed.

**ACKNOWLEDGMENTS:** NIH 1R01HL28592-01, Silvian Foundation Award, AHA 19TPA34850040, NIH UH2EB028908-02, DGE 2146752

**REFERENCES:** 1. Saha K, *et al.* Nature 2021;592:195-204. 2. Kotterman MA, *et al.* Annu Rev Biomed Eng 2015;17:63-89. 3. Gilad AA, *et al.* Nat Biotechnol 2007;25:217-9. 4. Farrar CT, *et al.* Radiology 2015;275:746-54. 5. Meier S, *et al.* Sci Rep 2018;8:4638. 6. Xie Q, *et al.* Proc Natl Acad Sci 2002;99:10405-10.

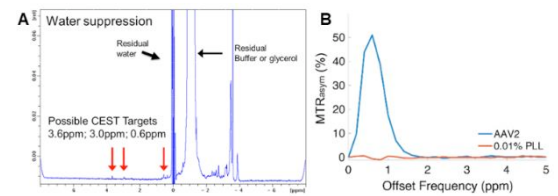


Figure 1. (A) Conventional NMR of AAV2 identifies potential CEST targets (B) NMR-CEST of AAV2 reveals high contrast

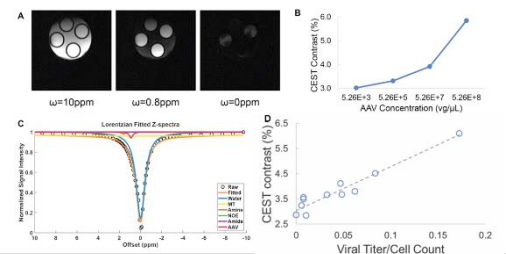


Figure 2. CEST-MRI of AAV2 phantoms (A) phantom scan images (B) CEST contrast at different concentrations (C) Lorentzian-fitted Z-spectrum (D) CEST contrast correlation with viral titer/cell count



## Simultaneous evaluations of pH and enzyme activity with a CEST MRI contrast agent

Chathuri J. Kombala,<sup>1,2</sup> Sanjaya D. Lokugama,<sup>1,2</sup> Aikaterini Kotrotsou,<sup>3</sup> Tianzhe Li,<sup>2</sup> Alyssa C. Pollard,<sup>2,3</sup> Mark D. Pagel<sup>2</sup>

<sup>1</sup> Department of Chemistry and Biochemistry, University of Arizona, Tucson, AZ, USA

<sup>2</sup> Department of Cancer Systems Imaging, University of Texas MD Anderson Cancer Center, Houston, TX, USA

<sup>3</sup> Department of Chemistry, Rice University, Houston, TX, USA

✉ Poster | Contact Email: [mdpagel@mdanderson.org](mailto:mdpagel@mdanderson.org)

KEYWORD: CEST agents

**INTRODUCTION:** The extracellular tumor microenvironment of many solid tumors has high acidosis and high protease activity. Simultaneously assessing both characteristics may improve diagnostic evaluations of aggressive tumors and the effects of anti-cancer treatments. Noninvasive imaging methods have previously been developed that measure extracellular pH or can detect enzyme activity using Chemical Exchange Saturation Transfer (CEST) MRI. Herein, we developed a single hybrid CEST agent that can simultaneously measure pH and evaluate protease activity using a combination of dual-power acidoCEST MRI and catalyCEST MRI.

**METHODS:** We synthesized the agent in 5 steps with a 24% overall yield. We recorded CEST spectra at 1 and 4  $\mu$ T saturation power. We compared CEST amplitudes at 9.2 ppm to measure pH, and we detected the disappearance of CEST signal at 5.0 ppm to monitor enzyme cleavage. We modeled the effect of enzyme cleavage on the pH measurement, to show that pH and enzyme cleavage can be independently measured. We performed Michaelis-Menten enzyme kinetics studies by monitoring the rate of the disappearance of the CEST signal at 5.0 ppm after adding cathepsin B to 10–40 mM of agent at pH 6.6–7.4. We performed similar enzyme kinetics studies using LC-MS to monitor the reactant and product.

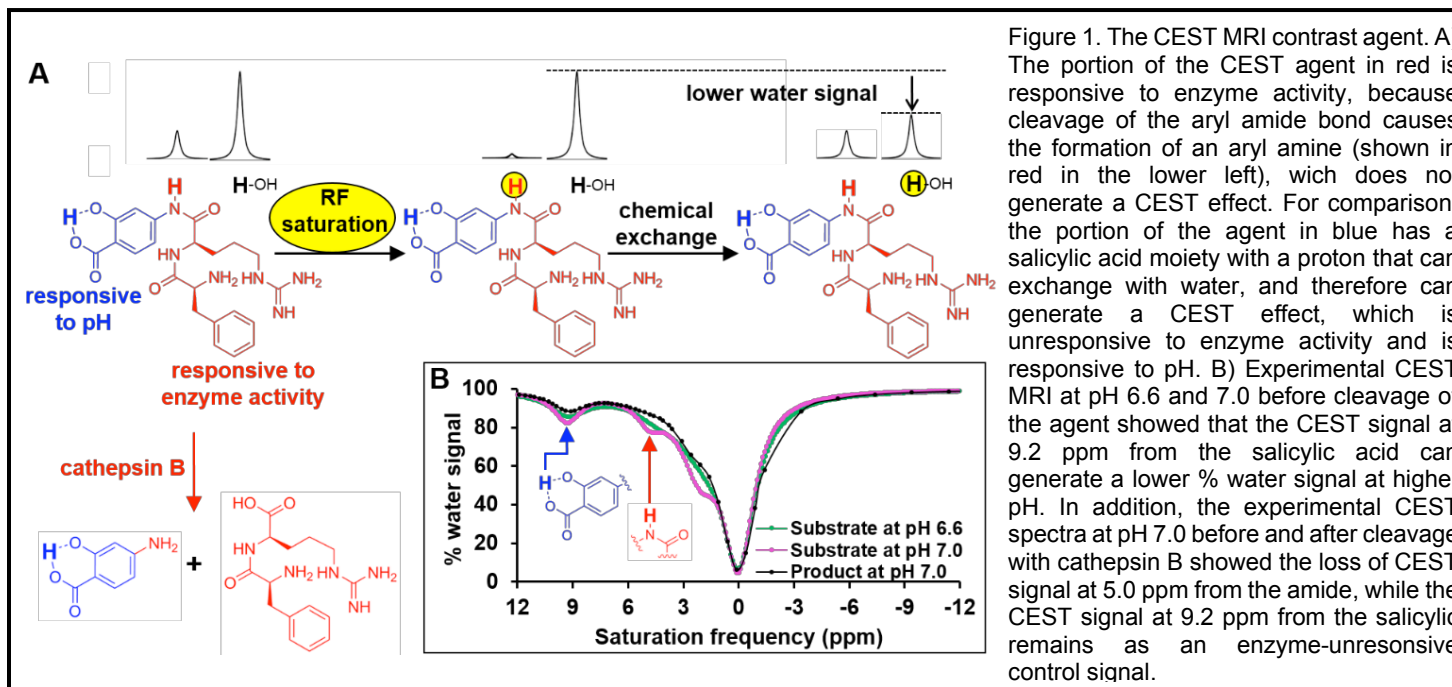
**RESULTS:** The CEST signal at 9.2 ppm at 1 and 4  $\mu$ T saturation powers could be used to measure pH with a precision of 0.029 pH units. Enzyme cleavage generated a product that has a different pH-dependence, but a modeling analysis showed that pH and enzyme activity can still be independently evaluated. The CEST signal at 5.0 ppm from the aryl amide disappeared after the agent was treated with cathepsin-B, while the CEST signal at 9.2 ppm remained, indicating that the agent could detect protease activity through the amide bond cleavage. Michaelis-Menten kinetics studies with catalyCEST MRI demonstrated that the binding affinity (as shown with the Michaelis constant  $K_M$ ), the catalytic turnover rate ( $k_{cat}$ ), and catalytic efficiency ( $k_{cat}/K_M$ ), were each higher for cathepsin B at lower pH.

**DISCUSSION:** The  $k_{cat}$  rates measured with catalyCEST MRI were lower than the comparable rates measured with LC-MS, which reflected a limitation of inherently noisy and relatively insensitive CEST MRI analyses. Although this level of precision limited catalyCEST MRI to semi-quantitative evaluations, these semi-quantitative assessments of high and low protease activity still had value by demonstrating that high acidosis and high protease activity can be used as synergistic, multi-parametric biomarkers.

**CONCLUSION:** These assessments of high and low protease activity at different pH values demonstrated that high acidosis and high protease activity can be used as synergistic, multi-parametric biomarkers.

**ACKNOWLEDGMENTS:** CJK was supported by NIH T32 GM008804. ACP was supported by NIH F31 CA247338. Support was provided through NIH R21 EB027197, R01 CA231513 and P30 CA016672. The authors thank Dr. Brian Engel at MDACC for LC-MS technical support. We also thank the Small Animal Imaging Facility at MDACC for their support.

**REFERENCES:** 1. Kombala CJ, Lokugaman SD, Kotrotsou A, Li T, Pollard AC, Pagel MD. Simultaneous evaluations of pH and enzyme activity with a CEST MRI contrast agent. ACS Sensors, 2021;6:4535-4544.



## Bioconjugation of Lactate CEST-Sensors to Virus Like Particles

Laurel M. Hagge<sup>1</sup>, Sara Chirayil<sup>2</sup>, Jeremiah J. Gassensmith,<sup>1</sup> and A. Dean Sherry<sup>1,2</sup>

<sup>1</sup>University of Texas at Dallas, Richardson, Texas, US <sup>2</sup>Advanced Imaging Research Center, University of Texas Southwestern Medical Center, Dallas, Texas, US

☒ Apply Travel Fund

☐ Oral Presentation ☐ Poster ☒ Either Oral or Poster Presentation |

Contact Email: Laurel.Hagge@utsouthwestern.edu

KEYWORD: You are encouraged to choose one or two keywords.

☒ CEST agents ☐ Contrast Mechanism

☒ Tumor ☐ Stroke ☐ Neurology ☐ Body & MSK ☐ Standardization ☐ Novel Acquisition ☐ Machine Learning

**INTRODUCTION:** Excess production of lactate from glucose is a hallmark of cancer. Most lactate is produced in glycolysis by reduction of pyruvate to L-lactate but D-lactate can also be generated from glucose via the lesser known methylglyoxal (MG) pathway. A recent report has shown that some cancer cells also produce D-lactate from glucose via the MG pathway (**Fig. 1A**). Since the stereoisomers of lactate cannot be distinguished by conventional <sup>1</sup>H NMR spectroscopy, a chiral NMR shift reagent (SR) was used to resolve the CEST signals of D- and L-lactate (**Fig. 1C**).<sup>1</sup> The goal of this project is to develop a nanoparticle system that can localize large amounts of this chiral SR into the extracellular space of tumors to allow real-time monitoring of D- versus L-lactate production by CEST. Our approach is to attach a large number of SR's to tobacco mosaic virus (TMV) particles known to localize in tumors. (**Fig. 1B**).

**METHODS:** TMV contains over 2,000 coat proteins with tyrosine residues that can be functionalized with alkynes and subsequently modified using conventional click chemistry. The original synthesis DO3A-tris-L-alanyl amide was modified to include an azide moiety on one of the three alanyl side-chains (**Fig 2**). The target ligand was synthesized and characterized by standard NMR and MS methods. The Yb<sup>3+</sup> complex was prepared ready for attachment to TMV nanoparticles (in progress).

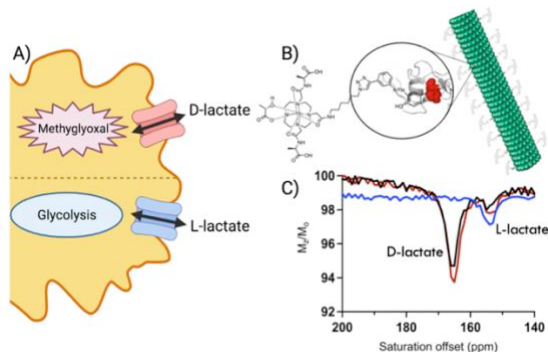


**Fig 1. A)** Glucose can produce both L-lactate and D-lactate in many cells, include cancer cells. **B)** A lactate SR can be attached to TMV nano-rods using simple click chemistry and using to localize high concentrations of the SR in the extracellular space of tumors. **C)** the CEST spectra of D- and L-lactate are fully resolved well downfield of bulk water protons.<sup>1</sup>

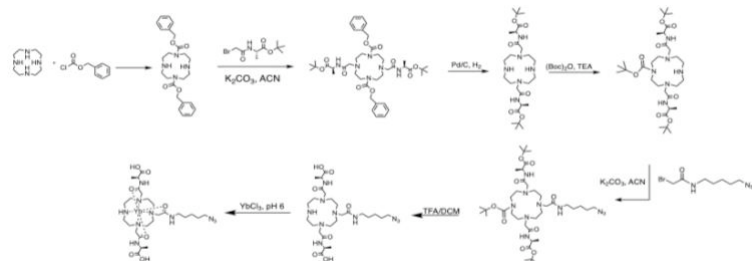


**Fig 2.** Scheme for synthesis of the chiral SR for attachment to TMV via a side-chain azide group.

incubated with a modified buffer containing only 5 mM glucose and glutamine for sustained growth. After an additional 4 h, the supernatant was collected, freeze-dried, and dissolved in 0.4 mL of water containing 5 mM Yb<sub>3</sub>. The resulting <sup>1</sup>H NMR and CEST spectra (not shown) indicate that both cell lines make appreciable D-lactate in an apparent *GLO1* expression-dependent manner (D-lac/L-lac = 0.63 in H1648 cells and 0.26 in H1395 cells).

**DISCUSSION:** The chiral Yb agent was successfully used *in vitro* to quantify production of D- and L-lactate in cancer cells grown tissue culture. We have now turned our attention to conjugation of several thousand copies of the SR to single TMV particles which should accumulate only in extracellular spaces of tumors to allow monitoring of real-time production of D- and L-lactate by CEST.

**CONCLUSION:** The MG pathway is considered a bypass of the glycolytic pathway and the toxic product, methyl glyoxal, is thought to cause mutagenesis, oxidative stress, and increased metastatic potential.<sup>7</sup> Hence, production of D-lactate from this metastatic intermediate is likely protective. Overproduction of lactate is a key identifier of cancer types and can be vital when diagnosing the progression of cancer but the role D-lactate plays in cancer metabolism is unclear. As written in one review, “D-lactate is at the crossroad of the eternal youth of cancer” and “further discovery could lead to novel metabolic therapies”.<sup>7</sup>

**REFERENCES:**[1] Suh, E.H., *et al. Cancer Metab* 9, 38 (2021). [2] L. Zhang, *et al. Accounts of Chemical Research*. 2003. 36(10). [3] Lin RD, Steinmetz, NF. *Nanoscale*. 2018; 10(34):16307-13. [4] Chariou, PL, *et al. J Phys Chem B*. 2016; [5] 120(26):6120-6129. Antognelli C, *et al. BMC Cancer*. 2009;9(1):115. [6] Thornalley PJ, *et al. Semin Cell Dev Biol*. 2011;22(3):318–25.[7] L. de Bari, *et al. Ageing Research Reviews* 53 (2019) 100915

# Determining the optimal saturation time for a CEST experiment

Julius Chung and Tao Jin

Department of Radiology, University of Pittsburgh, Pittsburgh, PA 15203

✉ Apply Student/Postdoc Travel Fund, ✉ Oral Presentation Contact Email: juc98@pitt.edu

KEYWORD: ✉ CEST agents ✉ Contrast Mechanism

**INTRODUCTION:** CEST is usually measured by long saturation pulses. When high saturation power is used, the larger MT effect and direction water saturation reduces the optimal saturation duration ( $T_{sat}$ ) to maximize CEST contrast (e.g., the difference between healthy and diseased tissues). The optimization of  $T_{sat}$  in *in vivo* studies can be achieved by comparing the CEST contrast measured with varied  $T_{sat}$ , but the result is affected by contrast to noise and can be time-consuming. Here we propose a method to determine optimal  $T_{sat}$  using the steady state signal or the asymmetry of the MT effect.

**METHODS:** Theory: Under a saturation pulse with a power of  $B_1$  and duration of  $T_{sat}$ , the normalized signal is 1:

$$S_{sat}/S_0 = \left(1 - \frac{R_{1\rho} \cos^2 \theta}{R_{1\rho}}\right) \cdot e^{-R_{1\rho} T_{sat}} + \frac{R_{1\rho} \cos^2 \theta}{R_{1\rho}} \quad [1]$$

where  $R_{1\rho}$  is the spin-lattice relaxation rate in the rotating frame. With a small difference in  $R_{1\rho}$ , the difference in  $S_{sat}$  is:

$$\frac{\Delta S_{sat}}{S_0} = -\left\{\left[\left(1 - \frac{R_{1\rho} \cos^2 \theta}{R_{1\rho}}\right) \cdot T_{sat} - \frac{R_{1\rho} \cos^2 \theta}{R_{1\rho}^2}\right] \cdot e^{-R_{1\rho} T_{sat}} + \frac{R_{1\rho} \cos^2 \theta}{R_{1\rho}^2}\right\} \cdot \Delta R_{1\rho} \quad [2]$$

Denote the steady state signal  $SS = R_{1\rho} \cos^2 \theta / R_{1\rho}^2$ , the optimal  $T_{sat}$  satisfies  $\frac{\partial \Delta S_{sat}}{\partial T_{sat}} = 0$ , which leads to

$$T_{sat_{optimal}} = \frac{1}{R_{1\rho} - R_{1\rho} \cos^2 \theta} = \frac{SS}{1 - SS} \cdot \frac{T_1}{\cos^2 \theta} \quad [3]$$

The SS can be obtained by using a long pulse or by monoexponential fitting to Eq. [1]. If  $\cos^2 \theta \approx 1$ , the  $T_{sat_{optimal}}$  equals  $T_1$  for  $SS = 1/2$  and  $T_1/2$  for  $SS = 1/3$ . Note that besides the CEST effect, in Eq. [2] the source of  $\Delta R_{1\rho}$  can also apply to other effects such as NOE or asymmetry of the intrinsic MT. Thus,  $T_{sat_{optimal}}$  can also be obtained by optimizing the asymmetry of the MT (if significant for the selected  $B_1$ ), without measuring a steady state signal and  $T_1$ .

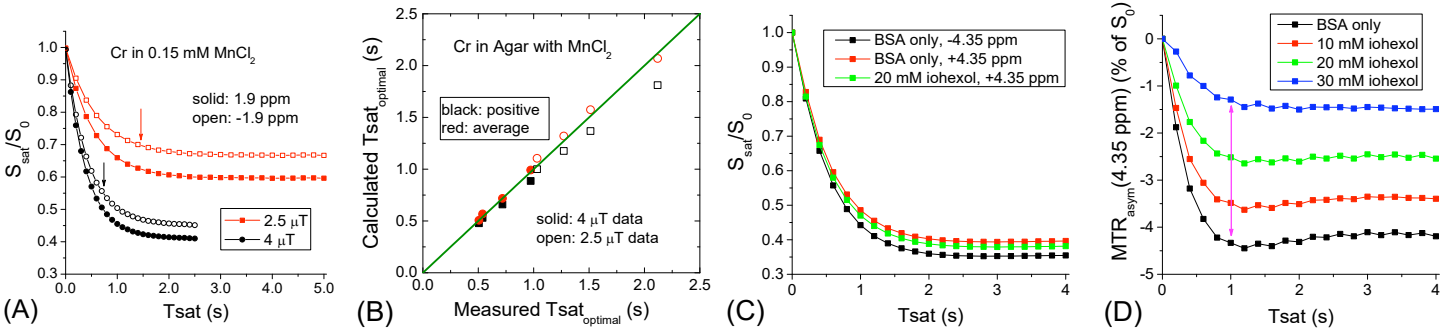
Experiments: Two sets of phantom experiments were performed at 9.4 T at room temperature.

(1). 40mM of creatine were prepared in 4 phantoms with varied concentrations of agar (1.5% to 3%) and  $MnCl_2$  (0.1 mM to 0.25 mM) to modulate the MT effect and  $T_1$  value. Saturated signals were measured with varied  $T_{sat}$  for two RF powers of 2.5  $\mu T$  and 4  $\mu T$ , at offsets of 1.9 and -1.9 ppm. (2). 10, 20 and 30 mM of iohexol were added to 15% bovine serum albumin (BSA), and the phantoms were heated to 90°C for 20 minutes to denature the BSA. Saturated signals were measured with varied  $T_{sat}$  for 2.5  $\mu T$  at offsets of 4.35 ppm and -4.35 ppm.

## RESULTS AND DISCUSSIONS:

Fig. A shows the saturated signal in one of the Cr phantoms for both  $B_1$  of 2.5  $\mu T$  and 4  $\mu T$ . With higher  $B_1$ , the steady state signal is lower, and the maximal CEST contrast between  $\pm 1.9$  ppm appears at a shorter  $T_{sat}$  (indicated by the arrows). Fig. B compares the measured  $T_{sat_{optimal}}$  and the  $T_{sat_{optimal}}$  calculated using Eq. [3] for the 4 phantoms. The black symbols indicate the  $T_{sat_{optimal}}$  calculated using the SS values at the guanidyl frequency of +1.9 ppm. Despite overall agreement, the calculated  $T_{sat_{optimal}}$  values are slightly smaller than the measured values, and the deviation increases with CEST effect magnitude. This is because Eq. [2] assumes  $\Delta S_{sat} \ll 1$ , but the CEST effects in the phantoms are not small (3% to ~10%). When the average value of SS at +1.9 ppm and -1.9 ppm was used in Eq. [3], the agreement is improved (red symbols).

Unlike agar phantoms, there is intrinsic MT asymmetry in the denatured BSA phantoms (Fig. C). Using the average SS of 0.37 and the measured  $T_1$  of 1.95 s for the BSA-only phantom, Eq. [3] yields an optimal  $T_{sat}$  of 1.14 s, similar to the measured maximum at  $T_{sat}$  of ~1.1 s (black, Fig. D). The addition of iohexol reduces the signal at +4.35 ppm (Fig. C), leading to higher  $MTR_{asym}$  values in Fig. D. The contrast between the phantoms with and without iohexol is maximized at  $T_{sat} = 1.0$  s (pink arrow, D), which is in good agreement with the calculated  $T_{sat_{optimal}}$  of 1.14 s.



**CONCLUSION:** We reported a method to determine the optimal  $T_{sat}$  based on the steady state signal or the intrinsic MT asymmetry of healthy tissue or a baseline before injection of contrast agent. This approach may simplify the optimization of  $T_{sat}$  for CEST experiments with relatively high saturation powers.

**REFERENCES:** 1. Jin T, *et al.* Magn Reson Med 2012;68:1056.

# High rotating frame relaxation MRI mapping for detecting ischemia in rats

Eleni Demetriou<sup>1,5</sup>, Silvia Mangia<sup>2</sup>, Hanne Laakso<sup>4</sup>, Timo Liimatainen<sup>3</sup>, Olli Gröhn<sup>4</sup>, Shalom Michaeli<sup>2</sup>, Xavier Golay<sup>1</sup>

<sup>1</sup>Brain repair and Rehabilitation, Institute of Neurology, University College London, UK

<sup>2</sup>Center for Magnetic Resonance Research, University of Minnesota, Minneapolis, MN, USA

<sup>3</sup> Research Unit of Medical Imaging, Physics and Technology University of Oulu, Oulu

University Hospital <sup>4</sup>A. I. Virtanen Institute for Molecular Sciences, University of Eastern

Finland, Kuopio, Finland, <sup>5</sup>Advanced imaging research centre, UTSW, Dallas, Texas

**Introduction:** The goal of this work is to evaluate the novel MRI technique entitled Relaxation Along a Fictitious Field (RAFF) in the rotating frame of rank  $n$  (RAFF $n$ , with  $n=5$ ) in its ability to detect ischemia, specifically when tuning the sensitivity of RAFF5 to exchange processes of amide protons (i.e. the periodicity of irradiation of RAFF5 was tuned to the 1.2 ppm chemical shift difference between amide protons (at 3.5 ppm) and water (at 4.7 ppm)) (1), (2). Enhanced exchanged-induced relaxation was demonstrated by theoretical modelling through the generation of side bands (14) by the instantaneous  $\pi$  shift of effective field that occurs between  $P$  and  $P^{-1}$  (and between  $P_{\pi}$  and  $P_{\pi}^{-1}$ ) of the  $PP^{-1}P_{\pi}P_{\pi}^{-1}$ -packet duration ( $T_p$ ), i.e., at  $T_p/4$  and  $3/4T_p$  (3), with an overall periodicity of  $T_p/2$ . A significant advantage of this technique is that it comprises both  $T_{1\rho}$  and  $T_{2\rho}$  relaxation pathways while the sine/cosine amplitude and frequency modulated pulses yield low power deposition, which was found to be 61% as compared to the RF power of a CW spin locking pulse with matched duration and  $\omega_1^{max}$  settings (3).

**Methods:** Experiments with Bovine Serum Albumin (BSA) at different concentrations, pH values and temperatures were conducted for validation purposes. Animals ( $N=7$ ) were scanned twice, before (within 48 hours) and 24-hour post-stroke induction. All the experiments were performed on a 9.4T Agilent MRI scanner and images were acquired in a single slice (thickness=2 mm), centred on thalamus. CEST measurements were acquired using a gradient-echo sequence (matrix: 64x64, TR=2.11 ms, TE=1.07 ms, FOV=20x20 mm<sup>2</sup>) with a saturation train of Gaussian pulses at 0.6  $\mu$ T ( $n=80$ , pulse duration=50 ms, flip angle=360°, 90% duty cycle). RAFF5 measurements were obtained using a train of RAFF5 pulses ( $N=0, 20, 50, 100, 150, 250, 350, 400, 450, 500$  pulses) with pulse parameters  $\omega_{1max} = 244$  Hz and pulse duration  $T_p = 4.526$  ms followed by a single shot spin echo EPI read out with parameters: TR=3 s, TE=25.5 ms, slice thickness=2 mm, FOV=20x20 mm<sup>2</sup>, matrix size=64x64. T1 and T2 maps were also acquired as described previously (4).

**Results:** Figure 1 displays the signal intensity during RAFF5 pulse trains acquired from phantoms with 1.25 % of BSA at pH =6.1, 6.4, 6.8, 7.0 and 7.4 and at various temperatures from 23 °C to 37 °C. Table 1 shows the mean  $\pm$  std of  $T_{RAFF5}$  for all the measured temperatures and pH values. Table 2 shows the mean  $\pm$  std of imaging metrics estimated as relative % difference between stroke lesion and contralateral side: (Stroke lesion - Contralateral region)/ Contralateral region) \* 100%. It can be seen that  $T_2$  and  $T_{RAFF5}$  exhibit the greatest sensitivity to stroke, by detecting 69% ( $p=0.001$ ) and 63% differences ( $p=0.002$ ), respectively, in stroke lesion as compared to the contralateral side, and by detecting 52% ( $p=0.001$ ) and 54% ( $p=0.003$ ) changes, respectively, post-stroke vs baseline in the stroke lesion. Sensitivities of RAFF5 and  $T_2$  for both changes and differences were similar. All other metrics had statistically significant lower sensitivities as compared to RAFF5. Figure 2 shows the measured  $T_{RAFF5}$  maps at baseline and 24h post-stroke from all investigated rats. **Discussion:** The present study shows great promise of RAFF5 to detect stroke-related tissue changes in vivo as compared to  $T_1$ , MTRasym and APT\*, while its sensitivity was similar to  $T_2$  mapping. During stroke an increase in  $T_1$ ,  $T_2$ , and  $T_{RAFF5}$  was observed, accompanied by a reduction in APT\* and MTR asymmetry maps. The area of tissue abnormalities delineated by APT\* and MTR asymmetry has a different size than by RAFF5,  $T_1$  and  $T_2$  (lesion



# 31ParaCEST: 31P MR-CEST Imaging based on the formation of ternary adduct between HPO<sub>4</sub><sup>2-</sup> and Eu(III)DO3A complexes

Giulia Vassallo, Francesca Garelo Silvio Aime, Enzo Terreno and Daniela Delli Castelli <sup>1</sup>

<sup>1</sup> Department of Molecular Biotechnology and Health Science, Turin, Italy

☐ Oral Presentation ☒ Poster ☐ Either Oral or Poster Presentation | [daniela.dellicastelli@unito.it](mailto:daniela.dellicastelli@unito.it)

**KEYWORD:** You are encouraged to choose one or two keywords. ☒ CEST agents ☐ Contrast Mechanism

☐ Tumor ☐ Stroke ☐ Neurology ☐ Body & MSK ☐ Standardization ☒ Novel Acquisition ☐ Machine Learning

## INTRODUCTION:

The development of the field of CEST contrast agents is hampered by the sensitivity issue. Conventional CEST agents based on <sup>1</sup>H detection rely on to the amplification effect associated to the saturation transfer to the much more abundant bulk water protons signal. The drawback associated to the use of such a huge signal is to reduce the sensitivity threshold that per single mobile proton is in the millimolar range as it depends on the molar fraction of the exchanging protons. The use of nuclei other than protons, exploiting much larger molar ratios, as a consequence of the decreased concentration of the bulk pool, is expected to proportionally decrease the sensitivity threshold, thus allowing the detection of nuclei present in concentrations much lower than millimolar. Bar-Shir and coworkers demonstrated the applicability of this concept by lowering down the sensitivity threshold through heteronuclear detection [1]. They reported a 900-fold signal amplification in the 19F-MRI-CEST detection of an inhalable fluorinated anesthetic. With this approach the required variation of the chemical shift was obtained by designing host-guest supramolecular non-covalent interactions with macrocyclic hosts. This approach led to an increase in CEST sensitivity (per nucleus) of 3 orders of magnitude, enabling a micromolar detection of the saturated pool, due to the reduction in the concentration of the bulk site. Unfortunately this method has a poor clinical traslability owing to the large amount of anesthetic to be inhaled. We thought that an improvement might be represented upon using the <sup>31</sup>P detection as the endogenous inorganic phosphate (Pi) has a sufficient concentration to behave as bulk pool. To create the condition to detect <sup>31</sup>P-MRI-CEST of Pi (*i.e.* to have two exchangeable sites with different chemical shifts), we exploited the well-established interaction between Pi and paramagnetic lanthanide complexes with coordinatively unsaturated ligands [2]. The exchange between free and Ln bound position of Pi is expected to match the condition for CEST detection ( $\Delta\omega > k_{ex}$ ) due to the strong lanthanide-induced paramagnetic effect at the metal coordination site (Pi<sup>bound</sup>). **METHODS:** A solution containing Eu(III)DO3A 40  $\mu$ M and H<sub>2</sub>PO<sub>4</sub><sup>-</sup> 10 mM (pH 7.0) was prepared. Then a high resolution <sup>31</sup>P NMR spectrum and a <sup>31</sup>P Z-spectrum at 14 T were acquired on this sample. Next, samples where the concentration of EuDO3A was systematically decreased while keeping constant H<sub>2</sub>PO<sub>4</sub><sup>-</sup> concentration were investigated. The samples were analyzed on a bruker 7T pharascan equipped with a <sup>31</sup>P micro imaging coil. MRS and <sup>31</sup>P CEST images were acquired. Experiments on cells were performed by labelling TS/A (breast cancer model) with EuDO3A by following the hypotonic swelling procedure.

**RESULTS:** The Z-spectrum centered at the Pi frequency, displayed a sharp CEST peak at -134 ppm, highlighting the occurrence of a large ST effect (*ca.* 70 %) caused by the saturation of the Pi<sup>bound</sup> pool (undetectable in the <sup>31</sup>P NMR spectrum). Then, the CEST effect was measured upon lowering the molar fraction of the Pi<sup>bound</sup> over Pi<sup>free</sup> (*i.e.* decreasing the concentration of the paramagnetic complex) and detection sensitivity of 2.5  $\mu$ M of Eu-DO3A was found assuming a ST threshold of 5 %. <sup>31</sup>P MR-CEST images and <sup>31</sup>P MR-CEST localized spectroscopy were acquired on a phantom containing 40  $\mu$ M solution of Eu-DO3A with 10 mM of HPO<sub>4</sub><sup>2-</sup> at pH 7.0 on a 7 T preclinical scanner. The difference in the intensity of the <sup>31</sup>P signal in the two images is clearly visible. A ST% of 50% was measured. The method was then tested in cellular imaging applications selecting TS/A murine breast cancer cells as a model. An amount of EuDO3A 120 $\mu$ M x cell was determined ICP-MS analyses. Labeled cell pellets containing about 2x10<sup>6</sup> cells underwent the Z spectra analyses. An ST% of 20% was measured.

**DISCUSSION:** The obtained results showed that a very low amount of EuDO3A (2.5  $\mu$ M) is sufficient to generate a detectable CEST signal in <sup>31</sup>P spectroscopy and imaging. This allow to forseen applications of this method whenever very low concentration of contrast agents should be detected such as cell tracking experiment. The change of nuclei from <sup>1</sup>H to <sup>31</sup>P CEST make it feasible to detect the substrate of interest at concentration as low as micromolar. This means that a three fold increase in ParaCEST sensitivity can be achieved in respect to the currently used proton exchange containing systems.

**CONCLUSION:** We have reported the use of a EuDO3A complex as the first <sup>31</sup>P based ParaCEST agent. The CEST sensitivity was proven to be three order of magnitude larger with respect to ParaCEST agents based on <sup>1</sup>H detection. It is straightforward to say that the advantage of reducing the bulk concentration to increase the molar fraction has the disadvantage of reducing the NMR signal intensity of the detected signal. From the MRI point of view this means longer acquisition times. However, by performing MRS acquisitions in selected voxel, the experiment can be carried out in few minutes. Given the large sensitivity gain we thought that a possible application could be in the field of Cell tracking that requires to be less invasive as possible in loading the cells with the contrast agent.

## REFERENCES:

1. R. Shusterman-Krush et al Angew.Chem.Int.Ed.2021,60,15405–15411.
2. Z.M Bhujwalla et al BshJournal of Cancer, 1998, 78(5), 606-611

# Effect of hyperoxia on dynamic glucose enhanced MRI in mouse brain at 3T

Jianpan Huang<sup>1#</sup>, Zilin Chen<sup>1#</sup>, Peter C. M. van Zijl<sup>2,3</sup>, Lok Hin Law<sup>1</sup>, Rohith Saai Pemmasani Prabakaran<sup>1,4</sup>, Se Weon Park<sup>1,4</sup>, Jiadi Xu<sup>2,3</sup>, Kannie W. Y. Chan<sup>1,3,4,5\*</sup>

<sup>1</sup> Department of Biomedical Engineering, City University of Hong Kong, Hong Kong, China; <sup>2</sup> F.M. Kirby Research Center for Functional Brain Imaging, Kennedy Krieger Research Institute, Baltimore, MD, USA; <sup>3</sup> Russell H. Morgan Department of Radiology and Radiological Science, The Johns Hopkins University School of Medicine, Baltimore, MD, USA; <sup>4</sup> Hong Kong Centre for Cerebro-Cardiovascular Health Engineering (COCHE), Hong Kong, China; <sup>5</sup> City University of Hong Kong Shenzhen Research Institute, Shenzhen, China; # Equally contributed; \* Corresponding Author.

☑ Apply Student/Postdoc Travel Fund

☐ Oral Presentation ☐ Poster ☑ Either Oral or Poster Presentation | Contact Email: [jp.huang@cityu.edu.hk](mailto:jp.huang@cityu.edu.hk)

**KEYWORD:** You are encouraged to choose one or two keywords. ☐ CEST agents ☐ Contrast Mechanism

☐ Tumor ☐ Stroke ☑ Neurology ☐ Body & MSK ☐ Standardization ☐ Novel Acquisition ☐ Machine Learning

**INTRODUCTION:** Inhaled oxygen (O<sub>2</sub>) has been used as a BOLD/CBF MRI contrast agent for decades as it has advantages of fast clearance and few contraindications.<sup>1</sup> Dynamic glucose enhanced (DGE) MRI is capable of noninvasively mapping cerebral glucose delivery and uptake using natural D-glucose as a tracer,<sup>2-9</sup> based on the mechanism of chemical exchange saturation transfer (CEST).<sup>10-12</sup> However, the influence of altered oxygen levels on DGE signal remains unknown currently. In this study, we investigated glucose response in brain parenchyma and cerebrospinal fluid (CSF), to normoxia (NO) and hyperoxia (HO) using on-resonance variable delay multi-pulse (onVDMP)<sup>13</sup> based DGE MRI at 3T.

**METHODS:** Six wild type (WT) mice (C57BL/6, female aged 2-3 months old) were used in this study. All MRI experiments were performed on a horizontal bore 3T Bruker Biospec system (Bruker, Germany). DGE data of each mouse under normoxia (air with 21% O<sub>2</sub>) or hyperoxia (concentrated air with 93% O<sub>2</sub>) was acquired in two independent experiments. The DGE MRI sequence was an onVDMP module followed by a RARE readout.<sup>7,8</sup> The onVDMP module consisted of a train of binomial pulses (bp) with a peak power of 3.1  $\mu$ T and a duration of 7.5 ms (15 ms for a bp pair). The number of bp pairs was set to 4 (60 ms) for parenchymal imaging and to 60 (900 ms) for CSF imaging.<sup>7</sup> Other parameters were as followings: TR=2.5 s, TE=5 ms, RARE factor=32, slice thickness=2 mm, matrix size=96 $\times$ 96 and FOV=18 $\times$ 18 mm<sup>2</sup>. Thus, the time resolution of an image pair (parenchymal and CSF images) was 15 s. The total imaging time per DGE acquisition was 55 min (220 image pairs). A bolus of 0.15-ml filtered 50% w/w D-glucose was injected into mouse body through the tail vein from 8<sup>th</sup> to 9<sup>th</sup> min. The area under curve (AUC) normalized with data points was used to assess the DGE results.<sup>2,3</sup>

**RESULTS & DISCUSSION:** For the parenchymal DGE results, an initially rapid enhancement (likely vascular) followed by a fast decrease and gradual elevation to steady state was observed under NO and HO (Figs. 1A,C,E). For the CSF DGE results, the initial enhancement quickly reached a maximum and then gradually washed out (Figs. 1B,D,F). The parenchymal DGE NO group signal change was significantly higher than that for HO (Fig. 2, 2.79 $\pm$ 0.39% versus 1.67 $\pm$ 0.28%, P=0.005), while the averaged CSF DGE NO and HO curves showed comparable amplitude (4.41 $\pm$ 6.58% versus 6.33 $\pm$ 3.26%, P=0.534) (Figs. 1E-F). We speculated that this difference could be related to the vasoconstriction caused by the hyperoxia, as the percentage change

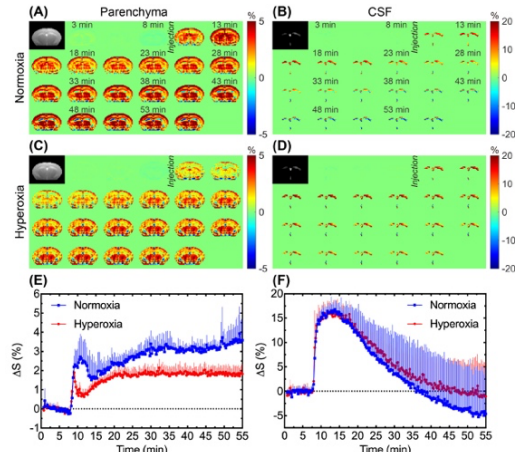


**Fig. 1.** DGE results of (A, C, E) Parenchymal and (B, D, F) CSF under normoxia and hyperoxia.

the vasoconstriction caused by the hyperoxia, as the percentage change  $([2.79-1.67]/2.79 \times 100\% = 40\%)$  was comparable to previously reported relative reduction (33%, from 53.6 to 36.1 ml $\cdot$ 100g<sup>-1</sup> $\cdot$ min<sup>-1</sup>) of global cerebral blood flow (CBF) from normoxia (21% O<sub>2</sub>) to hyperoxia (100% O<sub>2</sub>).<sup>14</sup> In addition, the T<sub>2</sub> of blood is increased, causing a narrowing of the blood Z-spectrum and an apparent reduction of the CEST effect. The changes may give an impression of the blood contribution to the CEST DGE effect, but this has to be further investigated.

**Fig. 2.** AUC results (n = 6) for (A) parenchyma and (B) CSF.

**CONCLUSION:** We performed DGE experiments under normoxia and hyperoxia on the same mouse. Significantly higher signal change under normoxia than under hyperoxia was observed in parenchyma but not in CSF, not unexpected in terms of the known BOLD effect when CBF changes.

**ACKNOWLEDGMENTS:** RGC: 11102218, PDFS2122-1S01; CityU: 7005210, 7005433, 9680247, 9667198 and 9609307; NSFC: 81871409.

**REFERENCES:** 1. Bulte DP, *et al.* J Cereb Blood Flow Metab 2007;27:69. 2. Xu X, *et al.* Magn Reson Med 2015;74:1556. 3. Xu X, *et al.* Tomography 2015;1:105. 4. Knutsson L, *et al.* Tomography 2018;4:164. 5. Schuenke P, *et al.* Magn Reson Med 2017;78:215. 6. Jin T, *et al.* J Cereb Blood Flow Metab 2018;38:869. 7. Huang J, *et al.* Sci Adv 2020;6:eaba3884. 8. Chen L, *et al.* J Cereb Blood Flow Metab 2021;41:1013. 9. Knutsson L, *et al.* NMR Biomed 2022;in press. 10. Chan KWY, *et al.* Magn Reson Med 2012;68:1764. 11. Van Zijl PCM, *et al.* Magn Reson Med 2011;65:927. 12. Walker-Samuel S, *et al.* Nat Med 2013;19:1067. 13. Xu J, *et al.* Magn Reson Med 2017;77:730-739. 14. Floyd TF, *et al.* J Appl Physiol 2003;95:2453.

**Creatine Chemical Exchange Saturation Transfer (CrCEST) MRI Reproducibility in healthy adults at 3T**  
Kasturee Chakraborty, Zane Coleman, Ayaz Khan, Shubo Wang, Pat Hanby, Donald Wallace, Zoltan Patay and Puneet Bagga  
*Diagnostic Imaging, St. Jude Children's Research Hospital, Memphis, TN, United States*

☑ Apply Student/Postdoc Travel Fund ☑ Either Oral or Poster Presentation |

Contact Email: [kasturee.chakraborty@stjude.org](mailto:kasturee.chakraborty@stjude.org)

KEYWORD: ☑ CEST agents

### INTRODUCTION:

Oxidative phosphorylation (OXPHOS) plays an essential role during muscle metabolism. Phosphocreatine (PCr) converts into creatine (Cr) to support ATP synthesis during OXPHOS. This conversion is usually measured using  $^{31}\text{P}$  MRS but has a limited spatial resolution. A complementary method to  $^{31}\text{P}$  MRS is CrCEST MRI which can perform muscle group specific estimation of relative free Cr concentrations with high spatial resolution. This technique can be used as an important tool to study mitochondrial bioenergetics *in vivo* in tissues with high energy demand, including exercising skeletal muscle. The objective of this current study is to understand the reproducibility of the CrCEST based creatine decay post exercise in healthy adults.

**METHODS:** 14 healthy adults (M7, F8, Age:  $39.13 \pm 9.8$  yrs) were scanned (written consent from all participants, approved by local IRB) for CrCEST imaging using plantar flexion exercise on a programmable MR compatible pneumatical ergometer (Trispect, Ergospect) at 45 BPM for 2 min. CrCEST contrast was measured in a 10 mm thick transverse slice placed in the right calf for two minutes before exercise and for eight minutes after exercise on a 3T scanner (Siemens, PRISMA). For CrCEST imaging, the calf was placed inside 15-channel knee coil. Water saturation was collected with shift reference (WASSR) and B maps for B0 and B1 correction. Six images were acquired over 24 s intervals with saturation frequency offsets of  $\pm 1.5$ ,  $\pm 1.8$ , and  $\pm 2.1$  ppm. A 500 ms saturation pulse train was applied consisting of five 99.6 ms Hanning windowed pulses with 150 Hz B1 amplitude separated by a 0.4 ms inter-pulse delay. A fat saturation pulse was applied, followed by a single-shot spoiled gradient-echo readout with centric encoding, flip angle  $10^\circ$ , FOV 160x160 mm, matrix 128x128, TR 6.0 ms, TE 3 ms, slice thickness 10mm. 4 Regions of interest (ROIs) were placed in the major calf muscle groups: lateral gastrocnemius (LG), medial gastrocnemius (MG), soleus (sol), and tibialis anterior (TA). After 15 minutes of rest outside scanner, the subject repeated exercise for second time. Both scans were processed on MATLAB for CrCEST mapping and creatine recovery time constant ( $\tau_{\text{Cr}}$ ).  $^1\text{H}$  MRS was also performed in the LG and Sol muscle groups, and data was processed with LCModel using unsuppressed water signal as reference. Intramyocellular lipid (IMCL), extramyocellular lipid (EMCL) concentrations were measured. Additionally, muscle fat fraction (FF) was measured using the 2-point-Dixon MRI.

**RESULTS:** MRI and  $^1\text{H}$  MRS Data from all fourteen participants was used for testing reproducibility of this method in skeletal muscle groups involved in plantar flexion exercise. Due to lack of engagement during exercise, TA and sol had a high variance in creatine recovery constant ( $\tau_{\text{Cr}}$ ) and were excluded from this analysis. Among all subjects, the average  $\tau_{\text{Cr}}$  in the LG and MG are  $148.9 \pm 106.2$  and  $105.1 \pm 77.9$  sec, respectively. Figure1 shows baseline and post-exercise CrCEST recovery maps in one subject.

**DISCUSSION:** Both LG and MG muscle groups were found to be good candidates for testing reproducibility of CrCEST method. The variation in  $\tau_{\text{Cr}}$  was higher in MG than LG. We found a negative association of IMCL/EMCL ratio with age. This can be explained by increased metabolism, energy expenditure and growth in young subjects. Further, lower FF was found to be associated with higher IMCL concentration, found in athletes.

**CONCLUSION:** Post plantar flexion exercise, both muscles (LG and MG) provide reproducible CrCEST data in healthy adults.

**REFERENCES:** 1. Chance *et al.* J Biol Chem. 1955;217(1):409-427. 2. Sedivy *et al.* J Appl Biomed. 2019;17(2):91-98.

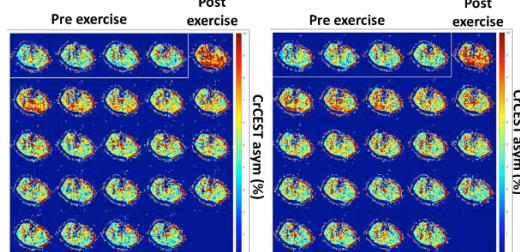


**Figure1.** Representative CrCEST maps in one subject after performing 2 minutes of exercise in two sessions. The second scan (right panel) was obtained after a 15-minute break. By ~2-3 minutes after exercise, the subject's CrCEST image resembles the baseline (left panel) in both sessions.



# Quantitative Study on Monitoring Cartilage Degeneration of Porcine Knee Based on 7.0T Multimodal MRI

Peihong Zhang<sup>1</sup>, Renhua Wu<sup>1,2</sup>

<sup>1</sup>Medical Imaging Department, The Second Affiliated Hospital, Medical College of Shantou University, Shantou, China

<sup>2</sup>Provincial Key Laboratory of Medical Molecular Imaging, Guangdong, Shantou, China

Contact Email: [zhangph2008@vip.qq.com](mailto:zhangph2008@vip.qq.com)

**KEYWORD:** GagCEST, Knee Osteoarthritis

**INTRODUCTION:** This study aims to explore the application value of cartilage imaging quantitative techniques based on 7.0T MR glycosaminoglycan Chemical Exchange Saturation Transfer (gagCEST), T<sub>1</sub> mapping and T<sub>2</sub> mapping in monitoring the early degeneration of articular cartilage through pathological and biochemical controlled study in porcine knee cartilage model, and to provide evidence for early assessment of knee osteoarthritis.

**METHODS:** A total of twenty-one healthy Raoping-black-pig was selected and divided randomly into 7 groups, of which 3 groups were injected with papain intra-articularly and the other 3 groups underwent anterior cruciate ligament transection (ACLT) in the left knee to establish porcine knee osteoarthritis (KOA) model respectively. The left knee joints of each group (n=3) were amputated at different time after successful modeling. Then the degeneration of articular cartilage were observed on 7.0T animal MR scanner based on gagCEST, T<sub>1</sub> mapping and T<sub>2</sub> mapping imaging, and the values of MTRasym, T<sub>1</sub> and T<sub>2</sub> were monitored subsequently. In addition, the left knee joints were amputated from three healthy pigs without modeling as a control group, and the same sequence of MR cartilage imaging and data measurement were performed. Immediately after MR scanning, the medial femoral condylar cartilage of each group were extracted for histological staining and biochemical content determination. Pearson correlation analysis was used to examine the correlation between cartilage matrix compositions and MRI quantitative values.

**RESULTS:** The knee cartilage can be physiological imaged with gagCEST, T<sub>1</sub> mapping and T<sub>2</sub> mapping imaging techniques, and MR values of MTRasym, T<sub>1</sub> and T<sub>2</sub> can be used as quantitative indicators. Glycosaminoglycan (GAG) content decreased significantly 24 hours after injection, then recovered to normal gradually ( $P<0.01$ ), but decreased gradually after surgery ( $P<0.01$ ). However, there was no significant change in collagen content before and after the two models ( $P>0.05$ ). With the progress of cartilage degeneration, the overall values of MTRasym and T<sub>1</sub> decreased gradually, while the overall value of T<sub>2</sub> increased gradually. The correlation analysis showed that MR values of MTRasym, T<sub>1</sub> and T<sub>2</sub> were highly correlated with the changes of GAG content in cartilage. Among them, MTRasym value ( $r=0.977$ ,  $P<0.001$ ) and T<sub>1</sub> value ( $r=0.956$ ,  $P<0.001$ ) were positively correlated with the changes of GAG content, while T<sub>2</sub> value ( $r=-0.913$ ,  $P<0.001$ ) were negatively related to the changes of GAG content. There was no significant correlation between collagen content and MTRasym value ( $r=-0.221$ ,  $P=0.336$ ), T<sub>1</sub> value ( $r=-0.241$ ,  $P=0.292$ ) and T<sub>2</sub> value ( $r=0.225$ ,  $P=0.324$ ) ( $P>0.05$ ). In addition, this study confirmed that the water content of cartilage was positively correlated with the increase of T<sub>2</sub> value ( $P<0.05$ ), and negatively related to the decrease of MTRasym value and T<sub>1</sub> value ( $P<0.05$ ). The thickness of cartilage in injection group and operation group decreased progressively. Pathological sections showed that the degree of articular cartilage degeneration was correlated with the change trend of MRI quantitative indicators.

**CONCLUSION:** Porcine KOA model can be established successfully through the above two methods. The quantitative techniques of gagCEST, T<sub>1</sub> mapping and T<sub>2</sub> mapping cartilage physiological imaging can reflect the cartilage degeneration of early osteoarthritis at the molecular level and the spatial distribution changes of quantitative indicators MTRasym, T<sub>1</sub> and T<sub>2</sub> were correlated with the pathological and biochemical changes of cartilage. Therefore, these multimodal MR cartilage imaging techniques can monitor the process of articular cartilage degeneration accurately and noninvasively in early stage, and provide a more sensitive and effective new means for clinical quantitative assessment of early KOA.

## REFERENCES:

1. Brinkhof S, *et al.* Eur Radiol. 2018;28(7):2874-2881.



## Reproducibility of 3D NOE-MTR in healthy human volunteers at 7T

Blake Benyard<sup>1</sup>, Ravi PR Nanga<sup>1</sup>, Neil Wilson<sup>1</sup>, Deepa Thakuri<sup>1</sup>, Ravinder Reddy<sup>1</sup>

<sup>1</sup>CAMIPM, Department of Radiology, University of Pennsylvania, Philadelphia, Pennsylvania, USA

☒ Apply Student/Postdoc Travel Fund

☒ Oral Presentation ☐ Poster ☐ Either Oral or Poster Presentation | Contact Email: [blake.benyard@pennmedicine.upenn.edu](mailto:blake.benyard@pennmedicine.upenn.edu)

**KEYWORD:** *You are encouraged to choose one or two keywords.* ☒ CEST agents ☒ Contrast Mechanism  
☐ Tumor ☐ Stroke ☐ Neurology ☐ Body & MSK ☐ Standardization ☐ Novel Acquisition ☐ Machine Learning

**INTRODUCTION:** An emerging technique to probe lipids and other macromolecules in the brain uses contrast arising from magnetization transfer due to the Nuclear Overhauser Effect (NOE)[1,2]. NOE is a cross-relaxation which occurs through space, likely between aliphatic moieties and bulk water, giving rise to a Z-spectrum signal (indicating saturation transfer) 3.5ppm upfield from bulk water. Imaging based on this NOE contrast mechanism has been investigating in both animal and human studies, at 3T, 7T and 9.4T [3–7]. These studies have shown in general that low power radiofrequency (RF) pulses and longer saturation lengths can saturate slower-tumbling protons with minimal direct effect of water [3-7]. However, no comprehensive studies to date have characterized the dependence of the in vivo NOE contrast on varying saturation power/length, while correcting for  $B_0$  and  $B_1$  inhomogeneities, particularly at 7T. The purpose of this study is to do an extensive characterization of the NOE contrast dependence on saturation parameters and demonstrate reproducibility of the technique with constant parameters, yielding robust 7T NOE maps of the human brain, corrected for  $B_0$  and  $B_1$  inhomogeneities.

**METHODS:** Five healthy volunteers (5 males) aged 22 to 45 years old participated in the study. Imaging was performed on a 7T Siemens scanner (Erlangen, Germany) with a Nova Medical volume coil transmit/32-channel receive proton head phased-array coil. Three scans were acquired on each subject ( $n = 3$ ). The  $B_0$  and  $B_1$  corrected NOE-MTR contrast maps were averaged over each subject's entire gray matter (GM) and white matter (WM) to compute the coefficient of variation (COV) for the reproducibility studies.

**RESULTS:** The NOE-MTR values were highly reproducible in each subject scanned (Figure 1). The statistical differences were not significant in the GM and WM regions between scans, with a coefficient of variation of less than 10% (Figure 2). From the MTR values, it shows that a saturation length of three seconds yielded the highest contrast in the WM where most of NOE signal arises.

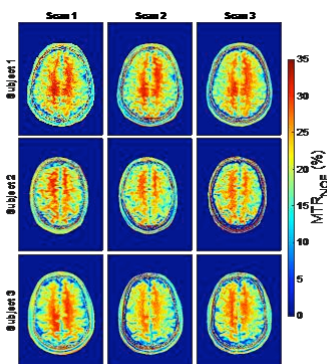


Figure 1: NOE-MTR maps from three subjects over three scans.

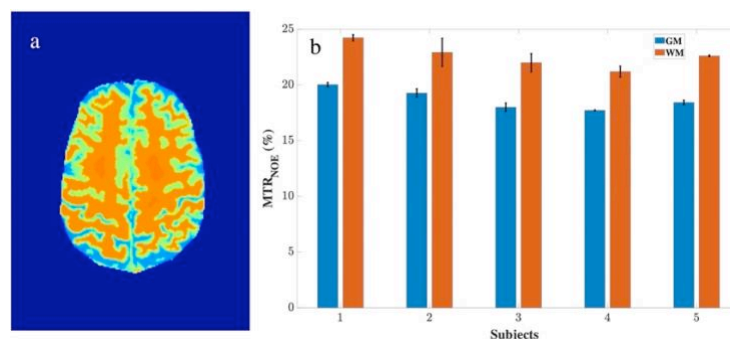


Figure 2: (a) Segmentation map of a partial 3D slab based on white matter (orange) and grey matter (green). (b) Bar plot of the NOE-MTR values for three subjects. For grey matter the COV ranged from 0.96% to 1.96% between all subjects. For white matter, the COV ranged from 1.15% to 5.49%.

**DISCUSSION/CONCLUSION:** In this longitudinal study, five healthy human volunteers were scanned for reproducibility for NOE-MTR in the GM and WM. This study shows that NOE-MTR provides highly reproducible measurements both within individual subjects and across a small group of individuals. Specifically, the COV was less than 10% in GM and WM regions of the brain for all subjects. We also show that NOE-MTR is reproducible with a fixed  $B_1$  power of  $0.72 \mu\text{T}$  and a saturation length of three seconds. Studies involving more subjects will confirm this reproducibility measurement at 7T.

## An automated and robust analysis pipeline for 7T GluCEST data

David R. Roalf<sup>1</sup>, Joelle Jee<sup>1</sup>, Ravi Prakash Reddy Nanga<sup>2</sup>, Abigail Cember<sup>2</sup>, Margaret Gardner<sup>1</sup>, Paul Jacobs<sup>2</sup>, Arianna Mordy<sup>1</sup>, Heather Robinson<sup>1</sup>, Mark A. Elliott<sup>2</sup>, Ravinder Reddy<sup>2</sup>

<sup>1</sup>Department of Psychiatry, University of Pennsylvania; <sup>2</sup>Department of Radiology, University of Pennsylvania

☐ Apply Travel Fund

☐ Oral Presentation ☐ Poster ☒ Either Oral or Poster Presentation | Contact Email: [roalf@pennmedicine.upenn.edu](mailto:roalf@pennmedicine.upenn.edu)

**KEYWORD:** You are encouraged to choose one or two keywords. ☐ CEST agents ☐ Contrast Mechanism

☐ Tumor ☐ Stroke ☐ Neurology ☐ Body & MSK ☒ Standardization ☐ Novel Acquisition ☐ Machine Learning

### INTRODUCTION:

Robust, reproducible methods are paramount in neuroimaging. To date, glutamate-chemical exchange saturation transfer (GluCEST) imaging data has been processed using in-house MATLAB code. Here our primary objective is to move GluCEST analysis towards a robust and reproducible analytical pipeline using python-based neuroimaging tools. The development of *GluCEST-prep* incorporates common neuroimaging analysis steps—brain extraction (HD-BET), tissue segmentation (FAST+FIRST), co-registration (ANTs) and normalization (ANTs)—that are optimized for 7T MRI and uses python-based code to generate post-processed 2D or 3D GluCEST images in both native and template space. The major goal of the updated *GluCEST-prep* pipeline is to translate in-house MATLAB analysis code to Python to improve accessibility and reproducibility of the pipeline.

**METHODS:** MRI data were acquired on a 7.0T Siemens Terra at the University of Pennsylvania. Acquisition of GluCEST images and B<sub>0</sub> and B<sub>1</sub> maps was completed as described in previous studies<sup>1,2</sup>. Briefly, both 2D and 3D GluCEST images were acquired. Structural images including T1-weighted uniform (UNI) images, T1 maps, and corresponding INV1 and INV2 images were acquired with a Magnetization Prepared 2 Rapid Acquisition Gradient Echoes (MP2RAGE) sequence.

GluCEST-prep calls upon state-of-the-art neuroimaging analysis tools. GluCEST-prep allows for flexibility in file selection, automatic or manual brain extraction, and employs branching logic to determine optimal brain segmentation based on available structural input. Brain extraction and segmentation are implemented using outputs of a multiecho MP2RAGE. HD-BET<sup>3</sup> is used to generate a robust binary brain mask and can be computed with the use of GPUs, if available, for more accurate brain extraction. Tissue segmentation is completed using a combination of multi-compartment segmentations (e.g. FSL's FAST; FSL's FIRST) of the structural data<sup>4</sup>. To further improve the processing pipeline, bias correction and registration to template space (e.g., MNI152) is performed using ANTs<sup>5</sup>. The output of GluCEST-prep for 2D images includes native space GluCEST, B<sub>0</sub>, B<sub>1</sub>, gray, white and CSF segmentation maps, and regions-of-interest that can be used for statistical analysis. 3D GluCEST output is similar but include standard space maps.

To validate the GluCEST-prep, 2D GluCEST data from 81 subjects and 3D data from five subjects were analyzed using both traditional in-house MATLAB analysis and the new python-based GluCEST-prep.

**RESULTS:** As expected, the original MATLAB and GluCEST-prep analysis were highly similar in the GluCEST datasets analyzed. Resulting Pearson correlation between outcome GluCEST images using MATLAB or the python based GluCEST-prep was 0.99. This validates the use of a python-based open-source tool in comparison to in-house MATLAB based scripts. GluCEST-prep analysis of five 3D GluCEST datasets covering the hippocampus provides robust GluCEST average signal map spanning left and right hippocampus.

**DISCUSSION:** GluCEST-prep, successfully replicates the processing steps of the existing version using robust, automated neuroimaging tools. This python-based tool implements optimized brain extraction and segmentation tools and produces robust measurements of GluCEST. Additionally, updates and upgrades are currently being made to this beta-version of GluCEST-prep prior to public release to improve usability. Future updates will include high-quality visual reports and logs of all processing steps. These reports will allow the user to easily view input data and output data, thereby improving the efficiency of quality assessment and improving reliability of GluCEST data.

**CONCLUSION:** In summary, we have developed a robust and reliable python-based analysis tool than can seamlessly and quickly analyze GluCEST data.

**ACKNOWLEDGMENTS:** Research reported in this work was supported by the National Institute of Biomedical Imaging and Bioengineering of the National Institutes of Health under award Number P41EB029460 and by the National Institute of Aging (R56AG066656) and National Institute of Mental Health (R01 MH120174) of the National Institutes of Health.

**REFERENCES:** References should use the suggested style below.

1. Roalf DR, Nanga RPR, Rupert PE, et al. *Mol Psychiatry*. 2017; 22(9): 1298- 305.
2. Sydnor V, Kohler CG, Crow AJD, et al. *Biol Psychiatry*. 2020; 87(9): S218-S219.
3. Isensee F, Schell M, Tursunova I, et al. *Hum Brain Mapp*. 2019; 40(17): 1–13.
4. Choi US, Kawaguchi H, Matsuoka Y, et al. *PLoS One*. 2019; 14(2): e0210803.
5. Tustison NJ, Cook PA, Klein A, et al. *Neuroimage*. 2014; 99: 166-179.

## 7T comprehensive CEST – a clinically feasible multi-exchange-regime CEST protocol

Moritz Simon Fabian<sup>1</sup>, Lukas Kamm<sup>1</sup>, Angelika Barbara Mennecke<sup>1</sup>, and Moritz Zaiß<sup>1,2</sup>

<sup>1</sup>Institute of Neuroradiology, University Hospital Erlangen, Erlangen, Germany, <sup>2</sup>High-field Magnetic Resonance Center, Max Planck Institute for Biological Cybernetics, Tübingen, Germany

✉ Either Oral or Poster Presentation | Contact Email: Moritz.fabian@uk-erlangen.de

KEYWORD: ☑ CEST agents ☑ Standardization

**Introduction** Chemical exchange saturation transfer (CEST) MR imaging detects the signal of low concentrated molecules utilizing proton exchange and selective RF saturation. The CEST effect is dependent on the RF saturation scheme, more specifically on RF pulse type, shape, duration and B1 level. So far, 7T CEST measurements in vivo [1-3] focus only on saturation parameters selecting one specific exchange regime, e.g. either low B1, intermediate B1 or high B1 CEST sequences are used in different patient studies. Therefore, we establish a 7T snapshot CEST protocol, which labels all of these CEST effects simultaneously. Applying this comprehensive protocol to patients suffering from multiple sclerosis, brain tumor or stroke is expected to provide deeper insight into the CEST properties of these pathologies.

CEST effect(s) @ reconstructed B1	Pulse No., Pulse shape	B1 level [ $\mu$ T]	$t_p$ [ms]	DC [%]	$t_{sat}$ [ms]	evaluation	# offsets	acquisition time [s]
Slow exchange: Amides, Amines, NOE, MT @0.6 $\mu$ T	120 Gaussian	0.72, 1.0	15.36	60.56	3043.8	Lorentz fitting	2 x 55	2 x 402
Intermediate exchange: Amine+Glutamate weighting @2.0 $\mu$ T	10 Gaussian	1.9, 2.5, 3.1	60.16	89.58	671.8	MTR asymmetry	3 x 26	3 x 329
Fast exchange: Hydroxyl @3.6 $\mu$ T	1 DGErho	4.5, 5.0, 5.5	120	100	120	MTR asymmetry	3 x 17	3 x 119

**Table 1:** Overview of the saturation schemes of the fully sampled CEST measurement protocol

**Methods** Measurements are conducted at a MAGNETOM Terra 7T scanner (Siemens Healthineers AG, Erlangen, Germany) with a 32Rx/8Tx-channel head coil (Nova Medical, Wilmington, MA), and are approved by the local ethics committee. The CEST image readout was the 3D snapshot GRE MIMOSA CEST [4,5]. Low B1 CEST measurements for detection of Amide, NOE, Amine and MT pool were done according to [1]. Intermediate B1 CEST (GluCEST) is measured according to [2]. High B1 CEST is realized by adiabatic spin-lock pulses for hydroxyl CEST [3]. An overview regarding the saturation scheme of the measurements is shown in Table 1.

### Results+Discussion

Figure 2 shows that we could generate all desired CEST contrast of all different exchange and B1 regimes with similar homogeneity within one protocol. All contrast show few imperfection (Figure 2), which can still be improved using better B0/B1 mitigation/correction and less sensitive evaluation metrics. From the original sampling with a total scan time of about 40 minutes, we were able to shorten this comprehensive CEST protocol down to 15 minutes [6].

### Conclusion

The proposed 7T snapshot CEST protocol is able to generate CEST contrasts of three different exchange and B1 saturation regimes simultaneously.

### References

1. Mennecke, A. et al., NMR in Biomedicine, e4717.
2. O'Grady, K. P et al., Multiple Sclerosis Journal, 25(12), 1580-1592.
3. Herz, K. et al., Magnetic Resonance in Medicine, 81(1), 275-290.
4. Zaiss M et al., NMR in Biomedicine 2018;31:e3879 doi: 10.1002/nbm.3879
5. Liebert, A. et al., Magnetic Resonance in Medicine, 82(2), 693-705.
6. Glang, F. et al., NMR in Biomedicine, e4697.

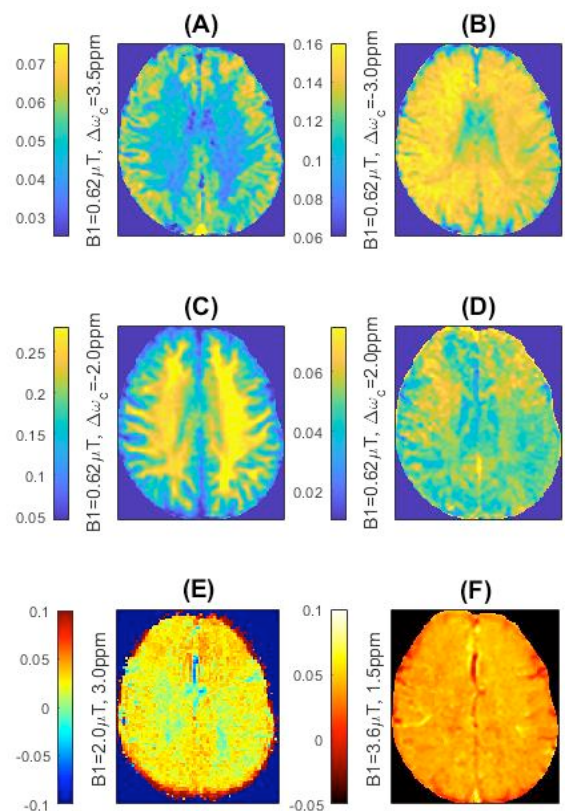


**Figure 2:** CEST parameter maps and asymmetry maps from a healthy male volunteer. Amide (A), NOE (B), MT (C) and Amine (D) Lorentz parameter amplitudes at B1=0.6 $\mu$ T. MTR asymmetry calculation at 3.0 ppm and B1=2 $\mu$ T (E) from the Amine and Glutamate weighted protocol; analogously the asymmetry calculation (F) at 1.5ppm and B1=3.6 $\mu$ T regarding hydroxyl protocol.



# comprehenCEST: a clinically feasible CEST protocol to cover all existing CEST preparation schemes by snapshot readout and reduction of overhangs

Lukas Kamm<sup>1</sup>, Moritz Fabian<sup>1</sup>, Felix Glang<sup>2</sup>, Kai Herz<sup>2</sup>, Moritz Zaiss<sup>1,2</sup>

<sup>1</sup> Friedrich-Alexander Universität Erlangen-Nürnberg (FAU), Institute of Neuroradiology, University Hospital Erlangen, Erlangen, Germany

<sup>2</sup> Max-Planck-Institute for Biological Cybernetics, Tuebingen, Baden Wurttemberg, Germany

□ Oral Presentation □ Poster □ Either Oral or Poster Presentation | Contact Email: lukas.kamm@fau.de

KEYWORD: □ Stroke □ Neurology □ Body & MSK □ Standardization □ Novel Acquisition □ Machine Learning

## INTRODUCTION:

CEST sequences preparing a selected metabolite normally sample the full Z-spectrum, allowing for asymmetry or model-based evaluations. To achieve good labelling efficiency for various metabolites, different physical preparations are required. Sparsity-enforcing machine learning algorithms help to select and combine the differently CEST-prepared images from a sequence pool covering the preparation parameter space, while preserving main contrast information. Together with a fast, single-shot 3D readout, we create a 3D CEST protocol containing 13 established contrasts in 10 minutes scan time.

## METHODS:

(1) 13 contrasts are evaluated conventionally (PCA-denoising, dB0-correction, MTR asymmetry or Lorentz fit) from six existing CEST sequences [2-5], which cover B1cwpe levels from 0.5 to 4 uT, offering the ground truth. Mz is prepared using standardized pulseseq-CEST building blocks [7-8], and probed with the fast snapshotCEST 3D readout [1]. (2) All Z-spectra are mapped to contrast via a linear projection, while sparsity-enforcing L1-regularization reduces the number of consumed offsets (rowLASSO [6,10]). The training is carried out on uncorrected, raw Z-spectra to generate a selection that provides robustness against noise and B0/B1 inhomogeneities. (3) Difference maps between ground truth and model output are created for the validation dataset.

## RESULTS:

5 of the 13 generated CEST maps are shown in Figure 1. Lowering CEST offsets down to 82 still yields similar imaging contrast. The normalized, mean absolute error (NMAE) between linear model and ground truth, averaged over all 13 contrasts, and for retaining offset rate  $r$  is:

$27 \pm 6\%$  ( $r = 1$ ),  $29 \pm 7\%$  ( $r = 0.8$ ),  $32 \pm 8\%$  ( $r = 0.6$ ),  $36 \pm 9\%$  ( $r = 0.4$ ),  $42 \pm 11\%$  ( $r = 0.2$ ). Residual errors visible here might still originate from an observed B0 drift during the whole data acquisition; it is expected that this can be further improved.

## DISCUSSION & CONCLUSION:

Instead of arguing which is the best CEST protocol to provide new insights into a pathology, and only measure one CEST contrast, we suggest measuring them all. By combining sparse sampling and snapshot readout, a comprehensive protocol covering most of the reported labellings of 10 minutes is conceivable. This allows to design powerful hypotheses generating clinical pilot studies.

## REFERENCES:

1. Zaiss M, et al. NMR Biomed 2018;31:e3879.
2. Nanga RPR, et al. MRM 2018;80:2033-2039.
3. Harris, et al. Magn Reson Med 2018;80:1962-1978.
4. Herz K, et al. Magn Reson Med 2019;82:1832-1847.
5. Yua n J, et al. NMR Biomed 2014;27:1239-1247.
6. Glang F, et al. NMR Biomed 2022;24:e4697.
7. Herz K, et al. Magn Reson Med 2021;00:1-14.
8. Herz K, et al. 2021; Pulseseq-CEST. <https://github.com/kherz/pulseseq-cest>.
9. Schuenke P, et al. Magn Reson Med 2017;77:571-580.
10. Glang F, et al. 2021; linearCEST. <https://github.com/fglang/linearCEST>

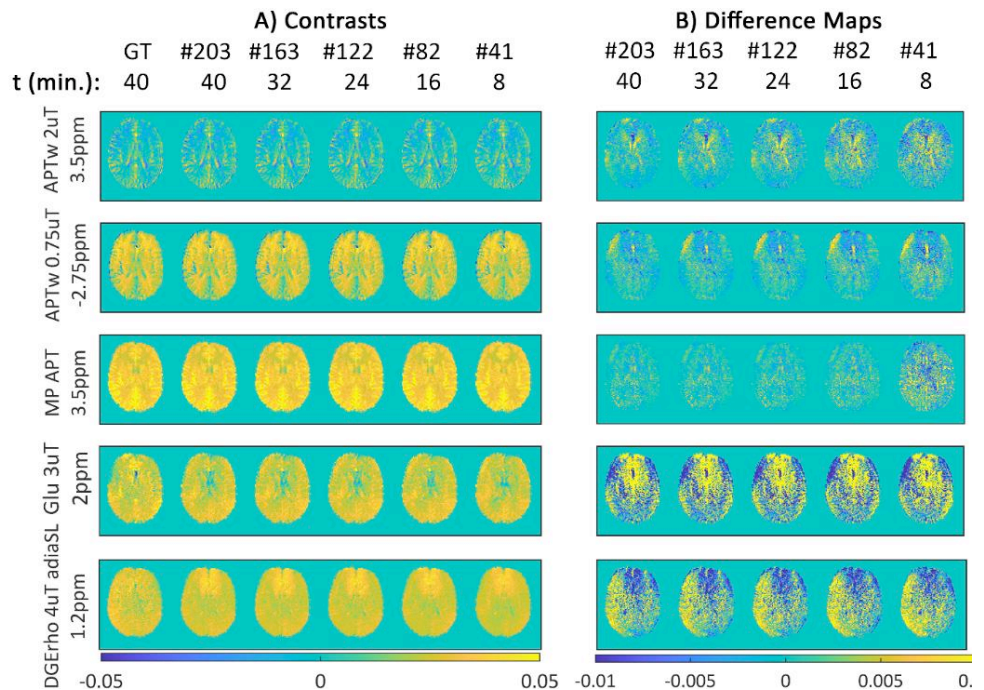


Fig.1: 5 of the 13 generated CEST contrasts (MP APT: Lorentz fit, Others: MTR asymmetry) for one volunteer (23m) in the validation set. A) Brain maps showing the Ground Truth (left column; PCA-denoising, dB0-correction (WASABI [9])) and linear model-output using numbers of offsets indicated with #. B) Difference maps to ground truth.



Rohith Saai Pemmasani Prabakaran<sup>1</sup>, Se Weon Park<sup>1,2</sup>, Kexin Wang<sup>3,4</sup>, Jiadi Xu<sup>3,4</sup>, Jianpan Huang<sup>2\*</sup>,  
Kannie WY Chan<sup>1,2,3,5\*</sup>


☒ **Apply Student/Postdoc Travel Fund**

**KEYWORD:** *You are encouraged to choose one or two keywords.* ☐ CEST agents ☐ Contrast Mechanism

**INTRODUCTION:** Reproducible CEST contrast is a requisite for early disease diagnosis and guided treatment<sup>1,2</sup> for which high-resolution CEST images are required. However, acquisition of high-resolution images increases the scanning time<sup>3</sup>, thereby, requiring a compromise between scanning time and image quality. Deep-Learning based Super-Resolution (DLSS), a technique that reconstructs high-resolution images from low-resolution images which require a shorter acquisition time, has been explored for a similar problem of scanning time in conventional MRI<sup>4</sup>. But adaptation of this technique to CEST MRI has been hindered by the lack of large, publicly available CEST datasets. Hence, this study aims to tackle these issues by proposing a deep-transfer learning based super-resolution method for fast CEST MRI acquisition using large, public MRI datasets for pretraining and a very small CEST datasets for training.

human brain and one CEST MRI datasets of tumor mouse brain were used for testing. For each high-resolution image in the datasets, the corresponding low-resolution image was generated by downsampling of the K-space, followed by inverse Fourier transform (Figure 1).

**RESULTS AND DISCUSSION:** From Figure 3, it is evident that the low-resolution images lack high frequency information, with increasing information loss at larger downsampling scales. Using these low-resolution acquisitions as input, the network improves the spatial resolution of the images across all scales. In the SRCEST reconstructed images, there is an improvement of 5.5%-7.2% in PSNR and an improvement of 1.2%-5.9% in SSIM when compared to the low-resolution CEST images across all scales, thus validating the improvement in spatial resolution. In Figure 4, the capability of SRCEST in accurately reconstructing the Z-spectrum is depicted.



**Fig 3.** Illustration of the improvement in spatial resolution in human brain.

reconstructed images and corresponding Z-spectrum from high-resolution images. Moreover, as seen in the difference plot, the difference in Z-spectrum value at each offset is less than 0.5%. The multi-offset SRCEST reconstructs the Z-spectra with a Mean Absolute Error (MAE) of 0.09% in Z-spectrum value at each offset frequency, thus preserving the molecular information in Z-spectrum. Interestingly, the Z-spectrum of the low-resolution CEST images also shows a negligible difference with that of high-resolution CEST images. This can be attributed to the average effect of calculating Z-spectrum from ROI and the downsampling method that preserves most pixel intensity information in the low-resolution images.

**CONCLUSION:** In this study, we have proposed the use of multi-offset SRCST network for reconstructing high-resolution CEST images from low-resolution acquisitions, and thereby, shortening the scanning time of CEST MRI.

**ACKNOWLEDGMENTS:** RGC: 11102218, PDFS2122-1S01; CityU: 7005210, 7005433, 9680247, 9667198 and 9609307; NSFC: 81871409.

**REFERENCES:** 1. Jones KM, *et al.* J Magn Reson Imaging 2018;47(1):11-27. 2. van Zijl PC, *et al.* Magn Reson Med 2011;65(4):927-948. 3. Wu B, *et al.* EJNMMI physics 2016;3(1):1-21. 4. Plenge E, *et al.* Magn Reson Med 2012;68(6):1983-1993. 5. Erickson B, *et al.* The Cancer Imaging Archive 2017;76. 6. Akkus Z, *et al.* arXiv preprint arXiv:161106939 2016. 7. Clark K, *et al.* Journal of Digital Imaging 2013;26(6):1045-1057.

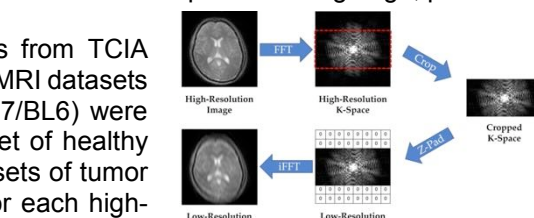


**Fig 1.** Downsampling method for generating low-resolution images.

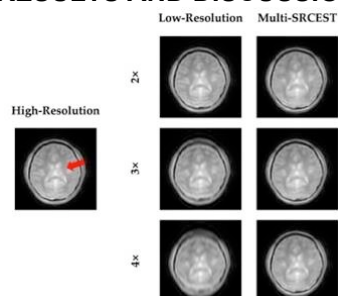


**Fig 3.** Illustration of the improvement in spatial resolution in human brain.

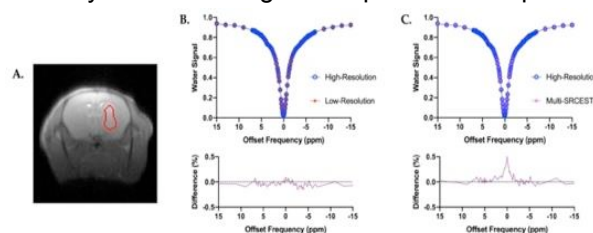


**Fig 4.** Illustration of the reconstruction of the Z-spectra at 4x downsampling scale in tumor mouse model.

# Simultaneous Mapping of $B_0$ , $B_1$ and $T_1$ With Aleatory and Epistemic Uncertainty Estimations

Patrick Schuenke<sup>1</sup>, George Henrik Narvaez<sup>1</sup>, Kerstin Kaspar<sup>1</sup>, Moritz Zaiss<sup>2</sup>, Christoph Kolbitsch<sup>1</sup>

<sup>1</sup> Physikalisch-Technische Bundesanstalt (PTB), Braunschweig and Berlin, Germany

<sup>2</sup> Institute for Neuroradiology, University Hospital Erlangen, Friedrich-Alexander Universität Erlangen-Nürnberg, Erlangen, Germany

☒ Apply Student/Postdoc Travel Fund

☐ Oral Presentation ☐ Poster ☒ Either Oral or Poster Presentation | Contact Email: [patrick.schuenke@ptb.de](mailto:patrick.schuenke@ptb.de)

**KEYWORD:** You are encouraged to choose one or two keywords.

☐ CEST agents ☐ Contrast Mechanism  
☐ Tumor ☐ Stroke ☐ Neurology ☐ Body & MSK ☐ Standardization ☒ Novel Acquisition ☒ Machine Learning

**INTRODUCTION:** The accurate determination of isolated CEST effects requires the correction of unwanted influences of  $B_0$ - and  $B_1$ -field inhomogeneities as well as the  $T_1$  relaxation time [1-3]. Therefore, quantitative maps of all three parameters are needed. In order to minimize and assess error propagation from these maps into the final CEST contrasts, accurate parameter predictions and knowledge about the prediction uncertainties are required. In this work, we show that the utilization of an ensemble of neural networks (NN) allows to estimate and differentiate the aleatory and epistemic uncertainty of the parameters  $B_0$ ,  $B_1$  and  $T_1$  that are predicted from a single modified WASAB1 [3] MRI sequence.

**METHODS:** We extended the WASAB1 approach by adding a preceding  $T_1$  preparation block and frequency offset-dependent recovery delays to enhance its intrinsic sensitivity to  $T_1$ . Additionally, we replaced a previously introduced evaluation network [4] with an ensemble of deep NNs (deep ensemble) implemented in PyTorch. A Gaussian negative log-likelihood loss function and a supervised learning approach was used to train the deep ensemble of  $M=30$  NNs with identical architecture and randomly initialized weights and biases ( $\theta_i$ ). This enables the prediction of  $B_0$ ,  $B_1$  and  $T_1$  using the deep ensemble mean values ( $\mu_i$ ), as well as the estimation of the aleatory and epistemic uncertainties given by the different terms of the deep ensemble variances ( $\sigma_i$ ):

$$\hat{\sigma}_f^2(x) = \underbrace{\frac{1}{M} \sum_{i=1}^M \hat{\sigma}_{f,\theta_i}^2(x)}_{\triangleq \text{aleatory uncert.}} + \underbrace{\frac{1}{M} \sum_{i=1}^M \hat{\mu}_{f,\theta_i}^2(x) - \hat{\mu}_f^2(x)}_{\triangleq \text{epistemic uncert.}} \quad (1)$$

Training spectra with varying  $B_0$  (range [-2; 2] ppm),  $B_1$  (range [20; 200] %),  $T_1$  (range [0.05; 7] s),  $T_2$  and noise values were simulated using the Pulseq-CEST simulation framework [5]. All MRI sequences were implemented using PyPulseq [6].

**RESULTS:** Using an unseen test data set with identical parameter ranges as the training data set, the accuracy of the proposed approach was evaluated. The coefficient of determination ( $R^2$ ) between the predicted and ground truth values was  $> 0.99$  for all three parameters resulting in mean errors  $\leq 0.004$  ppm for  $\Delta B_0$ ,  $\leq 0.008$   $\mu$ T for  $B_1$  and  $\leq 0.030$  s for  $T_1$ . Remaining prediction errors are highly correlated with both the estimated aleatory and epistemic uncertainty as well as the combination of both (table 1). Figure 1 shows the results of a measurement of an MR phantom consisting of various model solutions with varying relaxation times. The uncertainty estimations match the difference maps well, displaying higher uncertainties for regions with higher differences (e.g., in the walls of the tubes) and *vice versa*. Similar results were observed in an *in-vivo* measurement of the brain of a healthy volunteer (data not shown).

**DISCUSSION:** We demonstrated the feasibility of simultaneous mapping of  $B_0$ ,  $B_1$  and  $T_1$  using a modified WASAB1 sequence in combination with a NN-based analysis. The introduced deep ensemble yields a very high accuracy and allows the differentiation between aleatory and epistemic uncertainties, which both show a very good correlation with the prediction errors. Thus, they enable the identification of regions where the predicted parameter values should be treated with caution. The *in-vitro* and *in-vivo* applicability of the proposed approach was demonstrated and the findings from the simulation study could be confirmed.

**CONCLUSION:** The high robustness and accuracy of the proposed approach together with its similarity to a conventional CEST-sequence make it a highly valuable tool for the determination of quantitative  $B_0$ ,  $B_1$  and  $T_1$  maps that are required for the correction of CEST-MRI contrasts.

## REFERENCES:

- 1) Windschuh J, *et al.* NMR Biomed. 2015;28:529–37
- 2) Zaiss M, *et al.* NMR Biomed. 2014;27:240–52
- 3) Schuenke P, *et al.* Magn. Reson. Med. 2017;77:571–80

- 4) Schuenke P, *et al.* Proc. Intl. Soc. Mag. Reson. Med. 30:2714
- 5) Herz K, *et al.* Magn. Reson. Med. 2021;86:1845–58
- 6) Ravi K, *et al.* J. Open Source Softw. 2019;4:1725

	aleatory	epistemic	combined
$\Delta B_0$	0.688	0.768	0.693
$B_1$	0.700	0.701	0.707
$T_1$	0.680	0.613	0.680

Table 1: Pearson correlation coefficients (PCC) between the prediction errors and the different estimated uncertainties according to equation 1.

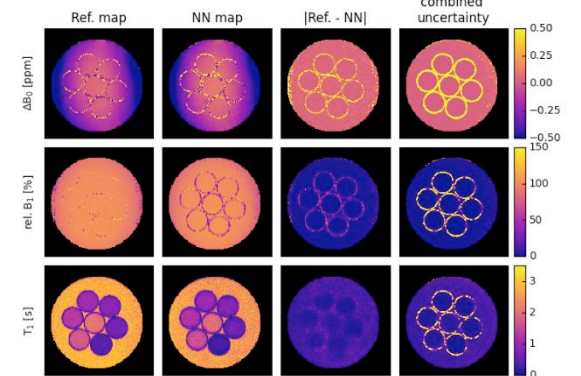


Figure 1: Results for measurement of seven 25 ml tubes filled with different model solutions ( $T_1$  range 400–2100 ms). Differences between reference maps (1<sup>st</sup> column) and predicted maps (2<sup>nd</sup> column) are shown in the 3<sup>rd</sup> column. Combined uncertainty estimates (4<sup>th</sup> column) and difference maps match well.

# Accelerating chemical exchange saturation transfer imaging using a model-based deep neural network

Jianping Xu<sup>1</sup>, Tao Zu<sup>1</sup>, Yi-Cheng Hsu<sup>2</sup>, Yi Sun<sup>2</sup>, Dan Wu<sup>1</sup>, Xiaoli Wang<sup>3</sup>, Yi Zhang<sup>1</sup>

<sup>1</sup>College of Biomedical Engineering & Instrument Science, Zhejiang University, Hangzhou, Zhejiang, China

<sup>2</sup>MR Collaboration, Siemens Healthcare Ltd., Shanghai, China

<sup>3</sup>Weifang Medical University, Weifang, Shandong, China

✉ Apply Student/Postdoc Travel Fund

□ Oral Presentation □ Poster ✉ Either Oral or Poster Presentation | Contact Email: [jianpingxu@zju.edu.cn](mailto:jianpingxu@zju.edu.cn)

**KEYWORD:** You are encouraged to choose one or two keywords. □ CEST agents □ Contrast Mechanism

□ Tumor □ Stroke □ Neurology □ Body & MSK □ Standardization □ Novel Acquisition ✉ Machine Learning

**INTRODUCTION:** CEST imaging has proven to be a powerful technique that can sensitively detect numerous biomolecules and pathologies<sup>1</sup>. However, the widespread clinical adoption of this technique has been hampered by its prolonged scan time, due to multiple data acquisitions over the varying saturation offset frequencies. Here, we aim to combine the deep reconstruction network and parallel imaging model for fast clinical CEST imaging.

**METHODS:** We propose a deep-learning-based approach to accelerate multi-coil CEST imaging based on the variational network (VN)<sup>2</sup>, termed CEST-VN<sup>3</sup>. As shown in Fig. 1, CEST-VN is unrolled from the numerical optimization scheme designed for the CEST image reconstruction, which is composed of two main modules: (i) a k-space data sharing block that takes advantage of adjacent k-space redundancies along the saturation frequency offset dimension; (ii) an image reconstruction network with a trainable regularization module and a model-based data consistency module in each iterative block, which progressively recovers CEST source images. To exploit the correlations in the spatial-frequency ( $x-\omega$ ) domain, 3D spatiotemporal kernels are used in our network.

To meet the need for large CEST datasets during network training, an efficient pipeline based on the multiple-pool Bloch-McConnell model is devised<sup>3</sup> to simulate multi-coil CEST data from publicly available anatomical FastMRI<sup>4</sup> data. CEST-VN is trained on simulated data with the supervision of a CEST-specific loss function which jointly measures the error of reconstructed source images and calculated CEST signals. Notably, no real CEST data is input into the CEST-VN network during model training. The performance of the trained network is evaluated on real CEST data from three healthy volunteers and five brain tumor patients with various acceleration factors, by standard image reconstruction quality metrics and CEST analysis metrics.

**RESULTS:** Fig. 2 shows results on a newly-diagnosed glioma patient with an acceleration factor  $R = 4$ . The proposed approach can provide high-quality reconstruction in terms of source images, APTw maps, and  $MTR_{asym}$  spectra, outperforming GRAPPA<sup>5</sup>, multi-coil blind compressed sensing (BCS)<sup>6</sup>, and the original VN<sup>2</sup>. Moreover, our approach can efficiently reconstruct a CEST map within 15 s on a single GPU card, which is fast enough to meet the clinical requirements.

**DISCUSSION:** Although CEST-VN is trained using the simulated CEST datasets without seeing any real CEST data, it shows high-performance reconstruction on clinical CEST data, indicating the excellent generalizability of the proposed network, as well as the effectiveness of the presented pipeline for simulating multi-coil CEST training data.

**CONCLUSION:** By integrating the deep-learning prior and multi-coil sensitivity encoding model, the proposed CEST-VN method can provide high-quality and rapid CEST image reconstruction from highly undersampled clinical multi-coil data, which effectively reduces the scan time and is beneficial for the clinical translation of CEST imaging.

**ACKNOWLEDGMENTS:** NSFC grant numbers: 81971605. Key R&D Program of Zhejiang Province: 2022C04031.

**REFERENCES:** 1. van Zijl PC, et al. Neuroimage 2018;168:222-241. 2. Hammernik K, et al. Magn Reson Med 2018;79(6):3055-3071. 3. Xu J, et al. arXiv preprint arXiv: 2205.10265. 4. Zbontar J, et al. arXiv preprint arXiv:1811.08839 2018. 5. Griswold MA, et al. Magn Reson Med 2002;47(6):1202-1210. 6. Bhawe S, et al. Magn Reson Med 2016;75(3):1175-1186.

**Fig. 1:** Illustration of the proposed CEST-VN framework.

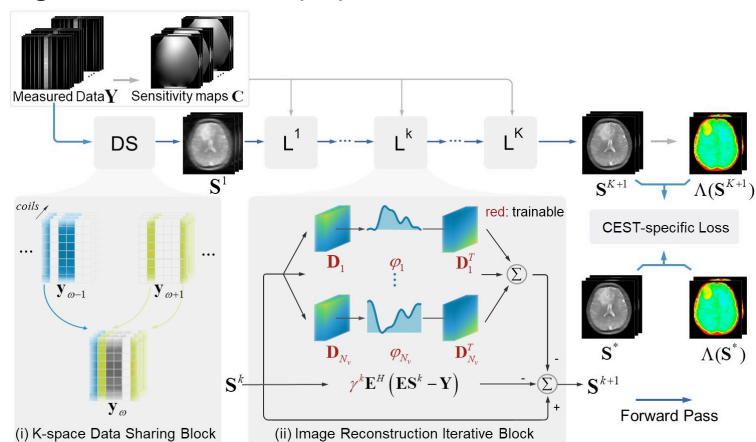
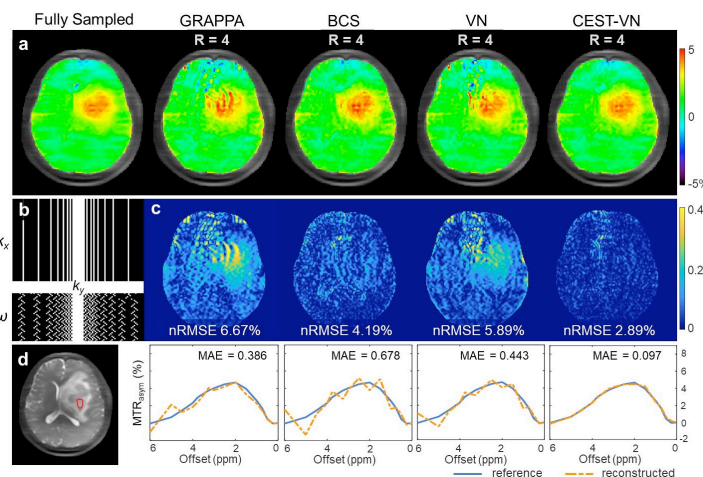


**Fig. 2:** Comparison of CEST-VN with state-of-the-art fast imaging approaches on a glioma patient.





# Saturation and Phase Sensitive Water Exchange Spectroscopy

Fabian T. Gutjahr<sup>1</sup>, Nils M.J. Plaehn<sup>2</sup>, Simon. Mayer<sup>1,3</sup>, Peter M. Jakob<sup>1</sup>

<sup>1</sup> Experimental Physics 5, University of Wuerzburg, Bavaria, Germany, <sup>2</sup> Department of Interventional, Diagnostic and Pediatric Radiology (DIPR), Translational Imaging Center (TIC), University of Bern, Switzerland, <sup>3</sup> Leibniz Institute of Plant Genetics and Crop Plant Research (IPK), Gatersleben, Germany

☐ Apply Travel Fund

☐ Oral Presentation ☐ Poster ☒ Either Oral or Poster Presentation | Contact Email: Fabian.T.Gutjahr@physik.uni-wuerzburg.de

**KEYWORD:** You are encouraged to choose one or two keywords. ☐ CEST agents ☐ Contrast Mechanism

☐ Tumor ☐ Stroke ☐ Neurology ☐ Body & MSK ☐ Standardization ☒ Novel Acquisition ☐ Machine Learning

## INTRODUCTION:

Even though methods like QUESP allow the quantification of exchange rates directly through CEST, WEX remains relevant, especially for slow exchange rates, where the sampling directly in the time domain allows accurate and spectroscopic quantification. However dynamic of the WEX signal curve is not only determined by the exchange rate but also  $T_1$ . In this abstract we demonstrate two variants of a new method (Saturation and Phase Sensitive WEX), that has a  $T_1$  independent signal dynamic. Furthermore PS-WEX can approximately double the dynamic range.

**METHODS:** In WEX the mixing time of a stimulated echo pathway is varied, to measure the amount of magnetization transferred in dependence on the time available for exchange. However by varying the total time interval between preparation and read out, the prepared magnetization also undergoes varying amounts of  $T_1$ -relaxation. We therefore propose to keep the mixing time constant, which leads to a constant amount of transferred magnetization and constant  $T_1$ -weighting. By adding a saturation (Sat-WEX) or inversion pulse (PS-WEX) in the mixing time interval and varying its position within this interval only the dependence on the exchange rate is then reintroduced. An analytical expression for the new method was found and validated using the extended phase graph formalism. Furthermore the method was implemented in Paravision 4 and phantom measurements on creatine solutions at different pH-values were carried out on 11.7 T and 17.4 T MRI systems.

**RESULTS:** It could be shown, that both PS- and Sat-WEX produce the intended signal behavior in both simulations and measurements. In SNR-simulations (EPG) the PS-WEX method outperformed both standard WEX and Sat-WEX in regards to noise sensitivity. This can be explained by the increased dynamic range and reduced complexity due to the  $T_1$ -independent signal behavior.

**DISCUSSION/CONCLUSION:** Both Sat-WEX and PS-WEX retain the desirable properties of WEX, to quantify exchange rates spectroscopically in the time domain. By reducing the  $T_1$ -dependence to a constant factor a simpler fit-model can be used, leading to improved quantification. This is especially the case for PS-WEX due to the increased dynamic range.

## REFERENCES:

1. McMahon MT, *et al.* Magn Reson Med 2006;55(4):836-847
2. Mori S, *et al.* J. Am. Chem. Soc, 1994;116(26), 11982–11984
3. Plaehn NMJ, *et al.* J Magn Reson. 2022;335:107141

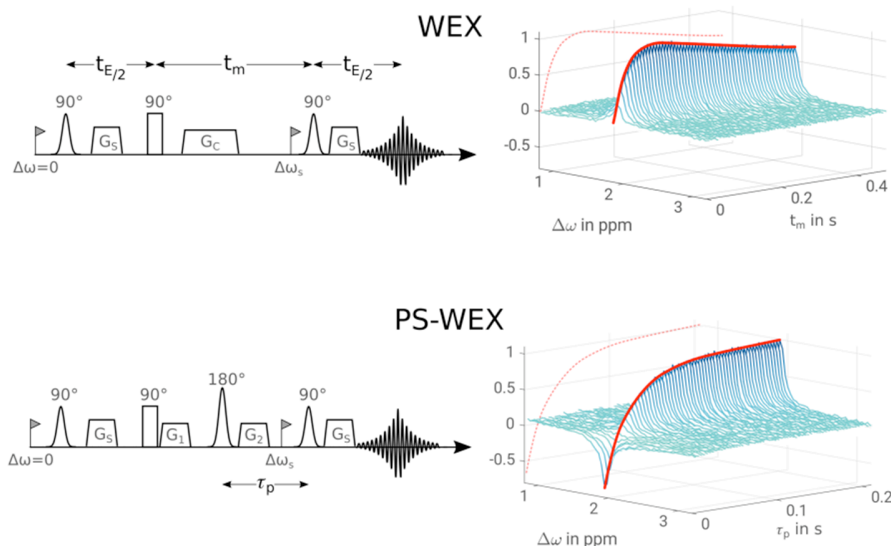


Fig. 1 Sequence diagram and partial spectrum of a creatine sample acquired at 11.7 T. The PS-WEX experiment exhibits an increased dynamic range as well as a mono-exponential dynamic.



# Toward *in vivo* MRI of tissue proton exchange rate

Mehran Shaghaghi<sup>1</sup>, Zimeng Cai<sup>2</sup>, Li Li<sup>3</sup>, Kejia Cai<sup>1\*</sup>

<sup>1</sup>University of Illinois at Chicago; <sup>2</sup>Guangdong Provincial People's Hospital <sup>3</sup>Tongji Hospital

☒ Apply Travel Fund

☒ Oral Presentation ☐ Poster ☒ Either Oral or Poster Presentation | \*Contact Email: [kcai@uic.edu](mailto:kcai@uic.edu)

KEYWORD: ☒ Contrast Mechanism ☒ Novel Acquisition

**INTRODUCTION:** Proton exchange occurs between bulk water and metabolites, such as proteins, peptides, amino acids, and other small molecules. Proton exchange plays important role in producing MR imaging contrasts, including T<sub>1</sub>- and T<sub>2</sub>- relaxations, CEST, MT, and NOE (1). *In vivo* tissue proton exchange rate ( $k_{ex}$ ) is a weighted averaged  $k_{ex}$  of all exchanging protons contributing to various MRI mechanisms, such as semi-solid MT, CEST, and exchange-relayed NOE or rNOE (1). Despite the importance of  $k_{ex}$  in various MRI contrasts, *in vivo* quantification and imaging remains a challenge. Current methods for  $k_{ex}$  measurement include MR spectroscopy (MRS), model-based fitting, and exogenous contrast agents.

**METHODS:** The omega plot method, initially developed for paramagnetic CEST experiments (2, 3), provides a direct way to determine  $k_{ex}$ . Here, we aim to improve this method for *in vivo* tissue  $k_{ex}$  imaging by removing the overlapping water direct saturation (DS) signal or with induced saturation steady-states to shorten the saturation time.

**RESULTS:** We have demonstrated the applicability of the DS-removed omega plot method for mapping  $k_{ex}$  of phantoms, *in vivo* healthy human brains (4), and patients with MS (5) or stroke lesions (6). However, in these studies, to avoid long scanning time and potential high SAR or RF heat deposition, steady-state saturation required by the omega plot was approximated with a 1.5-second-long saturation pulse. We are developing a new clinically translatable MRI method to further shorten the saturation time for greatly reduced SAR, based on induced Saturation Transfer REcovery Steady State (iSTRESS).

Proton exchange can be modeled as a two-pool exchanging system between pool A (such as bulk water protons) and pool B (such as metabolites with exchangeable protons). Pool A signal stays constant at a steady-state only when the signal loss due to saturation transfer balances the signal gain due to T<sub>1</sub> recovery. We name this Saturation Transfer REcovery Steady State (STRESS). By obtaining two STRESS states using two different powers ( $B_{11}$  and  $B_{12}$ ),  $k_{ex}$  can be analytically solved, as verified with simulations based on Bloch-McConnell equations.

Yet, it takes a long time (up to 10 s) to reach the STRESS with conventional sequence (Fig. 4A). We, therefore, innovated the induced STRESS or iSTRESS MRI, where the steady states can be quickly reached after a pre-excitation pulse ( $\beta$ ) that flips the magnetization close to the steady-state value (Fig. 4B). By adjusting the pulse flip angle  $\beta$  ( $\beta_1$  and  $\beta_2$ ), the two different steady states can be induced with shortened saturation time (< 1s), allowing us to quantify  $k_{ex}$  with iSTRESS MRI.

**DISCUSSION and CONCLUSION:** The elevated tissue  $k_{ex}$  in pathological lesions could be due to the overproduction of free radicals as we've discussed earlier (4-6). The novel iSTRESS MRI shows great advantages by providing steady states with greatly shortened saturation time, reduced SAR, and improved clinical translatability toward *in vivo* MRI of tissue proton exchange rate.

**REFERENCES:** 1. Jones CK, et al., Neuroimage. 2013;77:114-24. 2. Dixon WT, et al., MRM. 2010;63(3):625-32. 3. Zhang S, Accounts of chemical research. 2003;36(10):783-90. 4. Shaghaghi M, Quant Imaging Med Surg. 2019;9(10):1686-96. 5. Ye H, J Magn Reson Imaging. 2021; 53(2):408-415. 6. Wang Z, et al., J Neurosci Methods. 2020;346:108926.

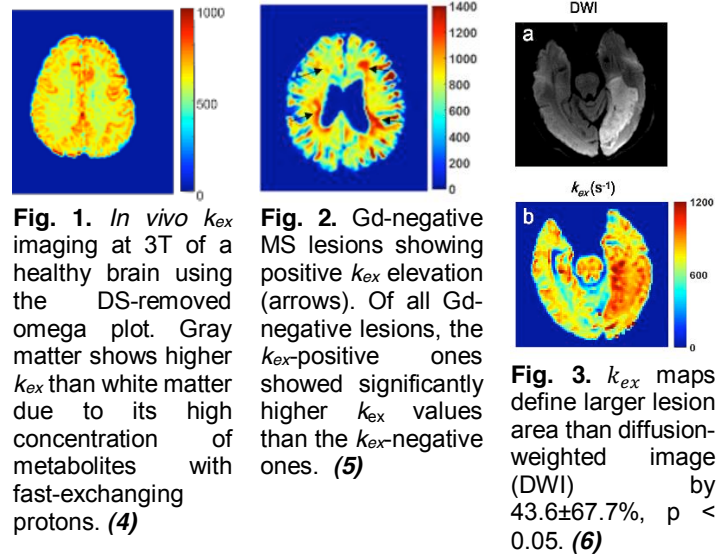


**Fig. 1.** *In vivo*  $k_{ex}$  imaging at 3T of a healthy brain using the DS-removed omega plot. Gray matter shows higher  $k_{ex}$  than white matter due to its high concentration of metabolites with fast-exchanging protons. (4)

**Fig. 2.** Gd-negative MS lesions showing positive  $k_{ex}$  elevation (arrows). Of all Gd-negative lesions, the  $k_{ex}$ -positive ones showed significantly higher  $k_{ex}$  values than the  $k_{ex}$ -negative ones. (5)

**Fig. 3.**  $k_{ex}$  maps define larger lesion area than diffusion-weighted image (DWI) by 43.6±67.7%,  $p < 0.05$ . (6)

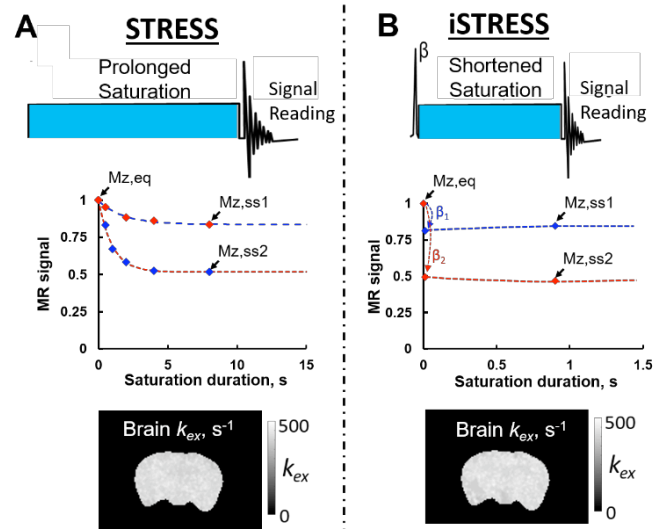


**Fig. 4.** A (top to bottom, 9.4T): STRESS MRI pulse diagram, MRI signals of the mouse brain, and brain  $k_{ex}$  map from 8s saturation. B) iSTRESS MRI uses a pre-excitation pulse ( $\beta^0$  flip) to greatly shorten the saturation time. In this example, iSTRESS MRI reduced saturation duration by 8 times compared to STRESS while producing a comparable  $k_{ex}$  map.

# CEST MRI Using Golden-Angle Cartesian Acquisition at 7T

Ding Xia, Rodolphe Leforestier, Li Feng, Xiang Xu

BioMedical Engineering and Imaging Institute, Icahn School of Medicine at Mount Sinai, New York, USA

✉ Apply Travel Fund

□ Oral Presentation □ Poster ✉ Either Oral or Poster Presentation | Contact Email: [xiang.xu@mssm.edu](mailto:xiang.xu@mssm.edu)

KEYWORD: You are encouraged to choose one or two keywords.

□ CEST agents □ Contrast Mechanism  
□ Tumor □ Stroke ✉ Neurology □ Body & MSK □ Standardization ✉ Novel Acquisition □ Machine Learning

## Introduction:

Chemical exchange saturation transfer (CEST) imaging enables indirect detection of molecules that contain labile protons through their exchange with water. In this study, we proposed a new 3D CEST MRI framework that combines golden angle rotated variable-density Cartesian acquisition<sup>1</sup> and multicoil compressed sensing reconstruction.

## Materials and Methods:

Our approach employs variable density golden-angle spiral acquisition that is sampled directly on a Cartesian grid. Following the CEST preparation, one “shot”, which include a number of phase-encoding steps predefined by the user in the  $k_y$ - $k_z$  plane, is acquired. Consecutive shots are rotated by the golden angle to allow for a uniform and continuous coverage of  $k$ -space.

The experiments were carried out at a Siemens Magnetom 7T scanner. Saturation was achieved by 20 gauss pulses, 50 ms each and 0.5 ms in between,  $B_{1rms}$  powers of 0.7 and 2.0  $\mu$ T. For image readout, 400  $k$ -space lines were acquired per shot after the saturation. 12 shots and 10 shots were acquired for the phantom and human study, respectively. The sampling trajectory was rotated by 137.5° between different shots, including those between each frequency steps (Fig. 1).

## Results and Discussions

We tested if reducing the number of shots used in image reconstruction can preserve the spectral features in the CEST spectra in the phantoms. We show that the spectra from images reconstructed using 3 shots showed negligible differences compared to that from images with 10 shots. (Fig. 1) For human brain study, no notable image artifacts or visible differences were observed. We calculated CEST maps using the Lorentzian fitting method.<sup>2, 3</sup> By using 3 shots with multicoil compressed sensing reconstruction with a spatiotemporal constraint, the CEST map is comparable to the map generated using 10 shots using a spatial constraint only, and potentially less noisy. (Fig. 2) The acceleration can bring the acquisition time down to approximately 5.5 min for 23 frequency steps with full brain coverage. Further works are needed to optimize the imaging acquisition and reconstruction method to improve the robustness against  $B_0$  and  $B_1$  inhomogeneities at ultra-high field and to test the method in dynamic CEST imaging studies.

## Conclusions

We proposed a 3D CEST imaging using a golden angle rotated and variable density Cartesian acquisition in combination with multi-coil compressed sensing reconstruction. We demonstrated that it is possible to obtain wholebrain CEST maps within approximately 5.5 min with this method, making it applicable to clinical applications.

## Reference

1. Cheng, J. Y.; et al, *J. Magn Reson Imag* **2015**, 42 (2), 407-20.
2. Deshmane, A.; et al, *Magn Reson Med* **2019**, 81 (4), 2412-2423.
3. Jones, C. K.; et al, *NeuroImage* **2013**, 77 (0), 114-124.

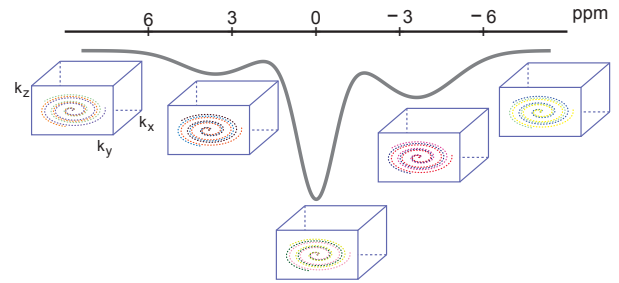


Figure 1. Illustration of the acquisition scheme. Consecutive shots are rotated by the golden angle, including shots between frequency steps.

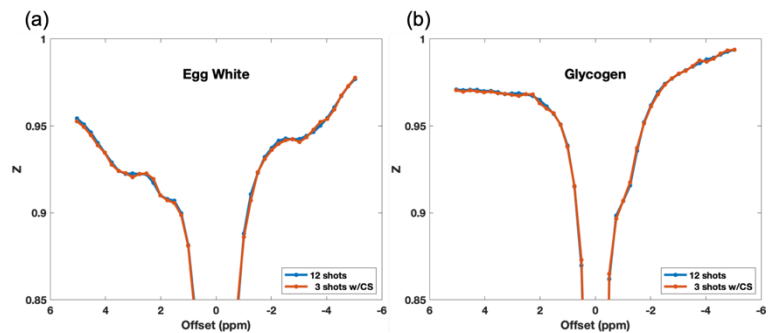


Figure 2. Z spectra generated from images reconstructed using 12 shots (blue) and 3 shots (orange) for the egg white (a) and the glycogen (b) phantoms.

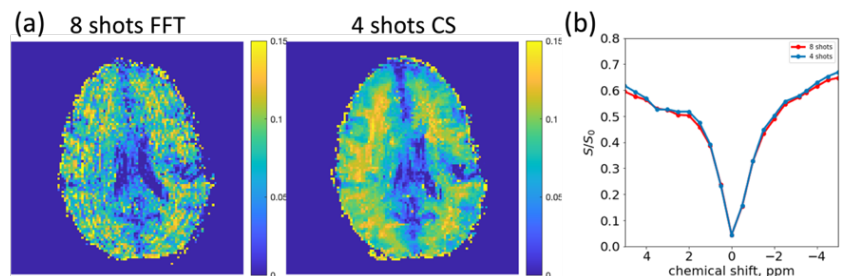


Figure 1. Amide proton transfer maps (a) from one slice and the corresponding Z spectra (b) from an ROI in the frontal white matter.

# Three-Dimensional Amide Proton Transfer (APT) Imaging Can Identify the Changes of Cerebral Cortex in Parkinson's Disease

Yaotian Tian<sup>1,2</sup>, Chunmei Li<sup>1</sup>, Min Chen<sup>1</sup>

<sup>1</sup> Department of Radiology, Beijing Hospital, National Center of Gerontology, Beijing, China

<sup>2</sup> Graduate School of Peking Union Medical College, Beijing, China

☒ Apply Student/Postdoc Travel Fund

☐ Oral Presentation ☐ Poster ☒ Either Oral or Poster Presentation | Contact Email:Charlotte3399@163.com

**KEYWORD:** You are encouraged to choose one or two keywords. ☐ CEST agents ☐ Contrast Mechanism  
☐ Tumor ☐ Stroke ☒ Neurology ☐ Body & MSK ☐ Standardization ☒ Novel Acquisition ☐ Machine Learning

**INTRODUCTION:** Parkinson's disease(PD) is a common neurodegenerative disorder. Researches has revealed the PD's early changes of the cerebral cortex in histopathology, metabolism, morphology and other aspects<sup>1</sup>. however, the specific mechanisms are unclear. Thus, new in vivo approaches to identify possible pathomechanisms of PD's cerebral cortex are highly desirable. Amide proton transfer (APT) imaging is a new molecular MRI method that allows detection of endogenous cellular proteins and peptides in tissue. Our previous studies has indicated that APT signal in substantia nigra decreased in PD patients, and it has a strong correlation with the progressive clinical manifestations of PD<sup>2-4</sup>. In this study, we hypothesized that Pathophysiology abnormality of PD will change the APT-related parameters in the cerebral cortex, and the signal changes can contribute to accurate diagnosis of Parkinson disease.

**METHODS:** 33 patients with sporadic Parkinson's disease and 37 age and sex matched healthy controls were enrolled in this prospective study. 3D-APT imaging with optimized turbo spin echo readout<sup>5</sup> was performed using a series of saturation pulse with a duration of 2 s and a saturation power level of 2.5  $\mu$ T. A dual-echo gradient echo sequence was used for B0 inhomogeneity mapping. 3D-T1WI was performed and segmented by using a volume-based morphometry algorithms and divide the cerebral cortex into 16 parts, including bilateral gray and white matter in the frontal, parietal, temporal and occipital lobes. Quantitative parameter maps of APT-related metrics, including CESTRnr, MTRasym and MTRRex, were calculated by using software SPM and MATLAB, and coregistered to 3D-T1WI to conduct a region-of-interest (ROI) analysis based on the predetermined anatomically relevant cortical areas. The unpaired Student t test or Mann-Whitney U test was used for comparison of these values between PD and controls. The receiver-operating characteristic (ROC) analysis were used to assess the diagnostic performances. The stepwise binary logistic regression model was used to combine the imaging parameters.

**RESULTS:** The CESTRnr, MTRasym and MTRRex had significantly higher values( $p < 0.01$ ) in the PD group than controls on the region of bilateral temporal gray matter. But only MTRRex on bilateral temporal gray matter regions showed a Significant difference ( $P < 0.05$ ) after a false discovery rate(FDR) correction. The binary logistic regression revealed that MTRRex and CESTRnr on the left temporal gray matter were significant predictors of PD ( $p < 0.05$ ), with an area under the ROC curve (AUC) of 0.72 and 0.68, separately. The combined parameters achieved the highest diagnostic performance(AUC: 0.76)

**DISCUSSION:** In this study, we compares the CESTRnr, MTRasym and MTRRex between PD group and Healthy controls, and evaluate their diagnostic performance towards PD. We found that the CESTRnr, MTRasym and MTRRex value on bilateral temporal gray matter increased in PD patients compared with controls, it may because of the abnormal accumulated protein in the PD's cortex<sup>6-8</sup>. In addition, MTRRex and CESTRnr on the left temporal gray matter were significant predictors of PD, the model combined these two parameters can achieved the highest diagnostic performance.

**CONCLUSION:** 3D-APT imaging could identify the changes of cerebral cortex in Parkinson's disease. The cortical changes of APT-related parameters could potentially serve as imaging biomarkers to aid in the non-invasive diagnosis of PD.

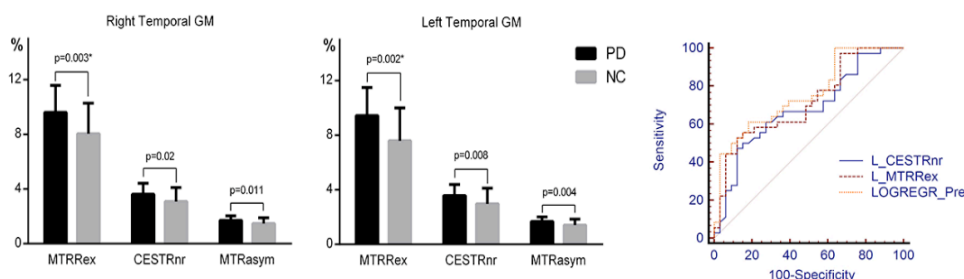


Figure 1 Group comparison of APT-related metrics on right temporal GM (a) and left temporal GM (b), (c) area under the ROC curve for MTRrex, CESTRnr and combined model on the left temporal GM.

\* indicate statistically significant differences between PD group and controls after a FDR Correction. GM= grey matter.

## REFERENCES:

Day 3 (Wednesday, 10<sup>th</sup> August 2022)



# Mapping pH using chemical exchange mediated stimulated echoes

Yu Zhao<sup>1</sup>, Zhongliang Zu<sup>1</sup>, Daniel F. Gochberg<sup>1</sup>

<sup>1</sup> Vanderbilt University Institute of Imaging Science, Vanderbilt University Medical Center, Nashville, Tennessee, USA

✉ Apply Student/Postdoc Travel Fund

✉ Either Oral or Poster Presentation | Contact Email: [yu.zhao.1@vumc.org](mailto:yu.zhao.1@vumc.org)

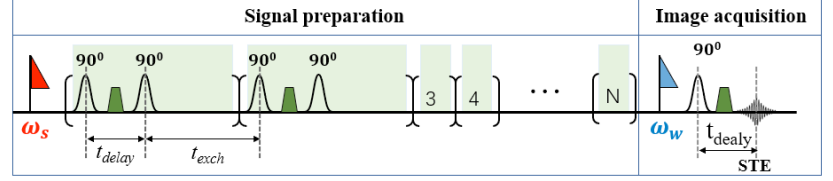
KEYWORD: Mapping pH. Contrast Mechanism

**INTRODUCTION:** RACETE (refocused acquisition of chemical exchange transferred excitations) is a recently developed approach to imaging solute exchange with water. We modified this sequence and further developed a protocol and corresponding metric with specific sensitivity to the solute exchange rate and hence a means for mapping pH.

**METHODS:** The RACETE approach has been well described in the original report [1], and the sequence is illustrated in Fig. 1A. The RACETE sequence makes two major changes to this conventional stimulated-echo (STE) sequence: 1) it applies the initial RF pulses at the solute resonance and the last RF pulse at the water resonance, hence creating an STE from magnetization that has moved from the solute to water; 2) it replaces the first two RF pulses by a train of labeling-transfer modules (LTMs), in which solute protons are selectively excited, labeled with a phase imprint, and stored as longitudinal magnetization, subsequently transferred to the bulk water. The labeled longitudinal magnetization accumulates in the bulk water with repeating LTMs. Finally, a 90° water-selective RF pulse is applied to the bulk water. Solute magnetization that was labeled by the gradients and then transferred to water is detected as a stimulated echo. In this study, in order to determine the exchange rate, dependency on other sample parameters ( $f_s$ ,  $T_{2s}$  and  $T_{1w}$ ) will be eliminated in a ratio metric (R) that is defined by two measurements. In the two measurements,  $t_{delay}$  is varied to encode the exchange rate, and  $t_{exch}$  is adaptively adjusted to keep  $t_{prep}$  and N unchanged.  $t_{delay}$  of two adjacent LTMs have a difference of  $\delta = \pi/\Delta\omega$  ( $\Delta\omega$ , the frequency offset of RF pulse), undesired stimulated echoes (induced by the off-resonance excitation on water) from the two LTMs will cancel due to their phase difference of  $\pi$  radians. A fast gradient-echo sequence with a variable flip angle (VFA-GE) that is tailored for the image readout. The proposed approach is validated by phantom experiments, in which the salicylic acid with a resonance at 9.4 ppm is used as contrast agent.

**RESULTS:** Fig. 6 shows results of phantom experiments, which demonstrates the influences of solute concentration ( $f_s$ ), relaxation times ( $T_{1s}$ ,  $T_{2s}$ ,  $T_{1w}$  and  $T_{2w}$ ), MT effects ( $f_m$ ),  $\Delta B_0$  ( $\Delta\omega$ ), and  $\Delta B_1$  ( $FA_{RACETE}$ ) on the ratio-metric based pH mapping. Fig. 6A shows the raw RACETE images in the two measurements with different  $t_{delay}$ , as well as their ratio-metric images for the pH mapping from Phantom #1. The ratio-metric images from Phantom #1 are used as reference (Fig. 6B) to be compared with results from other phantoms or acquisition conditions, each of which varies a single condition (pool size, relaxation rates, macromolecular concentration, or static or RF field homogeneity) that potentially confounds pH mapping. None of these variations have a significant effect on the ratio-metric dependence on pH, indicating that the RACETE

(A) The original sequence of RACETE:



(B) The modified sequence of RACETE:

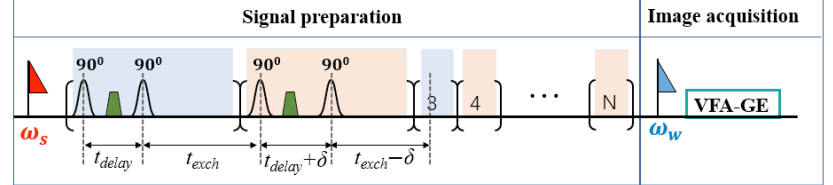


Fig. 1. Diagrams of RACETE sequences

approach to imaging pH is robust under both sample variations and field inhomogeneities. Note that  $\{T_{1w}, T_{2w}\}$  of phantoms with the concentrations of  $MnCl_2$  (0.12 mM, 0.8 mM) are measured as {1146 ms, 107 ms} and {703 ms, 59 ms}, respectively; although the relaxation times of the solute are not measured in this study, it can be inferred that these relaxation times also change with concentration of  $MnCl_2$ .

**DISCUSSION&CONCLUSION:** Based on RACETE, we proposed a fast ratio-metric pH-mapping method with minimal sensitivity to confounding factors such as the concentration of solute, relaxation rates, and MT effects, while remaining robust when there is inhomogeneous  $B_0$  and  $B_1$ .

**REFERENCES:** [1] Gutjahr FT, et al. Z Med Phys. 2019;29(2):184-191.

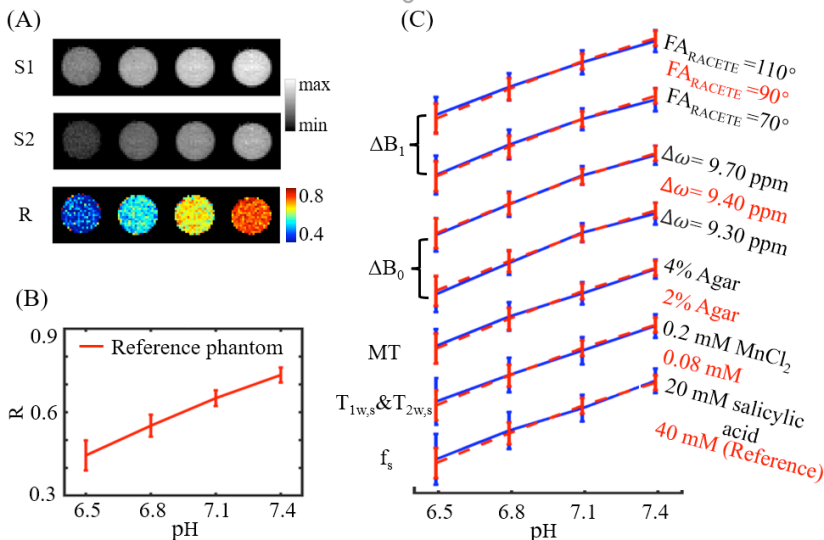


Fig. 2. Results of phantom experiments

# GraspCEST: 3D Steady-State CEST MRI Using Golden-Angle Radial Sparse MRI

Rodolphe Leforestier<sup>1</sup>, Ding Xia<sup>1</sup>, Kai Tobias Block<sup>2</sup>, Li Feng<sup>1</sup>, Xiang Xu<sup>1</sup>

1. BioMedical Engineering and Imaging Institute, Icahn School of Medicine at Mount Sinai, New York, USA
2. Center for Advanced Imaging Innovation and Research (CA<sup>2</sup>R) and Department of Radiology, New York University School of Medicine, New York, NY, USA

☑ Apply Student/Postdoc Travel Fund

☐ Oral Presentation ☐ Poster ☑ Either Oral or Poster Presentation | Contact Email: [xiang.xu@mssm.edu](mailto:xiang.xu@mssm.edu)

**KEYWORD:** You are encouraged to choose one or two keywords.

☐ CEST agents ☐ Contrast Mechanism  
☐ Tumor ☐ Stroke ☐ Neurology ☐ Body & MSK ☐ Standardization ☑ Novel Acquisition ☐ Machine Learning

## Introduction:

The purpose of this project was to develop a fast 3D CEST MRI technique called GraspCEST, which is based on the combination of CEST-prepared stack-of-stars golden-angle radial sequence and multicoil compressed sensing reconstruction [1]. Furthermore, multi-echo acquisition has been incorporated [2], enabling CEST quantification in water-only images without interrupting the steady state during data acquisition.

## Methods:

A CEST-prepared sequence with stack-of-stars golden-angle radial trajectory has been implemented, as shown in Figure 1. CEST preparation is performed right before the acquisition of each radial stack (i.e., all spokes corresponding to one acquisition angle). There is no delay between acquisitions of different stacks to achieve steady-state CEST imaging. Acquisition of each radial stack is done with centric-out ordering, and the rotation from one stack to the next follows the golden-angle scheme (i.e., adding 111.25°). Non-uniform fast Fourier transform (NUFFT) was first performed to reconstruct dynamic images using all acquired spokes. GRASP reconstruction was subsequently performed by exploiting spatiotemporal image correlations to reconstruct dynamic images using only a subset of stacks acquired in each measurement (43 stacks for phantom imaging, and 70 for liver imaging), corresponding to ~3 minutes and ~5 minutes scan time, respectively. For the multi-echo liver scan, fat/water separation was performed after image reconstruction.

## Results and Discussions

Figure 2 shows results from the glycogen phantom. The glycoNOE effect can be observed between -0.5 and -2 ppm. With GRASP, the number of views needed for image reconstruction can be reduced significantly without affecting the resulting Z-spectrum. This allows shortening the experiment from 10 min to 3 min, corresponding to 4 s per frequency offset per 3D volume. The in-vivo liver images were acquired using the multi-echo GRASP CEST method, which allows separation of water and fat using the Dixon technique. Throughout the dynamic acquisition, no motion-related artifact was observed. The GRASP reconstruction allows reducing the scan to 5 min while maintaining image quality. Compared to the glycogen phantom, the in-vivo Z-spectra show a broader resonance between -0.5 to -4 ppm, which represents glycoNOE (-0.5 to -2 ppm) and NOE exchange pathways from other mobile proteins (-2 to -5 ppm). GlycoNOE-weighted images were generated by taking the average difference between the acquired water Z-spectra and the Lorentzian fitted [3] spectra at -1 to -1.5 ppm (Figure 3).

## Conclusions

We present a new 3D steady-state CEST imaging method based on the GRASP technique. The improved motion robustness from radial sampling allows for free-breathing 3D CEST imaging of the liver. Moreover, the compressed-sensing reconstruction can accelerate imaging speed which allowing full Z-spectra acquisition of the liver within 5 min. In both phantoms and in vivo, we demonstrate that the GraspCEST technique can be used to detect the glycoNOE. Further validation and quantification of glycoNOE in vivo is needed.

## Reference

- [1] L Feng et al., Magnetic resonance in medicine **72** (3), 707 (2014).
- [2] T Benkert et al., Magnetic resonance in medicine **78** (2), 565 (2017).
- [3] CK Jones et al., Neuroimage **77**, 114 (2013).

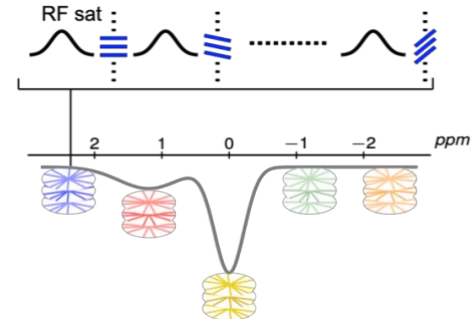


Figure 1. Illustration of steady-state GraspCEST acquisition scheme.

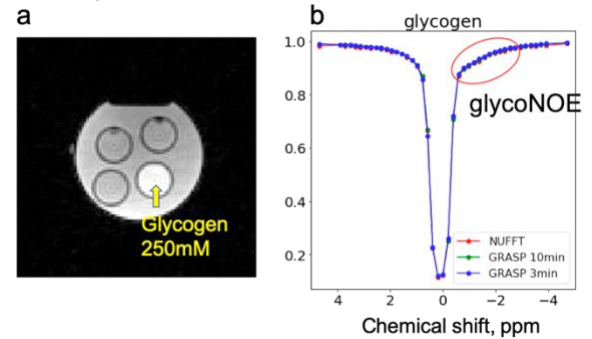


Figure 2. a, A phantom assembly that contains a vial of 250 mM glycogen in water; b, the z spectra from image generated from non-uniform fast Fourier transform (red), GRASP reconstruction using 150 stacks (green) and 43 stacks (blue).

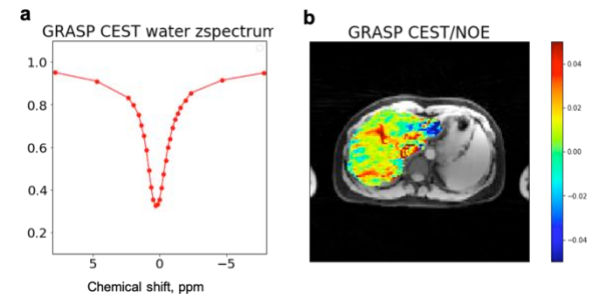


Figure 3. a. GraspCEST water Z-spectrum of the whole liver; b. The NOE map from GraspCEST

# SNR Optimized 3D EPI CEST Imaging Using Unevenly Segmented RF Irradiation

Hahnsung Kim<sup>1,2</sup>, Suhjung Park<sup>3,4</sup>, Phillip Zhe Sun<sup>1,2</sup>

<sup>1</sup> Emory National Primate Research Center, <sup>2</sup> Department of Radiology & Imaging Sciences, Emory University. <sup>3</sup> Department of Computer Engineering, Chonnam National University, South Korea, <sup>4</sup> Department of ICT Convergence System Engineering, Chonnam National University, South Korea

✉ Apply Travel Fund ✉ Either Oral or Poster Presentation ✉ Novel Acquisition

Contact Email: [hahnsung.kim@emory.edu](mailto:hahnsung.kim@emory.edu)

**INTRODUCTION:** 3D CEST MRI is often implemented with a long RF irradiation followed by a rapid image readout sequence such as echo-planar imaging (EPI) to cover the whole volume of the object [1]. However, it is challenging to increase the spatial and spectral coverage without extending the scan time or losing of CEST MRI effect. An unevenly segmented RF irradiation module, in which a long primary RF pulse generates the steady-state CEST effect with repetitive short secondary RF irradiation to maintain the CEST effect, has been developed for 2D multi-slice CEST imaging [2]. We proposed a novel 3D EPI acquisition in the framework of the segmented RF irradiation scheme to enhance CEST contrast. Numerical simulation and phantom studies were performed to validate optimal imaging protocols.

**METHODS:** Fig. 1 shows the proposed 3D CEST imaging with unevenly segmented RF irradiation configuration. Following a relaxation delay, a prolonged CW RF saturation is applied. Single-shot EPI readout encodes each kx-ky plane. Short secondary RFs are inserted between partition acquisition to maintain CEST contrast over the volumetric imaging.

Two-pool Bloch-McConnell simulations were performed to investigate the effect of FA on the SNR of CEST weighted image. The labile proton ratio and exchange rate were assumed to be 0.1% and 100 s<sup>-1</sup> at 3.5 ppm. We assumed Ts1/Ts2/Td = 1.5/0.3/1.5 sec, B<sub>1</sub> = 0.7 uT, and 40 partitions with centric reordering. Peak PSF amplitude was measured with varying FAs and shot/saturation.

Phantom data in the sagittal orientation were acquired at a 3T Siemens whole-body MAGNETOM Trio scanner (Siemens Medical Solution). The mixture of 1.5% agarose and 100 mM l-carnosine was doped with MnCl<sub>2</sub> (15μM, 30μM). Two vials were inserted into a 500 ml container with 1.5% agarose. The MRI parameters were: B<sub>1</sub> = 0.7 uT, offset frequencies from -5 to 5 ppm with increments of 0.125 ppm, Ts1/Ts2 = 1.5/0.3 sec, Td = 1.5 sec, FOV = 140 x 108 x 80 mm<sup>3</sup>, 2 mm isotropic spatial resolution, and number of partition = 40. CEST contrast was measured with varying FAs from 10° to 80° with a 10° increment. We compared 3D CEST images with/without short secondary RF in axial oriented images (y-z planes). The conventional 3D CEST imaging without short saturation took 6 min 23 sec, and the proposed method with 8 and 4 shot/sat took 8 min 26 s, and 10 min 29 s, respectively.

**RESULTS:** Fig. 2 shows contour plots of peak PSF amplitude at 3.5 ppm and effective volume acquisition time. Peak amplitude rises with increasing FA in a range of small FA (≤ 25°), while the amplitude of PSF gradually falls with increasing FA. The effective volume acquisition time ( $T_{eff,vol}$ ) was calculated by volume acquisition time of measured data/volume acquisition time without short saturation RF.  $T_{eff,vol}$  increased with decreasing shot/saturation. Fig. 3 demonstrates the effect of FA on the CEST contrast of the proposed 3D CEST imaging. As compared to the conventional 3D CEST imaging without short saturation RF configuration, the proposed method showed high SNR CEST contrast in the range of small FA. However, due to the signal modulation along the z-direction, imaging blurring leads to losing CEST contrast with high FA.

**CONCLUSION:** Our work demonstrated 3D CEST imaging with unevenly segmented RF irradiation configuration reduces the loss of CEST contrast during volumetric acquisition. With a compromise between SNR and imaging time, we can find the optimal parameters of FA (near 20°) and ranges of shot/sat (4~8). The proposed method integrated with the parallel imaging technique can be further extended to clinical applications.

**REFERENCES:** 1. Akeby S, *et al.* Magn Reson Med 2019;82:1741-1752. 2. Sun *et al.*, Magn Reson Med 2011;65:588-94

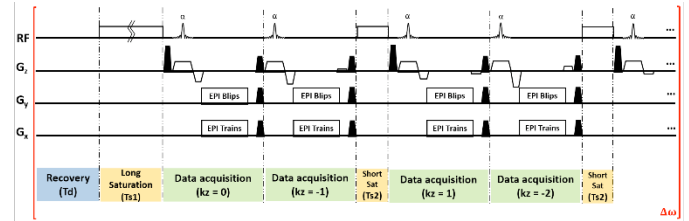


Fig 1. The schematic of the 3D CEST imaging with unevenly segmented RF irradiation

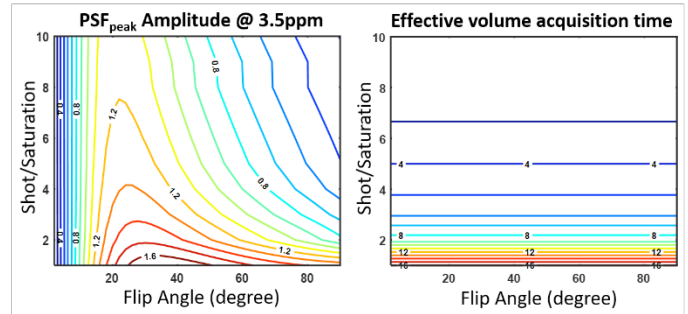


Fig 2. Contour plot of peak PSF amplitude and effective volume acquisition as a function of FA and shot/saturation.

Fig. 3. a) Axial oriented (y-z plane) CEST contrast images with varying FAs acquired from the conventional 3D CEST imaging (1<sup>st</sup> row), the proposed method with 8shot/sat (2<sup>nd</sup> row), and 4shot/sat (3<sup>rd</sup> row). Upper/lower vial was doped 15 / 30 μM MnCl<sub>2</sub>, respectively. b) Mean CEST contrast as a function of FA. Red circle indicated the ROI.

Fig. 3. a) Axial oriented (y-z plane) CEST contrast images with varying FAs acquired from the conventional 3D CEST imaging (1<sup>st</sup> row), the proposed method with 8shot/sat (2<sup>nd</sup> row), and 4shot/sat (3<sup>rd</sup> row). Upper/lower vial was doped 15 / 30 μM MnCl<sub>2</sub>, respectively. b) Mean CEST contrast as a function of FA. Red circle indicated the ROI.

Fig. 3. a) Axial oriented (y-z plane) CEST contrast images with varying FAs acquired from the conventional 3D CEST imaging (1<sup>st</sup> row), the proposed method with 8shot/sat (2<sup>nd</sup> row), and 4shot/sat (3<sup>rd</sup> row). Upper/lower vial was doped 15 / 30 μM MnCl<sub>2</sub>, respectively. b) Mean CEST contrast as a function of FA. Red circle indicated the ROI.

Fig. 3. a) Axial oriented (y-z plane) CEST contrast images with varying FAs acquired from the conventional 3D CEST imaging (1<sup>st</sup> row), the proposed method with 8shot/sat (2<sup>nd</sup> row), and 4shot/sat (3<sup>rd</sup> row). Upper/lower vial was doped 15 / 30 μM MnCl<sub>2</sub>, respectively. b) Mean CEST contrast as a function of FA. Red circle indicated the ROI.

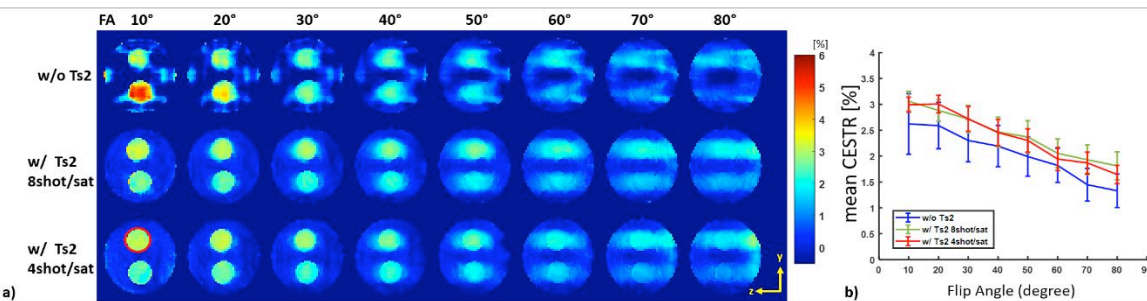


Fig 3. a) Axial oriented (y-z plane) CEST contrast images with varying FAs acquired from the conventional 3D CEST imaging (1<sup>st</sup> row), the proposed method with 8shot/sat (2<sup>nd</sup> row), and 4shot/sat (3<sup>rd</sup> row). Upper/lower vial was doped 15 / 30 μM MnCl<sub>2</sub>, respectively. b) Mean CEST contrast as a function of FA. Red circle indicated the ROI.



# New Advanced Principal Component Analysis method for an improved and safe clinical 3T CEST MRI denoising

Stefano Casagrande<sup>1</sup>, Christos Papageorgakis<sup>1</sup>, Feriel Romdhane<sup>1,2</sup>, Eleni Firippi<sup>1</sup>, Timothé Boutelier<sup>1</sup>, Laura Mancini<sup>3,4</sup>, Moritz Zaiss<sup>5</sup>, Sotirios Bisdas<sup>3,4</sup> and Dario Longo<sup>2</sup>

<sup>1</sup> Department of Research & Innovation, Olea Medical, La Ciotat, France, <sup>2</sup> Institute of Biostructures and Bioimaging (IBB), National Research Council of Italy (CNR), Torino, Italy, <sup>3</sup> Lysholm Department of Neuroradiology, University College of London Hospitals NHS Foundation Trust, London, United Kingdom, <sup>4</sup> Institute of Neurology UCL, London, United Kingdom, <sup>5</sup> Department of Neuroradiology, University Clinic Erlangen, Friedrich-Alexander Universität Erlangen-Nürnberg (FAU), Erlangen, Germany

☑ Oral Presentation ☐ Poster ☐ Either Oral or Poster Presentation

Contact Email: [stefano.casagrande@olea-medical.com](mailto:stefano.casagrande@olea-medical.com) KEYWORD: ☑ Neurology ☑ Standardization

**INTRODUCTION:** Principal Component Analysis (PCA) has been successfully used for denoising purposes in multi-acquisition MRI (including CEST MRI). Many methods rely on the eigenvalues<sup>1,2,3</sup> with the risk of discarding pathological information hidden in the noise of the extracted components, as eigenvalues measures blindly the variance of components regardless if it is noise or relevant clinical information. In this work we propose a PC-related-image-based method to overcome this problem. **METHODS: Technical Solution:** A Z-Spectrum for a given voxel can be expressed as:  $Z_i = \bar{z}_i + \sum_j \alpha_{ij} v_j$ , where  $\bar{z}_i$  is the mean value of the Z-Spectra,  $v_j$  is a principal component and  $\alpha_{ij}$  is the coefficient of  $v_j$  of voxel  $i$ . Collecting all  $\alpha_{ij}$  coefficients of a component  $j$ , we obtain the PC related image of the  $j^{th}$  component (see Figure1). Our proposed method, called Component Analysis based on Standard-deviation Attenuation (CASA) criterion is based on the decrease of the variance of a PC related image after a smoothing filter is applied on it, as detailed in the following steps (see Figure2). **STEP-1:** PCA is performed to obtain the  $N$  PC related images. The standard deviation (std) of the voxels of each PC related image is computed to form the vector  $\sigma^a = [\sigma_1^a, \dots, \sigma_N^a]$ . Then a Gaussian smoothing filter of a factor  $\Sigma$  is applied to each PC related image and std is recomputed on it to obtain  $\sigma^b = [\sigma_1^b, \dots, \sigma_N^b]$ , where  $\sigma^a \geq \sigma^b$ . The rate of decrease of std is then computed, for each component, as  $\sigma^r = (\sigma^a - \sigma^b) / \sigma^a$ , where  $0 \leq \sigma_i^r \leq 1$ . Components whose rate  $\sigma_i^r$  is on the plateau of the curve are rejected (see Figure2, components 12-29). **STEP-2:** Before the signal reconstruction a smoothing filter or denoising method can be applied on the retained PC related images. The strength of the applied filter is proportional to the amount of information that the  $i^{th}$  component carries, expressed in  $\sigma_i^r$ , as  $w_i^r = (\sigma_i^r - \sigma_1^r) / (\sigma_{plateau}^r - \sigma_1^r)$  (see Figure2, components 1-11). This allows to optimize the filtering method based on the amount of noise and information present in each component. **STEP-3:** The retained component coefficients are projected back in the original space and used for the denoised data reconstruction. Carrying out only the first and third step, we call the method "CASA basic", and "CASA advanced" when all three steps are applied. **Patient and synthesized data:** WASAB1 and APTw data on a glioma patient were acquired on a 3T MRI system (MAGNETOM Prisma; Siemens Healthcare, Erlangen, Germany) with a 3D snapshot-GRE CEST protocol<sup>4</sup> (C2PMPI03). Olea Sphere 3.0 (Olea Medical, La Ciotat, France) was used to compute B0/rB1 map from WASAB1 and correct the APTw-Z-Spectra. The Z-Spectra (25 offset, -6ppm/6ppm, step=0.5ppm) were then fitted with the Bloch-McConnell equations using a 5-pool model<sup>5,6</sup>. The phantom was corrupted by several percentage levels of Rician noise (0.25%, 0.5%, 1%, 3% of the maximum intensity for each Z-Spectrum) in the spectral domain. The phantom data were PCA denoised using both CASA methods, Malinowski, Nelson and Median selection criteria<sup>1</sup>. MTRAsym (at 3.5ppm) maps were computed on the ground truth and on various denoised data. These maps were used for comparison. **RESULTS:** PSNR, SSIM, Correlation and MSE were used to evaluate the goodness of the various denoising methods. For all noise levels "advanced CASA" metric leads to the best results (highest PSNR/SSIM/Correlation and LowestMSE). Figure3 shows the results for "1% Rician noise". **DISCUSSION:** A new PCA denoising methodology has been proposed for CEST MRI data, optimized to preserve anatomical structures and pathological information, leading to encouraging preliminary results. **CONCLUSION:** An additional investigation should be performed to compare the advanced CASA method with other PCA advanced denoising methods in the literature<sup>2,3</sup>. **ACKNOWLEDGMENTS:** AIRC MFAG 2017 - ID. 20153 project, the European Union's Horizon 2020 R&I programme under grant agreement No 667510 and the Department of Health's NIHR funded BRC at UCL. SB and LM are supported by the NI of HRBRC, UCLH NHS Trust. **REFERENCES:** 1- Breitling J, *et al.* NMR in Biomedicine 2019; 32(11):e4133. 2- Veraart J, *et al.* Neuroimage 2016; 142:394-406. 3- Ma X, *et al.* Neuroimage 2020; 215:116852. 4- Deshmane A, *et al.* Magn Reson Med 2019; 81(4):2412-23. 5- Khlebnikov V *et al.* NMR in Biomedicine 2017;30: e3687. 6- Zhang L *et al.*, Quant Imaging Med Surg 2019;9(10):1714-1730.

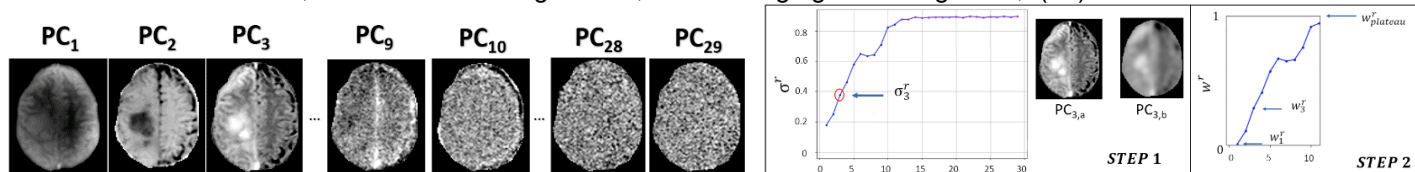


Figure1. PC images from APTw acquisition in a glioma patient.

Figure2. Steps 1 & 2 of the CASA PCA criterion for the same patient.

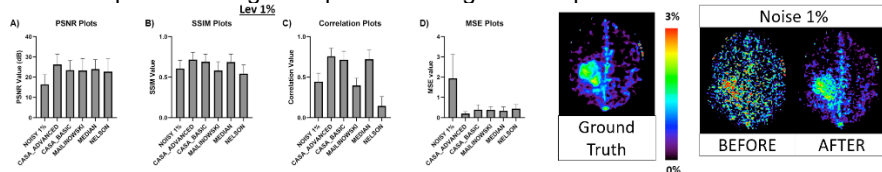


Figure3. Quantitative analysis of the performance of the PCA denoising methods on MTRAsym (3.5ppm) maps for "1% Rician noise".



Thank you for our sponsors



EMORY  
UNIVERSITY



SIEMENS  
Healthineers

PHILIPS  
Healthcare

